

REPORT DOCUMENTATION PAGE			Form Approved OMB No. 0704-0188		
Public reporting burden for this collection of information is estimated to average 1 hour per response, including the time for reviewing instructions, searching existing data sources, gathering and maintaining the data needed, and completing and reviewing this collection of information. Send comments regarding this burden estimate or any other aspect of this collection of information, including suggestions for reducing this burden to Department of Defense, Washington Headquarters Services, Directorate for Information Operations and Reports (0704-0188), 1215 Jefferson Davis Highway, Suite 1204, Arlington, VA 22202-4302. Respondents should be aware that notwithstanding any other provision of law, no person shall be subject to any penalty for failing to comply with a collection of information if it does not display a currently valid OMB control number. PLEASE DO NOT RETURN YOUR FORM TO THE ABOVE ADDRESS.					
1. REPORT DATE (DD-MM-YYYY) 13-07-2009		2. REPORT TYPE Dissertation		3. DATES COVERED (From - To)	
4. TITLE AND SUBTITLE Three Dimensional Imaging of Helicon Wave Fields Via Magnetic Induction Probes				5a. CONTRACT NUMBER	
				5b. GRANT NUMBER	
				5c. PROGRAM ELEMENT NUMBER	
6. AUTHOR(S) Michael P. Reilly (ERC)				5d. PROJECT NUMBER	
				5e. TASK NUMBER	
				5f. WORK UNIT NUMBER 33SP0708	
7. PERFORMING ORGANIZATION NAME(S) AND ADDRESS(ES) Air Force Research Laboratory (AFMC) AFRL/RZST 4 Draco Drive Edwards AFB CA 93524-7160				8. PERFORMING ORGANIZATION REPORT NUMBER AFRL-RZ-ED-TP-2009-282	
9. SPONSORING / MONITORING AGENCY NAME(S) AND ADDRESS(ES) Air Force Research Laboratory (AFMC) AFRL/RZS 5 Pollux Drive Edwards AFB CA 93524-7048				10. SPONSOR/MONITOR'S ACRONYM(S)	
				11. SPONSOR/MONITOR'S NUMBER(S) AFRL-RZ-ED-TP-2009-282	
12. DISTRIBUTION / AVAILABILITY STATEMENT Approved for public release; distribution unlimited (PA #09340).					
13. SUPPLEMENTARY NOTES For authors Ph.D. Dissertation at the University of Illinois at Urbana-Champaign, 2009.					
14. ABSTRACT The majority of data presented in this work is for a helicon plasma discharge driven at 13.56 MHz, 500 Watts input power, 900 Gauss applied magnetic field, 10 mTorr neutral Argon gas, and cylindrical plasma of 5 cm diameter approximately 50 cm long. High frequency magnetic induction probes were developed to measure helicon wave propagation using a new technique for frequency calibration through an impedance analyzer; up to 100 MHz. This work demonstrates magnetic field measurements in high frequency plasma are greatly simplified through this new frequency characterization method. Line-lengths and transmission-cable-types are readily identified as diagnostic limiting factors. The magnetic probe design enables the first 3-dimensional imaging of plasma waves through detailed radial and axial measurements. Strong agreement is obtained between the measured br, bθ, and bz radial profiles with the numerical solutions of helicon waves when a non-uniform radial density profile is considered. The axial helicon wavelength predicted by the non-uniform radial density theory also agrees with the measured wavelength when the full three dimensional wave is accurately analyzed. In some cases, the differences between the three dimensional wavelength and the numerically solved values are less than 30%. This is in contrast to the two dimensional wavelengths which can differ from the numerical values by greater than 100%. We show a complete visual representation of helicon waves through 3-d imaging...					
15. SUBJECT TERMS					
16. SECURITY CLASSIFICATION OF:			17. LIMITATION OF ABSTRACT	18. NUMBER OF PAGES	19a. NAME OF RESPONSIBLE PERSON
a. REPORT	b. ABSTRACT	c. THIS PAGE			Dr. Brian Beal
Unclassified	Unclassified	Unclassified	SAR	222	19b. TELEPHONE NUMBER (include area code) N/A

THREE DIMENSIONAL IMAGING OF HELICON WAVE FIELDS
VIA MAGNETIC INDUCTION PROBES

BY

MICHAEL P. REILLY

B.S., University of Illinois at Urbana-Champaign, 2003

M.S., University of Illinois at Urbana-Champaign, 2005

DISSERTATION

Submitted in partial fulfillment of the requirements
for the degree of Doctor of Philosophy in Nuclear Engineering
in the Graduate College of the
University of Illinois at Urbana-Champaign, 2009

Urbana, Illinois

Doctoral Committee:

Professor George H. Miley, Chair

Professor Roy A. Axford

Professor David N. Ruzic

Professor J. Gary Eden

Dr. Brian E. Beal, Air Force Research Laboratory

THREE DIMENSIONAL IMAGING OF HELICON WAVE FIELDS VIA MAGNETIC INDUCTION PROBES

Michael P. Reilly, Ph.D Candidate.
Department of Nuclear Engineering
University of Illinois at Urbana-Champaign, 2009
George H. Miley, Adviser

The majority of data presented in this work is for a helicon plasma discharge driven at 13.56 MHz, 500 Watts input power, 900 Gauss applied magnetic field, 10 mTorr neutral Argon gas, and cylindrical plasma of 5 cm diameter approximately 50 cm long.

High frequency magnetic induction probes were developed to measure helicon wave propagation using a new technique for frequency calibration through an impedance analyzer; up to 100 MHz. This work demonstrates magnetic field measurements in high frequency plasma are greatly simplified through this new frequency characterization method. Line-lengths and transmission-cable-types are readily identified as diagnostic limiting factors. The magnetic probe design enables the first 3-dimensional imaging of plasma waves through detailed radial and axial measurements. Strong agreement is obtained between the measured b_r , b_θ , and b_z radial profiles with the numerical solutions of helicon waves when a non-uniform radial density profile is considered. The axial helicon wavelength predicted by the non-uniform radial density theory also agrees with the measured wavelength when the full three dimensional wave is accurately analyzed. In some cases, the differences between the three dimensional wavelength and the numerically solved values are less than 30%. This is in contrast to the two dimensional wavelengths which can differ from the numerical values by greater than 100%. We show a complete visual representation of helicon waves through 3-d imaging which provides significantly more accurate analysis of the helicon wavelength.

This work also observed a density peak downstream of the antenna / source through axial density measurements with a RF compensated Langmuir probe (calibrated against a 90 GHz microwave interferometer). Here, the downstream density peak is explained in terms of a global energy balance modeled by an axially decaying electron temperature peaked at the source; $T_e \rightarrow 3 - 7$ eV. This model does not require an assumption of a RF plasma or additional heating by helicon wave absorption; rather the model demonstrates excellent agreement with the measured axial density profiles when radial losses are assumed to be less than 10%, which is reasonably attributed to the axially applied static magnetic field.

The new diagnostic methods developed in this work (both probe characterization and analysis of measured data) provide fundamental insight into laboratory helicon plasma. The methods and results derived here will supplement and aid the design of future helicon plasma sources.

ACKNOWLEDGEMENTS

I would like to start by thanking my adviser, Dr. George H. Miley. He has completely supported and guided me over the past six years of graduate school. Dr. Miley has always been completely accessible even on vacation; I would cite my visit to discuss helicons with him when he was visiting family in Walnut Creek, CA. I sometimes forget that as an undergraduate senior in Aerospace Engineering, he gave me an opportunity to work in his Fusion Studies Lab in 110 NRL. It was here that I became enamored with doing research and made the decision to pursue graduate school. I would say that my very first lesson regarding experimental research was the great difficulty in using a Dremel on Alumina ceramic. Thank you.

I would next like to thank every member of my committee: Dr. Roy A. Axford, Dr. David N. Ruzic, Dr. J. Gary Eden, and Dr. Brian E. Beal. These men exemplify “open-door policy”. They have always been willing to take time for a discussion and offer advice and suggestions. They are immensely intelligent and my only fear is I did not exploit them as a resource as frequently as I should have.

Many great thanks go to Brian Jurczyk and Robert Stubbers of Starfire Industries. It was working with them in which I was first introduced to RF plasma. Brian and Robert have always taken time to look at data I show them and have discussions on all types of plasma work. I recall the first time I met Brian in NRL; I was an undergraduate and was seeking someone to get advice from on graduate school, I went into his office where he was a post-doc having a discussion with some students. I asked if “Dr. Jurczyk” was

here, smiles and some laughter from nearby students immediately followed. Apparently it was okay to call him “Brian”; the “Dr.” title was not frequently used. To this day, I still get a little confused on when to use the titles “Dr.”, “Prof.”, or “first name”. I think I’ve defaulted to just assuming everyone I meet is “Dr.”. Regardless, Starfire has been an extraordinary resource that will forever shape who I am. I like to think that I was Starfire’s first employee and have always let them know I wish to return to Starfire when they finally open their “West-Coast Operations”.

The Air Force Research Laboratory at Edwards AFB, CA should also be thanked for giving me the opportunity to freely explore RF plasma work. They gave me the ability to design and implement an entire experiment / program on RF plasma from the ground up. Although very isolated, Edwards AFB allowed me the opportunity to be within 10 miles of the best margaritas in the country at Domingo’s Restaurant and the opportunity to witness several Space Shuttle landings. The double sonic boom is truly amazing to hear upon reentry. On the professional side, I thank Garrett Reed for help in Labview and with the microwave interferometer. I know there were times when both of us just wanted to take a sledge-hammer to it (that would have been a costly fix). Also, I would like to thank William Lewis, he greatly assisted in performing some of the magnetic probe frequency analysis with the impedance analyzer as well as quickly learning IGOR to assist in developing the code to analyze the thousands of probe traces we collected. I know at times it was mindless busy work, but you did an awesome job. I’d also like to thank the Skipworth family (David and Linda) who provided me with some comic relief and a sounding board for when the Air Force protocol grew frustrating. John Morrow

and David Skipworth both were immensely helpful in building the faraday cage and wiring all things which require power. Without them, the Electric Propulsion lab at Edwards would not function. I'd also like to thank Dr. David Kirtley. A graduate of the University of Michigan and the Electric Propulsion lab (now at MSNW, LLC) Dave is a great personal friend and colleague who I hope to know for many years. He's someone that's always been willing to have long conversations regarding serious science questions that are often too simply answered i.e., "what's an electron?" or "what's gravity?".

Thanks Dave.

My parents, Dennis and Christine Reilly, deserve much gratitude. They are both unconditionally loving parents and have always encouraged me to do what makes me happy. They are patient and respectful and I never would be as successful without them. Your company and home have always offered a serene safe haven from the business of the world. I love you both always. Thank you.

I'd also like to thank the many friends (brothers and sisters count too) that have helped shape the person I am today. You are too many to name and we have too many memories to recount (you could check out my Picasa page for a few). You know who you are and your contributions to my life are worthy of a second dissertation alone. I love you all. Thank you.

TABLE OF CONTENTS

NOMENCLATURE	x
LIST OF FIGURES	xiii
LIST OF TABLES	xix
CHAPTER 1: INTRODUCTION	1
1.1 Whistler Waves	1
1.2 Helicon History	2
1.3 Helicon Research	4
1.4 Relevant Previous Work	10
1.5 Objective of This Work	14
1.6 References	16
CHAPTER 2: THEORY OF HELICON WAVES	25
2.1 Plasma Waves	26
2.2 Bounded, Collisionless, Uniform Density Dispersion Relation	29
2.3 Uniform Density with Collisions: The Trivelpiece-Gould Mode Revealed	33
2.4 Non-uniform Radial Density Distribution: Numerical Solutions	40
2.5 Chapter Summary	46
2.6 References	47
CHAPTER 3: EXPERIMENT AND TEST SETUP	49
3.1 Vacuum System	49
3.2 Experiment	50
3.3 Antennae	53
3.4 References	56
CHAPTER 4: DIAGNOSTICS	57
4.1 High Frequency b-dot Probes	57
4.1.1 Magnetic Probe Theory	58
4.1.2 Magnetic Probe Calibration	60
4.1.3 Magnetic Probe Capacitive Pickup	63
4.1.4 Probe Characterization	66
4.1.4.1 Selection	66
4.1.4.2 Frequency Response	67
4.1.5 Discussion	70
4.1.6 Probe Analysis in Plasma	72
4.2 RF Compensated Langmuir Probe and Microwave Interferometer	76

4.2.1 RF Compensation.....	76
4.2.2 Obtaining the RF IV Characteristic	80
4.2.3 Microwave Interferometer	83
4.2.4 Testing and Calibration.....	85
4.3 Error Analysis	86
4.4 Chapter Summary	89
4.3 References.....	90
CHAPTER 5: RESULTS AND DISCUSSION.....	93
5.1 Identification of Helicon Waves	94
5.1.1 Forward – Reflected Power Spectrum	94
5.1.2 Density ‘Jumps’	98
5.1.3 Radial b_z - Profiles	100
5.2 Axial b_r , b_θ , and b_z - Profiles	108
5.2.1 Single Axis b_z Profiles	109
5.2.2 Two- and Three- Dimensional b_z Profiles	111
5.2.3 Three Dimensional Wavelengths	117
5.2.4 b_r , b_θ Measurements.....	119
5.3 Axial Density Measurements.....	122
5.3.1 Downstream Density Peak.....	125
5.3.1.1 Global Energy Balance Model.....	125
5.3.1.2 Sample Temperature Profiles.....	129
5.3.1.3 Application to the Present Data	132
5.4 Additional Cases of Interest: Conical Antennae.....	140
5.4.1 Converging Conical Antenna.....	140
5.4.2 Diverging Conical Antenna	141
5.5 Ionization Cost Analysis	143
5.6 Chapter Summary	145
5.7 References.....	146
CHAPTER 6: Conclusions AND FUTURE WORK	148
6.1 On Theory	148
6.2 On Diagnostics.....	150
6.3 On Three Dimensional Results	152
6.4 On Downstream Density Peak and Model	153
6.5 On Possible Use as an Electric Propulsion Device	155

6.5 Final Summary	156
6.6 References.....	157
APPENDIX A: PLASMA WAVES MODEL	158
A.1 Derivation of the CPDR.....	158
A.2 The CMA Diagram	161
A.3 References	165
APPENDIX B: CODE FOR NON-UNIFORM DENSITY WAVE FIELDS	166
B.1 MATHEMATICA Code	166
APPENDIX C: IGOR CODE FOR FFT OF B-DOT SIGNALS	170
C.1 Code Written and Implemented in IGOR	172
APPENDIX D: SAMPLE IV CHARACTERISTIC AND ANALYSIS	175
D.1 Constructing an IV Characteristic.....	175
D.2 Analysis of IV Characteristic	178
D.3 Plasma Potential, Electron Temperature, and Density.....	182
D.4 References	185
APPENDIX E: μ WAVE INTERFEROMETER: CALIBRATION – ANALYSIS	186
E.1 AFRL’s Microwave Interferometer.....	186
E.2 Calibration and Analysis	191
APPENDIX F: RADIAL b_z FIELDS – PRESSURE, POWER, MAGNETIC FIELD ...	196
CURRIVULUM VITAE.....	200

NOMENCLATURE

a	radius	meter
A	area	m ²
AC	alternating current	
A _{eff}	effective area	m ²
AFRL	Air Force Research Laboratory	
A _{probe}	probe area	m ²
b _r	radial magnetic field	Gauss
b _x	x-direction magnetic field	Gauss
b _y	y-direction magnetic field	Gauss
b _θ	azimuthal magnetic field	Gauss
b _z	radial magnetic field	Gauss
B ₀	magnetic field strength	Tesla or Gauss
c	speed of light	m/s
c _s	acoustic velocity	m/s
C	capacitance	Farads
cpdr	cold plasma dispersion relation	
CTT	center tapped transformer	
d	distance between end rings	m or cm
D	difference of right and left handed waves	hybrid resonance
DAQ	data acquisition	
DC	direct current	
e	electric charge	C
E	electric field	Volt/meter
EMI	electro-magnetic interference	
EP	Electric Propulsion	
f	driving frequency	Hz or 1/s
f _{co}	cutoff frequency	Hz or 1/s
FFT	Fast Fourier Transform	
h _a	radial sheath density ratio	
h _L	axial sheath density ratio	
HPH	High Power Helicon	
I	current	Amperes
ID	inner diameter	m or cm
I _{electron}	electron saturation current	Amps
IV	current-voltage	
j	current density	A/m ²
k	wave number or Boltzmann constant	m ⁻¹ or J/K
K _{el}	elastic scattering rate constant	m ³ /s
K _{ex}	excitation rate constant	m ³ /s
K _{iz}	ionization rate constant	m ³ /s
k _{TOT} or β	total wave number	m ⁻¹
k _z	axial wave number	m ⁻¹
k	parallel wave number	m ⁻¹
k _⊥	perpendicular wave number	m ⁻¹

l	plasma chord length & coil length	m or cm
l_a	antenna length	m or cm
L	inductance	Henries
L	left handed wave	ion cyclotron resonance
m_j	mass of ion or electron	kilogram
mHTX	mini Helicon Thruster eXperiment	
M	Argon mass	kilogram
n	plasma density or index of refraction	m^{-3} or unit
N or n	number of turns	unit
n_{sa}	density of radial sheath	m^{-3}
n_{sL}	density of axial sheath	m^{-3}
n_0	neutral gas density	m^{-3}
OD	outer diameter	m or cm
p	pressure	Torr or mTorr
P	plasma wave	
P_{abs}	absorbed power	Watts
P_{FWD}	forward power	Watts
P_{RFL}	reflected power	Watts
P_{TOT}	total power	Watts
q_j	charge of ion or electron	Coulomb
r	radius or radial direction	m or cm
r_p	probe radius	m or cm
R	right handed wave	electron cyclotron resonance
RC	resistor-capacitor	
RF	radiofrequency	
R_{sheath}	sheath resistance	Ω
S	sum of right and left handed waves	hybrid resonance
$S.A._{cyl}$	surface area of a cylinder	m^2
$S.A._{disk}$	surface area of a disk	m^2
t	time	seconds
T_e	electron temperature	eV
T_{e0}	initial electron temperature	eV
TG	Trivelpiece-Gould	
u_B	Bohm velocity	m/s
UCLA	University of California – Los Angeles	
UHP	ultra high purity	
VASIMR	VARIABLE Specific IMPulse Rocket	
v_j	velocity of ion or electron	meter/second
V_{cap}	capacitive voltage	Volts
V_{ind}	inductive or induced voltage	Volts
$V_{floating}$	probe floating potential	Volts
V_{plasma}	plasma potential	Volts
v_p or v_{phase}	phase velocity	m/s
V_s	sheath voltage	Volts
w	Gaussian beam width & coil width	cm
WOMBAT	Waves On Magnetized Beams and Turbulence	

z	axial direction	m or cm
Z_0	impedance	Ω
Z_{eq}	equivalent impedance	Ω
Z_L	inductor impedance	Ω
Z_{LOAD}	load capacitor impedance	Ω
Z_{plasma}	plasma impedance	Ω
Z_{probe}	probe impedance	Ω
Z_{series}	series impedance	Ω
Z_{sheath}	sheath impedance	Ω
Z_{TUNE}	tuning capacitor impedance	Ω
$Z_{ }$	parallel impedance	Ω
α	exponential decay constant	
χ_{CYL}	axial loss factor or confinement factor	
χ_{DISK}	radial loss factor or confinement factor	
ϵ_c	collisional energy loss	eV
ϵ_e	electron kinetic energy loss	eV
ϵ_{ex}	excitation energy	eV
ϵ_i	ion kinetic energy loss	eV
ϵ_{iz}	ionization energy	eV
ϵ_j	dimensional charge of ion or electron	
ϵ_0	permittivity of free space	F/m
ϵ_{TOT}	total energy loss	eV
Φ_B	magnetic flux	Tesla-m ²
λ_0	mean free path or beam width	m or cm
λ_D	Debye length	m or cm
$\lambda_{Helicon}$	helicon wavelength	m or cm
λ_z	axial wavelength	m or cm
λ_{\perp}	perpendicular wavelength	m or cm
μ	atomic mass ratio	a.m.u.
μ_0	Permeability of free space	N/A ²
η	plasma resistivity	Ω -m
σ	electrical conductivity	S/m
σ_{10}	standard deviation	
θ	phase angle or azimuthal direction	degrees
ν_{ei}	electron-ion collision frequency	Hz
ω	driving frequency	rad/s
ω_{ci}	ion cyclotron frequency	rad/s
ω_{ce}	electron cyclotron frequency	rad/s
ω_{LH}	lower hybrid frequency	rad/s
ω_{pi}	ion plasma frequency	rad/s
ω_{pe}	electron plasma frequency	rad/s

LIST OF FIGURES

Figure 1.1. Axial b_z and density measurements from Franck 2005 Ref. [69]. Plots (a) and (b) are for different B_0 field strengths and the line-types correspond to the density scans.....	11
Figure 1.2. Axial b_r and b_z measurements from Boswell 1984 Ref. [8].	12
Figure 1.3. Axial b_z measurements from Chen 1995-1996 Refs. [15,17].....	12
Figure 1.4. Axial density profile illustrating downstream density peak from Chen 1995-1996 Refs. [16-17]. The antenna end rings are shown by the shaded lines straddling the $z=0$ location.	13
Figure 1.5. Axial density profile with downstream density peak from Tysk 2003-2004 Ref. [71]. Density scale is logarithmic.	14
Figure 2.1. CMA diagram with $m_i / m_e = 5$	27
Figure 2.2. CMA diagram in terms of n vs. B	28
Figure 2.3. Internal b_r , b_θ and b_z fields for $a = 2.5$ cm, $m = +1$ antenna driven at 13.56 MHz in a 900 Gauss uniform magnetic field with a uniform radial density of $n_0 = 1 \times 10^{19} \text{ m}^{-3}$	33
Figure 2.4. Separation of TG branch and Helicon branch for $n_0 = 1 \times 10^{19} \text{ m}^{-3}$	36
Figure 2.5. Difference when finite electron mass effects are considered. The secondary TG branch is revealed. This is for $B_0 = 900$ Gauss and $n_0 = 1 \times 10^{19} \text{ m}^{-3}$	37
Figure 2.6. TG-H dispersion curves different densities at $B_0 = 900$ Gauss.	38
Figure 2.7. Gaussian profiles of waist size ' w ' for $n_0 = 1 \times 10^{19} \text{ m}^{-3}$ and tube radius $a = 2.5$ cm.....	43
Figure 2.8. b_z fields for Gaussian radial density profiles.	44
Figure 2.9. $-ib_r$ fields for Gaussian radial density profiles.....	44
Figure 2.10. b_θ fields for Gaussian radial density profiles.....	45
Figure 2.11. Influence of density profiles on wavenumber between two wave branches.	46
Figure 3.1. Schematic of vacuum diffusion chamber with pump locations.....	49
Figure 3.2. RF power delivery system incorporating the auto-match network circuit.	51
Figure 3.3. Schematic of AFRL Experimental Helicon research station.....	52

Figure 3.4. Axial applied magnetic field.	53
Figure 3.5 a,b,c. Examples of different antennae used in helicon research.	54
Figure 3.6. Conical geometry tube; can be converging with B_0 or diverging with B_0	55
Figure 3.7. Applied Magnetic Field with Location and Lengths of Tested Antennas.	55
Figure 4.1 Low inductance 120 Ω resistor; impedance frequency response.	61
Figure 4.2. Frequency response of 50 Ω resistor and coaxial alligator breakouts as measured with a function generator and oscilloscope.	63
Figure 4.3. Illustration of inductive and capacitive signals present when magnetic field probes are used in plasma.	64
Figure 4.4. Two B-dot probes orientated 180 degrees with respect to one another; signal is subtracted through CTT.....	65
Figure 4.5. Center-Tapped Transformer with b-dot probes and differential voltage probe.....	66
Figure 4.6. Coil inductance and parasitic capacitance that will determine probe / coil resonance frequency.....	67
Figure 4.7. Impedance frequency response for twisted shielded pair and coaxial cable.	69
Figure 4.8. Line length effect from probe to CTT.....	70
Figure 4.9. Two probe 180 degree spatial orientation;.....	71
Figure 4.10. Raw Magnetic Probe Signal.....	73
Figure 4.11. FFT of Raw Probe Signal.....	73
Figure 4.12. Raw Voltage Data Trace.	75
Figure 4.13. FFT of Raw Voltage Data Trace.....	75
Figure 4.14. Schematic of Langmuir Probe Notch Filters and Compensation Circuitry.	77
Figure 4.15. Impedance Curve for Four Series Notch Filters.....	78
Figure 4.16. Overall Langmuir probe circuit frequency response.	79
Figure 4.17. Electrical schematic of Langmuir probe data acquisition.	81

Figure 4.18. Langmuir Probe IV trace.....	82
Figure 4.19. Langmuir Probe IV trace.....	82
Figure 4.20. Schematic of the millimeter I/Q Phase Bridge Interferometer.	84
Figure 4.21. Calibration deflections in the I and Q branches of the microwave interferometer.....	86
Figure 4.22. 10 T_e values for the corresponding IV characteristics with error bars shown.	87
Figure 4.23. 10 n values for the corresponding IV characteristics with error bars shown.....	88
Figure 5.1. Forward vs. Reflected Power at 47 sccm; 10 mTorr fill pressure.	95
Figure 5.2. RF power delivery system incorporating the auto-match network circuit.	96
Figure 5.3. Radial plasma density profiles at 900 Gauss for various input power levels on a 5 cm diameter quartz tube at 13.56 MHz.	98
Figure 5.4. Downstream radial density profiles at 500 Watt, 900 Gauss.	99
Figure 5.5. b_z profiles at 10 mTorr and various input power and magnetic field strengths. Green borders indicate well matched with theory where 'w' indicates the Gaussian density profile width. Yellow borders indicate probe interference with helicon wave mode. Red borders indicate insufficient conditions for wave propagation.	102
Figure 5.6. Radial density profiles corresponding to the b_z data.	103
Figure 5.7. Theoretical density profiles compared with experimentally measured.	105
Figure 5.8. Differences in calculated b_z wave profiles for radial density profiles $w = 1.0, 1.7$ as compared with the experimentally measured profiles.	106
Figure 5.9. Applied Magnetic Field with Location and Lengths of Tested Antennas.	108
Figure 5.10. Single axis scan for the b_z wave fields taken at three different radial locations.....	110
Figure 5.11. Single axis scan for the b_z wave fields for the 14.2 cm antenna length.....	111
Figure 5.12. Single axis scan for the b_z wave fields for the 11.2 cm antenna length.....	111
Figure 5.13. Phase shift for 2-d representation of 3-d helix.	112
Figure 5.14. 2-d representation of single phase helix.	113

Figure 5.15. 3-d helix represented by the series of 2d phase shifted waves.	113
Figure 5.16. Node numbering scheme for typical 2-d b_z cross-section.	114
Figure 5.17. Three dimensional helicon b_z fields. Antenna lengths: 22.6, 14.24, and 11.19 cm. Antenna edge located at $z = 0$ cm. Wave propagation and static magnetic field in the $+z$ direction.....	115
Figure 5.18. Two dimension b_z wave fields taken across center of tube. Antenna lengths of 22.6, 14.2, and 11.2 cm. Antenna location is at $z = 0$ cm and wave propagation and static magnetic field are in the $+z$ direction.....	115
Figure 5.19. Radial density profiles matched with Gaussian to be numerically solved for the wavelength. The full antenna length is 22.6 cm.	116
Figure 5.20. Wavelength solution based on axial varying Gaussian density profiles.....	117
Figure 5.21. 2-d cross sections showing the radial decrease in the wave over an axial length. Radial length decreases from ~ 1 cm to ~ 0.75 cm over ~ 15 cm axially.....	118
Figure 5.22. b_r , b_θ , b_z wave fields for 14.24 cm antenna. All scans were taken in the $y=0$ plane and therefore b_r and b_θ can also be designated as b_x and b_y , respectively.	121
Figure 5.23. Comparison of b_r contour plots for 14.2 cm and 11.2 cm antenna lengths.	122
Figure 5.24. Axial density profile down tube centerline for 22.6 cm antenna. Dashed lines indicate end rings of antenna.....	123
Figure 5.25. Axial density profile down tube centerline for 14.24 cm antenna. Dashed lines indicate end rings of antenna.....	123
Figure 5.26. Axial density profile down tube centerline for 11.19 cm antenna. Dashed lines indicate end rings of antenna.....	124
Figure 5.27. Representation of plasma volume for energy balance.....	126
Figure 5.28. Exponentially decaying axial temperature profile.....	130
Figure 5.29. Axial density variation based on an exponentially decaying temperature profile illustrating a downstream peak in the plasma density.	130
Figure 5.30. Rate constants K_{xx} variation due to temperature profile.	131
Figure 5.31. Total energy loss ϵ_{TOT} due to temperature profile.	131
Figure 5.32. Measured density and electron temperature profiles for 11.2 cm antenna.	132

Figure 5.33. Modeled and measured electron temperature profiles.....	133
Figure 5.34. Modeled and measured density profiles for 11.2 cm antenna.	134
Figure 5.35. Refined calculated profile assuming confinement factors for particle loss areas.....	136
Figure 5.36. Measured density and temperature profiles for 14.2 cm antenna.	136
Figure 5.37. Measured and modeled temperature profiles for the 14.2 cm antenna.....	137
Figure 5.38. Measured and calculated density profiles for the 14.2 cm antenna.	138
Figure 5.39. Measured and calculated axial density profiles for the 22.6 cm antenna.	138
Figure 5.40. Modeled axial electron temperature; axial decay.....	139
Figure 5.41. Converging conical axial b_z scans.....	140
Figure 5.42. Converging conical tube axial density profile.....	141
Figure 5.43. Diverging conical axial b_z scans.	142
Figure 5.44. Diverging conical tube axial density profile.	143
Figure 5.45. Ionization “cost” for the three different antennae tested.	144
Figure A.1. CMA diagram with $m_i / m_e = 5$	161
Figure A.2. Density vs. Magnetic field graphs for Helium, Argon, and Xenon driven at 13.56 MHz.....	163
Figure C.1. Output from IGOR code of analysis of b-dot probe signals.	170
Figure D.1. Representative IV Characteristic with clearly defined regions and transitions.	175
Figure D.2. Voltage vs. time; Current vs. time data used to construct raw IV Characteristic.	176
Figure D.3. Raw IV Characteristic with 1000 point cubic spline fit.	176
Figure D.4. Lafromboise plot for various values of probe radius to Debye length.	179
Figure D.5. Approximate constant values for probe radius to Debye length ratios.....	180
Figure D.6. Plot of $\ln(I_e)$ vs. Voltage for determine the plasma potential.	181
Figure D.7. Plot of I^2 vs. Voltage.	183

Figure E.1. Schematic of the millimeter I/Q Phase Bridge Interferometer.....	185
Figure E.2. Raw signals from both I- and Q- branch as the Mica sheet is incrementally inserted further into the waveguide causing a phase shift.	191
Figure E.3. Normalized and horizontally shifted I- and Q- branches as the Mica sheet is traversed across the waveguide.	192
Figure E.4. Normalized and 2π scaled location of the Mica sheet insertion for the point where interferometry data was taken.	193
Figure E.5. Voltage deflections in the I- and Q- branches of the microwave interferometer used to obtain β	194
Figure F.1. b_z profiles at 10 mTorr and various input power and magnetic field strengths.....	196
Figure F.2. b_z profiles at 8 mTorr and various input power and magnetic field strengths.....	196
Figure F.3. b_z profiles at 6 mTorr and various input power and magnetic field strengths.....	197
Figure F.4. b_z profiles at 4 mTorr and various input power and magnetic field strengths.....	197
Figure F.5. b_z profiles at 2 mTorr and various input power and magnetic field strengths.....	198
Figure F.6. b_z profiles at 0.5 mTorr and various input power and magnetic field strengths.....	198

LIST OF TABLES

Table 5.1. Summary of Expected and Measured Wavelengths.	116
---	-----

CHAPTER 1: INTRODUCTION

The primary objective of this research will be to accurately quantify the helicon wavelength. This will be accomplished through a detailed and innovative method toward magnetic probe design used to measure the helicon plasma wave fields. The purpose is to provide thorough analysis of helicon waves through three dimensional imaging in support of future design and understanding of helicon plasma sources.

The term ‘helicon’ was first used in 1960 by Aigrain [1], to describe waves that propagate in the presence of a magnetic field for the frequencies between the ion and electron cyclotron frequencies. More generally, helicon waves are a subclass of whistler waves in the sense helicons propagate in a bounded system [2], specific to this study, a cylindrical boundary. There exist other complexities to helicon waves that separate them from the theory of whistler waves and these differences will be evident in Chapter 2. This chapter will introduce helicon waves and discuss the evolution of studying helicon waves since the 1960’s. Specifically, this chapter will highlight the simplicity in generating helicon plasma but the difficulty in characterizing the plasma and understanding the results. A layout for the remainder of the dissertation is also provided.

1.1 Whistler Waves

Whistler waves were first investigated by Storey in the 1950’s [3]. Storey performed measurements on ‘whistling atmospherics’ which were described as waves which follow “the lines of force of the earth’s magnetic field” and were recorded by audible “clicks” or a descending “whistling” tone. The theory predicts right-handed circularly polarized

waves that propagate in free space where ion effects and collisions are neglected.

Whistler waves are typically referenced when helicons are discussed due to the similarity in deriving both dispersion relations.

1.2 Helicon History

Helicon plasma is generated by driving an antenna at a frequency between the electron and ion cyclotron frequencies. The antenna is usually wrapped around an insulating cylinder. As the power is increased, the antenna current induces a magnetic field which drives an electric field within the cavity according to Faraday's law of induction. The power to the antenna is continually increased until the electric field creates a breakdown of the neutral gas. This is considered inductively generated plasma. To drive helicon waves, a DC magnetic field surrounds the cylindrical cavity altering the properties of the plasma dielectric medium. Typically, this is accomplished by increasing the plasma density (through input power) or increasing the applied magnetic field. Helicon waves propagate when these quantities reach appropriate levels (determined by the dispersion relation). Typical laboratory parameters are: pressure (mTorr), driving frequency (MHz), input power (100's Watts), DC magnetic field (100's Gauss), tube diameter (cm), and tube length (10's cm).

Early research on helicons primarily consisted of characterizing the wave generated plasma source without a specific application for the device [4-7]. It was not until the 1970's and 1980's when groups in Australia [6, 8-12] and at the University of California

Los Angeles (UCLA) [2, 13-31] began extensive investigation into helicon waves for plasma processing.

One benefit of helicons for plasma processing lies in the efficient generation of high densities ($> 10^{18} \text{ m}^{-3}$) for relatively low input powers (0.1 – 1 kW) while maintaining low plasma potentials ($< 100 \text{ Volts}$) [12]. Additionally, the ability to generate uniform density plasma over large areas is attractive for etching onto large wafers or substrates [19].

More recently, helicons have been considered for plasma space propulsion [22, 32-46]. They have been considered either as an ionization source with a secondary stage for acceleration or as a stand-alone propulsion device. Concepts such as VASIMR [33, 35, 42] utilize helicons as an ionization source and worry about magnetic field detachment separately. Similarly, annular geometry helicon plasma is being investigated as a primary stage for space propulsion [45, 47] and will have to address detachment and / or acceleration scenarios following the source. Conversely, other devices such as the High Power Helicon (HPH) [38] at the University of Washington or the mini Helicon Thruster eXperiment (mHTX) [46] at MIT are utilizing helicons as stand-alone propulsion devices however, these experiments do not clearly address the mechanisms for particle detachment or thrust.

A proposed method to circumvent the problem of detachment is utilizing double layer formation [36, 37, 39, 44, 48] in helicon plasma. The claim for this acceleration

mechanism is that a ‘sharp’ potential drop occurs downstream at lower pressures (< 1 mTorr) in helicon plasma, which can accelerate ions to supersonic speeds. This reported mechanism still has many questions as to what causes the double layer formation (helicon plasma/geometry discontinuities/expansion along B-field lines). Additionally, generating helicon plasma at such low pressures may prove more difficult in terms of power or B-field requirements since the medium will have a relatively lower plasma density than at higher pressure (mTorr vs. sub-mTorr). In any event, it is the author’s belief that adapting helicons to space propulsion stands a greater chance of success when utilized solely as an ionization source. The mechanism of laboratory helicon double layers has yet to be explained whereas the use of helicons as a high-density ionization source is well documented.

1.3 Helicon Research

Helicon waves were initially studied in metals and semiconductors by Libchaber [49] and Rose [50] in the early 1960’s. They observed wave propagation at frequencies much less than the electron cyclotron frequency with wave vector \mathbf{k} parallel to the applied DC magnetic field. However, it was Lehane and Thoneman [4] who performed the first comprehensive study of helicon waves in gaseous Xenon where neutral gas pressures ranged 10 – 70 mTorr. The experiment consisted of a cylindrical Pyrex tube; 10 cm diameter – 100 cm length. Power was fed to an exciting coil by a 3 kW generator at frequencies variable from 15 – 17 MHz. An axial B_0 -field of up to 500 Gauss was applied over the middle 50 cm of the discharge cylinder. A goal of the work was to compare experimental results with the theory of plasma wave propagation in an insulated

cylinder for a uniform radial density profile originally derived by Legendy in 1964 [51, 52] and Klozenberg, McNamara, and Thoneman in 1965 [53] (KMT theory). Good agreement was shown with wave field measurements through b-dot probes scanned across the diameter of the cylinder. Peak densities of $3 - 15 \times 10^{18} \text{ m}^{-3}$ were obtained with a double Langmuir probe as the magnetic field was increased from 70 – 510 Gauss. Results at the higher magnetic fields did not agree as well with the lower field tests; however, the radial density profiles also indicated a greater non-uniformity which could account for the discrepancies [4].

Kuckes (1968) [5] and Nyack (1975) [7] also observed good agreement with uniform radial density theory observing right handed circularly polarized waves. However, it was Nyack and Christiansen [7] in 1974 who first considered a non-uniform radial density profile. They considered a “top-hat” (step function) and parabolic profile which were solved numerically and compared with experimental results for the wave fields. They found good agreement with results provided the density profile used was similar to the one measured experimentally.

Some of the more extensive measurements on helicons consisted of the work by Boswell [6, 8-11] at Flinders University in Australia and Chen [2, 13-31] at UCLA. Both groups have thoroughly characterized a range of sources with variables including: antenna configuration, source diameter, input power, matching network configuration, applied B_0 field, driving frequency, and neutral gas pressure. The primary diagnostics used by both

groups have been b-dot probes and RF compensated Langmuir probes with the intent of measuring the wave fields, plasma density, and electron temperature.

Beginning in 1970 [6] and later in 1984 [8], Boswell performed plasma wave field measurements on a 5 cm and 10 cm diameter Pyrex tube; although measurements on the 5 cm tube were “highly distorted due to the plasma being significantly perturbed by the probes”. Experiment conditions were driving frequency of 8.8 MHz, pressure 1.5 mTorr, applied DC magnetic field up to 1500 Gauss. Radial b_r , b_θ , and b_z measurements were taken and agreement with the theoretical profiles was shown. Axial b_r and b_z measurements down the centerline of the tube were also taken and the axial wavelength was reported by phase changes of 180 degrees being observed at successive minima in wave amplitude. During density measurement, Boswell also observed density jumps at distinct but not all operating conditions as the antenna length and power were altered. The observed density jumps will be discussed later in this work in Chapter 5.

In 1987, Boswell published further density ‘ n ’ vs. B_0 magnetic field measurements for the Waves On Magnetized Beams And Turbulence (WOMBAT) experiment again showing density ‘jumps’ at some operating conditions [10]. This time the experiments were run on a 20 cm diameter tube with antenna driven at 7 MHz, pressure 30 mTorr, and power up to 1.5 kW. Later in 1989, Boswell performed similar density measurements on a 6 cm diameter, 13.56 MHz, 1200 Gauss source tube [11]. The point being conveyed for work on helicon plasma is the large variety of source variables which can often make comparisons between different research groups difficult. Most groups have now settled

on operation at 13.56 MHz; which will be the frequency used throughout the current study.

Beginning in the early 1990's, UCLA and Chen began publishing work on their helicon efforts. In 1991, Chen provided a detailed derivation for wave field solutions due to uniform radial density profiles in terms of Bessel function solutions [2]. Although this work had been previously considered, a comprehensive analysis for experimental design aspects was also considered. It was also in this work that Chen introduced a thorough analysis including a collisional damping term in Ohm's law when solving for the plasma wave field. Collisional effects gave rise to a second branch in the theoretical derivation which was deemed an electrostatic wave; in helicon literature, now commonly referred to as the radial Trivelpiece-Gould (TG) wave.

In 1993, Chen thoroughly derived numerical solutions for non-uniform radial density profiles based off of parabolic distributions [15] for obtaining the b_r , b_θ , and b_z wave fields. Although this work was first considered by Shoji [54] in 1993, the results were not as comprehensive, though Shoji did provide similar numerical results and describes the electrostatic wave branch in addition to the helicon branch. Shoji also discusses the merging of the two branches at low frequency or low magnetic field as the parallel and perpendicular wave numbers become equal. Further numerical solutions and wave absorption effects were considered by Kramer in 1999 and 2007 [55-57] with similar results. The TG branch will be described in further detail in Chapter 2.

In 1994, Sudit and Chen published RF compensation techniques for making density and temperature measurements in RF plasma [58]. Their technique is similar to earlier work by Godyak [59, 60] where sheath impedances are considered with respect to probe impedances for filtering or removing unwanted RF pickup. Previous density and temperature measurements on helicons had not thoroughly described whether compensation had been considered and the impact on quantitative results.

ULCA's experiment consisted of a 2.5 cm and 5.0 cm diameter tube with an antenna driven at 27.12 MHz. Pressures considered were approximately 10 – 20 mTorr, powers up to 2 kW, and applied magnetic fields from 0 – 900 Gauss. In the mid 1990's UCLA performed extensive investigation into radial and axial density, temperature, and wave field measurements. Axial measurements to determine the helicon wavelength were based on single axis b_z scans down the discharge centerline using magnetic induction (b-dot) probes. Wavelengths on the order of 10's cm (or approximately the length of the antenna) were reported based off phase measurements where local wavelengths agreed with the dispersion relation [29, 31]. The work of UCLA in 1995 was also one of the first to report on a "downstream density peak" up to several wavelengths away from the antenna (source). This phenomenon has been explained as a consequence of decay in electron temperature away from the source [31]. At this location "the ionization rate is low and the diffusion rate is large, so that production and loss mechanisms would not be expected to produce a peak". However, performing an energy balance, they were able to show a density rise due to the temperature decay. Additionally, since nearly all power is

absorbed in the near field antenna region of the helicon discharge the density peak was not due to any significant wave absorption downstream [31].

Transition between capacitive – inductive – helicon modes (E-H-W modes respectively) were investigated in 1996 by Ellingboe and Boswell [61] which were described by differences between the radial wave profiles and radial density profiles. Radial density profiles of helicon plasma are more centrally peaked whereas capacitive and inductive plasma exhibit more uniform profiles.

Work on helicon plasma prior to 2000 had suggested the high efficiency and absorption of the discharge was due to Landau damping, however, no significant population of high energy electrons had been observed and this effect has since been ruled out [21].

Following 2000, some of the more basic research has been on identifying the existence of TG waves (predicted by including electron mass effects) in the region of the antenna.

Inclusion of these effects reveals the electrostatic radial wave; considered radial because the perpendicular wave number k_{\perp} is approximately equal to the total wave number \mathbf{k} .

The first experimental evidence of TG waves was reported by Blackwell in 2002 [26] using a J-dot current probe (miniature Rogowski coil). Success in observing helicon TG waves was observed for an $m = 0$ antenna at low (< 100 Gauss) magnetic fields. The lower magnetic fields ‘expand’ the TG wavelength by lowering the perpendicular wavenumber whereas at higher magnetic fields the TG waves have been too localized (sub-cm) to accurately measure.

The vast majority of theoretical work has neglected ion effects; the ions being massive and slow allow this to be a reasonable assumption. However, some groups have recently considered this effect to be non-negligible due to discharge operation near the lower hybrid frequency where it is possible for the ions to exchange energy with the wave [62-66]. The impact of ion effects on the helicon wave profiles is not yet known, especially considering how strongly the theoretical consideration of non-uniform radial density profiles agrees with experimental results. Additionally, some groups have considered radially localized helicon modes (RLH modes) as opposed to TG waves to explain the high power absorption within helicon plasma. However, experimental evidence of this has been limited [67, 68] and the implication of this theory is not yet understood.

1.4 Relevant Previous Work

Previous research relevant to analyzing the helicon wavelength and plasma discharge focus on two primary aspects: measurements of the b_z -field on the z-axis centerline and understanding the downstream density peak away from the antenna / source. Much work to date has taken an axial location (typically underneath an end ring of the antenna) and performed radial scans here. It has been fortuitous that this location for radial scans was selected because helicon waves are truly three-dimensional helices (this will be shown later). Consequently, the radial wave profiles will ‘turn over’ (rotate in phase) as the axial distance away from the source is traversed. Additionally, axial measurements to date have been performed along the centerline of the plasma discharge for quantifying the helicon wavelength. This method will be shown to be inaccurate because valuable information regarding the axial wavelength is lost in the radial direction. Inclusion of the

radial helix component which contributes to the axial wavelength may assist in the explanation of why theoretical predictions apparently overestimate the helicon wavelength. A discussion of this overestimation was provided by Franck in 2005 [69] where helicon wavelengths were identified based on b_z scans for a 10 cm diameter tube as shown in Figure 1.1 along with the axial density profile.

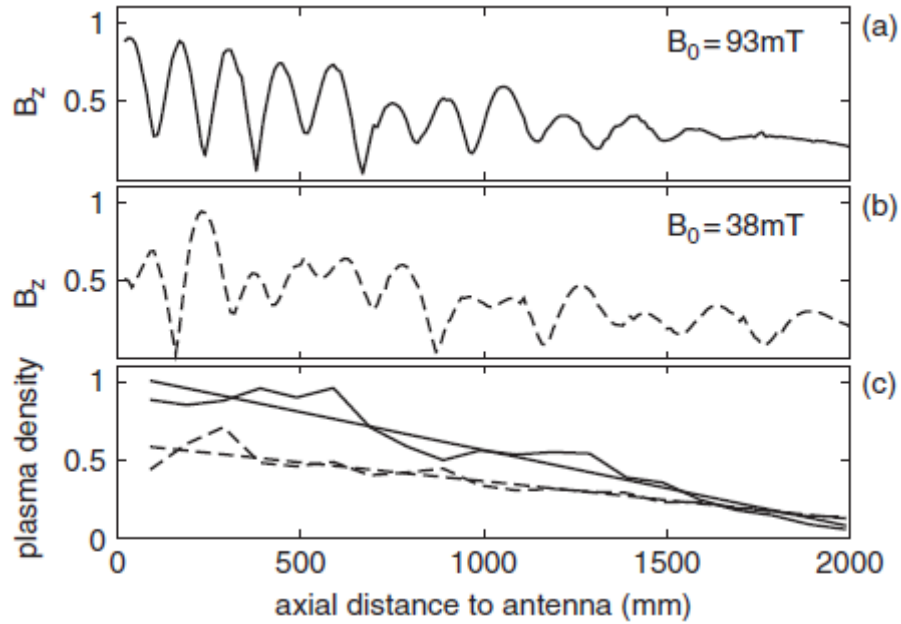


Figure 1.1. Axial b_z and density measurements from Franck 2005 Ref. [69]. Plots (a) and (b) are for different B_0 field strengths and the line-types correspond to the density

Boswell showed similar measurements in 1984 [8] on a 10 cm diameter tube for b_r and b_z with axial scans taken down the discharge centerline shown in Figure 1.2 while Chen performed a similar measurement in 1995 [16, 17] on a 5 cm diameter tube with axial b_z profiles shown in Figure 1.3. All results were much less than the predicted values as calculated from the dispersion relation and boundary conditions.

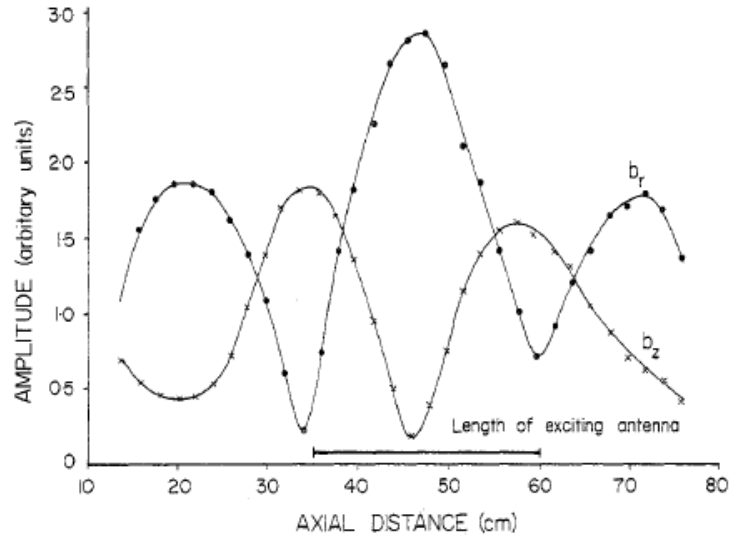


Figure 1.2. Axial b_r and b_z measurements from Boswell 1984 Ref. [8].

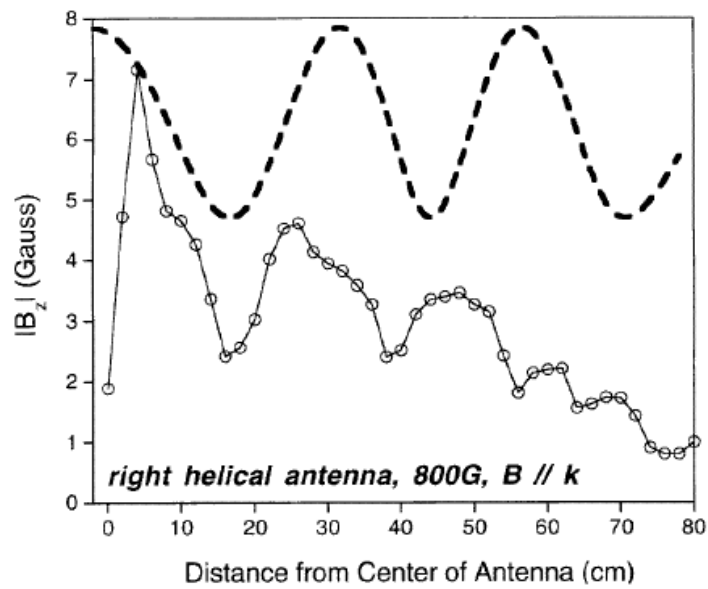


Figure 1.3. Axial b_z measurements from Chen 1995-1996 Refs. [15,17].

An additional aspect of this work will focus on the downstream density peak observed by Sudit and Chen in 1995 [16, 17, 31]. This is shown in Figure 1.4 for the same discharge described above. Another group to have observed this effect is Tysk [70, 71] from the University of Wisconsin as shown Figure 1.5 but little is mentioned regarding the observation. Perusing much helicon literature reveals two popular presentations of data:

power vs. density plots and radial density or radial wave profiles. The axial data reported is surprisingly limited to the few groups summarized here. It will be the primary focus of this work to investigate the axial variation in plasma wave profiles and axial density profiles. Ultimately, three dimensional mapping of the plasma waves will reveal new insight into helicons. The axial measurements will establish a new definition for the helicon wavelength.

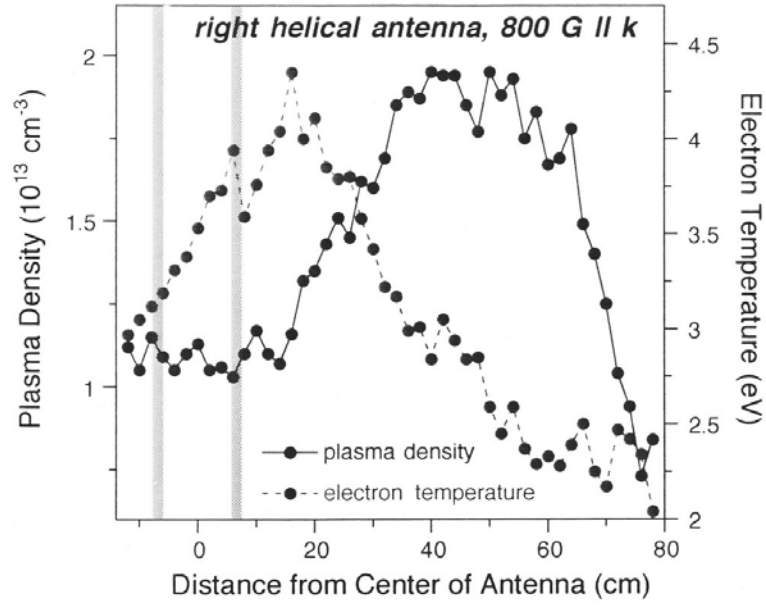


Figure 1.4. Axial density profile illustrating downstream density peak from Chen 1995-1996 Refs. [16-17]. The antenna end rings are shown by the shaded lines straddling the $z=0$ location.

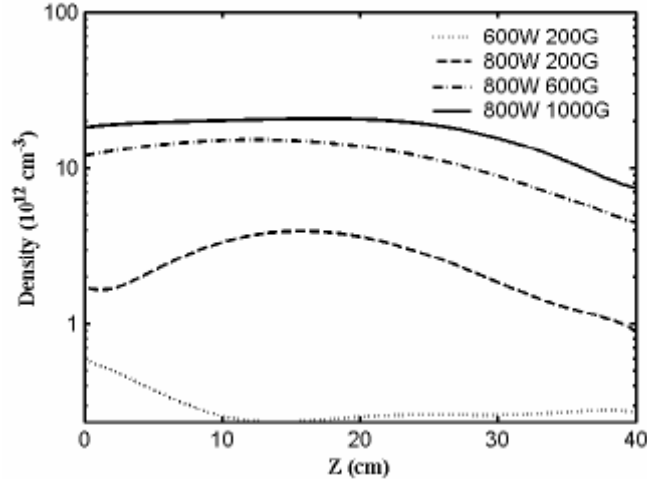


Figure 1.5. Axial density profile with downstream density peak from Tysk 2003-2004 Ref. [71]. Density scale is logarithmic.

1.5 Objective of This Work

This work was performed with the following quote from Stephen Hawking’s “A Brief History of Time” kept close in mind throughout:

“A theory is a good theory if it satisfies two requirements. It must accurately describe a large class of observations on the basis of a model that contains only a few arbitrary elements, and it must make definite predictions about the results of future observations.”

Therefore, we begin by applying this idea to helicon plasma waves. The model that will be utilized throughout this work is for a non-uniform radial density distribution where electron and ion mass effects can be ignored to predict the helicon radial wave profiles; ions assumed infinitely massive with respect to electrons and the electron cyclotron frequency is much higher than the driving frequency. The arbitrary elements included in this model are driving frequency f , static magnetic field B_0 , tube radius a , operating gas (Argon here), and radial density profiles $n(r)$ (Gaussian profiles are used in this work). Finally, the definite predictions this work will provide include: helicon wavelength

predictions based off of three dimensional imaging of the b_r , b_θ , and b_z profiles and the ability to predict axial density profiles provided an input temperature profile. This work will also demonstrate some important features of diagnostic implementation in short time scale environments; not just limited to radio frequency plasma environments but inclusive of magnetic fields due to fast-pulsed currents i.e., ringing discharges.

The format of this dissertation is as follows:

Chapter 2 analyzes the theory of helicon waves beginning from a simplified uniform density profile to a theory that predicts TG waves to explain the high absorption of helicon plasma, and finally where non-uniform radial density distributions predict radial helicon wave profiles.

Chapter 3 details the facility and apparatus used in this work.

Chapter 4 thoroughly characterizes magnetic induction probes for use in high frequency plasma and describes the careful implementation of using these probes in plasma.

Additionally, RF compensated Langmuir probes are examined with a full frequency spectrum characterization of the probe impedance.

Chapter 5 illustrates how strongly the numerically solved wave profiles agree with those measured by b -dot probes. The initial radial results are expanded into a three dimensional contour image of helicon waves providing visual representation of a helicon

wave. The results will also identify the downstream density peak and provide a quantitative model based on an exponentially decaying electron temperature profile peaking at the antenna / source 'exit'.

Chapter 6 will identify the successes and contributions reported in this study as well as the areas where this work (both observational and predictive) may exhibit shortcomings. This will provide a basis for where additional investigation is warranted, specifically obtaining better accuracy in determining the electron temperature and areas where the model which predicts axial density can be improved and further validated.

1.6 References

- [1] P. Aigrain, "Les 'helicons' dans les semiconducteurs," *Proceedings of the International Conference on Semiconductor Physics, Prague*, 1960.
- [2] F. F. Chen, "Plasma Ionization by Helicon Waves," *Plasma Physics and Controlled Fusion*, vol. 33, no. 4, pp. 26, 1991.
- [3] L. R. O. Storey, "An Investigation of Whistling Atmospherics," *Philosophical Transactions of the Royal Society of London. Series A, Mathematical and Physical Sciences*, vol. 246, no. 908, pp. 30, 1953.
- [4] J. A. Lehane, and P. C. Thonemann, "An experimental study of helicon wave propagation in a gaseous plasma," *Proceedings of the Physical Society* vol. 85, 1965.
- [5] A. F. Kuckes, "Resonant Absorption of Electromagnetic Waves in a Non-Uniformly Magnetized Plasma," *Plasma Physics*, vol. 10, pp. 14, 1968.

- [6] R. W. Boswell, "A study of Waves in Gaseous Plasma," Dissertation, School of Physical Sciences, The Flinders University of South Australia, 1970.
- [7] C. A. Nyack, and P. J. Christiansen, "Dispersion relation of high frequency waves in a beam-plasma system," *Plasma Physics*, vol. 17, no. 5, pp. 355-9, 1975.
- [8] R. W. Boswell, "Very Efficient Plasma Generation by Whistler Waves Near the Lower Hybrid Frequency," *Plasma Physics and Controlled Fusion*, vol. 26, no. 10, pp. 16, 1984.
- [9] R. W. Boswell, and D. Henry, "Pulsed high rate plasma etching with variable Si/SiO₂ selectivity and variable Si etch profiles," *Applied Physics Letters*, vol. 47, no. 10, pp. 3, 24 June 1985, 1985.
- [10] R. W. Boswell, and R. K. Porteous, "Large volume, high density rf inductively coupled plasma," *Applied Physics Letters*, vol. 50, no. 17, pp. 4, 24 February 1987, 1987.
- [11] R. W. Boswell, A. J. Perry, and M. Emami, "Multipole confined diffusion plasma produced by 13.56 MHz electrodeless source," *Journal of Vacuum Science and Technology: A*, vol. 7, no. 6, pp. 6, 1989.
- [12] A. J. Perry, D. Vender, and R. W. Boswell, "The application of the helicon source to plasma processing," *Journal of Vacuum Science and Technology: B*, vol. 9, no. 2, pp. 8, 1991.
- [13] F. F. Chen, *Introduction to Plasma Physics and Controlled Fusion*, Second ed., UCLA: Plenum Press, 1984.
- [14] F. F. Chen, "Experiments on helicon plasma sources," *Journal of Vacuum Science and Technology: A*, vol. 10, no. 4, pp. 13, 1992.

- [15] F. F. Chen, M. J. Hsieh, and M. Light, "Helicon waves in non-uniform plasma," *Plasma Sources Science and Technology*, vol. 3, pp. 9, 1994.
- [16] F. F. Chen, "Physics of helicon discharges," *Physics of Plasmas*, vol. 3, no. 5, pp. 11, 1996.
- [17] F. F. Chen, I. D. Sudit, and M. Light, "Downstream physics of the helicon discharge," *Plasma Sources Science and Technology*, vol. 5, pp. 8, 1996.
- [18] F. F. Chen, and D. Arnush, "Generalized theory of helicon waves. I. Normal modes," *Physics of Plasmas*, vol. 4, no. 9, pp. 3411-3421, 1997.
- [19] F. F. Chen, and R. W. Boswell, "Helicons-The Past Decade," *IEEE Transactions on Plasma Science*, vol. 25, no. 6, pp. 13, December, 1997.
- [20] F. F. Chen, X. Jiang, J. D. Evans *et al.*, "Low-field helicon discharges," *Plasma Physics and Controlled Fusion*, vol. 39, pp. 10, 1997, 1997.
- [21] F. F. Chen, and D. D. Blackwell, "Upper Limit to Landau Damping in Helicon Discharges," *Physical Review Letters*, vol. 82, no. 13, pp. 2677, 1999.
- [22] F. F. Chen, "Permanent magnet helicon source for ion proplulsion," University of California, Los Angeles, 2007, p. 19.
- [23] F. F. Chen, and H. Torreblanca, "Large-area helicon plasma source with permanent magnets," *Plasma Physics and Controlled Fusion*, vol. 49, no. 5 A, pp. 81-93, 2007.
- [24] F. F. Chen, and H. Torreblanca, "Density jump in helicon discharges," *Plasma Sources Science and Technology*, vol. 16, no. 3, pp. 593-596, 2007.

- [25] D. D. Blackwell, and F. F. Chen, "2D Imaging of a Helicon Discharge,"
University of California, Los Angeles, Electrical Engineering Department, 1997,
p. 17.
- [26] D. D. Blackwell, T. G. Madziwa, D. Arnush *et al.*, "Evidence for Trivelpiece-
Gould Modes in a Helicon Discharge," *Physical Review Letters*, vol. 88, no. 14,
pp. 4, 2002.
- [27] M. Light, and F. F. Chen, "Helicon wave excitation with helical antennas,"
Physics of Plasmas, vol. 2, no. 4, pp. 10, 1995.
- [28] M. Light, F. F. Chen, and P. L. Colestock, "Quiescent and unstable regimes of a
helicon plasma," *Plasma Sources Science and Technology*, vol. 11, pp. 6, 2002.
- [29] M. Light, I. D. Sudit, F. F. Chen *et al.*, "Axial propagation of helicon waves,"
Physics of Plasmas, vol. 2, no. 11, pp. 10, 1995.
- [30] D. G. Miljak, and F. F. Chen, "Helicon wave excitation with rotating antenna
fields," *Plasma Sources Science and Technology*, vol. 7, pp. 14, 1998.
- [31] I. D. Sudit, and F. F. Chen, "Discharge equilibrium of a helicon plasma," *Plasma
Sources Science and Technology*, vol. 5, pp. 11, 1995.
- [32] R. Winglee, J. Slough, T. Ziemba *et al.*, "Mini-magnetospheric plasma propulsion
(M2P2): High speed propulsion sailing the solar wind." pp. 962-967.
- [33] A. V. Arefiev, "Theoretical Studies of the VASIMR Plasma Propulsion Concept,"
Texas at Austin, 2002.
- [34] A. V. Arefiev, and B. N. Breizman, "MHD scenario of plasma detachment,"
Institute for Fusion Studies, The University of Texas at Austin, 2004, p. 23.

- [35] A. V. Arefiev, and B. N. Breizman, "Theoretical components of the VASIMR plasma propulsion concept," *Physics of Plasmas*, vol. 11, no. 5, pp. 8, 2004.
- [36] C. Charles, "Hydrogen ion beam generated by a current-free double layer in a helicon plasma," *Applied Physics Letters*, vol. 84, no. 3, pp. 3, 2004.
- [37] C. Charles, and R. W. Boswell, "Laboratory evidence of a supersonics ion beam generated by a current-free "helicon" double layer," *Physics of Plasmas*, vol. 11, no. 4, pp. 9, 2004.
- [38] T. Ziemba, J. Carscadden, J. Slough *et al.*, "High Power Helicon Thruster," in Joint Propulsion Conference, Tucson, Az, 2005.
- [39] C. Charles, R. W. Boswell, P. Alexander *et al.*, "Helicon double layer thrusters," *Collection of Technical Papers - AIAA/ASME/SAE/ASEE 42nd Joint Propulsion Conference*. pp. 5139-5142.
- [40] J. M. Pucci, N. Sinenian, J. Palaia *et al.*, "Preliminary characterization of a helicon plasma source for space propulsion," *Collection of Technical Papers - AIAA/ASME/SAE/ASEE 42nd Joint Propulsion Conference*. pp. 8904-8913.
- [41] J. Slough, R. Winglee, and T. Ziemba, "Performance enhancement and modeling of the high power helicon plasma thruster," *Collection of Technical Papers - AIAA/ASME/SAE/ASEE 42nd Joint Propulsion Conference*. pp. 8928-8936.
- [42] J. P. Squire, F. R. Chang-Diaz, T. W. Glover *et al.*, "High power light gas helicon plasma source for VASIMR," *Thin Solid Films*, vol. 506-507, pp. 579-82, 2006.
- [43] K. Toki, T. Hashimoto, K. Makita *et al.*, "Small helicon source for electrodeless plasma production and electromagnetic acceleration," *Collection of Technical*

- Papers - AIAA/ASME/SAE/ASEE 42nd Joint Propulsion Conference.* pp. 5156-5163.
- [44] R. Walker, N. Plihon, P. Chabert *et al.*, "Experimental studies of helicon double layers for future high power plasma propulsion," *Collection of Technical Papers - AIAA/ASME/SAE/ASEE 42nd Joint Propulsion Conference.* pp. 5164-5175.
 - [45] D. Palmer, C. Akinli, L. Williams *et al.*, "Characterization of an Annular Helicon Plasma Source," in International Electric Propulsion Conference, Florence, Italy, 2007, pp. 10.
 - [46] O. Batishchev, "Mini-Helicon Plasma Thruster Characterization," in 44th AIAA/ASME/SAE/ASEE Joint Propulsion Conference & Exhibit, Harford, CT, 2008, pp. 12.
 - [47] M. Yano, and M. L. R. Walker, "Plasma ionization by annularly bounded helicon waves," *Physics of Plasmas*, vol. 13, no. 6, pp. 063501-5, 2006.
 - [48] C. Charles, and R. Bowell, "Current-free double-layer formation in a high-density helicon discharge," *Applied Physics Letters*, vol. 82, no. 9, pp. 3, 2003.
 - [49] A. Libchaber, and R. Veilex, "Wave Propagation in a Gyromagnetic Solid Conductor: Helicon Waves," *Physical Review*, vol. 127, no. 3, pp. 3, 1962.
 - [50] F. E. Rose, T. Taylor, and R. Bowers, "Low-Frequency Magneto-Plasma Resonances in Sodium," *Physical Review Letters*, vol. 127, no. 4, pp. 3, 1962.
 - [51] C. R. Legédy, "Macroscopic Theory of Helicons," *Physical Review*, vol. 135, no. 6A, pp. A1713, 1964.
 - [52] C. R. Legendy, "Existence of Proper Modes of Helicon Oscillations," *Journal of Mathematical Physics*, vol. 6, no. 1, pp. 153-157, 1965.

- [53] J. P. Klozenberg, B. McNamara, and P. C. Thonemann, "The dispersion and attenuation of helicon waves in a uniform cylindrical plasma," *Journal Of Fluid Mechanics*, vol. 21, pp. 545-563, 1965.
- [54] T. Shoji, Y. Sakawa, S. Nakazawa *et al.*, "Plasma production by helicon waves," *Plasma Sources Science and Technology*, vol. 2, no. 1, pp. 6, 1993.
- [55] Agilent. "Agilent 4294A Precision Impedance Analyzer," <http://cp.literature.agilent.com/litweb/pdf/5968-3809E.pdf>.
- [56] M. Kramer, "Propagation and damping of $m=+1$ and $m=-1$ helicon modes in an inhomogeneous plasma column," *Physics of Plasmas*, vol. 6, no. 4, pp. 7, 1999.
- [57] M. Kramer, "Helicon mode formation and rf power deposition in a helicon source," in Mini-conference on Optimizing helicon source performance, 2007.
- [58] I. D. Sudit, and F. F. Chen, "RF compensated probes for high-density discharges," *Plasma Sources Science and Technology*, vol. 3, pp. 7, 1994.
- [59] V. A. Godyak, and R. B. Piejak, "Probe measurements of the space potential in a radio frequency discharge," *Journal of Applied Physics*, vol. 68, no. 7, pp. 6, 1990.
- [60] V. A. Godyak, R. B. Piejak, and B. M. Alexandrovich, "Measurements of electron energy distribution in low-pressure RF discharges," *Plasma Sources Science and Technology*, vol. 1, pp. 36-58, 1992.
- [61] A. R. Ellingboe, and R. W. Boswell, "Capacitive, inductive and helicon-wave modes of operation of a helicon plasma source," *Physics of Plasmas*, vol. 3, no. 7, pp. 8, 1996.

- [62] M. M. Balkey, R. Boivin, J. L. Kline *et al.*, "Ion heating and density production in helicon sources near the lower hybrid frequency," *Plasma Sources Science and Technology*, vol. 10, pp. 11, 2001.
- [63] C. S. Corr, N. Plihon, P. Chabert *et al.*, "Spatially limited ion acoustic wave activity in low-pressure helicon discharges," *Physics of Plasmas*, vol. 11, no. 10, pp. 7, 2004.
- [64] P. A. Keiter, E. E. Scime, and M. M. Balkey, "Frequency dependent effects in helicon plasmas," *Physics of Plasmas*, vol. 4, no. 7, pp. 7, 1997.
- [65] J. L. Kline, E. E. Scime, R. F. Boivin *et al.*, "Slow wave ion heating in the HELIX helicon source," *Plasma Sources Science and Technology*, vol. 11, pp. 13, 2002.
- [66] S. Cho, "The role of the lower hybrid resonance in helicon plasmas," *Physics of Plasmas*, vol. 7, no. 1, pp. 7, 2000.
- [67] B. N. Breizman, and A. V. Arefiev, "Radially Localized Helicon Modes in Nonuniform Plasma," *Physical Review Letters*, vol. 84, no. 17, pp. 4, 2000.
- [68] G. Chen, A. V. Arefiev, R. D. Bengtson *et al.*, "Resonant power absorption in helicon plasma sources," *Physics of Plasmas*, vol. 13, no. 12, pp. 123507, 2006.
- [69] C. M. Franck, O. Grulke, A. Stark *et al.*, "Measurements of spatial structures of different discharge modes in a helicon source," *Plasma Sources Science and Technology*, 2005, p. 10.
- [70] S. M. Tysk, C. M. Denning, J. E. Scharer *et al.*, "Experimental Measurements and Modeling of a Helicon Plasma Source with Large Axial Density Gradients," in *Radio Frequency Power in Plasma*, 2003.

- [71] S. M. Tysk, C. M. Denning, J. E. Scharer *et al.*, "Optical, wave measurements, and modeling of helicon plasmas for a wide range of magnetic fields," University of Wisconsin, Department of Electrical and Computer Engineering, 2004, p. 40.

CHAPTER 2: THEORY OF HELICON WAVES

The theory of helicon waves has steadily evolved over the past several decades. The foundation is rooted in the theory of plasma waves in an infinite uniform magnetic field which results in the cold plasma dispersion relation (cpdr). This simple theory can quickly become mathematically complex and so the results manifest themselves in the form of a Clemmow-Mullaly-Allis (CMA) diagram. Since helicon waves are bounded whistler waves which otherwise propagate in free space, the CMA diagram provides a good starting point for analysis. However, for the actual bounded plasma considered in this work, the theory will correspondingly evolve and become more complex.

This chapter will track the evolution of helicon waves from simplified uniformity assumptions where solutions for the wave field's b_r , b_θ , b_z are solved analytically. When collisional effects and finite electron mass are considered, the internal plasma fields reveal a secondary wave branch (the Trivelpiece-Gould mode) which can also be studied analytically. Finally, when a non-uniform radial density distribution is considered, the differential equation to be solved becomes non-linear and complex enough that only numerical solutions are valid. However, these will later be shown to provide a superbly accurate description of the helicon wave fields under investigation in this work. While some groups have considered more elaborate theories such as incorporating ion mass effects [1-3] or wave propagation based on radially localized modes [4, 5], the experimental results accompanying these descriptions is ambiguous or incomplete as far as describing the wave patterns. This is not to say that they may not also accurately describe helicon wave propagation when studied more thoroughly. However, the

mathematical complexities introduced do not provide for any more ease to the physical understanding or significantly alter the results obtained than those when considering a non-uniform radial density distribution.

2.1 Plasma Waves

Due to the multitude of parameters that can change the operational modes within plasma, the subject of plasma waves is often termed a ‘plasma zoo’. Considering a two species plasma, ions and electrons, immersed in a uniform magnetic field and homogeneous in space, Maxwell’s equations with the linearized equation of motion yield the cold plasma dispersion relation. The mathematical derivation of the equations for the cutoffs and resonances of various plasma waves is given in Appendix A. The graphical representation was first given by Clemmow and Mullaly in 1955 [6] and later updated by Allis in 1959 [7]; commonly referred to as a CMA diagram in Figure 2.1. To accurately show the entire frequency spectrum, an ion-electron mass ratio of 5 was selected.

The axes on the CMA diagram in terms of the plasma frequency and electron cyclotron frequency can be transformed according to their definitions as density and magnetic field.

Here the electron plasma frequency is given by $\omega_{pe}^2 = \frac{e^2 n_e}{\epsilon_0 m_e}$ and the electron cyclotron

frequency is given by $\omega_{ce} = \frac{eB_0}{m_e}$. The n vs. B_0 diagram is given in Figure 2.2 for Argon

gas and a driving frequency of $f = 13.56 \text{ MHz}$. Within each region, only certain waves are allowed to propagate within the dielectric. A detailed description of the various

regions which allow right- or left- handed waves and either ordinary or extraordinary waves to propagate is given by Stix [8] and Swanson [9] among others.

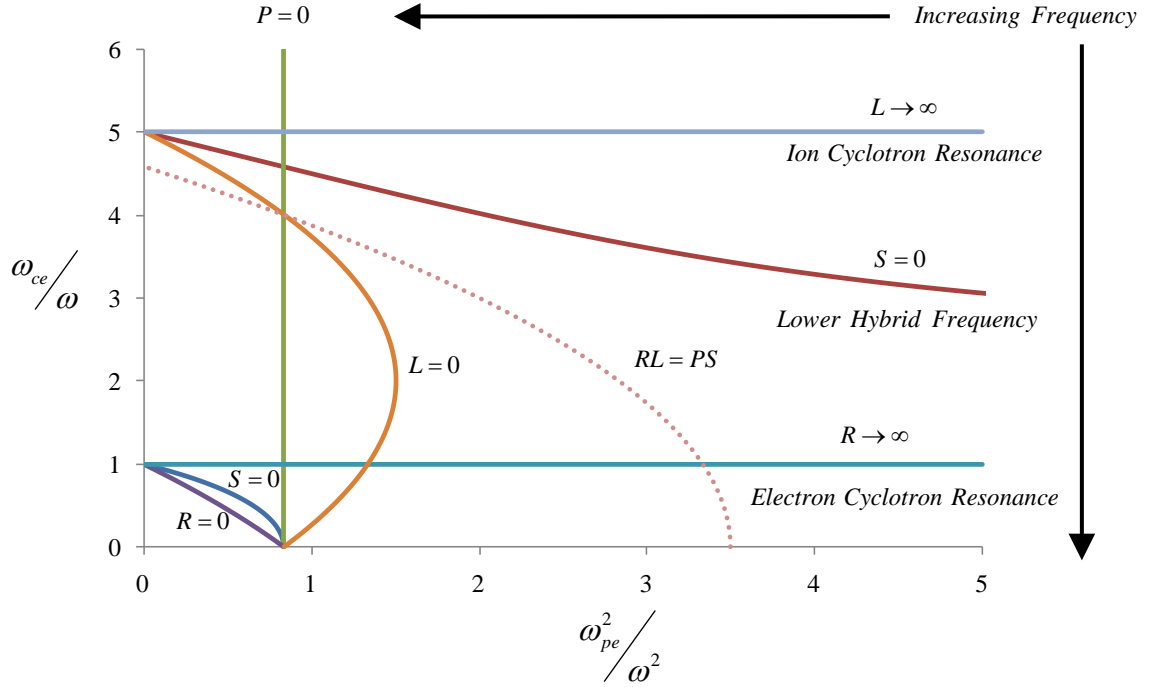


Figure 2.1. CMA diagram with $m_i / m_e = 5$.

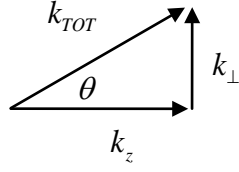
We will elaborate on one result of relevance to the current work and that is the dispersion relation obtained for right-handed wave propagation at an angle θ with respect to a magnetic field in a +z direction. The result drawn on from Appendix A is given by

$$n_R^2 = R = \frac{k^2 c^2}{\omega^2} = 1 - \frac{\omega_{pe}^2}{\omega(\omega - \omega_{ce} \cos \theta)} \quad (2.1)$$

where ion effects have been neglected and the index of refraction 'n' is defined by

$$n = \frac{kc}{\omega} \quad (2.2)$$

and $k = k_{TOT}$ is the total wave number according to



Simplifying where $k_z = k \cos \theta$ and where $\omega \ll \omega_{ce}$ yields

$$k_{TOT} = \frac{\omega}{k_z} \frac{\omega_{pe}^2}{\omega_{ce} c^2} \quad (2.3)$$

This is the basic dispersion relation for right-handed whistler wave propagating in free space. Later, the dispersion relationship between whistler waves described by this result and those for helicon wave propagation will be discussed.

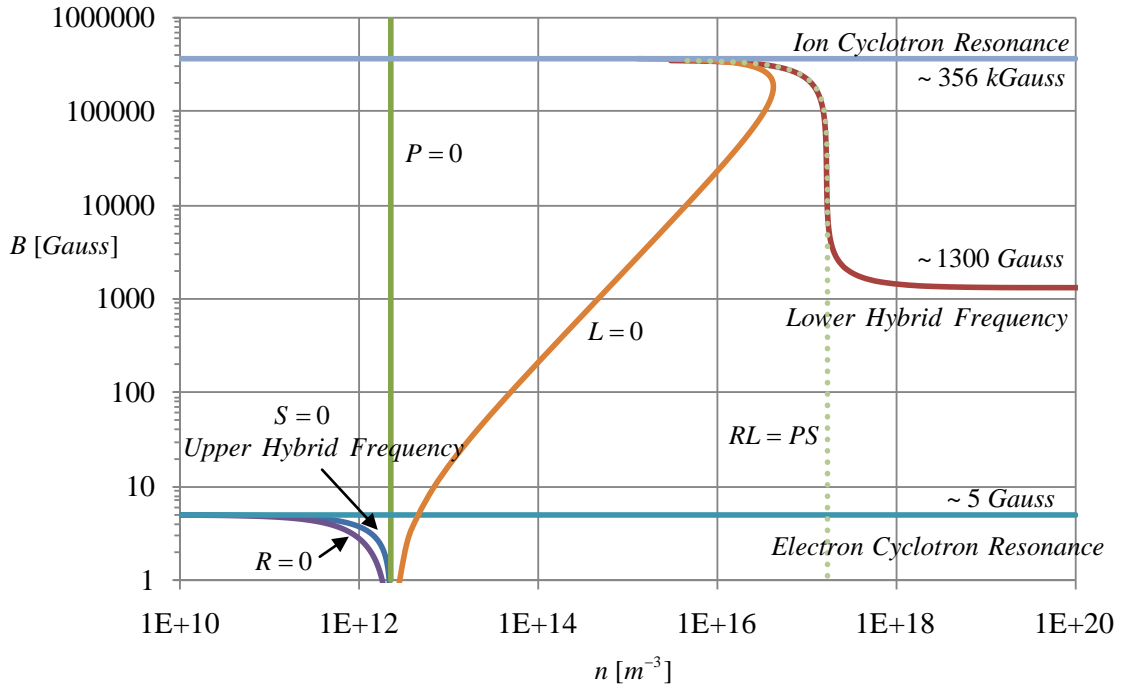


Figure 2.2. CMA diagram in terms of n vs. B.

Thus far, we have described plasma waves that propagate in an unbounded medium and have only put a restraint on the operating gas and driving frequency. In the following sections, the subject of bounded laboratory helicon waves will be addressed. We will describe waves that propagate between the lower hybrid frequency and electron cyclotron

frequency $\omega_{LH} < \omega < \omega_{ce}$. This frequency space within the $\omega_{pe}^2 - \omega_{ce}$ and $n - B$ space of the CMA diagram envelopes the conditions where helicon waves propagate. Although the CMA diagram is a cursory analysis for studying bounded plasma, it provides one of the simplest representations toward understanding the restrictions when designing a laboratory system to drive helicon plasma.

2.2 Bounded, Collisionless, Uniform Density Dispersion Relation

Consider a cylindrical plasma discharge of radius ‘ a ’, uniform radial density distribution $n_0(r) = n_0$, subject to an infinite homogenous magnetic field B_0 in the $+z$ direction. Maxwell’s equations are then

$$\nabla \times \vec{E} = -\frac{\partial \vec{b}}{\partial t} \quad (2.4)$$

$$\nabla \times \vec{b} = \mu_0 \vec{j} \quad (2.5)$$

$$\nabla \cdot \vec{b} = 0 \quad (2.6)$$

Here, we have neglected the displacement current on the assumption that the wave phase velocity \ll the speed of light, i.e.,

$$v_p = \frac{\omega}{k} \ll c \quad (2.7)$$

Assuming for now that the entire plasma current is carried by the $E \times B$ motion of the electrons where the driving frequency is much smaller than the electron cyclotron frequency $\omega \ll \omega_{ce}$ and is much larger than the lower hybrid frequency

$\omega \gg \omega_{LH} \cong \sqrt{\omega_{ce}\omega_{ci}}$ such that ion motions can also be neglected, the Ohm’s law

expression to be evaluated is given by

$$en_0 \vec{E} = \vec{j} \times \vec{B}_0 \quad (2.8)$$

Additionally, we have assumed here that the resistivity is zero, i.e, $\eta = 0$, where η is defined by

$$\eta = \frac{m_e \nu_{ei}}{ne^2} \quad (2.9)$$

Essentially collisional effects have been neglected where the electron mass \sim zero. These effects will be included in the subsequent section. Returning to Maxwell's equations (2.4) - (2.6) and Ohm's law (2.8), 1st order wave perturbations of the form

$$\exp i(m\theta + k_z z - \omega t)$$

where $|B_0| \gg |b|$ simplify the expressions for the wave magnetic fields such that

$$\vec{b} = \left(\frac{\omega}{k_z} \frac{\mu_0 en_0}{B_0} \right)^{-1} \nabla \times \vec{b} \quad (2.10)$$

or

$$\alpha \vec{b} = \nabla \times \vec{b} \quad (2.11)$$

where the total wave number is defined as

$$k_{TOT} = \alpha = \frac{\omega}{k_z} \frac{\mu_0 en_0}{B_0} \quad (2.12)$$

Inserting the definitions of the electron plasma and cyclotron frequency yields

$$k_{TOT} = \alpha = \frac{\omega}{k_z} \frac{\mu_0 en_0}{B_0} = \frac{\omega}{k_z} \frac{\omega_{pe}^2}{\omega_c c^2} \quad (2.13)$$

which is the identical result to (2.3) for right-handed whistler wave propagation in free space. Taking the curl of (2.10) yields a second order differential equation for the plasma wave fields

$$\nabla^2 \vec{b} + \alpha^2 \vec{b} = 0 \quad (2.14)$$

The \mathbf{z} component of the wave magnetic field in cylindrical coordinates is

$$\frac{\partial^2 b_z}{\partial r^2} + \frac{1}{r} \frac{\partial b_z}{\partial r} + \frac{1}{r^2} \frac{\partial^2 b_z}{\partial \theta^2} + \frac{\partial^2 b_z}{\partial z^2} + \alpha^2 b_z = 0 \quad (2.15)$$

upon applying the wave perturbations reduces to

$$\frac{\partial^2 b_z}{\partial r^2} + \frac{1}{r} \frac{\partial b_z}{\partial r} + \left(T^2 - \frac{m^2}{r^2} \right) b_z = 0 \quad (2.16)$$

where

$$T^2 = k_{\perp}^2 = k_{TOT}^2 - k_z^2 = \alpha^2 - k_z^2 \quad (2.17)$$

The differential equation (2.16) is Bessel's equation subject to the finite boundary condition at the origin so that

$$b_z(r) = C J_m(Tr) \quad (2.18)$$

The r and θ components of the wave magnetic field are obtained from (2.10) as

$$b_r(r) = \frac{iC}{T^2} \left(\frac{m\alpha}{r} b_z(r) - k_z b_z'(r) \right) \quad (2.19)$$

$$b_{\theta}(r) = \frac{C}{T^2} \left(\frac{mk_z}{r} b_z(r) - \alpha b_z'(r) \right) \quad (2.20)$$

The second boundary condition is given by

$$b_r(a) = 0 \quad (2.21)$$

regardless of whether the plasma dielectric is surrounded by a conducting or insulating boundary [10]. This is demonstrated by the fact that substitution of (2.10) into (2.5) yields

$$\mu_0 \vec{j} = \alpha \vec{b} \quad (2.22)$$

so that on an insulating boundary $j_r(a) = 0 \rightarrow b_r(a) = 0$. On a perfect conducting boundary $E_\theta(a) = 0$, and (2.4) gives

$$k_z E_\theta(r) = -\omega b_r(r) \quad (2.23)$$

so that $E_\theta(a) = 0 \rightarrow b_r(a) = 0$. Therefore, the second boundary condition is obtained from (2.19)

$$\frac{m\alpha}{a} b_z(a) = k_z b'_z(a) \quad (2.24)$$

which assures a unique value to k_z provided other inputs for tube radius ' a ', plasma density n_0 , static magnetic field B_0 , antenna configuration mode ' m ', and driving frequency ' f '. For example, consider a 2.5 cm radius tube, with a uniform 900 Gauss magnetic field, and a $m = +1$ helical antenna driven at 13.56 MHz. The boundary condition given by (2.24) provides a $k_z = 11.58 \text{ m}^{-1} \rightarrow \lambda_z = 54.25 \text{ cm}$ via

$$\lambda_z = 2\pi / k_z \quad (2.25)$$

defining the axial helicon wavelength. Finally, the internal plasma wave fields can be solved from (2.18) thru (2.20) and are shown in Figure 2.3.

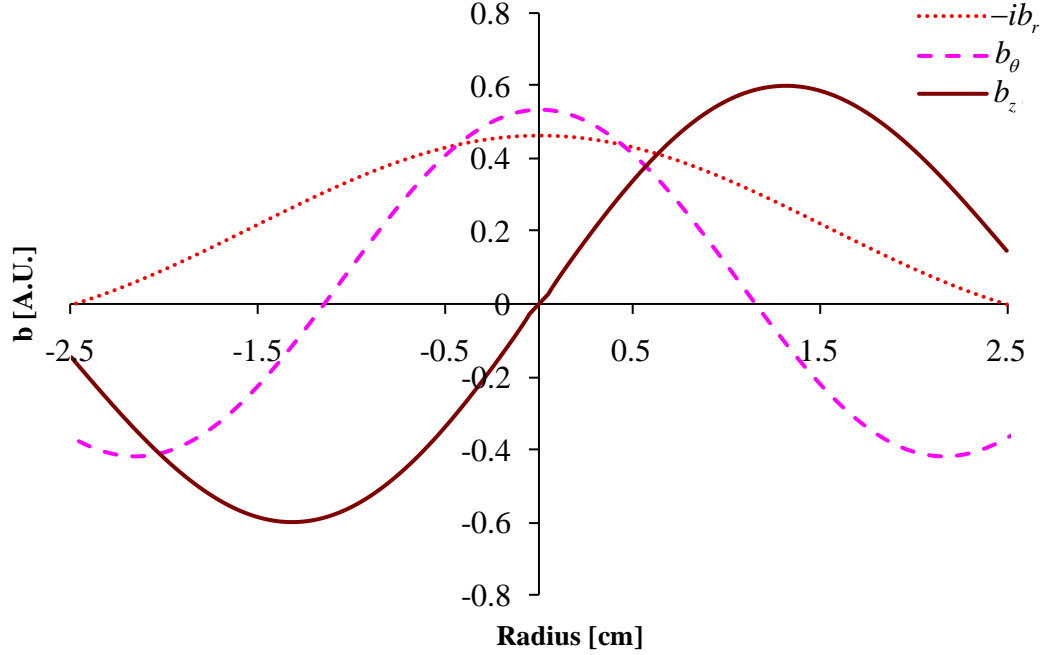


Figure 2.3. Internal b_r , b_θ and b_z fields for $a = 2.5$ cm, $m = +1$ antenna driven at 13.56 MHz in a 900 Gauss uniform magnetic field with a uniform radial density of $n_0 = 1 \times 10^{19} \text{ m}^{-3}$.

2.3 Uniform Density with Collisions: The Trivelpiece-Gould Mode Revealed

Previously, we assumed the component E_z was zero and helicon wave propagation in the $+z$ -direction was undamped; i.e., the plasma current \mathbf{j} was driven by $E \times B$ motion of electrons. However, when considering wave damping due to collisions or Landau damping, an E_z field arises to move electrons in the $+z$ direction. This is taken into consideration in the j_z component of the plasma current for motion parallel to the B_0 field. When this is considered, the Ohm's law equation (2.8) has to be altered to include this component. Specifically,

$$en_0 \vec{E} = \vec{j} \times \vec{B}_0 - \frac{im}{e} (\omega + iv) \vec{j} \quad (2.26)$$

or

$$\vec{E} = \frac{\vec{j} \times \vec{B}_0}{en_0} - \frac{im}{e^2 n_0} (\omega + iv) \vec{j} \quad (2.27)$$

Maxwell's equations (2.4) thru (2.6) are then used with Ohm's law (2.27) and a similar formulation to the uniform density case previously considered is followed. Taking the curl of (2.27) and substituting into (2.4)

$$\nabla \times \vec{E} = \frac{\nabla \times \vec{j} \times \vec{B}_0}{en_0} - \frac{im}{e^2 n_0} (\omega + i\nu) \nabla \times \vec{j} = i\omega \vec{b} \quad (2.28)$$

$$\frac{ik_z B_0}{en_0} \vec{j} - \frac{im}{e^2 n_0} (\omega + i\nu) \nabla \times \vec{j} = i\omega \vec{b} \quad (2.29)$$

taking the curl of (2.5)

$$\nabla \times \nabla \times \vec{b} = \mu_0 \nabla \times \vec{j} \quad (2.30)$$

substituting (2.5) and (2.30) into (2.29) for the plasma current \vec{j} yields

$$\frac{m(\omega + i\nu)}{e^2 n_0 \mu_0 \omega} \nabla \times \nabla \times \vec{b} - \frac{k_z B_0}{en_0 \mu_0 \omega} \nabla \times \vec{b} + \vec{b} = 0 \quad (2.31)$$

utilizing the previous definition of α from (2.12) with the electron cyclotron frequency

ω_{ce}

$$\frac{(\omega + i\nu)}{\omega_{ce} \alpha k_z} \nabla \times \nabla \times \vec{b} - \frac{1}{\alpha} \nabla \times \vec{b} + \vec{b} = 0 \quad (2.32)$$

additionally defining

$$\gamma = \frac{(\omega + i\nu)}{\omega_{ce} k_z} \quad (2.33)$$

so that (2.32) becomes

$$\gamma \nabla \times \nabla \times \vec{b} - \nabla \times \vec{b} + \alpha \vec{b} = 0 \quad (2.34)$$

and the characteristic equation to solve is

$$\gamma \beta^2 - \beta + \alpha = 0 \quad (2.35)$$

where roots are given by

$$\beta_{1,2} = \frac{1 \pm \sqrt{1 - 4\gamma\alpha}}{2\gamma} = \frac{1 \pm (1 - 2\gamma\alpha - 2\gamma^2\alpha^2)}{2\gamma} \quad (2.36)$$

and the square root term has been Taylor series expanded to second order. Taking the ‘bottom’ root of (2.36) gives

$$\beta_2 = \alpha(1 + \alpha\gamma) \quad (2.37)$$

and when the electron mass is zero, i.e, $m_e = 0$; $\gamma \rightarrow 0$ and (2.37) gives $\beta_2 = \alpha$ which is the previously derived helicon root; (2.12). When finite electron mass effects are considered β_2 becomes

$$\beta_2 = \alpha \left[1 + \alpha^2 \left(\frac{c^2}{\omega_p^2} + i \frac{\eta}{\mu_0 \omega} \right) \right] \quad (2.38)$$

where the resistivity is defined as

$$\eta = \frac{m_e \nu}{n_0 e^2} \quad (2.39)$$

and the collision frequency here is assumed to the electron-ion collision frequency ν_{ei}

$$\nu_{ei} \simeq 2.906 \times 10^{-12} \ln \Lambda n_e T_e^{3/2} \quad (2.40)$$

Returning to the characteristic equation (2.35), the second root is revealed when we expand α and γ using (2.13) for α and (2.33) for γ and taking the real part of γ

$$\frac{\omega}{\omega_{ce} k_z} \beta^2 - \beta + \frac{\omega \omega_{pe}^2}{\omega_{ce} k_z c^2} = 0 \quad (2.41)$$

$$k_z = \frac{\omega / \omega_{ce}}{\beta} \left(\beta^2 + \frac{\omega_{pe}^2}{c^2} \right) \quad (2.42)$$

Here, $\beta = k_{TOT}$ analogous to where $\alpha = k_{TOT}$ for the uniform density undamped case.

The ‘new’ total wavenumber β now includes the damping term. The effects are best

illustrated as demonstrated by the dependence of k_z on β at different magnetic field strengths. For the first example a density of $n_0 = 1 \times 10^{19} \text{ m}^{-3}$ is used. The graphical results are shown in Figure 2.4.

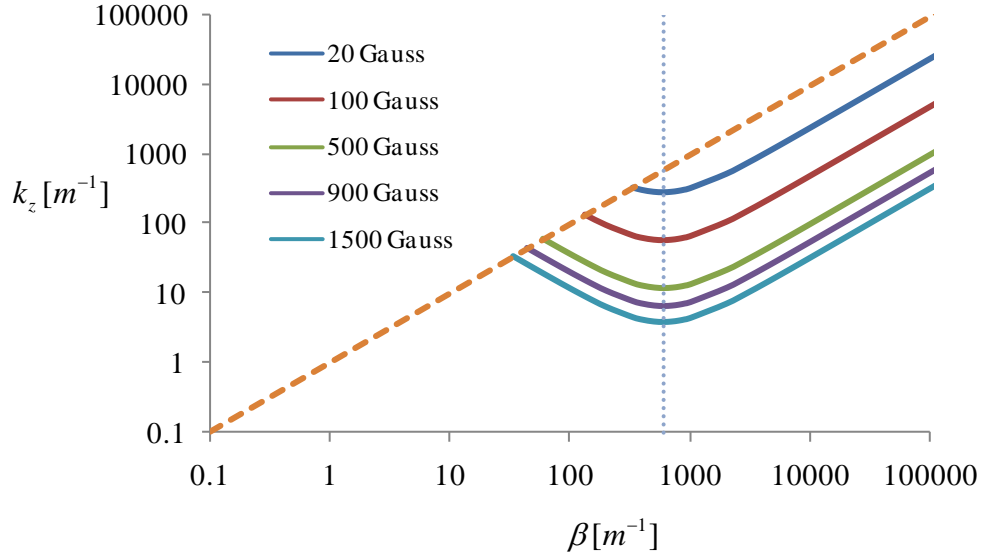


Figure 2.4. Separation of TG branch and Helicon branch for $n_0 = 1 \times 10^{19} \text{ m}^{-3}$.

Analysis demonstrates that as the magnetic field is increased a second branch to the dispersion relation is observed. To the left of the minimum k_z value is the helicon branch and to the right is the Trivelpiece-Gould branch. The difference between the two branches can be seen in Figure 2.5.

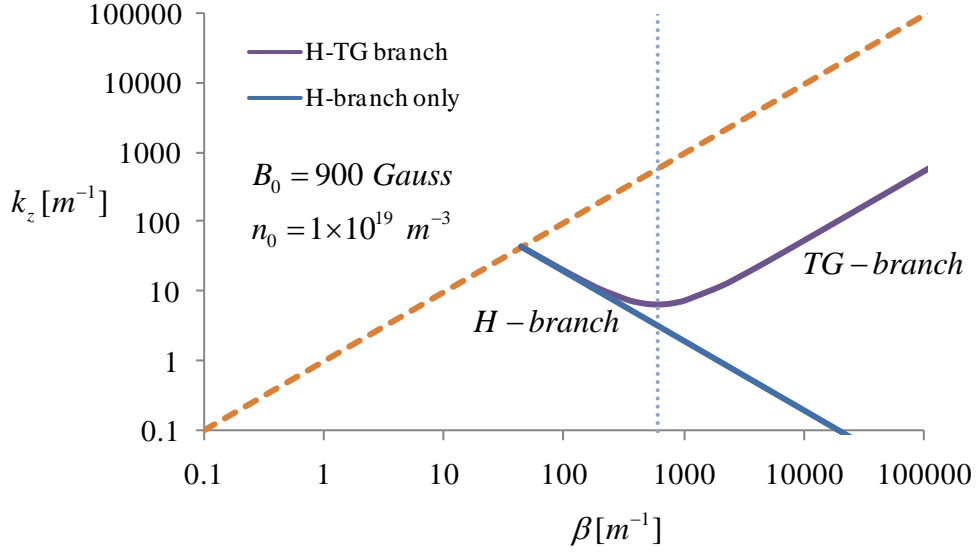


Figure 2.5. Difference when finite electron mass effects are considered. The secondary TG branch is revealed. This is for $B_0 = 900$ Gauss and $n_0 = 1 \times 10^{19} \text{ m}^{-3}$.

The diagonal line where $k_z = \beta$ occurs from the axial wavenumber being required to be less than the total wavenumber, i.e, $k_z^2 + k_\perp^2 = k_{TOT}^2 = \beta^2$ as $k_\perp \rightarrow 0$ and determines a maximum k_z for helicon waves. Additionally, the minimum value of k_z is obtained by differentiating (2.42) for k_z , equating the result to zero and obtaining the value of β according to

$$\frac{\partial k_z}{\partial \beta} = \frac{\omega}{\omega_{ce}} - \frac{1}{\beta^2} \frac{\omega}{\omega_{ce}} \frac{\omega_{pe}^2}{c^2} = 0 \quad (2.43)$$

$$\beta_{k_z=\min} = \frac{\omega_{pe}}{c} \quad (2.44)$$

so that a minimum in k_z occurs at

$$k_{z\min} = 2 \frac{\omega \omega_{pe}}{\omega_{ce} c} = 2 \omega \sqrt{m_e \mu_0} \frac{\sqrt{n}}{B_0} \quad (2.45)$$

Therefore, knowing the minimum and maximum values of the axial wavenumber for helicon waves at a designated density and magnetic field places an additional restraint on the axial wavelength range according to

$$\begin{aligned}\lambda_{z_{\min}} &= \frac{2\pi}{k_{z_{\max}}} \\ \lambda_{z_{\max}} &= \frac{2\pi}{k_{z_{\min}}}\end{aligned}\tag{2.46}$$

Different densities for $B_0 = 900$ Gauss yield the following dispersion curves, Figure 2.6.

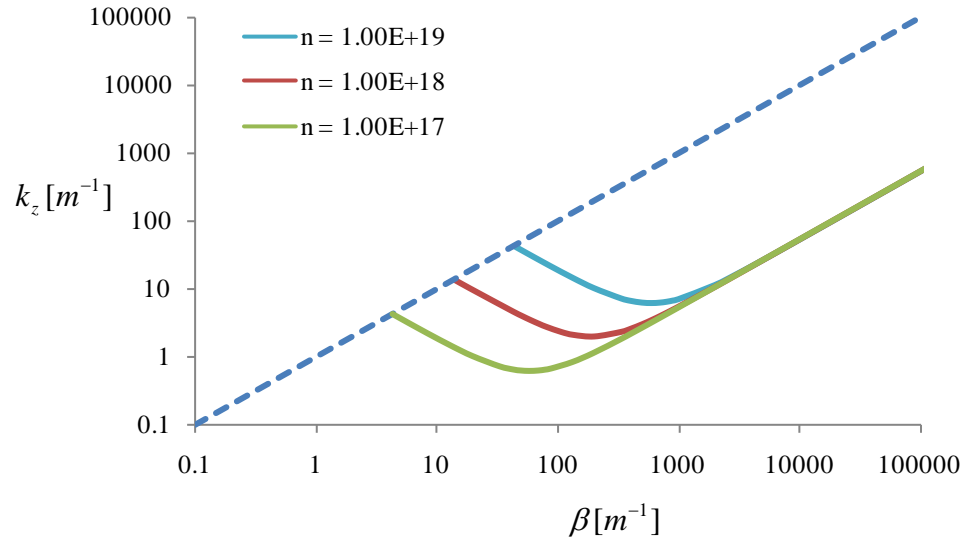


Figure 2.6. TG-H dispersion curves different densities at $B_0 = 900$ Gauss.

Here the minimum k_z value is decreasing as the density is decreased according to (2.45) and the axial wavelength range is increasing according to (2.46).

The TG-branch can be better understood by considering that as the magnetic field is decreased, the two branches (TG- and H-) begin to come together, until the magnetic field is so low that only the TG-branch can propagate. Referring back to the CMA diagram for n_0 vs. B_0 , Figure 2.2 will demonstrate that the TG-branch is an electron

cyclotron wave. This can be viewed for $n_0 = 1 \times 10^{19} \text{ m}^{-3}$ as beginning on the n_0 vs. B_0 diagram at ~ 1 kGauss and ‘traveling’ vertically downward (decreasing magnetic field) toward the $R \rightarrow \infty$ resonance, which is an electron cyclotron wave at ~ 5 Gauss for Argon at this density. However, for stronger magnetic fields (on the order of ~ 1 kGauss) Figure 2.4 shows that the two branches are well separated. When this is the case, for each value of k_z there exist two values for β . Regardless, for the TG-branch where $\beta \gg k_z$, the total wavenumber β is dominated by the perpendicular component k_{\perp} and hence the TG wave is a radial electron cyclotron wave of short wavelength (large k_{\perp}) given by

$$\lambda_{\perp} = 2\pi / (k_{\perp} \approx \beta_{TG}) \quad (2.47)$$

As an example, assuming the above conditions for density $n_0 = 1 \times 10^{19} \text{ m}^{-3}$ and magnetic field $B_0 = 900$ Gauss), β varies from 43.78 m^{-1} to 8090.16 m^{-1} with the helicon branch increasing until $k_{z_{\min}}$ at $\beta = 595.07 \text{ m}^{-1}$. Therefore, for a plasma with an axial wavenumber of $k_z = 25 \text{ m}^{-1}$ the two values of β are 77.53 m^{-1} and 4567.25 m^{-1} . According to (2.25) the axial helicon wavelength will be $\lambda_z = 25.13 \text{ cm}$. For $\beta_{TG} = 4567.25 \text{ m}^{-1}$ the total wavenumber again is dominated by the perpendicular component, i.e. $\beta^2 = k_{TOT}^2 = k_z^2 + k_{\perp}^2 \approx k_{\perp}^2$ and the TG wave has a perpendicular wavelength of $\lambda_{\perp} = 0.14 \text{ cm}$. Conversely, when the branches are not well separated, i.e., at a low magnetic field, $B_0 = 100$ Gauss, β varies between 134.26 m^{-1} and 2637.31 m^{-1} with the helicon branch again increasing until $k_{z_{\min}}$ at $\beta = 595.07 \text{ m}^{-1}$. If $k_z = 60 \text{ m}^{-1}$, then (2.25) gives $\lambda_z = 10.47 \text{ cm}$ while the corresponding $\beta_{TG} = 790.84 \text{ m}^{-1}$ and $\lambda_{\perp} = 0.79 \text{ cm}$.

The wave fields: b_r , b_θ , and b_z , with finite electron mass now included, will not greatly alter the wave patterns [11]. This is a consequence of the additional terms only altering the total wave number k_{TOT} by a numerical factor as shown in (2.37) and (2.38). This can be recognized that in the limit of strong magnetic fields (~ 1 kGauss) the dispersion relation returns only the helicon wave portion, namely $\beta = \alpha$. It is not until we consider any perpendicular or non-uniform effects that the plasma wave patterns will substantially change.

2.4 Non-uniform Radial Density Distribution: Numerical Solutions

Up to this point a uniform radial density distribution has been assumed. In what follows we will again neglect the wave damping aspect in order to simplify the analysis, however a non-uniform radial density will be used. Maxwell's equations (2.4) thru (2.6) remain unaltered except that the displacement current will be included as

$$\nabla \times \vec{b} = \mu_0 \vec{j} + \mu_0 \epsilon_0 \frac{\partial \vec{E}}{\partial t} = \mu_0 \vec{j} - i\omega \mu_0 \epsilon_0 \vec{E} \quad (2.48)$$

Additionally, Ohm's law must now change to include the radial distribution according to

$$en(r) \vec{E} = \vec{j} \times \vec{B}_0 \quad (2.49)$$

or

$$\vec{E} = \frac{\vec{j} \times \vec{B}_0}{en(r)} \quad (2.50)$$

The analysis follows the exact formulation as the uniform density distribution except that some of the curl and vector dot products must take into account the radial density component. Therefore, combining Maxwell's equations with Ohm's law yields

$$\alpha \vec{b} = (\nabla \times \vec{b})_{\perp} + \left(1 - \frac{k_0^2}{k_z^2}\right) (\nabla \times \vec{b})_z \hat{z} + \frac{i}{k_z} \left(k_0^2 \vec{b} \times \hat{z} - \alpha'(r) b_r \hat{z}\right) \quad (2.51)$$

where

$$\alpha(r) = \frac{\omega}{k_z} \frac{\mu_0 e n(r)}{B_0} \quad (2.52)$$

and

$$k_0 = \omega/c \quad (2.53)$$

Looking at (2.51) the displacement current gives rise to the terms including k_0 where

$$\frac{k_0}{k_z} = \frac{\omega/c}{k_z} = \frac{v_{phase}}{c} \quad (2.54)$$

and is typically on the order of 0.01 for laboratory helicon plasma and can be neglected

by letting $k_0/k_z \rightarrow 0$ since $v_{phase} \ll c$; similar to the assumption in (2.7). Similarly, the

density gradient gives rise to the last term in (2.51) where $\alpha'(r) \propto n'(r)$ such that the

derivative would be zero for constant radial density. Returning to (2.51), neglecting the

displacement current and assuming a constant density will return equation (2.10) as

$$\alpha \vec{b} = (\nabla \times \vec{b})_{\perp} + (\nabla \times \vec{b})_z \hat{z} = \nabla \times \vec{b} \quad (2.55)$$

To obtain the individual components of \mathbf{b} , (2.51) is expanded as

$$\alpha b_r = \frac{im}{r} b_z - ik_z \gamma b_{\theta} \quad (2.56)$$

$$\alpha b_{\theta} = -b_z' + ik_z \gamma b_r \quad (2.57)$$

$$\alpha b_z = \gamma \left(\frac{1}{r} (r b_{\theta})' - \frac{im}{r} b_r \right) - \frac{i}{k_z} \alpha' b_r \quad (2.58)$$

and (2.56) - (2.57) can be reduced in terms of b_z

$$\beta b_r = \frac{im}{r} \alpha b_z + i k_z \gamma b_z' \quad (2.59)$$

$$\beta b_\theta = -\alpha b_z' - \frac{m}{r} k_z \gamma b_z \quad (2.60)$$

where

$$\beta = \alpha^2 - k_z^2 \gamma^2 \quad (2.61)$$

and

$$\gamma = 1 - \left(\frac{k_0}{k_z} \right)^2 \quad (2.62)$$

To obtain the differential equation for the plasma fields, (2.59) and (2.60) are substituted into (2.58) and reduced to

$$b_z''(r) + f(r) b_z'(r) + g(r) b_z(r) = 0 \quad (2.63)$$

where

$$f(r) = \frac{1}{r} - \frac{2\alpha\alpha'}{\beta} \quad (2.64)$$

$$g(r) = \frac{\beta}{\gamma} - \frac{m^2}{r^2} - \frac{m}{k_z} \frac{\alpha'}{\gamma r} \left(1 + \frac{2k_z^2 \gamma^2}{\beta} \right) \quad (2.65)$$

The same boundary conditions as before are utilized, namely the wave field is finite at the origin and the radial component $b_r(a) = 0$ vanishes on the boundary; (2.21) which follows from (2.51) for the vanishing radial plasma current j_r

$$\alpha \vec{b} = \left(\nabla \times \vec{b} \right)_\perp = \mu_0 \vec{j}_\perp \quad (2.66)$$

Therefore, (2.59) can be evaluated for $b_r(r=a) = 0$

$$\frac{m}{a} \alpha(r=a) b_z(r=a) + k_z \gamma b_z'(r=a) = 0 \quad (2.67)$$

The radial density profiles studied for this analysis were given by Gaussian profiles according to

$$n(r) = n_0 e^{-(r/w)^2} \quad (2.68)$$

where ‘ w ’ is the waist size of the profile or $\frac{1}{2}$ the width of the radial distance for the density to drop to $1/e$ of n_0 . Taking $n_0 = 1 \times 10^{19} \text{ m}^{-3}$ the radial density profiles are shown in Figure 2.7.

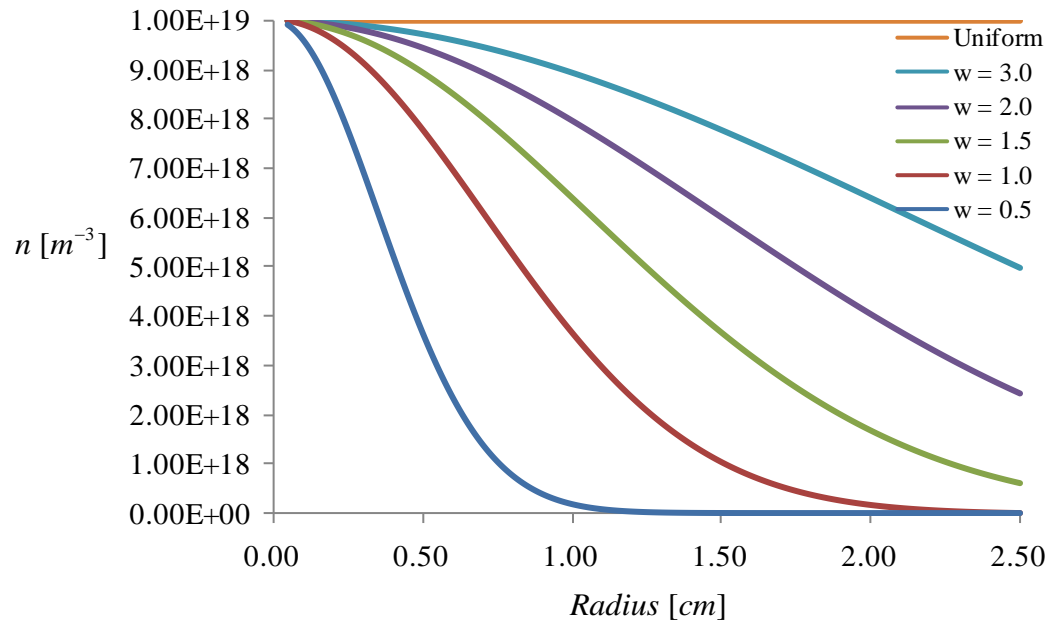


Figure 2.7. Gaussian profiles of waist size ‘ w ’ for $n_0 = 1 \times 10^{19} \text{ m}^{-3}$ and tube radius $a = 2.5 \text{ cm}$

The following conditions were used as a baseline in the numerical simulation of the b_z profiles according to (2.63): $B_0 = 900 \text{ Gauss}$, $m = +1$ antenna, $f = 13.56 \text{ MHz}$, and $a = 2.5 \text{ cm}$. The differential equation was solved using *Mathematica*: NDSolve function (see Appendix B for the code). It uses an interpolation scheme with a specified step size. In this case, the step size was 0.005 cm which provided approximately 500 points between $r \langle 0, a \rangle$. The b_z results for each of the radial density profiles are given in Figure 2.8.

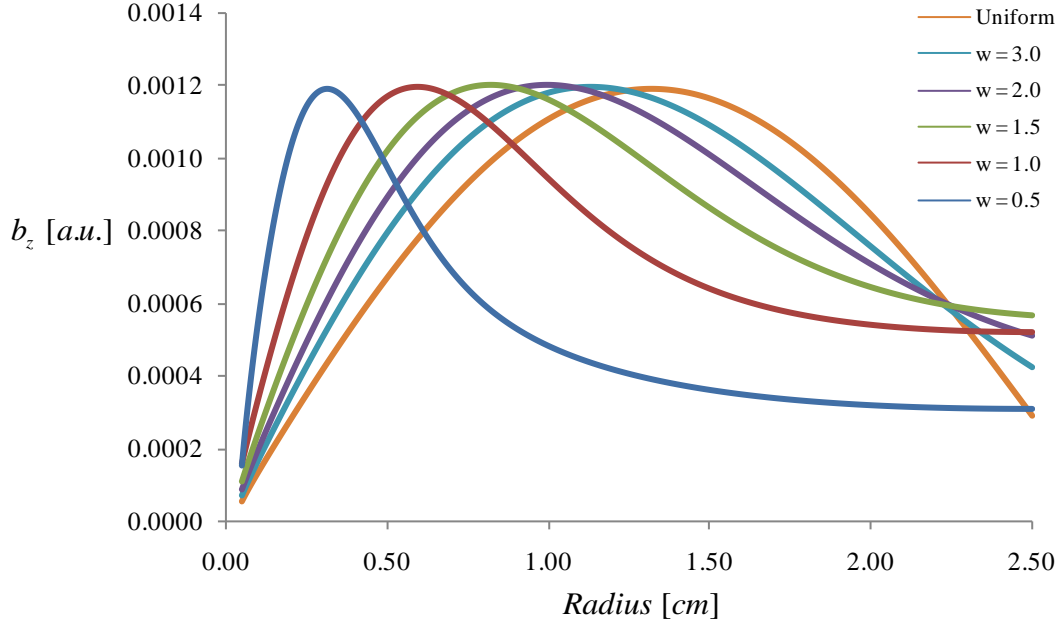


Figure 2.8. b_z fields for Gaussian radial density profiles.
 $B_0 = 900$ Gauss, $m = +1$ antenna, $f = 13.56$ MHz, and $a = 2.5$ cm

The derivative of b_z was numerically solved in the same manner such that the remaining b_r and b_θ components could be solved according to (2.56) and (2.57). These results are shown in Figure 2.9 and Figure 2.10.

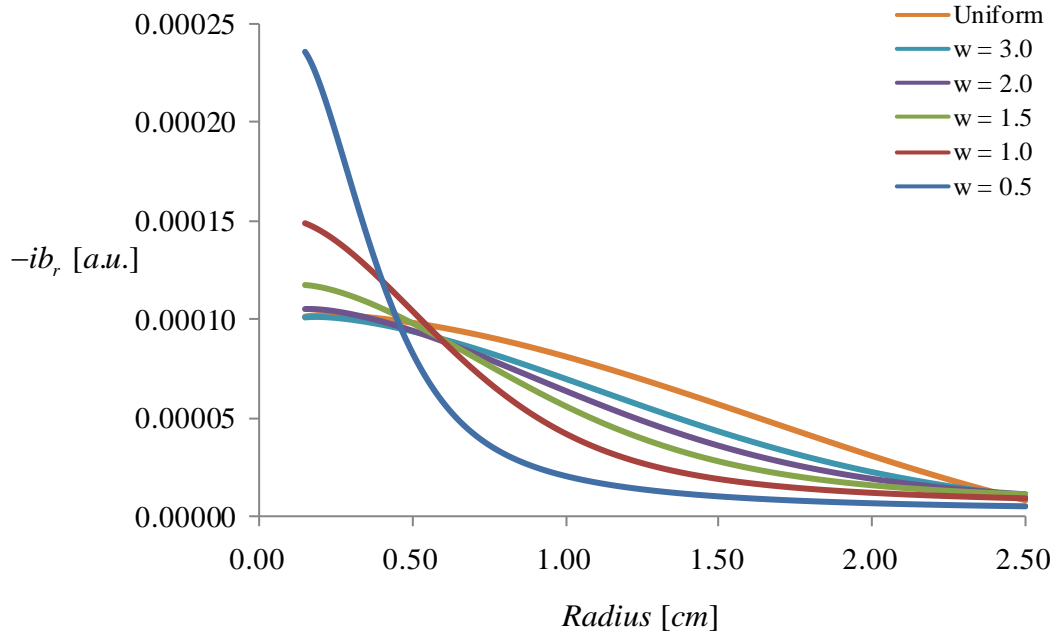


Figure 2.9. $-ib_r$ fields for Gaussian radial density profiles.
 $B_0 = 900$ Gauss, $m = +1$ antenna, $f = 13.56$ MHz, and $a = 2.5$ cm

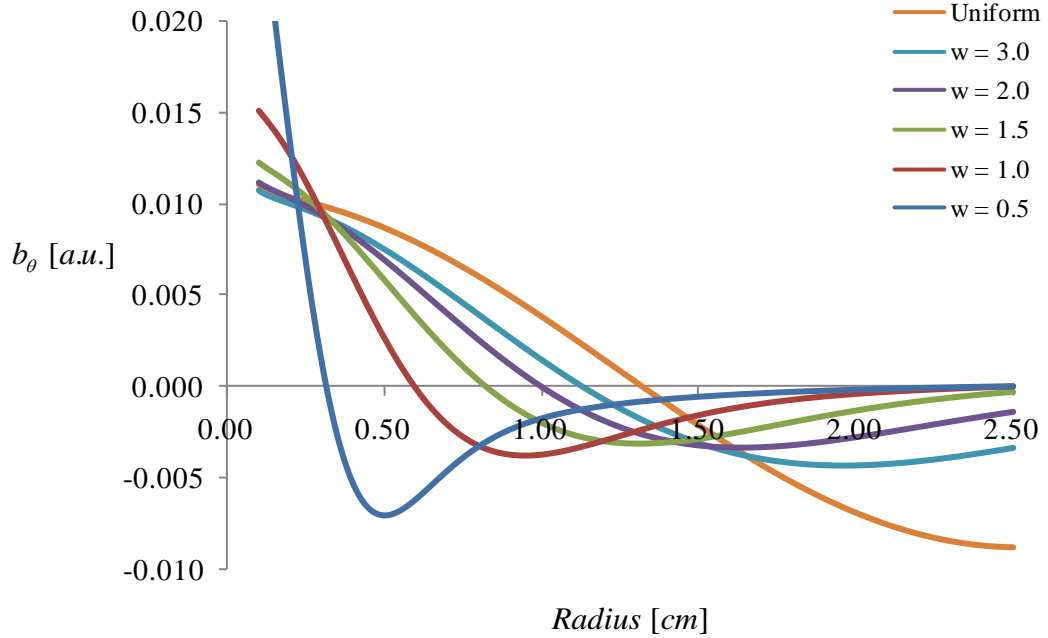


Figure 2.10. b_θ fields for Gaussian radial density profiles.
 $B_0 = 900$ Gauss, $m = +1$ antenna, $f = 13.56$ MHz, and $a = 2.5$ cm

The accuracy of the results for the numerical simulation in Figure 2.8 through Figure 2.10 is verified when the uniform density fields are compared against those obtained in Figure 2.3 and complete agreement is achieved. Additionally, both boundary conditions are satisfied when b_z is solved for, namely the radial component of the b_r fields go to zero for each profile studied; Figure 2.9.

Returning to the boundary condition (2.67) and expanding α , γ and rearranging

$$\frac{\omega m \mu_0 e}{a B_0} n(r) b_z + (k_z^2 - k_0^2) b_z' = 0 \quad (2.69)$$

shows that when the boundary condition is applied for a given density profile, the only free parameter is the axial wavenumber k_z . In particular, k_z is adjusted until the condition is satisfied for the plasma wave fields. The impact of the radial density profiles can be seen in Figure 2.11.

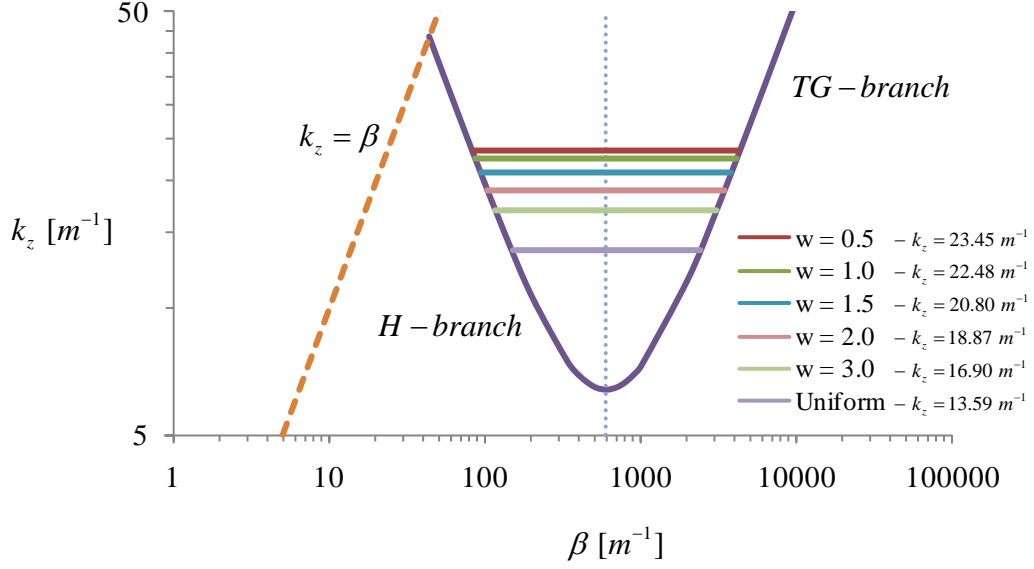


Figure 2.11. Influence of density profiles on wavenumber between two wave branches.
 $n_0 = 1 \times 10^{19} \text{ m}^{-3}$, $B_0 = 900 \text{ Gauss}$, $m = +1$ antenna, $f = 13.56 \text{ MHz}$, and $a = 2.5 \text{ cm}$

Essentially, the k_z values act as eigenmodes between the branches. The β value for the TG branch then becomes $k_{\perp}^2 = \beta^2 - k_z^2 \cong \beta^2$. This again shows the TG-branch to be a dominantly radial wave. For these values of β the radial wavelength is extremely short; varying between $\lambda_{\perp} \rightarrow (0.15 \text{ cm} - 0.26 \text{ cm})$ whereas the axial helicon wavelength $\lambda_z \rightarrow (26.79 \text{ cm} - 46.23 \text{ cm})$.

2.5 Chapter Summary

This chapter has summarized the derivation of the helicon wave radial b-profiles. The two primary considerations were: finite vs. zero electron mass, and uniform vs. non-uniform radial density distributions. These derivations have been independently considered in the variously referenced journal articles; however this chapter compiles the results into the comprehensive layout presented here.

Inclusion of electron mass revealed an additional wave of very high perpendicular wave number; the TG-wave. The associated wavelength with this radial TG-wave is typically less than 1 cm. When considering a non-uniform radial density, the helicon wave b-profiles notably alter their radial structure. As the density profile more centrally peaked, so too do the radial b-profiles.

This chapter has much more thoroughly quantified the results for the axial wavelength than has been previously considered. We have shown the helicon wavelength varies over the 10's cm range dependent on the density and applied magnetic field. Additionally, we demonstrated that for each Gaussian density profile considered, the axial wavelength must be varied until the boundary condition is satisfied. Finally, the significance of this chapter is manifest in the derived measureable quantities: b_r , b_θ , b_z , λ_z , and $n(r)$ which will be verified in the laboratory.

2.6 References

- [1] M. M. Balkey, R. Boivin, J. L. Kline *et al.*, "Ion heating and density production in helicon sources near the lower hybrid frequency," *Plasma Sources Science and Technology*, vol. 10, pp. 11, 2001.
- [2] S. Cho, "The role of the lower hybrid resonance in helicon plasmas," *Physics of Plasmas*, vol. 7, no. 1, pp. 7, 2000.
- [3] J. L. Kline, E. E. Scime, R. F. Boivin *et al.*, "Slow wave ion heating in the HELIX helicon source," *Plasma Sources Science and Technology*, vol. 11, pp. 13, 2002.

- [4] B. N. Breizman, and A. V. Arefiev, "Radially Localized Helicon Modes in Nonuniform Plasma," *Physical Review Letters*, vol. 84, no. 17, pp. 4, 2000.
- [5] G. Chen, A. V. Arefiev, R. D. Bengtson *et al.*, "Resonant power absorption in helicon plasma sources," *Physics of Plasmas*, vol. 13, no. 12, pp. 123507, 2006.
- [6] P. C. Clemmow, and R. F. Mullaly, "Dependence of the Refractive Index in Magneto-ionic Theory on the Direction of the Wave Normal."
- [7] W. P. Allis, "Waves in Plasma."
- [8] T. H. Stix, *The Theory of Plasma Waves*: McGraw-Hill, 1962.
- [9] D. G. Swanson, *Plasma Waves*, Second ed.: IOP Publishing, 2003.
- [10] F. F. Chen, "Plasma Ionization by Helicon Waves," *Plasma Physics and Controlled Fusion*, vol. 33, no. 4, pp. 26, 1991.
- [11] D. Arnush, "The role of Trivelpiece-Gould waves in antenna coupling to helicon waves," *Physics of Plasmas*, vol. 7, no. 7, pp. 9, 2000.

CHAPTER 3: EXPERIMENT AND TEST SETUP

To maintain consistency, the experiments performed in this work were designed and scaled based off of earlier helicon efforts [1-4]. This also allowed validation of preliminary work and later allowed for comparison with current results. The experimental work performed here was conducted at the Air Force Research Laboratory's (AFRL) Electric Propulsion (EP) facility in Edwards Air Force Base, California. This chapter will describe the apparatus used for testing.

3.1 Vacuum System

All testing was conducted with a quartz tube attached to a large diffusion chamber (the details of each tube will be discussed with the antennae tested). The diffusion chamber is a cylindrical, stainless steel, 0.5 meter diameter by 1.0 meter long vacuum chamber. It has 24 access ports / flanges of varying diameter for diagnostic feed-throughs, pumping connections, and internal viewing and access. The schematic is shown in Figure 3.1.

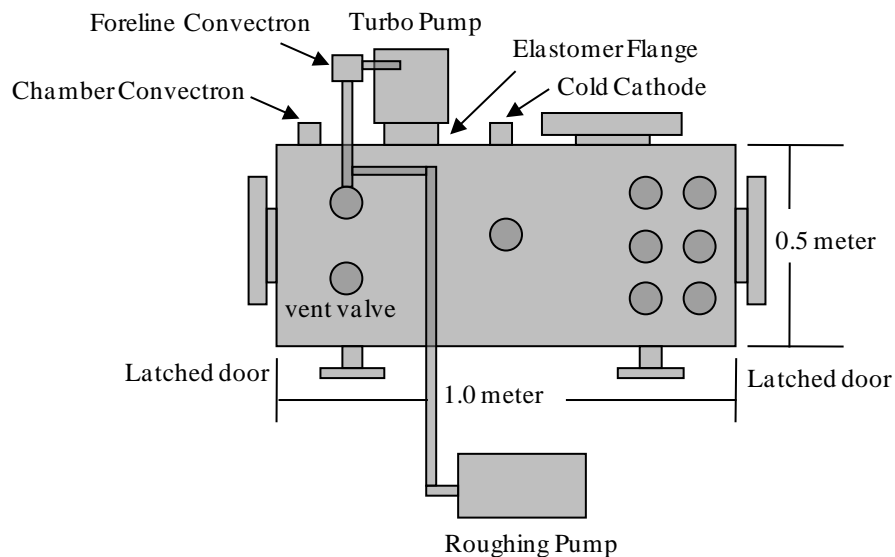


Figure 3.1. Schematic of vacuum diffusion chamber with pump locations

The chamber is pumped by a Varian TV-300 HT turbomolecular vacuum pump with a pumping speed of 250 l/s backed by a dry scroll pump. The chamber and foreline pressure are monitored with two Varian convectron gauges from atmosphere to $\sim 1 \times 10^{-3}$ Torr. Below this pressure a Varian cold cathode gauge is used to monitor the chamber to a base pressure of $\sim 2.4 \times 10^{-6}$ Torr. For tests in this work, the pressure range varied from $0.5 - 10 \times 10^{-3}$ Torr. Neither the convectron nor cold cathode gauge provided reliable or accurate pressure measurement in this range. Therefore, a MKS 629D Baratron capacitance manometer with a full scale range of $10^{-4} - 10^{-2}$ Torr was used for the intermediary pressure monitoring. This gauge was positioned on the ‘downstream’ end of the antennae / source at a location in between the quartz tube and diffusion chamber. All vacuum equipment is mounted on a 120 x 300 x 30 cm optics table supported by vibration suppressing pneumatic legs. Additionally, the turbomolecular pump is vibrationally isolated with an elastomer flange inserted between the foreline and diffusion chamber. The optics table not only provided a ‘good’ environment for suppressing mechanical noise but also provided a solid electrical ground for the vacuum chamber and other equipment.

3.2 Experiment

Power to the antennae was supplied by an ENI A1000 broadband power amplifier. The unit is an all solid state linear Class A amplifier which takes a 0 - 1 Volt input signal and outputs up to 1000 Watts over 0.3 - 35 MHz and 50 Ω input / output impedance. The amplifier input is taken from a Tektronix AFG 3102 100 MHz arbitrary waveform function generator. The forward and reflected power to the amplifier was monitored with

a Bird 4021 directional power sensor (1.8 - 32 MHz; 0.3 - 1000 Watts) connected to a Bird 4421 RF power meter. The matching network was a Manitou Systems ACM-1500L-12-MC-VC. It is an L-network capable of delivering up to 1500 Watts at 13.56 MHz with automated feedback to tune two variable capacitors to ensure the total load to the amplifier is matched to $50\ \Omega$. The capacitor in series with the plasma is a COMET 50 - 500 pF 8 kV and the shunt capacitor to ground is a COMET 20 - 2000 pF 5 kV capacitor. There is also an inductor in series with the plasma load that is variable to 14 μH but during operation remains at a set value. It is only variable in the sense that the internal connectors to the inductor can be moved between 7 consecutive taps which increase or decrease the total number of turns which RF current is driven through. The inductance varies $\sim 2\ \mu\text{H}$ / tap, however, for all measurements and testing conducted in this work, the lowest value of inductance was used at 2 μH . A schematic of the RF power system is shown in Figure 3.2.

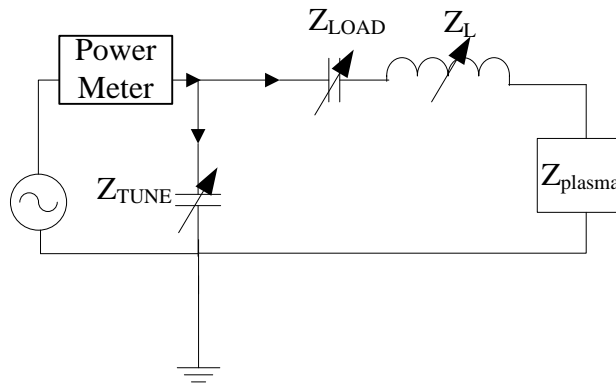


Figure 3.2. RF power delivery system incorporating the auto-match network circuit.

All tests were conducted using UHP Grade (99.999 %) Argon gas. The mass flow rate was controlled through an Alicat Scientific MC-100SCCM-D (Ar) flow controller. Flow rates were varied for operating test pressures from 0.5 - 10 mTorr and were performed for

100 – 500 Watts input power at 300, 600, and 900 Gauss static B_0 -field. A schematic of the test setup with electrostatic shield and diagnostic entry ports is shown in Figure 3.3.

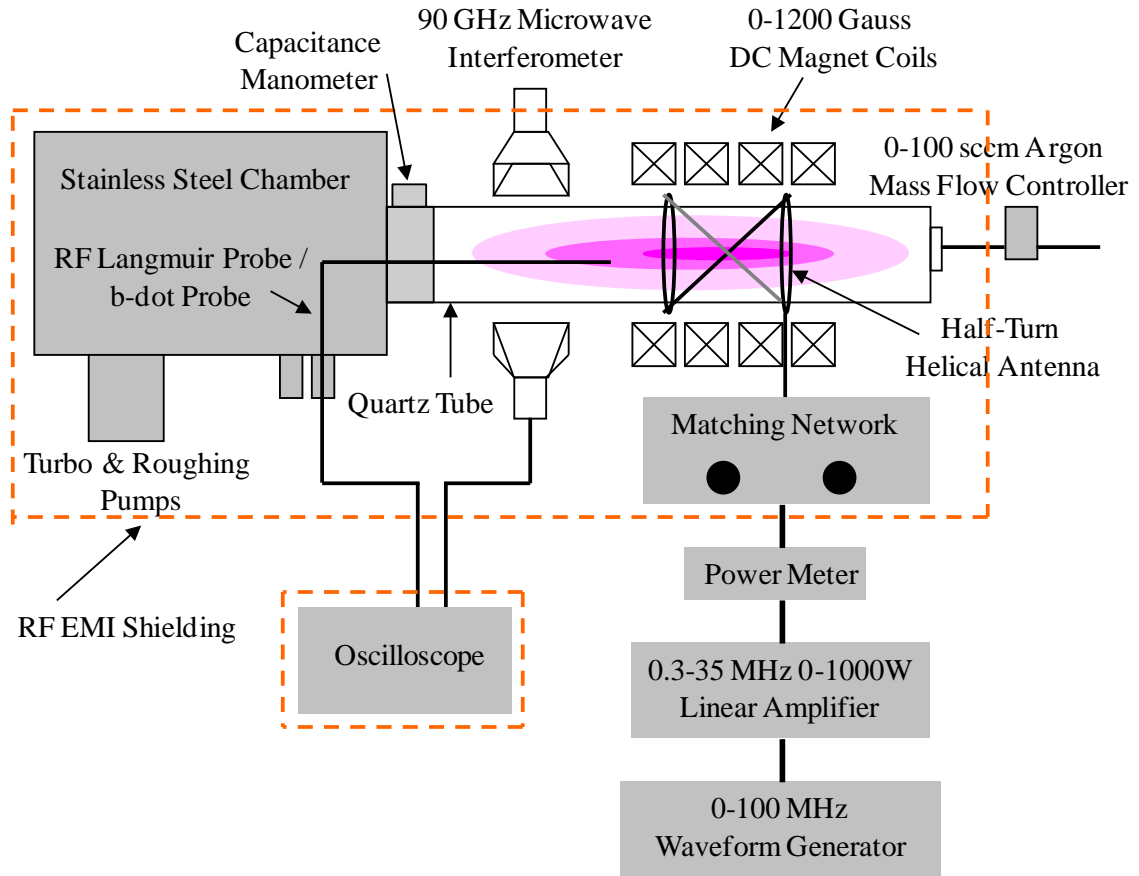


Figure 3.3. Schematic of AFRL Experimental Helicon research station.

The static magnetic field is generated by 4 glycol cooled magnets that can supply a continuous uniform field up to 1200 Gauss (custom designed by Arnold Magnetics). They operate using a 100 Volt 100 Amp EMS DC power supply. The electromagnets span a distance of 45 cm and provided uniform magnetic field over approximately 30 cm. The DC magnetic field was measured with a F.W. Bell Gauss meter (Model 7030). The determination of the static field as measured on the quartz tube centerline for varying input currents is shown in Figure 3.4.

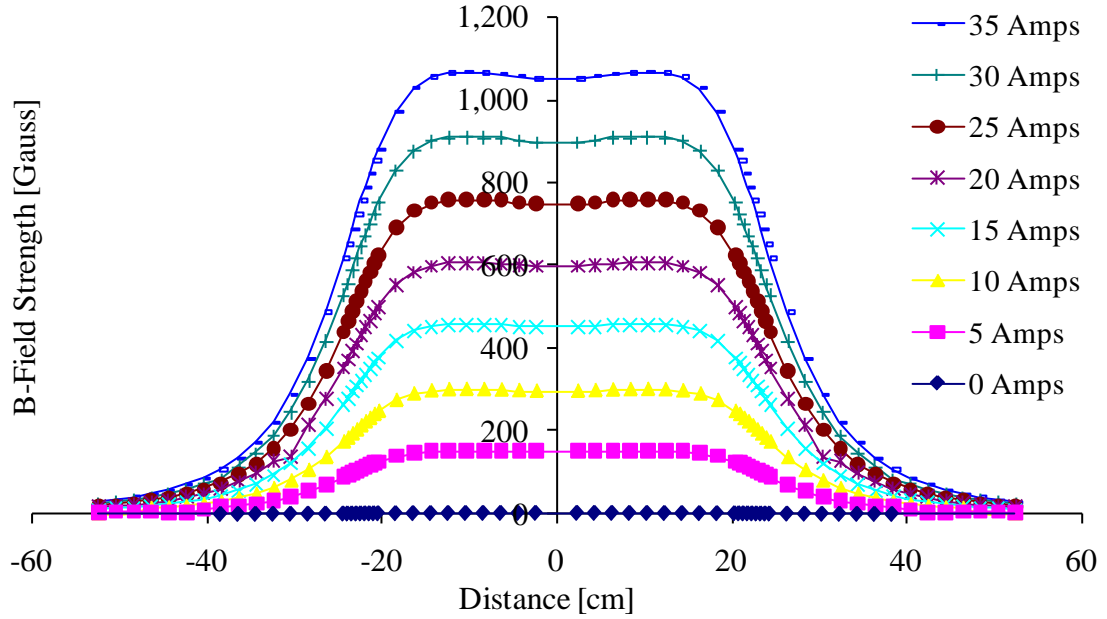


Figure 3.4. Axial applied magnetic field.

The majority of experimental measurement was conducted for a driving frequency $f = 13.56$ MHz at 500 Watts input power and 900 Gauss axially applied magnetic field. The gas used was Argon at a flow rate of 47 sccm which corresponded to an operating pressure of approximately 10 mTorr. These were the conditions where previous measurements for the helicon wave profiles matched those predicted analytically [2, 3, 5, 6] as shown in Chapter 2. Additionally, these test conditions provided signals of adequate strength for internal probe measurement so that diagnostic intrusion was limited; this will be discussed in further detail in Chapter 4-5.

3.3 Antennae

Previous helicon work has typically utilized three different antenna configurations [7]. These being the Nagoya, Boswell, or twisted Nagoya (also known as a full turn or half turn helical antenna). The three antennae are shown in Figure 3.5 a,b,c.

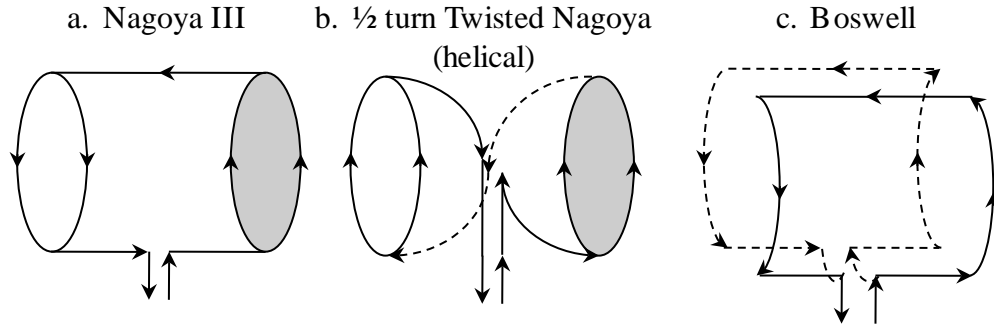


Figure 3.5 a,b,c. Examples of different antennae used in helicon research.

Throughout this study, the $\frac{1}{2}$ turn twisted Nagoya or $\frac{1}{2}$ turn helical antenna was tested. This antenna structure has been extensively tested and provided the most data for comparison with the current work. Additionally, since it was wrapped as a right-handed antenna with respect to the static magnetic field, the antenna structure is known to propagate the $m = +1$ helicon wave fields described throughout Chapter 2. If the direction of the magnetic field is reversed then the antenna would be left-handed and the $m = -1$ wave fields should propagate.

The antennae consisted of wrapping copper strap around the outside diameter of quartz tubes that were glass welded to stainless steel vacuum feed-throughs. This meant that the antennae current loop was in atmosphere whereas the induced currents from the antenna were within the cylindrical quartz cavity under vacuum. The hardware consisted of three quartz cylinders, each ~ 45 cm length. Two are straight cylinders with an outside diameter of 1.5 inches (3.8 cm) and 2.5 inches (6.4 cm), while the last is a conical design starting at 1.5 inches (3.8 cm) outside diameter and ending at 4.0 inches (10.2 cm) diameter as shown schematically in Figure 3.6. This quartz tube and antenna structure can either be converging or diverging with respect to the magnetic field in a manner

similar to the right- and left- handed helicity of the helical antennae. Antenna lengths tested ranged from 2.0 inches (5.1 cm) to 8.0 inches (20.3 cm) between the end rings.

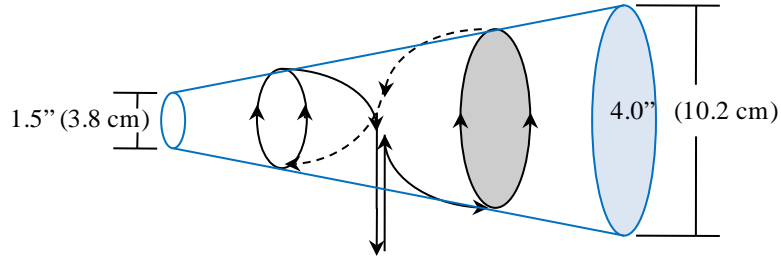


Figure 3.6. Conical geometry tube; can be converging with B_0 or diverging with B_0 .

The primary tube tested (the 6.35 cm OD cylindrical tube ~ 5 cm ID) consisted of $\frac{1}{2}$ turn helical antenna lengths of approximately 20.3 ± 0.1 cm, 10.2 ± 0.1 cm, and 5.1 ± 0.1 cm. The antenna lengths and their location within the static magnetic field are shown in Figure 3.7. Here, the antenna length measurement is reported as the distance between the two end-rings. Typically, this has been how the antenna length has been defined; however, we will refine this to more accurately represent the true antenna length in Chapter 5.

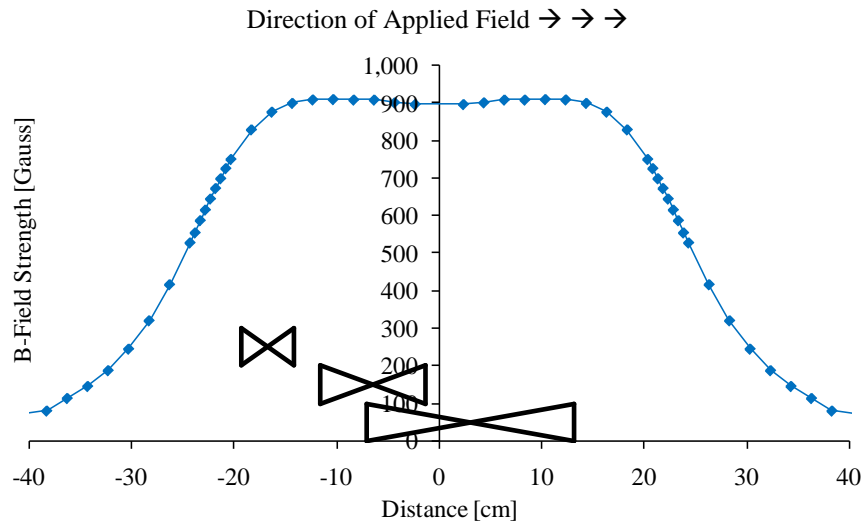


Figure 3.7. Applied Magnetic Field with Location and Lengths of Tested Antennas.

3.4 References

- [1] J. A. Lehane, and P. C. Thonemann, "An experimental study of helicon wave propagation in a gaseous plasma," *Proceedings of the Physical Society* vol. 85, 1965.
- [2] R. W. Boswell, "Very Efficient Plasma Generation by Whistler Waves Near the Lower Hybrid Frequency," *Plasma Physics and Controlled Fusion*, vol. 26, no. 10, pp. 16, 1984.
- [3] F. F. Chen, "Plasma Ionization by Helicon Waves," *Plasma Physics and Controlled Fusion*, vol. 33, no. 4, pp. 26, 1991.
- [4] F. F. Chen, "Experiments on helicon plasma sources," *Journal of Vacuum Science and Technology: A*, vol. 10, no. 4, pp. 13, 1992.
- [5] R. W. Boswell, "A study of Waves in Gaseous Plasma," Dissertation, School of Physical Sciences, The Flinders University of South Australia, 1970.
- [6] J. P. Klozenberg, B. McNamara, and P. C. Thonemann, "The dispersion and attenuation of helicon waves in a uniform cylindrical plasma," *Journal Of Fluid Mechanics*, vol. 21, pp. 545-563, 1965.
- [7] D. G. Miljak, and F. F. Chen, "Helicon wave excitation with rotating antenna fields," *Plasma Sources Science and Technology*, vol. 7, pp. 14, 1998.

CHAPTER 4: DIAGNOSTICS

As stated in Chapter 2, the two parameters that predominate the structure of helicon waves are the plasma b_z fields and the radial density profiles $n(r)$. It will be these two quantities that will be the focus of measurement. Additionally, since interest lies in the three-dimensional nature of the radial cross-section and axial propagation, internal probes are necessary. Toward this end, many considerations owing to the intrusive nature of plasma probes will be taken into account as well as the precarious measurements that can persist in a high frequency plasma environment generated by MHz plasma. This chapter will specifically address using b-dot probe measurements to obtain the plasma b_r , b_θ , and b_z fields as well as discuss the use of a RF compensated Langmuir probe and its calibration against a 90 GHz microwave interferometer. Finally, an error analysis will be discussed.

4.1 High Frequency b-dot Probes¹

Magnetic induction probes have been used as a diagnostic to measure plasma and other transiently induced fields since the 1960's [2-4]. When sized appropriately with respect to the measuring area, a spatial distribution of internal fields can be measured without much disturbance to the plasma or media of interest. However, when designing a probe for use in a high frequency environment the probe's calibration, sensitivity, and frequency response must all be considered. This is especially important since a probe's behavior is not only dependent upon its physical geometry (coil size, etc) but also by non-

¹ The work on High Frequency b-dot probes has been previously published by Reilly [1] M. P. Reilly, W. Lewis, and G. H. Miley, "Magnetic field probes for use in radio frequency plasma," *Review of Scientific Instruments*, vol. 80, no. 5, pp. 053508-5, 2009. W. Lewis is thanked for his review of the manuscript and assist in data collection.

ideal factors such as cable lengths, cable types, capacitive pickup due to plasma or other sources, and impedance matching of the probe to an oscilloscope or other measuring device. More thorough qualitative considerations on probe characteristics are given in References [2-4]. In this paper, each of these will be addressed and quantified specifically for b-dot probes that were designed to take measurements on 13.56 MHz RF cylindrical plasma.

4.1.1 Magnetic Probe Theory

Inductive probes in the most general sense consist of a loop of wire which when subject to a time varying magnetic flux obey Faraday's Law

$$V_i = -\frac{d\Phi_b}{dt} \quad (4.1)$$

where V_i is the induced voltage in the wire and Φ_b is the magnetic flux through the loop or coil. We consider the coil's cross sectional area small enough that the flux and magnetic field do not vary over this area and obtain

$$V_i = -A_{eff} \frac{db}{dt} \quad (4.2)$$

where b is the component of the field that lies along the axis of the coil and A_{eff} is the effective area over which the magnetic flux is measured. A_{eff} can be described by

$$A_{eff} = nA \quad (4.3)$$

where n is the number of turns in the sensing coil and A is the cross sectional area of each turn. Substituting for A_{eff} yields,

$$V_i = -nA \frac{dB}{dt} \quad (4.4)$$

However, this will most likely not be the voltage present at the measuring instrument (oscilloscope) due to many non-ideal factors that cause signal attenuation through impedance mismatch. A thorough analysis and theory on the non-ideal characteristics of b-dot probes is given in References [2, 5].

To obtain a large voltage, it is desirable to have a coil with a large cross-sectional area and many turns. However, if the area of the coil is large, the probe can disturb the plasma and measurements become spatially limited. A large number of turns in the sensing coil with a large radius will cause the inductance to rise. This is seen by looking at the inductance of a single layer solenoidal coil [3]

$$L = \frac{r^2 N^2 \pi}{l} \left(1 - \frac{8w}{3\pi} + \frac{w^2}{2} - \frac{w^4}{4} + \frac{5w^6}{16} - \frac{35w^8}{64} + \dots \right) \text{ where } w = r/l \quad (4.5)$$

Clearly, as the radius of the coil increases, so does the inductance. Consequently, when the inductance L rises, the cutoff frequency f_{co} of the coil decreases according to [5]

$$f_{co} = \frac{Z_0}{2\pi L} \quad (4.6)$$

Therefore, a compromise must be found that provides an adequate induced voltage (probe sensitivity; large n & A) while maintaining good spatial resolution (small A) and an adequate frequency response (small $L \rightarrow$ small n & A).

Considering a time varying field $b(t) = b \sin(\omega t)$, equation (4.4) for the resulting magnitude of the magnetic field, as measured by the probe, becomes

$$|b| = \frac{V_i}{nA\omega} \quad (4.7)$$

Therefore, in order to characterize a magnetic induction probe for use at a specific frequency f , we must determine the product nA . This is also known as the calibration factor.

4.1.2 Magnetic Probe Calibration

Previous work has shown that there are typically three ways in which magnetic probe calibration is accomplished [2-4]:

- 1) direct geometrical inspection of the coil dimensions (count n , measure A)
- 2) measuring the output voltage when the coil is put in a known pulsed field
- 3) comparison of the probe output with that of a coil of known dimensions, i.e., a Helmholtz coil, and calculate what ' b ' should be generated compared with what ' b ' is measured.

More recently, characterization of magnetic induction probes have also utilized network analyzers in conjunction with one of the above methods to gain a more detailed measurement of the probes behavior [5, 6] . However, there exist limitations to all three methods regardless of the instrumentation used.

For example, with direct geometrical inspection, accurate measurement when the probe is nominally small can become difficult. Method (2) requires having a known field near the frequency of interest, which is often difficult. Method (3) has been found to be the preferred method of calibration amongst many authors [2-4, 6]; however, careful attention must be used when this method is considered.

A Helmholtz coil is utilized most frequently due to the uniform field at the center. This field is given by

$$B_z = \left(\frac{\mu_0 N I}{a} \right) \left(\frac{8}{5^{3/2}} \right) \quad (4.8)$$

where ‘ a ’ is the coil radius and is equal to the coil separation distance, N is the number of turns in each coil, and I is the current in the coils. Immediately, we see that geometrical inspection is used in determining the number of turns and the radius of the calibrating Helmholtz coil. Additionally, we must accurately know the current in the calibration circuitry as well as the frequency response of the Helmholtz coil based upon its capacitance and inductance. As an example, utilizing a low inductance resistor to measure the current through a Helmholtz coil, we find deviations for the ideal impedance response resulting in a 3 dB point of 66.5 MHz for a 120 Ω resistor with < 0.1 μH at 100 kHz as shown in Figure 4.1. (Noted at 100 kHz because the resistive / inductive values will vary at higher frequencies due to factors such as skin depth).

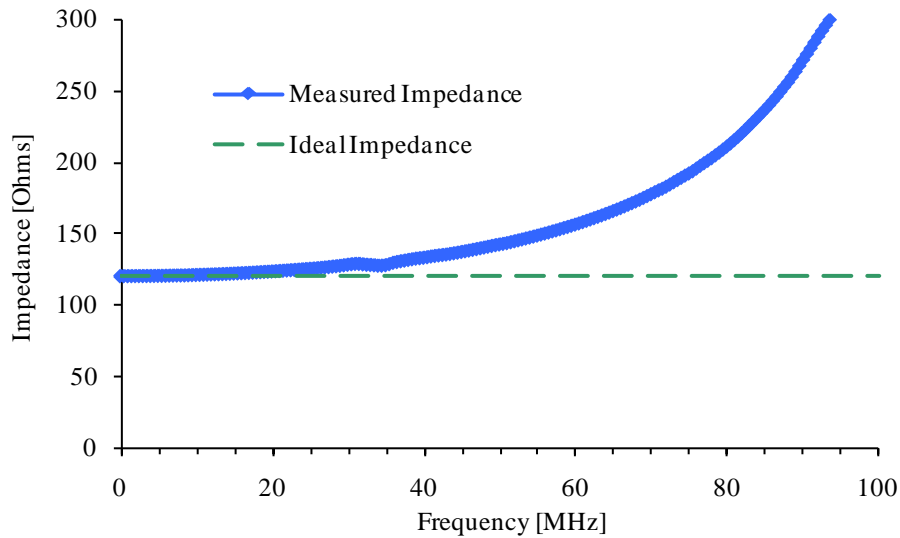


Figure 4.1 Low inductance 120 Ω resistor; impedance frequency response.

Attention must also be paid to the connection wires for the Helmholtz coil (as well as in the case of the magnetic induction probe). For example, the current source for the Helmholtz coil will most likely have some connection lead wires both prior to the Helmholtz windings as well as exiting from the Helmholtz windings. Also, if the current through the calibrating coil is measured as the current through a low inductance resistor, the connection wires that sense the resistor current will have some inherent inductance to them and likewise a cutoff frequency which will dictate the frequency to which a Helmholtz coil can be utilized; the limitation either being the resistor itself, or the cutoff frequency due to the coils inductance. For example, coaxial (BNC) cable is typically rated for 50 Ω use to a few GHz; however, if the load is not 50 Ω , or breakouts are used, the useful frequency range drastically changes. If alligator clip coax breakouts are used to either measure the resistor current or the connectors for the Helmholtz source current, then the useful frequency range of these breakouts is limited to ~ 10 MHz, as shown in Figure 4.2. This measurement was not made with an impedance analyzer to illustrate the frequency limitation of connection wires. This resistor has a similar inductance to that of the 120 Ω resistor previously used; however, when the frequency response is measured with a function generator and oscilloscope, we find that the frequency is limited by the inductance in the connection wires. Therefore, great care must be taken when utilizing method (3) as a method of calibration because errors in the calibration circuitry and setup can easily propagate into the magnetic probe's circuitry.

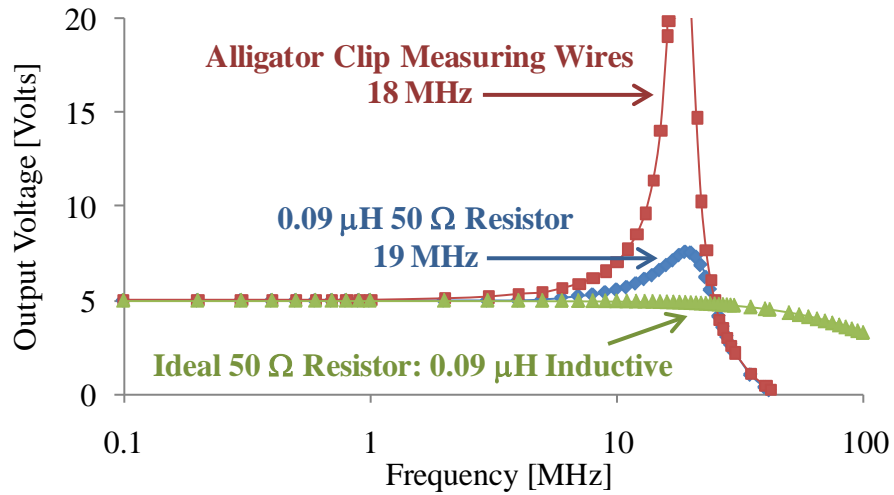


Figure 4.2. Frequency response of 50 Ω resistor and coaxial alligator breakouts as measured with a function generator and oscilloscope.

Due to the limitations of each of the calibration methods described above, it is the author's preference that when using prefabricated coils, the manufacturer's geometrical specifications be used for the number of turns and area based on the bobbin size. This is typically the case when using a surface mount inductor as the sensor coil as is used in this work.

4.1.3 Magnetic Probe Capacitive Pickup

Due to the nature of the plasma environment, there are two sources from which a probe will measure pickup: inductive signals (which are due to the magnetic flux lines which pass through the sensing coil) and capacitive pickup (which is due to a potential difference between the plasma discharge and coil). These differences are illustrated in Figure 4.3.

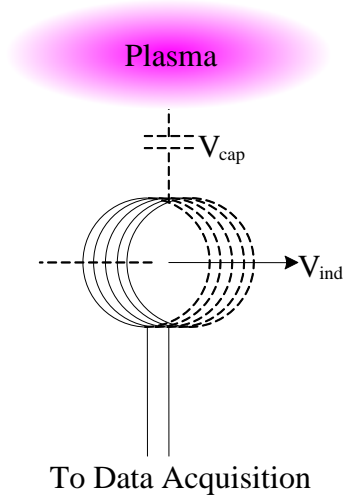


Figure 4.3. Illustration of inductive and capacitive signals present when magnetic field probes are used in plasma.

For the purpose of measuring the plasma magnetic field ‘b’, the only signal of interest is that induced in the sensing coil. To remove unwanted capacitive pickup, we consider putting two separate sensing coils next to each other but geometrically orientated 180 degrees with respect to the other. The two signals are then combined through a Center-Tapped Transformer (CTT) such that the capacitive voltage signal is subtracted out when the leads from the two probes are connected to opposite ends of the CTT. The two probe orientation is shown in Figure 4.4.

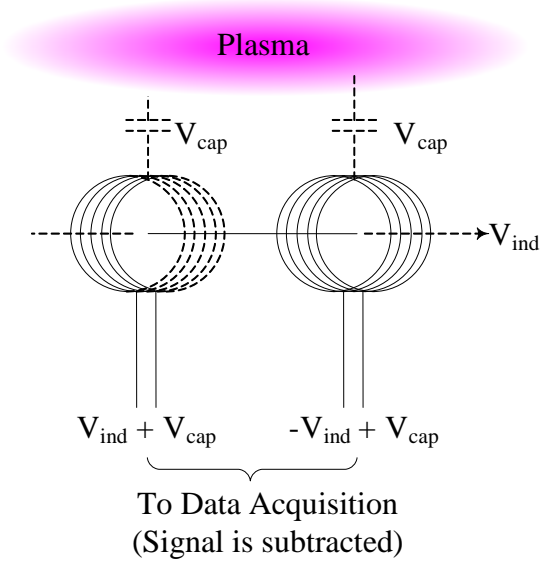


Figure 4.4. Two B-dot probes orientated 180 degrees with respect to one another; signal is subtracted through CTT.

The CTT used with these probes is a Mini-Circuits T16-6T+, which has a flat frequency response to 75 MHz. Additionally, it is an unbalanced to 50 Ω balanced load transformer with an impedance ratio of 16 [7]. To further reduce unwanted noise and pickup, a differential voltage probe is used. The differential voltage probe used in this setup is the Tektronix P6246, which has a 400 MHz bandwidth, < 1 pF input capacitance, 200 k Ω input resistance, and a 60 dB common mode rejection ratio (cmrr); the b-dot probe/CTT/differential voltage probe schematic is shown in Figure 4.5.

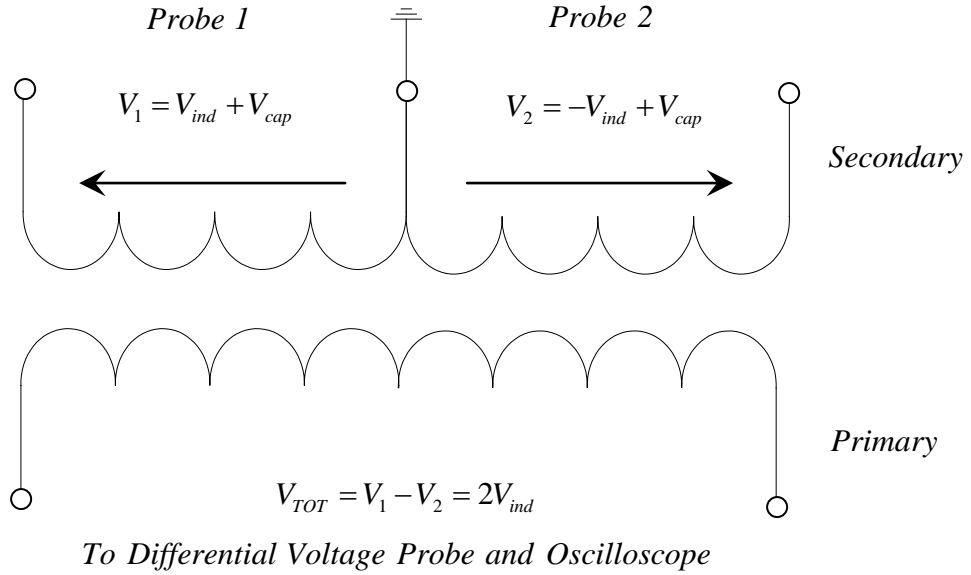


Figure 4.5. Center-Tapped Transformer with b-dot probes and differential voltage probe.

4.1.4 Probe Characterization

4.1.4.1 Selection

With the knowledge that the leads from the magnetic induction probe lowers the overall frequency response, it was desirable to design a coil with significantly lower inductance such that when the connection wires to the coil are made, allowance for use at 13.56 MHz (desired operating frequency) is accomplished. With this in mind and the desire for good probe sensitivity, a surface mount inductor was selected. This also allowed miniaturization of the sensing coil while providing a larger number of turns for a small cross sectional area.

The inductor selected was a Vishay Dale high frequency surface mount inductor, P/N IMC1008ERR39J. This surface mount inductor has 20 turns wound on a rectangular bobbin measuring 0.83 mm x 1.29 mm. Physically, the inductor is 2.5 mm x 2.0 mm x

1.6 mm with a ceramic core and solder-able end connector plates. The specified inductance is 390 nH with a self-resonant frequency of 530 MHz [8].

4.1.4.2 Frequency Response

The most important consideration when using a magnetic induction probe is identifying the resonant frequency of the entire measuring circuit. This is based upon many factors beyond just the coil inductance and the parasitic capacitance between successive turns of wire as shown in Figure 4.6. They include effects such as transmission line lengths, the types of cable used, and the circuit's termination impedance. An impedance analyzer quantified these effects on the probe's frequency response.

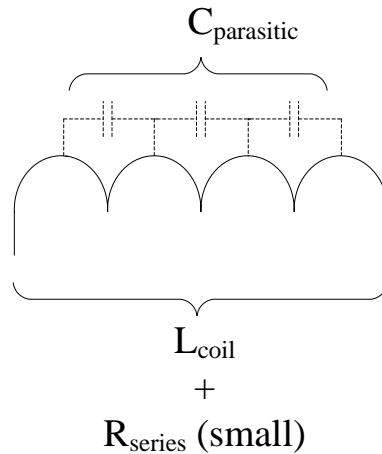


Figure 4.6. Coil inductance and parasitic capacitance that will determine probe / coil resonance frequency.

The impedance analyzer used in this work is the Agilent 4294A Precision Impedance Analyzer. The analyzer can be swept over any specified frequency range from 40 Hz - 110 MHz with a user-defined number of points from 2 - 801 between the frequency intervals. Sweeps can be specified to be linear or logarithmic and typically take < 1 s [9]. The 16047E test fixture was utilized with the 4294A unit. This fixture is attached to the

front of the unit and allowed for easy test and measurement of cables and axial leaded components, such as those utilized in this work. All tests were conducted with a 500 mV sinusoidal signal. The analyzer simultaneously displays the impedance magnitude Z and the phase delay θ . While it has the ability to display a variety of other parameters such as resistance, inductance, and capacitance (both series and parallel values) as a function of frequency, the one of primary interest in probe design is the magnitude of the impedance at the frequency under investigation; $f = 13.56$ MHz.

The frequency response of the probe was investigated and found to heavily rely on two things: 1) the length of cable from the sensing coils to the CTT; and 2) the type of cabling used (in this case either a twisted shielded pair or coaxial). The length of cable from the 50 Ω balanced side of the CTT to the oscilloscope differential voltage probe was found to have a small effect on the overall frequency response in comparison to the cable length on the unbalanced side of the CTT; this is the result of the CTT being a 50 Ω balanced load in conjunction with the transmission line to the differential voltage probe.

The relationship between frequency response and transmission line length for a twisted shielded pair of wires and coaxial wire was tested using a single sensing coil. The results are shown in Figure 4.7.

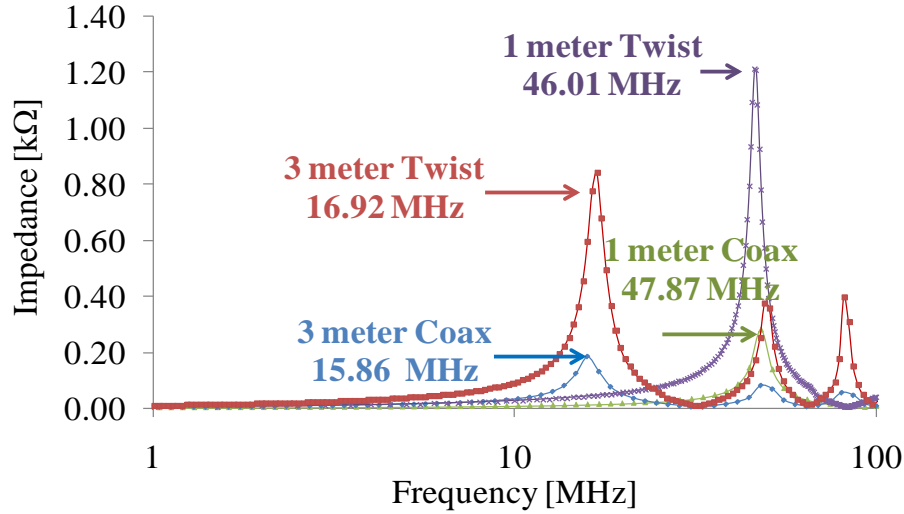


Figure 4.7. Impedance frequency response for twisted shielded pair and coaxial cable.

Both cables exhibit nearly identical resonance frequencies for the same length transmission line. However, at the resonant frequency, the coaxial cable has an impedance value that is five times smaller than the twisted shielded pair. For the intent of this probe, the frequency of interest is 13.56 MHz, so that if the transmission line length is kept to less than 1 meter, the type of cable chosen should not have much effect on the passing signal. It is prudent to note that probes used in environments such as plasma discharge will be subject to harmonic signals as well as the fundamental. Therefore, depending upon the application, higher or lower impedance at frequencies larger than the fundamental may be desirable.

In this work, the twisted shielded pair of cable was chosen specifically for the aforementioned reason. Since 13.56 MHz was the desired frequency of study, higher order harmonics are viewed as spurious signals. Additionally, the twisted shielded pair of cable was used on the primary winding side of the CTT so that when connected to the differential voltage probe, a differential measurement could take place between two lines

not directly connected with an instrument ground. The line length effect on the twisted shielded pair from the probe to the CTT was then investigated (with the CTT now inserted in-line whereas the CTT was not present previously). These results are shown in Figure 4.8 and clearly illustrate that shorter line lengths yield a higher resonant frequency and allow the probe to have a wider operating regime.

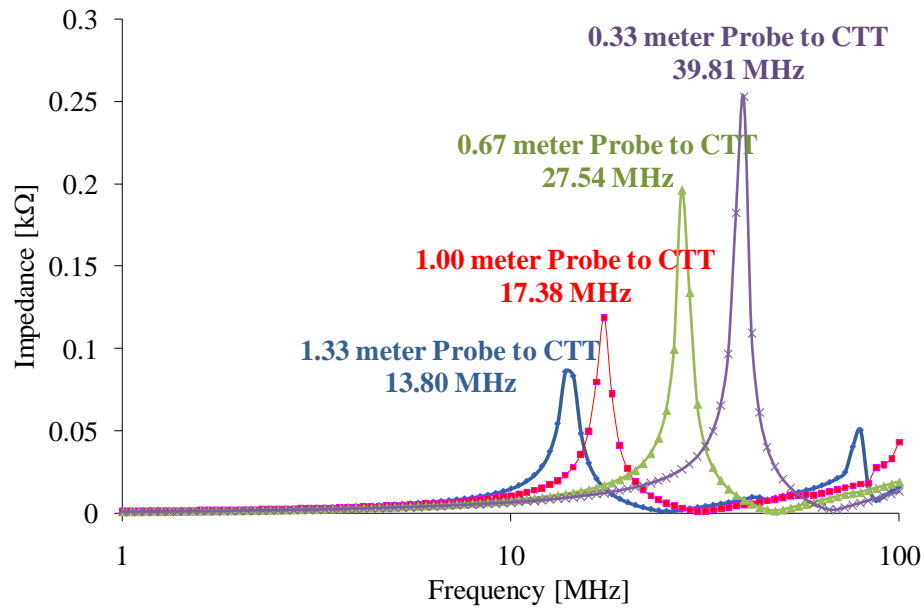


Figure 4.8. Line length effect from probe to CTT.

4.1.5 Discussion

The final probe characteristics were selected based upon some experimental and laboratory limitations. First of all, the 2-probe combination (180 degree spatial orientation) was measured to be approximately 5.0 mm in length and 2.5 mm in height. The probe was sized specifically to be close to this dimension so that spatial ‘*b*’ profiles could be resolved when probing the ~ 5 cm diameter cylindrical plasma. This ensures that the physical disturbance to the plasma is an order of magnitude smaller than the discharge. The probe is shown in Figure 4.9.

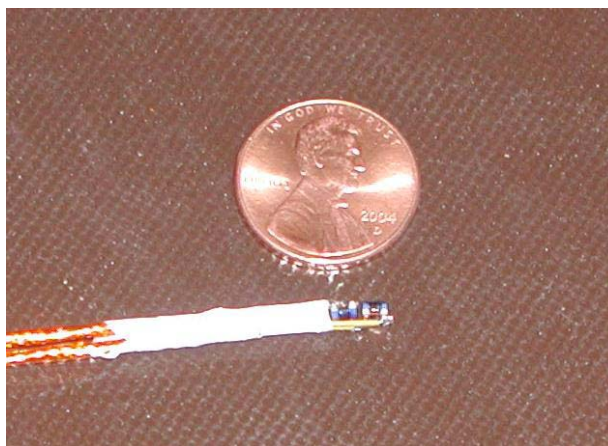


Figure 4.9. Two probe 180 degree spatial orientation; shown with twisted shielded leads to the CTT.

Second, the size of the CTT was significantly larger than the sensing inductors and if they were placed close together (so as to increase the circuit resonant frequency), the probe / CTT combination would become large and disturb the magnetic environment under investigation. As such, the probe-to-CTT length selected was 0.67 meters with a resonant frequency of 27.54 MHz. For the investigation of 13.56 MHz, this resulted in an impedance of approximately $10\ \Omega$'s. The calibration factor nA , based off manufacturer specifications was $21.27\ \text{mm}^2$.

The method of using an impedance analyzer eliminated many of the previous difficulties in magnetic induction probe design. Previously, discrete data points would be taken over a large frequency range rather than swept over the range of interest; this allows distinct features in the probe / circuit to be readily identified. It is not only a more time efficient method of probe characterization but it also allows the user to measure the entire circuit as a function of frequency. One can clearly see the effect transmission line length has as well as cable type on the circuit resonance.

For example, connecting a 1 meter cable to a 390 nH inductor with a self resonant frequency of 530 MHz, quickly drops the circuit resonance to ~ 17 MHz, more than an order of magnitude. The only way to circumvent this problem is to move a balanced - unbalanced CTT closer to the inductor (probe). However, for the 13.56 MHz design point in this work, we were fortuitous that transmission line lengths did not cause significant concern. While this work does approach the limitation of small physical size (small A), with good signal strength (nA), design for much higher frequencies may prove difficult. Although, if higher frequency operation is desired, one technique recently investigated has been that of frequency mixing where a high signal frequency is mixed with a local oscillator (LO) resulting in a more manageable intermediate frequency (IF) [10]. This method proved unnecessary for the work done here, though a comparison between the two methods is probably warranted.

4.1.6 Probe Analysis in Plasma

As previously mentioned, often times in work with radio frequency plasma discharge, there exists the potential for probes to pickup ‘noise’ or spurious signal contributions from harmonics of the driving frequency. In the case of plasma driven at 13.56 MHz, harmonics of this fundamental can be found at 27.12 MHz, 40.68 MHz, 54.24 MHz, etc. These are contributions to the primary signal that are not filtered out by proper probe characterization and not necessarily due to plasma oscillations. To illustrate this point, we consider a raw magnetic probe signal obtained from the oscillating plasma fields (driven at 500 Watts with a 900 Gauss applied static magnetic field) as shown in Figure 4.10. Additionally, we consider the Fast-Fourier Transform (FFT) of the raw signal in

order to view contributions due to harmonics; the FFT in Figure 4.11 was calculated as

$$wave_{FFT}[n] = \sum_{k=0}^{N-1} wave_{orig}[k] \cdot e^{2\pi i \cdot kn/N} \quad (4.9)$$

where $N = 25,000$ is the total number of data points sampled at the interval $\Delta t = 1.6 \times 10^{-11}$ s. In order to accurately report what the fundamental (13.56 MHz) contribution is, a Gaussian fit was then applied to the FFT in the vicinity of the fundamental and the peak value was interpolated with the amplitude calculated as

$$V_{13.56MHz}^{Amplitude} = \frac{2}{N} \times V_{13.56MHz}^{FFT} \quad (4.10)$$

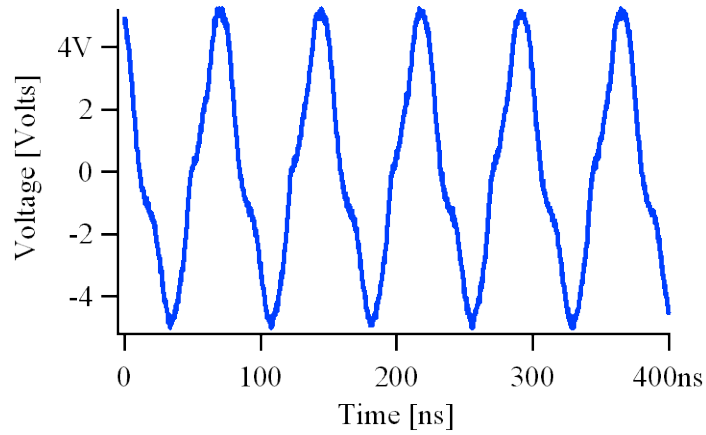


Figure 4.10. Raw Magnetic Probe Signal.

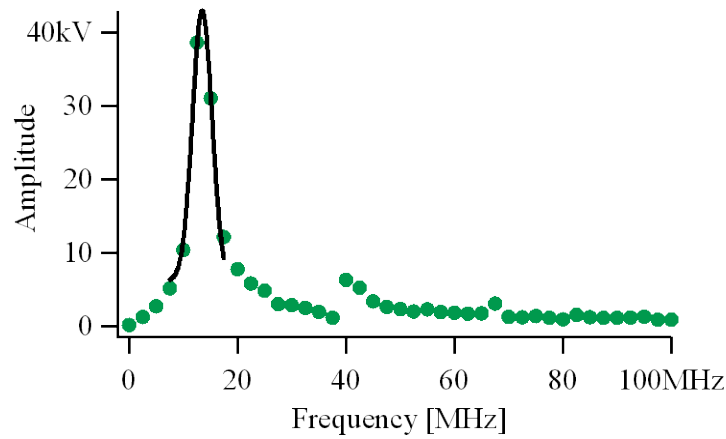


Figure 4.11. FFT of Raw Probe Signal.

Immediately evident from Figure 4.10 is that the signal obtained is not a pure sinusoid. It has slight distortions due to frequency harmonic contributions. Similarly, Figure 4.11 shows clear contributions at the 3rd and 5th harmonics; 40.68 MHz and 67.80 MHz respectively. In this case, what appears to be a greater than 4 Volt amplitude signal from the raw data is actually a 3.43 Volt amplitude signal when the FFT is analyzed according to (4.9) and (4.10); or about 22.5% signal measurement error due to frequency harmonics.

For a more demonstrative example of frequency harmonic contribution, we consider a second raw data trace obtained in a 500 Watt, 600 Gauss plasma shown in Figure 4.12. The signal appears much more distorted due to harmonic contributions and when the FFT (Figure 4.13) of the raw data is analyzed, contributions due to the 2nd, 3rd, 4th, 5th, 6th, and 7th harmonics are found. Again, fitting a Gaussian to the fundamental, we can calculate the signal amplitude to be 0.42 Volts where upon inspection the amplitude may be reported as $\frac{(\sim 0.90 + \sim 0.50)}{2} \approx 0.70 \text{ Volts}$; or about a 67% signal measurement error if harmonic contribution is ignored.

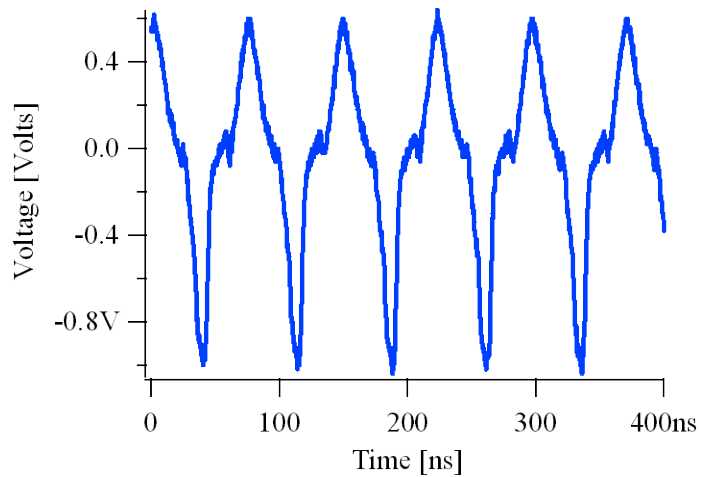


Figure 4.12. Raw Voltage Data Trace.

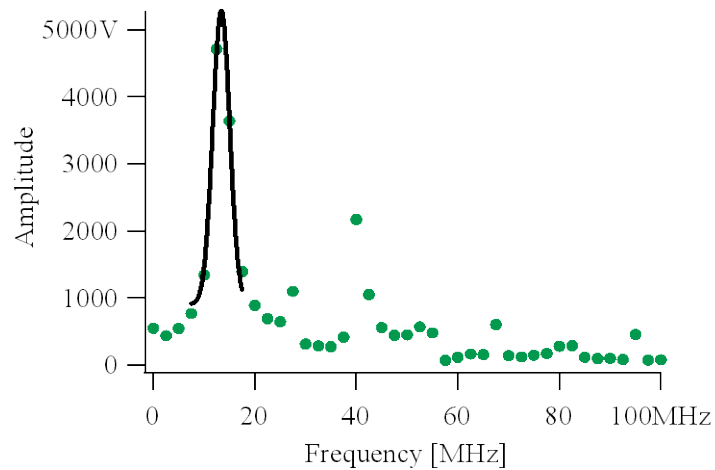


Figure 4.13. FFT of Raw Voltage Data Trace.

Obviously, in order to properly interpret results obtained from magnetic probes in plasma, it is necessary to remove any spurious contributions due to frequency harmonics. The most accurate method to accomplishing this is to record the raw signal, perform a FFT, and take the peak of a Gaussian fit to the area of interest. Although, this can often be more time consuming than utilizing an RC integrating circuit before data acquisition in order to directly record the presumed magnetic field amplitude, it is the more accurate approach and allows the user to see harmonic contributions to the signal that will

introduce error. The routine used to analyze all magnetic probe data in this work was performed and coded in IGOR and can be found in Appendix C.

4.2 RF Compensated Langmuir Probe and Microwave Interferometer

Metallic probes in plasma have been used for decades as one of the most readily implemented diagnostics of obtaining plasma parameters such as densities, temperatures, and potentials. They provide a method toward obtaining spatially resolved measurements of plasma discharge; however, they are also an intrusive diagnostic to the plasma environment if care is not taken to minimize this effect. The classical theory of Langmuir probes extends back to the 1920's although significant advancements in theory have been adapted to plasma regions where classical theory is no longer valid, i.e., interpretation and use in strong magnetic fields, impact of sheath thickness relative to probe size (Laframboise), and most importantly for this work, the implementation for use in a RF plasma environment. This section will discuss the important results of constructing a RF compensated Langmuir probe, which include characterization of the probe's circuit impedance and calibration against a 90 GHz microwave interferometer.

4.2.1 RF Compensation

RF compensated Langmuir probes were constructed in-house with four notch filters; two at the fundamental and two at the second harmonic. Additionally, a 1 nF capacitor was placed between the measuring probe and compensation electrode as shown in Figure 4.14.

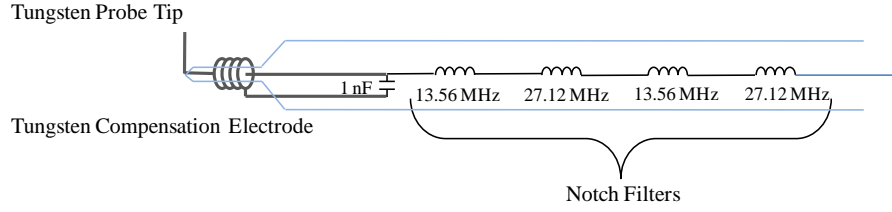


Figure 4.14. Schematic of Langmuir Probe Notch Filters and Compensation Circuitry.

The compensation electrode allows the probe tip to follow the RF fluctuations in the potential while the filters provide a large impedance for the AC voltage component with respect to the plasma sheath impedance [11, 12]. The rationale for this is that the ratio of the sheath-probe impedance should be made as small as possible so that the overall circuit (probe and sheath) acts as a voltage divider and the RF voltage component is primarily across the large probe impedance; since the DC current is the quantity of interest when obtaining the IV characteristic. The relationship that needs to be satisfied when performing RF Langmuir probe measurements is given by

$$|Z_{probe}| \gg |Z_{sheath}| \quad (4.11)$$

This is the simplified definition when designing RF probe circuitry. A more thorough analysis is given in [11, 12] but the result of minimizing the RF potential distortion to the sheath can be accomplished by following (4.11). When considering inductive plasma this requires that the compensation electrode be on the order of a few nF's while the choke impedance be $\gg 1 \text{ k}\Omega$ [12-14]. This is because the sheath resistance can be defined as [12]

$$R_{sheath} = \frac{kT_e}{eI_{electron}} \quad (4.12)$$

which in practice is on the order of a few $\text{k}\Omega$'s. Therefore, the probe's circuit or notch filters must have an impedance much larger than a few $\text{k}\Omega$'s.

The filters used in the construction of the probe are high frequency inductors from Vishay Dale where the series inductance and parallel parasitic capacitance between the number of successive turns results in the resonance curve for each notch filter. Due to the fact that each inductor is slightly different in the values of series inductance and parallel capacitance, the resonant frequency for each individual inductor will vary. Additionally, the manufacturer's listed self resonant frequency is not always exact due to non-testing of every inductor. However, for our purpose, this was very important and consequently, hundreds of inductors impedance curves were analyzed. To do this quickly, efficiently, and accurately, frequency sweeps were again performed with the Agilent 4294A Precision Impedance Analyzer; the same one used in the calibration of the b-dot probes. This made it possible to rapidly test many different inductors to determine which would yield the highest impedance at the fundamental and second harmonic frequencies. The frequency response of the four notch filters in series is shown in Figure 4.15.

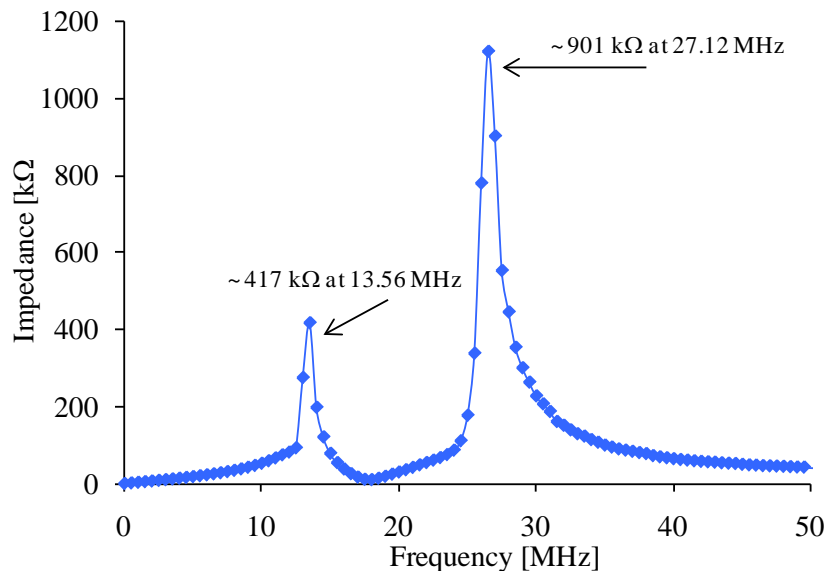


Figure 4.15. Impedance Curve for Four Series Notch Filters.

There should be caution that in actual probe implementation the impedance curves in Figure 4.15 are higher than the overall circuitry impedance response. Once the connection wires and the compensation electrode are connected, the impedance values here drop by nearly an order of magnitude due to shunt capacitances and line length effects. This can often be a limiting factor on the accuracy of Langmuir probe measurements in RF. For 3 eV plasma temperature with 1.0 mA electron current, the sheath resistance according to (4.12) is approximately $3 \text{ k}\Omega$'s. Therefore, at 13.56 MHz, where the total circuit impedance (shown in Figure 4.16) measured is $85.38 \text{ k}\Omega$, the best accuracy due to estimated sheath impedances would be about 5%, or $\pm 0.15 \text{ eV}$ for a 3 eV temperature. However, this accuracy will vary in accordance with (4.12). It is noteworthy to point out that to the best of the author's knowledge, impedance traces for circuit filters such as those shown in Figure 4.15 have been produced in the literature; however, it is the first time that the entire measuring circuit's frequency response has been identified.

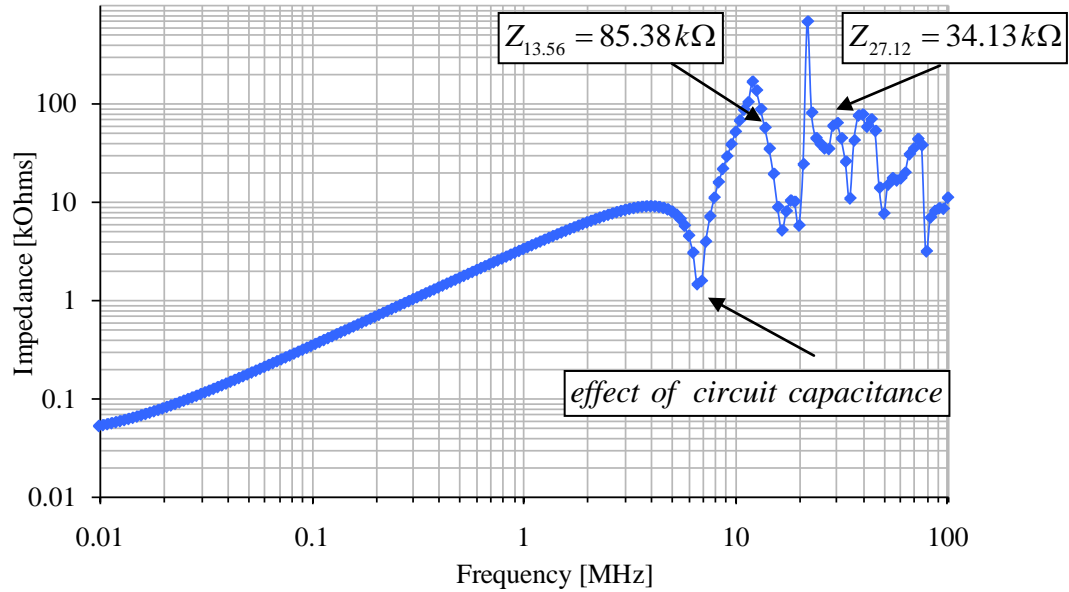


Figure 4.16. Overall Langmuir probe circuit frequency

The resonances in Figure 4.16 are for the same inductors used in producing the series resonance curves of Figure 4.15, the only difference being that the curves are distorted and overall circuit impedance lowered due to line and shunt capacitances. A basic rule to keep in mind is: *capacitors ‘pass’ high frequency signals and inductors ‘pass’ low frequency signals*. This is similar to the RF chokes where the inductor’s parasitic capacitance in parallel with the coil inductance acts as a bandpass or notch filter. The relations discussed here are simple enough in theory, though complex when actual inductor and capacitor values are considered with line lengths and series / parallel combinations. The use of the impedance analyzer greatly reduced this difficulty in the probe circuit characterization.

4.2.2 Obtaining the RF IV Characteristic

In order to take actual plasma measurements, the probe tip was swept from ± 100 Volts over 200 ms and the DC component of the current was measured across a 1 k Ω resistor. The measuring circuitry consisted of a Kepco Bi-polar voltage power supply, while the current was measured with a Tektronix P5205 100 MHz high voltage differential probe to minimize any common mode signal. The probe tip and compensation electrode were made from 0.009” diameter (0.02286 cm) tungsten wire. A typical probe tip was 3.0 mm in length while the compensation electrode was wound 20 times on a 0.025” OD (0.0635 cm) alumina tube spanning 6.0 mm. This yielded an effective probe surface area of 2.91 mm² and a compensation electrode surface area of 18.87 mm²; such that the compensation electrode’s surface area was approximately 6.5 times larger than the probe’s surface area. The electrical schematic is shown in Figure 4.17.

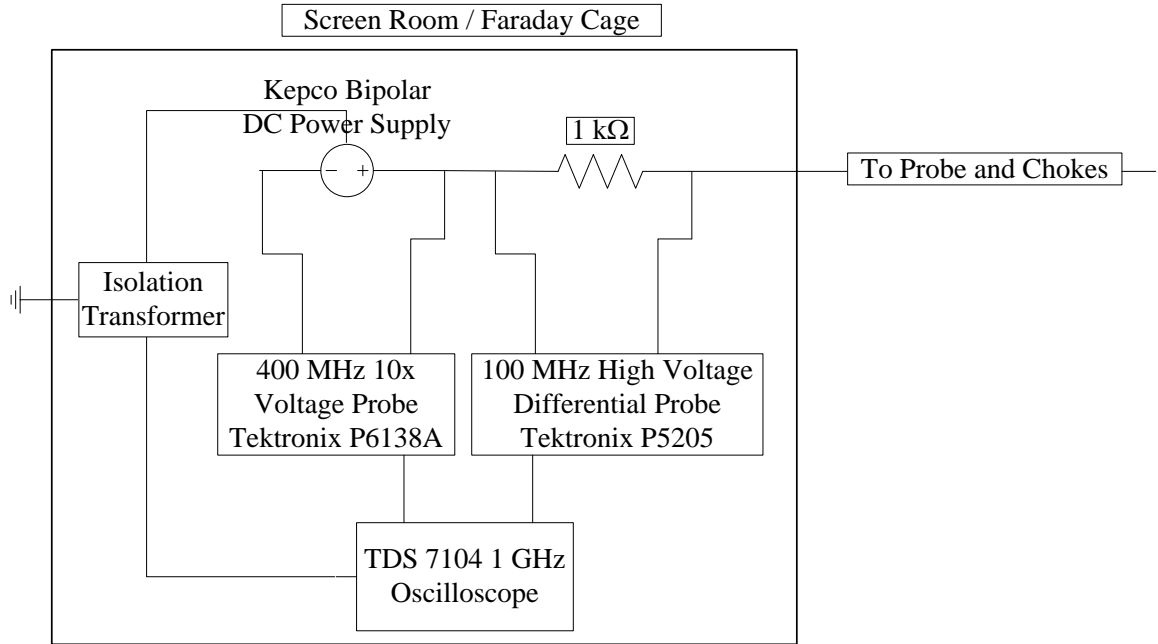


Figure 4.17. Electrical schematic of Langmuir probe data acquisition.

A representative example of two raw IV traces along with accompanying cubic spline fits are shown in Figure 4.18 and Figure 4.19. The cubic spline fit is 1000 data points approximating the 25,000 obtained for a raw oscilloscope trace. This was done for two reasons: 1) to remove some low-level RF noise in the trace; and 2) to reduce the data set to a more manageable number of points. As the data shows, no relevant information is lost in performing the cubic spline fit. The data analysis follows [15] for the Lafromboise method and a complete representative analysis can be found in Appendix D. A difficulty in analyzing the RF IV characteristic is ambiguity in identifying the plasma potential. Typically, the difference between the floating and plasma potential will be several times higher than the electron temperature due to differences between treating the thick vs. thin sheath scenarios. However, most IV characteristics analyzed in this work did not exhibit this effect and consequently the plasma potential is most likely higher than what is reported. This will result in an error for the electron temperature. The value of the

density reported will only be affected by the sheath to probe impedance ratio with the associated error from the electron temperature calculation.

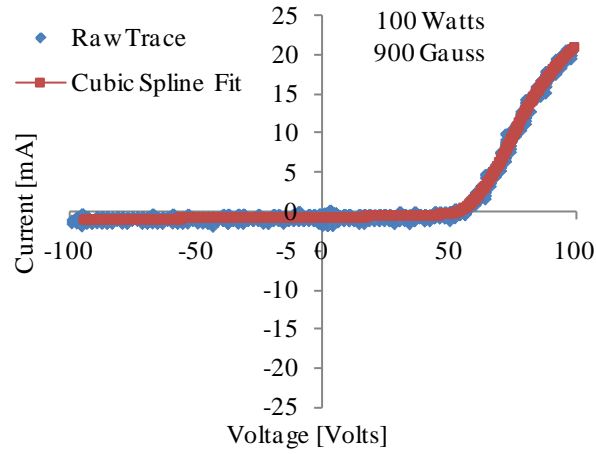


Figure 4.18. Langmuir Probe IV trace
47 sccm; 10 mTorr; 100 Watt; 900 Gauss; 6.35 cm OD

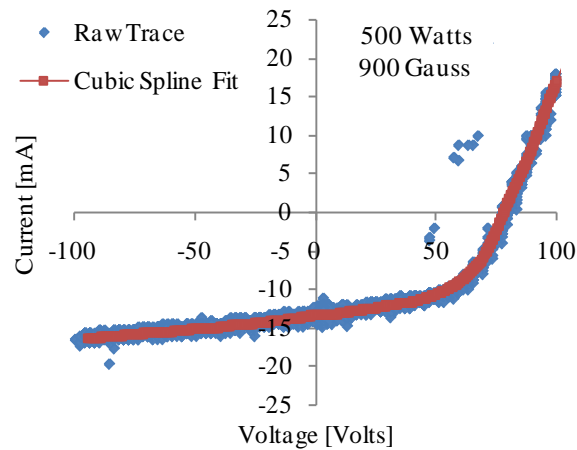


Figure 4.19. Langmuir Probe IV trace
47 sccm; 10 mTorr; 500 Watt; 900 Gauss; 6.35 cm OD

In Chapter 2, the structure of helicon waves (b_r , b_θ , and b_z fields) changed with the anisotropic nature of the plasma cavity based on the radial density distribution.

Therefore, the primary focus of Langmuir probe measurements will be based off of the radial and axial density distributions. The electron temperature obtained from the IV characteristic can often be a very subjective process; however, results for the electron temperature will later be reported as the role of the axial temperature distribution plays an

important part in the axial plasma density distribution. Since the density is of immediate importance, it is necessary to verify that the density measurements obtained from the IV characteristic are validated against another method. For this, a 90 GHz microwave interferometer was used.

4.2.3 Microwave Interferometer

Microwave interferometry measurements have previously been used to calibrate Langmuir probe results [16, 17]. The diagnostic has both its advantages and disadvantages with respect to electrostatic probes. While it is a non-intrusive diagnostic in the sense that no perturbation to the plasma environment occurs, this also means that no spatially resolved plasma quantity is obtained. The result is a radially integrated electron density. For collisionless plasma where the collision frequencies ν_{arb} are much less than the electron plasma frequency ω_{pe} , the electron density is given by

$$\frac{1}{n_e} = \frac{4\pi m_e \epsilon_0 c^2}{e^2} \frac{\Delta \theta_{plasma}}{\lambda_0 l} \quad (4.13)$$

where θ_{plasma} is the phase change in the path length ' l ' of the interferometer. λ_0 is the wavelength of the oscillator frequency, in this case for $f = 90 \text{ GHz}$, $\lambda_0 = 3.33 \text{ mm}$.

Therefore, the two quantities that must be determined are the path length ' l ' and the phase change of the wave which passes through the plasma θ_{plasma} . Each individual interferometer can have a unique method toward properly calibrating its system such that thermal and mechanic vibrations are quantified or calibrated to minimize error or noise in the phase change. For this particular interferometer, a unique calibration analysis was developed so that each branch (reference arm and plasma arm) could individually be

characterized in terms of the signal amplitude and phase change associated with each arm. A schematic of the interferometer setup is given in Figure 4.20 and the technique used to calibrate the microwave interferometer is given in Appendix E.

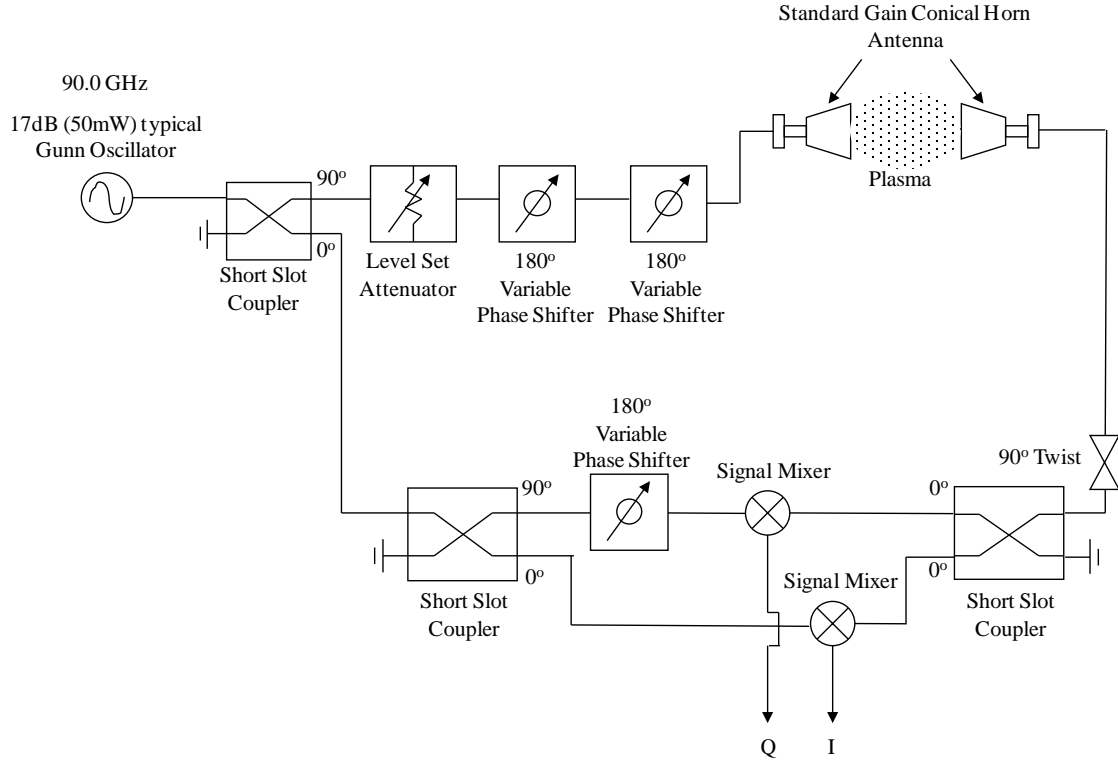


Figure 4.20. Schematic of the millimeter I/Q Phase Bridge Interferometer.

The relevant expression for the phase change due to the plasma is then given by

$$\theta_{plasma} = \tan^{-1} \left\{ \frac{\beta \cos(\theta_Q) - \sin(\theta_I)}{\cos(\theta_I) + \beta \sin(\theta_Q)} \right\} \quad (4.14)$$

where

$$\beta = \frac{A_Q}{A_I} \frac{V_{OUT_I} - V_{OFF_I}}{V_{OUT_Q} - V_{OFF_Q}} \quad (4.15)$$

and A_Q , A_I are the sinusoidal signal amplitudes of each arm and the voltages are the output and offset voltages of each arm (the details of the definitions are also found in Appendix E). Similarly, the quantities θ_Q and θ_I are the phases of each arm during

testing, which due to manufacturing tolerances, are not necessarily taken at the zero location. The results show that for an ideal interferometer, where there is no offset voltage, the phase changes due to vibrations, thermal effects, or small changes in signal path length are zero, and the signal amplitude within each arm is the same, i.e.,

$$V_{OFF_I} = V_{OFF_Q} = \theta_I = \theta_Q = 0$$

$$A_Q = A_I$$

then the expression for the plasma phase change θ_{plasma} reduces to

$$\theta_{plasma} = \tan^{-1} \left\{ \frac{V_{OUT_I}}{V_{OUT_Q}} \right\} \quad (4.16)$$

which is the ratio of the voltage deflection in each arm due to the presence of plasma.

This is of course the description for an ideal situation when in practice and for the purposes of this experiment, the technique in Appendix E according to (4.14) and (4.15) were followed.

4.2.4 Testing and Calibration

Calibration was conducted on a 500 Watt inductive plasma discharge with no magnetic field while ten consecutive IV characteristics were measured against the microwave interferometry phase measurement. The average density value from the Langmuir probe analysis was $9.97 \times 10^{16} \text{ m}^{-3}$ while the average phase deflection was 7.9 degrees or 0.14 radians resulting in a chord length averaged density of $2.94 \times 10^{17} \text{ m}^{-3}$; these measurements yielded a 34 % difference between average density values and a calibration factor of 2.95 for density measurements. Again, the densities in both cases were obtained through the analysis found in Appendix D and Appendix E. Typical

microwave interferometry measurements consisted of measuring the DC voltage deflection in each arm of the interferometer as shown in Figure 4.21.

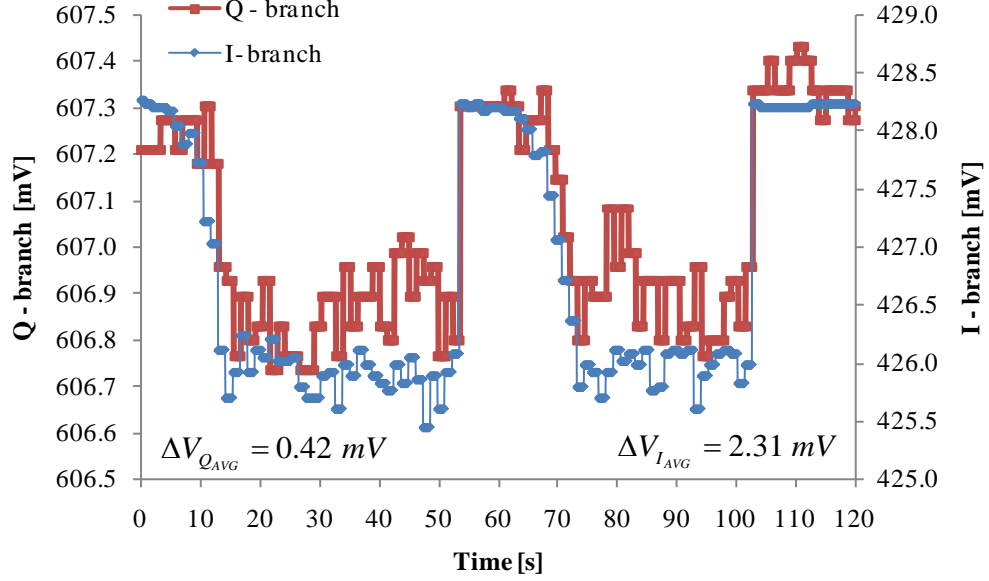


Figure 4.21. Calibration deflections in the I and Q branches of the microwave interferometer.

4.3 Error Analysis

The data presented in the following chapters will incorporate an error analysis which will focus on two primary reported measurements, plasma density n and electron temperature T_e . The uncertainty in these measurements will be discussed in terms of the dominant sources of error.

The uncertainty in electron temperature will be due to the sum of the standard deviation of 10 consecutive IV characteristic analysis' plus the error due to the ratio of the estimated sheath impedance to the measured probe impedance i.e.,

$$\Delta T_e = \sigma_{10traces}^2 + \frac{Z_{sheath}}{Z_{probe}} \quad (4.17)$$

An example of 10 consecutive T_e measurements with corresponding error bars calculated from (4.17) is shown in Figure 4.22.

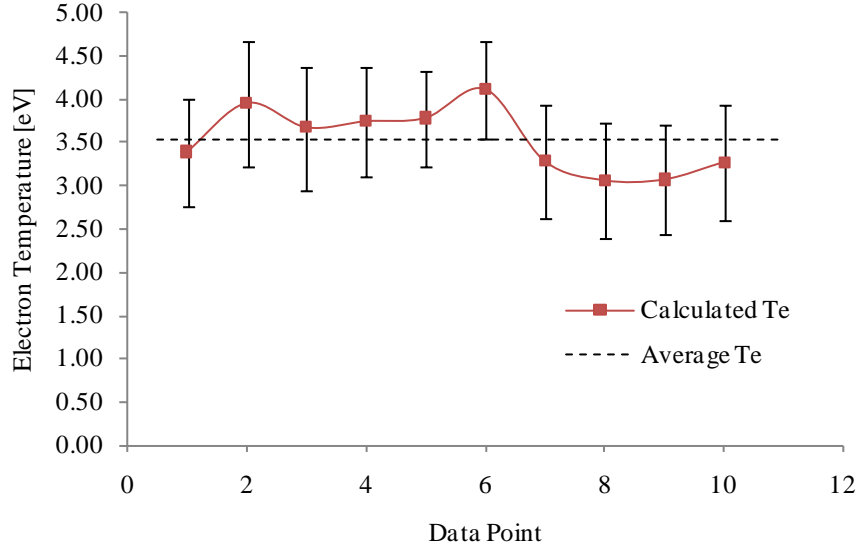


Figure 4.22. 10 T_e values for the corresponding IV characteristics with error bars shown.

The electron temperature is then reported according to

$$T_e = T_e(avg) + \Delta T_e(avg) \quad (4.18)$$

For the example case considered here: $T_e = 3.5 \pm 0.6 \text{ eV}$. While the uncertainty to the standard deviation does not change as it is calculated from the 10 T_e values, the uncertainty due to sheath / probe impedance ratios does because the sheath impedance is not a fixed value and is calculated according to [12]

$$Z_{sheath} = \frac{kT_e}{eI_e} \quad (4.19)$$

varying with the collected saturation current at each data point.

The density error analysis was calculated in much the same way although we also include the error present in the microwave interferometer which manifests in the calibration factor of 2.95. The error in density measurements can be calculated according to

$$\Delta n = \sigma_{10traces}^2 + \frac{Z_{sheath}}{Z_{probe}} + \sigma_{10traces}^2 (\mu wave) \quad (4.20)$$

The standard deviation of the 10 traces is a straightforward calculation and the impedance ratio error is the same percent error calculated for the electron temperature. The uncertainty in the calibration factor can be obtained from the voltage data in Figure 4.21. The I-branch and Q-branch have σ^2 values of 0.15 mV and 0.09 mV, respectively. This translates to an error in the phase measurement of 4.3 degrees and an error in the calibration factor of 1.6. Therefore, the calibration factor of 2.95 becomes 2.95 ± 1.6 . The error in density can then be calculated utilizing (4.20). The density values with corresponding error bars are shown in Figure 4.23.

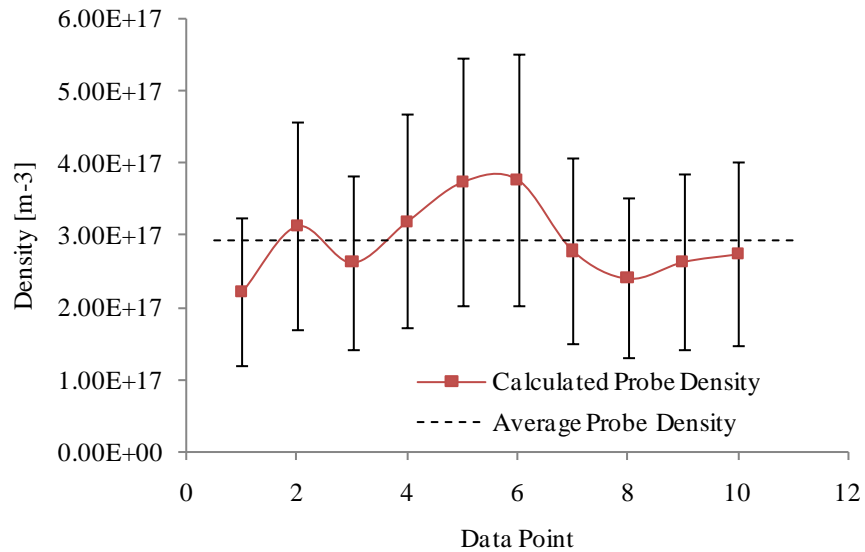


Figure 4.23. 10 n values for the corresponding IV characteristics with error bars shown.

For this example, the density is reported as $2.94 \pm 1.4 \times 10^{17} \text{ m}^{-3}$. There exist other sources of error such as uncertainty in the exact probe tip length of 3.0 mm; however, these will likely be much less than those due to the sheath / probe compensation and standard deviations which are present. In summary, the average error in the density measurements was 46 % where approximately $\frac{1}{2}$ of this uncertainty is due to calibration against the 90 GHz microwave interferometer. The average error in the electron temperature measurements was a more modest 18 %; however this is likely the consequence of not calibrating against a well known electron temperature diagnostic or source.

4.4. Chapter Summary

This chapter described the impedance-frequency characterization of magnetic induction probes. A novel technique was developed to calibrate the entire probe's frequency response; up to 100 MHz using an impedance analyzer. The effects of line-lengths and cable-types were investigated were the key results showed that longer line-lengths between the probe and data acquisition device significantly decrease the overall probe circuit frequency response; limiting the probe's useful frequency range. A proper technique to ensure the correct induced voltage in the sensing probe was also developed such that plasma capacitive voltage was not being measured. Finally, we illustrated the necessity of performing FFT's on the raw data signals in order to remove harmonics where errors were found to be as great as 67% had the correct data analysis through FFT's not been performed.

The same impedance-frequency analysis was applied to our RF compensated Langmuir probe such that we ensured a much higher overall probe impedance with respect to the plasma sheath impedance at the driving frequency and 2nd harmonic. Additionally, the compensation electrode allowed the probe tip to float with the 13.56 MHz oscillating plasma potential. This form of probe compensation provides a more accurate measurement of the probe current (for density calculations) as well as a more accurate measurement of the plasma potential (for electron temperature calculations) had no compensation been implemented. Finally, the RF Langmuir probe density measurements were calibrated against a 90 GHz microwave interferometer to obtain the chord averaged calibration factor of 2.95 ± 1.6 .

4.5 References

- [1] M. P. Reilly, W. Lewis, and G. H. Miley, "Magnetic field probes for use in radio frequency plasma," *Review of Scientific Instruments*, vol. 80, no. 5, pp. 053508-5, 2009.
- [2] W. Lochte-Holtgreven, *Plasma Diagnostics*, New York: American Institute of Physics, 1968.
- [3] R. H. Lovberg, "Magnetic Probes," *Plasma Diagnostic Techniques*, R. H. Huddleston and S. L. Leonard, eds., New York: Academic Press INC., 1965.
- [4] R. C. Phillips, and E. B. Turner, "Construction and Calibration Techniques of High Frequency Magnetic Probes," *Review of Scientific Instruments*, vol. 36, no. 12, pp. 1822-1825, 1965.

- [5] S. Messer, D. D. Blackwell, W. E. Amatucci *et al.*, "Broadband calibration of radio-frequency magnetic induction probes," *Review of Scientific Instruments*, vol. 77, no. 11, pp. 115104-7, 2006.
- [6] J. G. Yang, J. H. Choi, B. C. Kim *et al.*, "A calibration method of a radio frequency magnetic probe," *Review of Scientific Instruments*, vol. 70, no. 9, pp. 3774-5, 1999.
- [7] Mini-Circuits. "Surface Mount RF Transformer,"
<http://www.minicircuits.com/pdfs/T16-6T.pdf>.
- [8] Vishay-Dale. "IMC-1008 High Frequency, Surface Mount Inductor,"
<http://www.vishay.com/docs/34041/imc1008.pdf>.
- [9] Agilent. "Agilent 4294A Precision Impedance Analyzer,"
<http://cp.literature.agilent.com/litweb/pdf/5968-3809E.pdf>.
- [10] G. S. Eom, G. C. Kwon, I. D. Bae *et al.*, "Heterodyne wave number measurement using a double B-dot probe." pp. 410-412.
- [11] V. A. Godyak, and R. B. Piejak, "Probe measurements of the space potential in a radio frequency discharge," *Journal of Applied Physics*, vol. 68, no. 7, pp. 6, 1990.
- [12] I. D. Sudit, and F. F. Chen, "RF compensated probes for high-density discharges," *Plasma Sources Science and Technology*, vol. 3, pp. 7, 1994.
- [13] V. A. Godyak, and R. B. Piejak, "Abnormally low electron energy and heating-mode transition in a low-pressure argon RF discharge at 13.56 MHz," *Physical Review Letters*, vol. 65, no. 8, pp. 996-9, 1990.

- [14] V. A. Godyak, R. B. Piejak, and B. M. Alexandrovich, "Measurements of electron energy distribution in low-pressure RF discharges," *Plasma Sources Science and Technology*, vol. 1, pp. 36-58, 1992.
- [15] D. N. Ruzic, *Electric Probes for Low Temperature Plasmas*, New York: The American Vacuum Society Education Committee, 1994.
- [16] G. Neumann, U. Banziger, M. Kammeyer *et al.*, "Plasma-density measurements by microwave interferometry and Langmuir probes in an rf discharge," *Review of Scientific Instruments*, vol. 64, no. 1, pp. 7, 1993.
- [17] I. D. Sudit, and F. F. Chen, "Discharge equilibrium of a helicon plasma," *Plasma Sources Science and Technology*, vol. 5, pp. 11, 1995.

CHAPTER 5: RESULTS AND DISCUSSION

An important aspect of helicon wave plasma is the parameter space of operation. Chapter 2 described helicon conditions dependent on frequency f , density n , and applied magnetic field B_0 . These quantities are intricately related through the helicon dispersion relation, which also incorporates some geometrical aspects of the experiment such as tube radius a , antenna configuration m , and to a lesser extent, the antenna length l . In addition, there is a pressure and power aspect to the operational parameter space because density is also a function of the neutral gas pressure and how well the antenna couples or transfers energy to the plasma

In light of these many quantities it is prudent to experimentally determine the range of parameters that satisfy helicon wave propagation; or rather, determine the conditions where the onset of helicon waves occur and then to further investigate those conditions. Additionally, in accordance with Chapter 2, helicon waves are described by radial variations in the wave b_r , b_θ , and b_z - profiles which are dependent on radial density profiles $n(r)$. Therefore, this chapter will begin with determining and discussing the identification of helicon waves at various operating conditions and comparing the measured and theoretically predicted profiles. The chapter will progress to follow the evolution of radial b_r , b_θ , and b_z - scans to two- and three- dimensions illustrated by contour maps of helicon waves over an entire wavelength. The results of mapping helicon waves in three dimensions reveals important information regarding the wavelength of helicon waves and quantifying them as a true 3-d helix whereas single axis measurements only reveal what would otherwise appear to be a 2-d plane wave.

Finally, this chapter will show axial density profiles which correspond to the wave b-field measurements. In some cases, the axial density measurements reveal an unexpected density peak downstream of the antenna. The explanation of this effect will be shown to be independent of helicon wave plasma and the model provided is solely based off of performing an energy balance within a plasma volume while assuming a decaying (cooling) electron temperature away from the source (antenna).

5.1 Identification of Helicon Waves

Identification of helicon wave propagation was originally based upon the magnetic field, b_r , b_θ , and b_z - profile measurements conducted with b-dot probes [1]. The results were then compared to the b_r , b_θ , and b_z - field solutions in a cylindrical plasma discharge subject to a uniform plasma density distribution [2]. For a prescribed driving frequency, tube radius, and gas, the power and the static magnetic field B_0 could be varied (typically increased) until they very nearly satisfied the dispersion relation. At that point, the internal measured magnetic field profiles would nearly resemble the calculated profiles and the conclusion was that the dielectric could support the propagation of helicon waves. However, there have been several other methods commonly used to determine helicon wave propagation. These methods and their accuracy will be briefly addressed.

5.1.1 Forward – Reflected Power Spectrum

The first method does not utilize internal plasma diagnostics. Identification is based on monitoring the forward-to-reflected power ratios at a given magnetic field. As the power is increased, a sharp decline in the reflected power level is observed and helicon waves

are assumed to propagate. An example of this situation is given for a 5 cm cylindrical m = +1 half turn helical antenna (20.32 cm between end rings). The gas is Argon at 47 sccm (~ 10 mTorr neutral gas pressure). The forward and reflected powers were recorded at different input powers and magnetic field strengths and the results are shown in Figure 5.1.

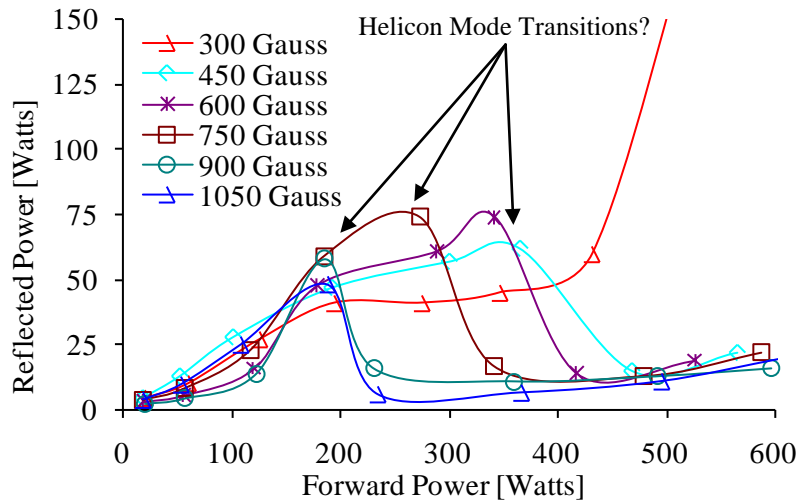


Figure 5.1. Forward vs. Reflected Power at 47 sccm; 10 mTorr fill pressure.

During each condition, the reflected power begins as a minimum and then slowly increases as the input power is raised until some point where there is a ‘sharp’ decline in the reflected power. At this point, the power is said to couple more efficiently to the plasma and could be used as a method to identify the onset of helicon wave propagation. Also, Figure 5.1 shows that as the magnetic field is increased, the decline in reflected power occurs at a lower input power level. The transitional power value is equivalent to analyzing the dispersion relation for helicon wave propagation [3-6] at a fixed frequency and magnetic field; the relation is satisfied once the density reaches a critical value. Since density is proportional to input power [5], once the forward power level generates this critical density value for a given magnetic field, helicon waves can propagate.

Utilizing the power spectrum as a method to identify helicon wave propagation can be vague and inaccurate. Since power loss can come in many forms, i.e., transmission line loss, radiated loss, antenna coupling efficiency, etc, using the power spectrum as a tool to identify helicon waves can be ambiguous. Although, as a qualitative observation, some revealing information can be gained, i.e., there exists a magnetic field strength threshold where little is gained by further increasing the power. This is shown by the similarities in the 900 Gauss and 1050 Gauss curves of Figure 5.1. The forward power threshold is nearly identical in each case suggesting strengthening the magnetic field beyond 900 Gauss for these conditions does not generate a transition to helicon mode at lower forward powers.

Finally, the rise in reflected power can also be attributed to the initial settings of the capacitors within the auto-match network and the tolerances set within the feedback circuit. For example, referring to the circuit of the matching network with plasma as given in Chapter 3 and repeated here in Figure 5.2.

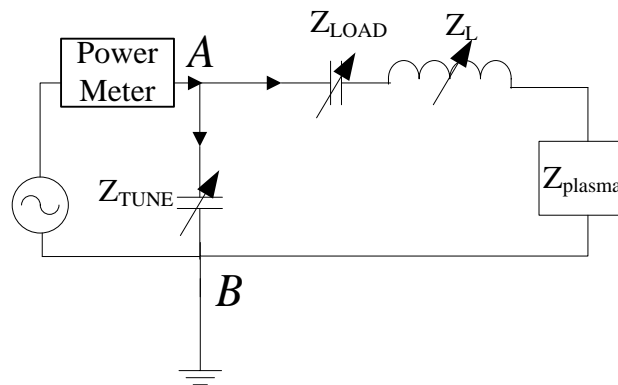


Figure 5.2. RF power delivery system incorporating the auto-match network circuit.

The RF voltage source will output power into an equivalent $50\ \Omega$ load at point A. The total applied power to the matching network and antenna will be given by the difference between the forward and reflected power measured at point A according to

$$P_{TOT} = P_{FWD} - P_{RFL} \quad (5.1)$$

Also, the impedance in each “branch” is given by

$$Z_{series} = Z_{Load} + Z_L + Z_{plasma} \quad (5.2)$$

$$Z_{||} = Z_{TUNE} \quad (5.3)$$

For an equivalent circuit impedance of

$$Z_{eq} = \frac{Z_{series} Z_{||}}{Z_{series} + Z_{||}} \quad (5.4)$$

Therefore, regardless of the plasma impedance, there exist capacitance values in which the equivalent load can be set to $50\ \Omega$ resistive. The restraint on the matching network lies with the dynamic range of the variable capacitors. To match the $50\ \Omega$ load, the plasma complex impedance may attempt to force the capacitors to values outside their working range. In this case, the auto-match network searches for a minimum value or minimum reflected level within the feedback tolerance. If no suitable values are found, the reflected power will continue to rise until the plasma load again returns to the operational range of the variable capacitors. This explains the rise in reflected power as a consequence of the matching network and not necessarily a mode transition, although the power spectrum result will be shown to closely coincide with the onset of helicon wave fields.

5.1.2 Density ‘Jumps’

Another method utilized to identify helicon waves has been through observation of apparent density ‘jumps’ as the input power is increased. This is a sharp increase in density from a capacitive or inductive mode to helicon wave mode. For the case of 900 Gauss static magnetic field on the same cylindrical tube as above, radial density profiles were analyzed for various input powers as shown in Figure 5.3.

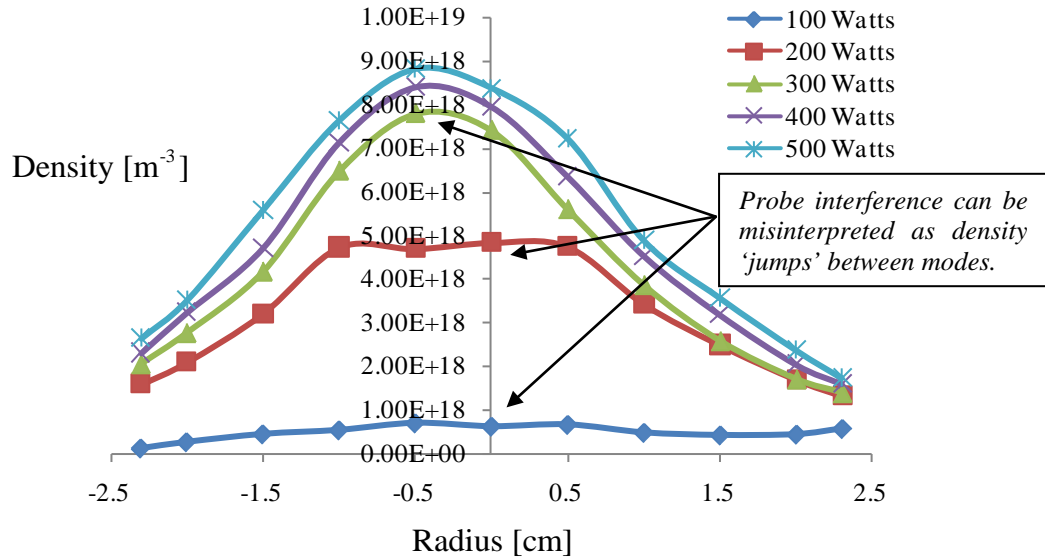


Figure 5.3. Radial plasma density profiles at 900 Gauss for various input power levels on a 5 cm diameter quartz tube at 13.56 MHz.

The density profiles and power spectrum analysis show helicon wave plasma exhibits a radial parabolic profile whereas the inductive (lower power) discharge maintains a relatively flat density profile. As can be seen for the 200 Watt case, the ‘small’ Langmuir probe used to measure the density destroys or interferes with the helicon wave from about -1 cm to +1 cm as the probe is swept radially through the discharge. However, at higher powers, the density is large enough to overcome the presence of the probe in order to maintain helicon wave propagation around the probe. This also provides a complementary explanation to the observation of a density ‘jump’ which was explained

in terms of overcoming parasitic circuit losses [7] (sharp drop in reflected power due to plasma load). The rationale here is that helicon waves would exist at this condition if the probe were not present (or if the capacitors had a wider dynamic range). It is the presence of the measuring probe in this case which inhibits the propagation of the wave until the plasma discharge conditions are sufficient to overcome the probe's presence.

Additionally observed in Figure 5.3, the peak density appears to be shifted slightly left of center (~ 0.5 cm); this can be attributed to several factors. First, the alignment of the probe in the center of the quartz tube has some associated error as this was not given significant importance. Similarly, the quartz tube may not have been perfectly aligned within the center of the magnets. In order to ensure that the 'peak' did not shift or oscillate, radial profiles at different downstream locations from the antenna were taken and shown to consistently be shifted to the left of the presumed center as shown in Figure 5.4.

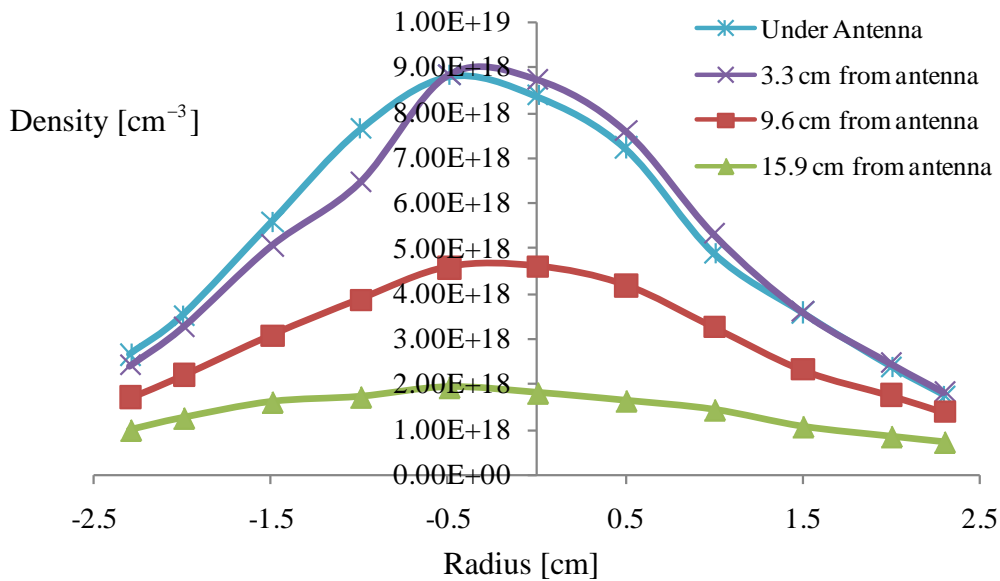


Figure 5.4. Downstream radial density profiles at 500 Watt, 900 Gauss.

The density jumps exhibited in Figure 5.3 have been previously modeled off of the matching network configuration (L-, T-, Π -), its component values (capacitances and inductances), and transmission lines [7]. The experimental data presented here validates the model's results, yet also demonstrates the effect of probe intrusion at lower power levels, which can inhibit helicon waves.

Consequently, in both the case of analyzing the power spectrum and utilizing plasma density measurements, both methods can be inaccurate at identifying the propagation of helicon waves. Furthermore, when starting the analysis of helicon waves, the only derived measurement is that for the internal magnetic fields. Therefore, the next section will address identifying helicons through the measurement of the internal radial plasma wave fields.

5.1.3 Radial b_z - Profiles

Helicon wave fields can have many different structures as shown in Chapter 2. These different profiles are dependent on the radial density profiles. Therefore, once the radial density distribution is measured, the wave profiles (b-dot probes) should match the theoretical ones. The corollary of this statement should also be true: measuring the internal wave profiles i.e., the b_z component of the wave, the radial density distribution can be predicted.

This section will examine the radial magnetic field profiles for the b_z wave component. Measurements are made from pressures of 0.5 mTorr – 10 mTorr on a 5 cm quartz tube

with a $m = +1$ half turn helical antenna (20.3 ± 0.1 cm length between end rings) driven at 13.56 MHz. Magnetic fields of 300, 600, and 900 Gauss are tested at input power levels from 100 - 500 Watts. The onset of helicon wave propagation in each instance is examined and compared with theoretical profiles derived from Chapter 2 and correlated with a radial density distribution.

The first test conditions were 47 sccm (~ 10 mTorr) Argon gas, input power 300, 400, and 500 Watts, and peak magnetic fields of 300, 600, and 900 Gauss. Those results are shown in Figure 5.5. For the nine conditions tested at this pressure, five were found to be in excellent agreement with theoretical profiles. Those five are indicated in Figure 5.5 by a GREEN border and are listed here as

500 Watts – 600 & 900 Gauss

400 Watts – 600 & 900 Gauss

300 Watts – 900 Gauss

The ones identified with a YELLOW border are radial scans where the measured profiles near the tube radius would seem to indicate the start of a helicon b_z profile. However, similar to the 200 Watt density scan performed in Figure 5.3, the probe's presence interferes with the wave propagation at these conditions, i.e., the wave field intensity is too low to overcome the presence of the probe. Finally, the RED border case,

300 Watts – 300 Gauss

indicates no wave field. This is a condition where the density and magnetic field do not sufficiently create a dielectric medium to support helicon waves.

An alternative argument for the RED border cases still propagating helicon waves considers the following:

Suppose at the condition 300 Watts – 300 Gauss helicon waves are present. And perhaps the data do not show identifiable wave profiles due to the measuring b-dot probe exhibiting insufficient signal detection

The response is helicon waves either do not exist below some critical levels or the wave information carried by the plasma is so small that it is undetectable by the means presented here. To support this rationale, the results show b-dot probes which “pick-up” the start of a helicon wave profile near the radius of the cylinder; however, the probe interference destroys these signals, altering the dielectric medium. Helicon waves exist at the YELLOW border conditions though the probe presence obscures this result.

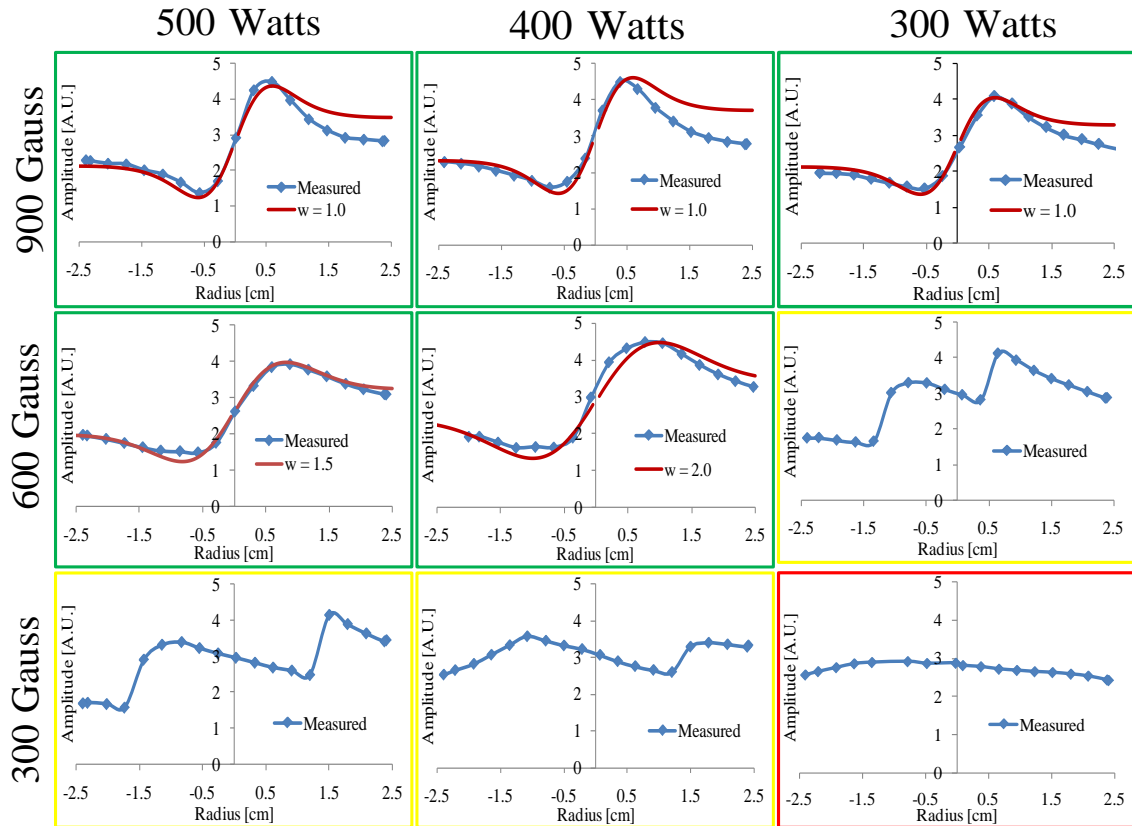


Figure 5.5. b_z profiles at 10 mTorr and various input power and magnetic field strengths. Green borders indicate well matched with theory where ‘w’ indicates the Gaussian density profile width. Yellow borders indicate probe interference with helicon wave mode. Red borders indicate insufficient conditions for wave propagation.

Similar power (density) / magnetic field matrices are presented in Appendix F for the pressures of 0.5, 2, 4, 6, and 8 mTorr. In all cases, as the pressure is further decreased, the wave profiles only match the theoretical predictions at higher powers and magnetic field strengths. For example, in the 2 mTorr analysis, there is only one condition where the wave profile nearly matches a theoretical profile; 500 Watts – 900 Gauss.

Consequently, for each of the neutral gas pressures tested where helicon wave-like structures were observed, the measured wave profiles were correlated (overlaid) with the theoretical profiles and the onset of helicon waves was determined by their agreement.

Returning to the GREEN border cases, the theoretical curves based on radial density profiles were fit to the measured b_z data. The radial density profiles which identify the conditions above are shown in Figure 5.6 where the densities have been set to a center value of $n_0 = 1 \times 10^{19} \text{ m}^{-3}$ which closely approximates the measured centerline density.

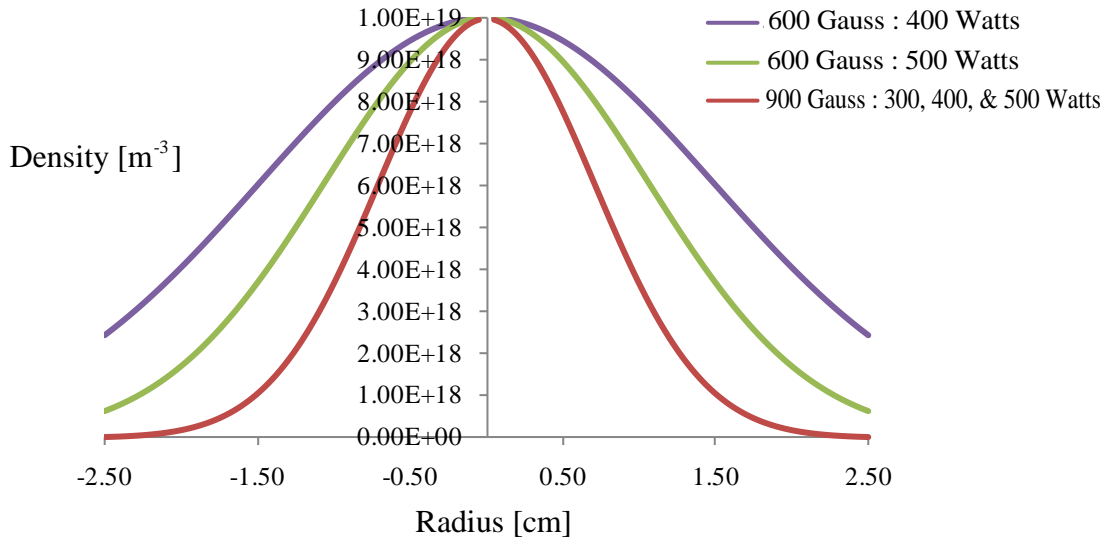


Figure 5.6. Radial density profiles corresponding to the b_z data.

Recalling Figure 5.3 for the measured radial density profiles at 900 Gauss and 300, 400, and 500 Watts, the measured density profiles are compared to the theoretical profiles

derived from the b_z data. This is shown in Figure 5.7. However, the theoretical density profiles do not necessarily identically match those measured. The Gaussian profiles defined in Chapter 2 and shown in Figure 5.6 for $w = 1.0$ are much narrower than those measured. In fact, the best Gaussian fit is for $w = 1.7$; also shown in Figure 5.7 for comparison with the measured density profiles.

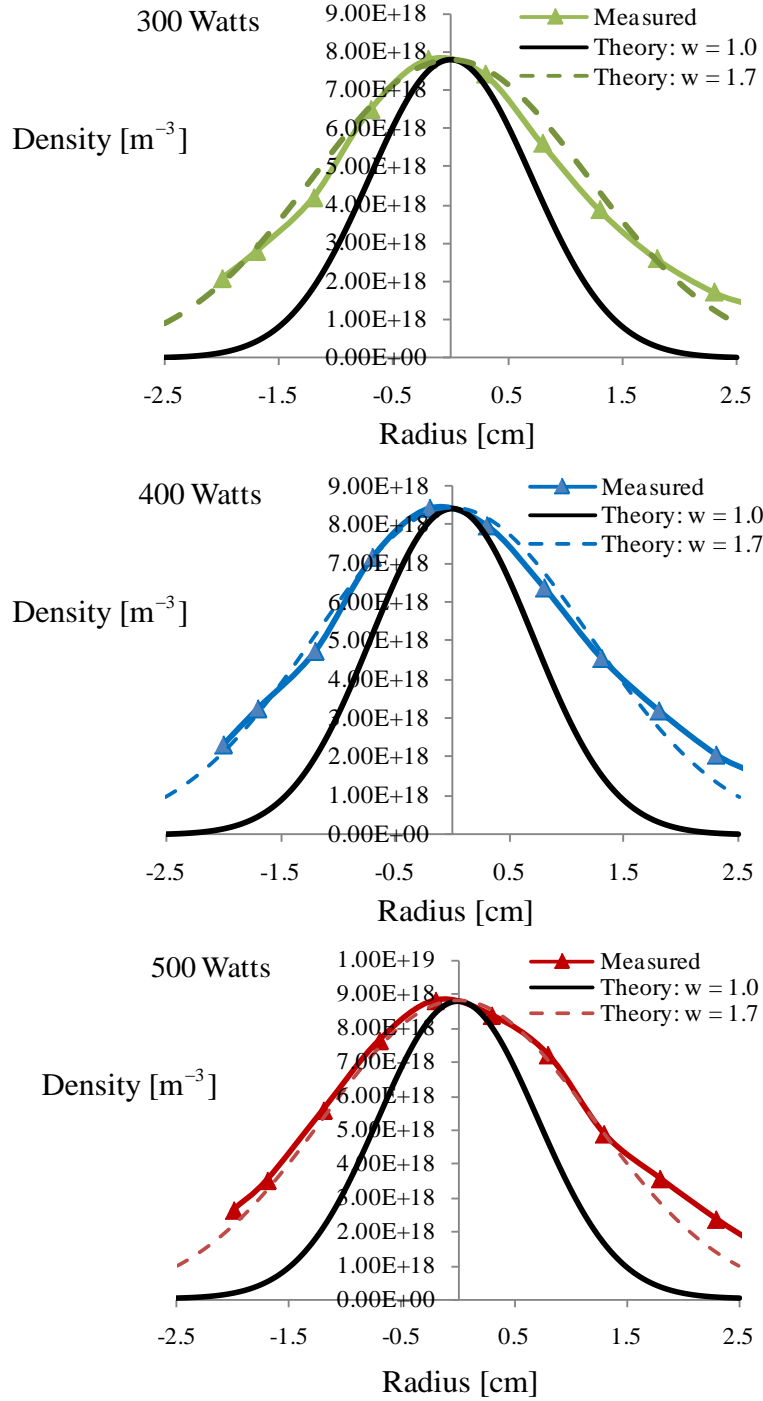


Figure 5.7. Theoretical density profiles compared with experimentally

The differences in the wave profiles are demonstrated using the two theoretical density profiles ($w = 1.0$ and $w = 1.7$) and numerically solving for b_z as outlined in Chapter 2.

The differences between both are illustrated in Figure 5.8.

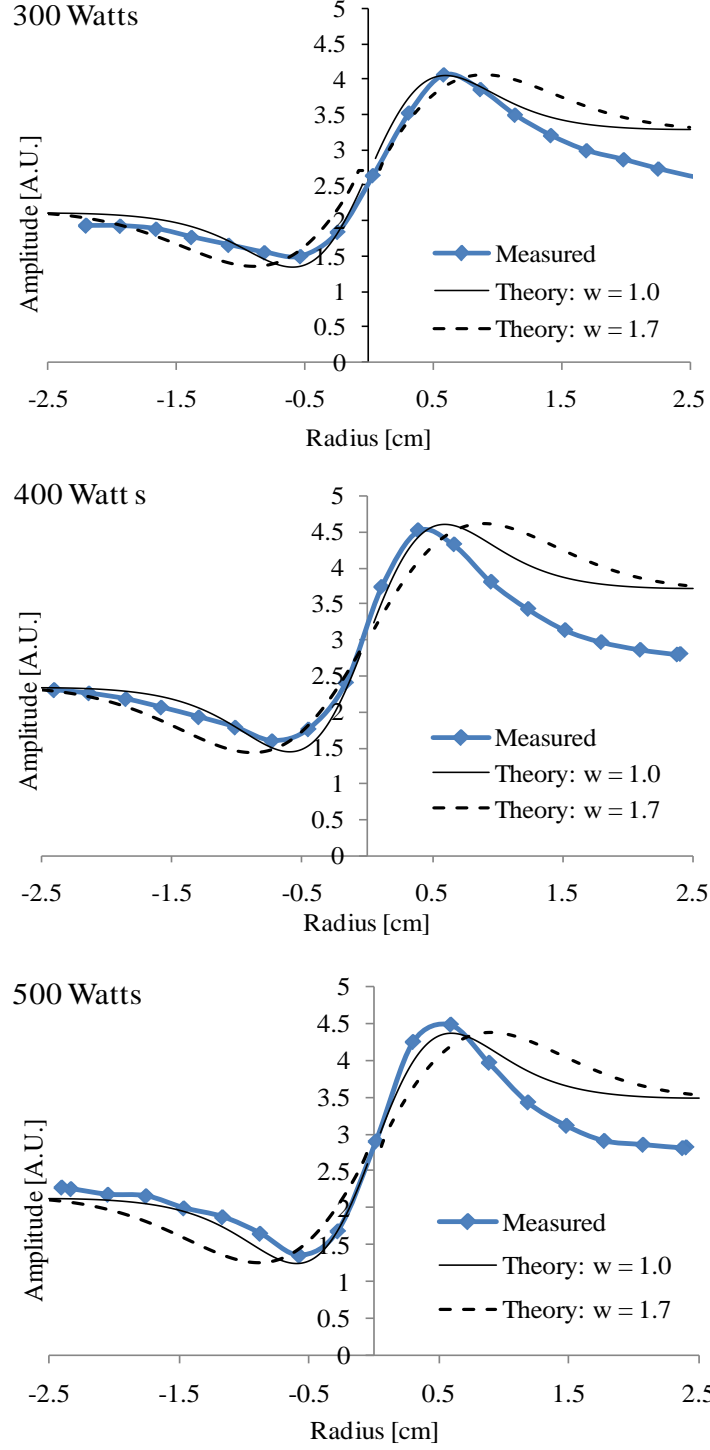


Figure 5.8. Differences in calculated b_z wave profiles for radial density profiles $w = 1.0, 1.7$ as compared with the experimentally measured profiles.

While the theoretical curves for $w = 1.0$ better represent the experimental b_z values as opposed to $w = 1.7$, the differences in the calculated wave fields are minimal. An

explanation to resolve the small difference may be due to a non-vacuum gap between plasma and cylindrical tube boundary when considering the theoretical analysis. If the model were further developed to include an additional vacuum layer between the boundary and plasma, this may account for the difference.

Regardless, the results clearly show helicon wave theory which incorporates a non-uniform radial density distribution provides the most accurate representation of the measured plasma wave fields. Additionally, a suitable operational space for helicon waves has been determined, which will allow more in depth study. The 500 Watt – 900 Gauss operating condition at 10 mTorr neutral gas pressure will be used as the control condition.

Each density profile also provides a unique value of k_z for the propagating wave. This value was provided when the wave profiles and boundary conditions were solved. Calculating these value for both the $w = 1.0$ and $w = 1.7$ profiles yields a wavelength range of $\lambda_z = 29.95 - 33.85 \text{ cm}$ for the 500 Watt – 900 Gauss plasma. The expected wavelength (as will be shown) is most likely an underestimate. This is due to the Gaussian density profile not remaining constant in the axial direction. As the wave propagates away from the source, the density profile will no doubt ‘relax’. In fact, this was already shown in Figure 5.4, when the downstream radial density profiles were examined. For each profile, one would expect a different value for the axial wavenumber, and hence the axial wavelength. In essence, the wave should be expected to be damped in the axial direction. This point was already implied at the end of Chapter

2 where the various Gaussian density profiles returned a different axial wavelength; however, the results imply this occurs in the axial direction due to the non-uniformity in the +z direction. This also explains some reported results in which the wavelength in the axial direction varies [8] which should be expected from the decreasing axial density where the wavelength will increase. Additionally, the measured wavelengths reported do not exhibit a smooth increase in the axial wavelength. In fact, the wavelength initially decreases before smoothly increasing. This has been an unexplained feature in the axial wavelength to date; however, we will later show the initial decrease in axial wavelength is due to a downstream rise in density. Regardless, this provided enough motivation to further investigate the helicon wavelength and its relation to the plasma dielectric properties through axial measurements.

5.2 Axial b_r , b_θ and b_z - Profiles

The location of the three separate antennae tested as shown in Chapter 3 are repeated here as shown in Figure 5.9.

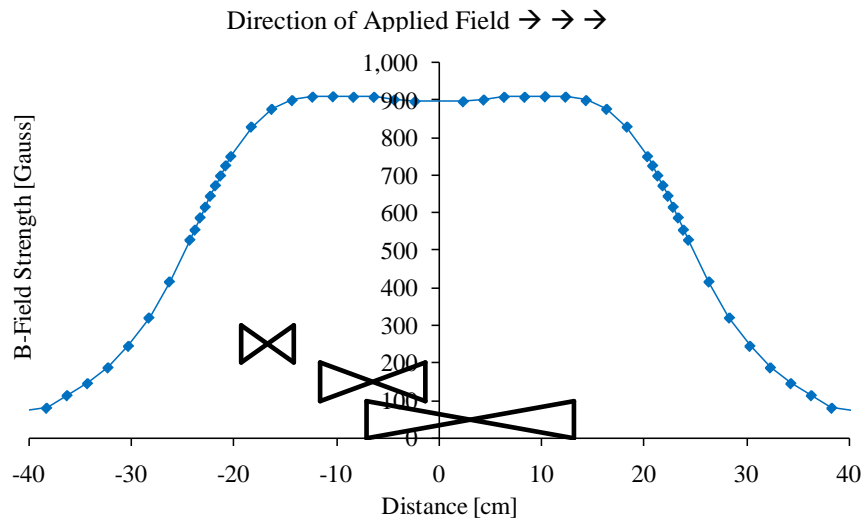


Figure 5.9. Applied Magnetic Field with Location and Lengths of Tested Antennas.

It is necessary to redefine the antenna lengths in terms of their full three dimensional helix. Where previous lengths have been defined in terms of the distance between the antenna end rings, the full antenna length must include the radial wrapped component. We define this for a full turn and ½ turn helical antenna as it relates to the anticipated helicon wavelength by

$$l'_a = \sqrt{d^2 + (2\pi a)^2} \quad \text{full turn} \quad \lambda_{\parallel} \rightarrow l'_a \quad (5.5)$$

$$l'_a = \sqrt{d^2 + (\pi a)^2} \quad \frac{1}{2} \text{ turn} \quad \lambda_{\parallel} \rightarrow 2l'_a \quad (5.6)$$

where d is the distance between the end rings and a is the radius of the tube the antenna is wrapped around. For the previous defined antenna lengths of 20.3 cm, 10.2 cm, and 5.1 cm wrapped around a ½ turn helical 6.4 cm OD quartz tube, the new antenna lengths according to (5.6) are 22.6 ± 0.1 cm, 14.2 ± 0.1 cm, and 11.2 ± 0.1 cm respectively. Shorter distances between antenna end rings, where $a \sim d$, has the effect of significantly miscalculating the anticipated helicon wavelength λ_{\parallel} if the three dimensional lengths are not considered. For example, in the case of the 5.1 cm distance between end rings, the true antenna length given by (5.6) is 11.2 cm, or an error of 55 % between the antenna lengths.

5.2.1 Single Axis b_z Profiles

A routinely used method toward measuring the helicon wavelength has been to take an axial scan and report either the phase difference between the sensing probe and the antenna current or to take the length between successive maxima and minima in the wave amplitude. The successive maxima amplitude method was repeated in this study;

however, it is inaccurate in reporting the helicon wavelength even though the results appear correct upon initial inspection. For the 22.6 cm antenna, the results of a single axis scan for the b_z wave field at three different radial ‘x’ values are shown in Figure 5.10.

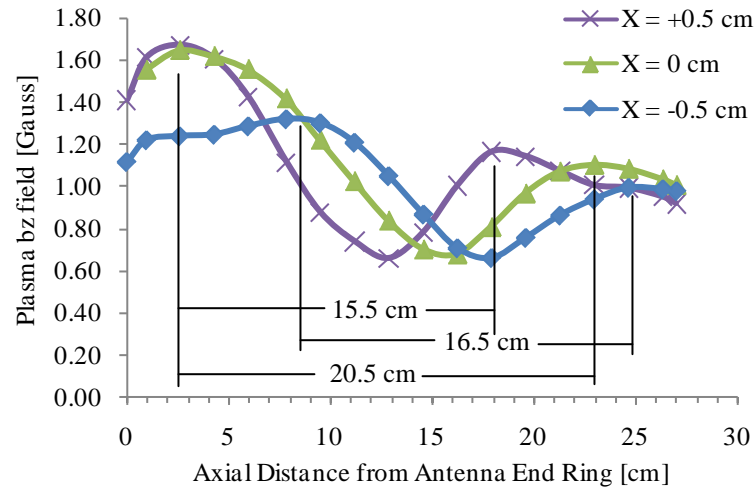


Figure 5.10. Single axis scan for the b_z wave fields taken at three different radial locations.

For each scan, a different value for the helicon wavelength is reported, often differing by as much as ~ 5 cm. The same measurement for the 14.2 cm and 11.2 cm antenna lengths are shown in Figure 5.11 and Figure 5.12. In all three cases, the single axis measured two dimensional helicon wavelengths are ambiguous. The scans are out of ‘phase’ depending on where you are performing the measurement and the resulting length is seen to vary by up to 50 %. While the scans do appear to represent a wave with an associated wavelength, three dimensional scans of the helicon wave provide a much more meaningful representation of the true wavelength and the apparent phase difference between successive locations is readily explained when the three dimensional wave is considered.

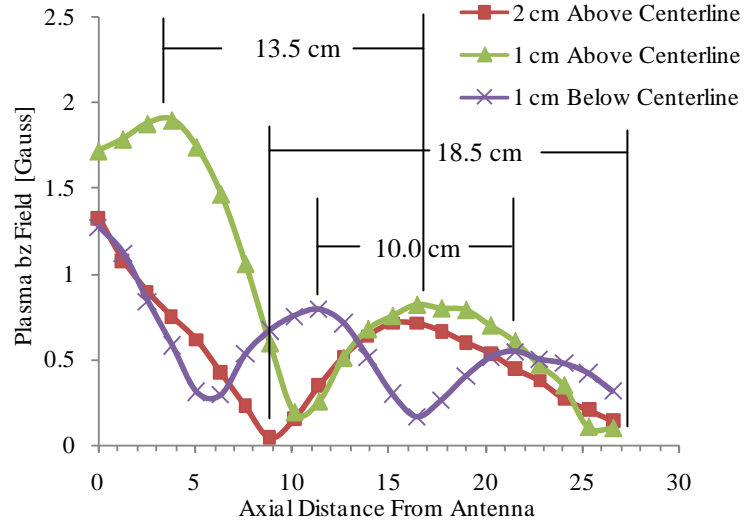


Figure 5.11. Single axis scan for the b_z wave fields for the 14.2 cm antenna

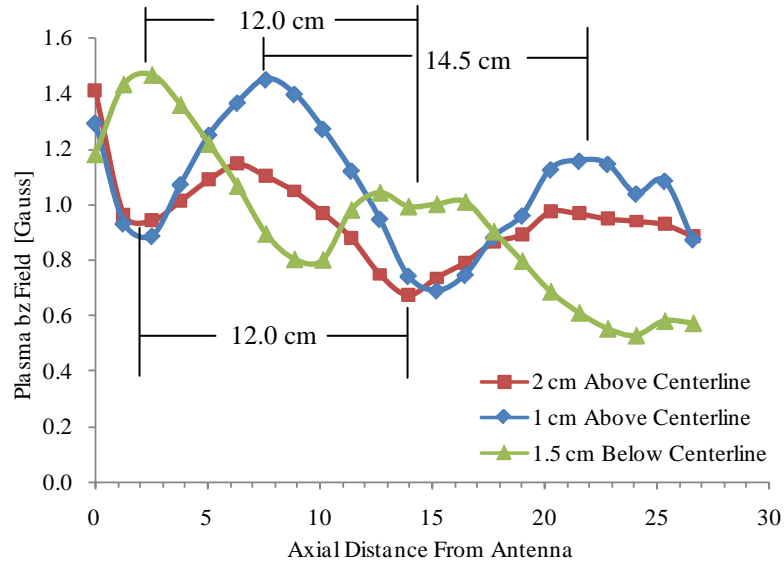


Figure 5.12. Single axis scan for the b_z wave fields for the 11.2 cm antenna length.

5.2.2 Two- and Three- Dimensional b_z Profiles

The scans at different radial locations being out of ‘phase’ are the result of the two-dimensional representation of a helix as shown in Figure 5.13. The result for the helix (which is three-dimensional) is a single wave with only one associated wavelength.

Figure 5.13 provides an explanation for why previous results of the helicon wave appear to be ‘phase’ shifted when measured at different radial locations.

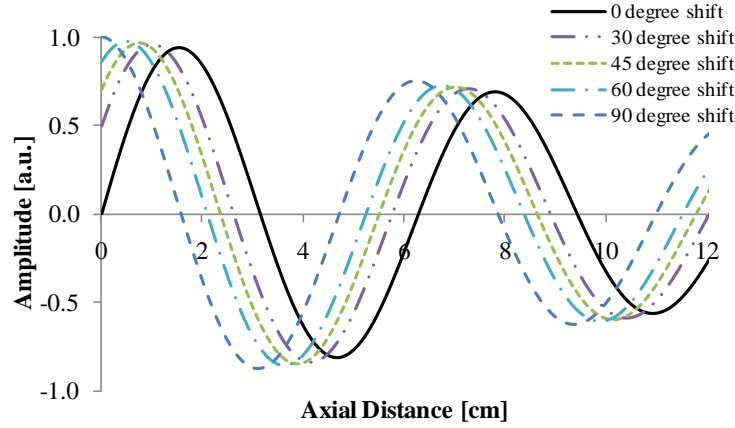


Figure 5.13. Phase shift for 2-d representation of 3-d helix.

When wavelengths have been previously reported based off of the two-dimensional single axis scans for the b_z profiles [1, 4, 9-13] they have been reported based off of measurements as shown in Figure 5.10 – Figure 5.12. However, utilizing the 3-d representation of an attenuating wave as modeled in Figure 5.14 (in 2-d) and Figure 5.15 (in 3-d) as one that linearly decreases in the radial direction from 1 cm to 0.5 cm over two wavelengths, the actual length of this modeled wave can be then calculated from Equation (5.5) or (5.6) which will include the azimuthal component of the wave. The waves in Figure 5.14 – Figure 5.15 are the exact same waves; with Figure 5.14 being the 2-d projection. This clearly illustrates how the 2-d measurement will underestimate the full wave helix. The 2-d wavelength is observed to be 6 cm while the 3-d wavelength is 6.6 cm; 9 % error.

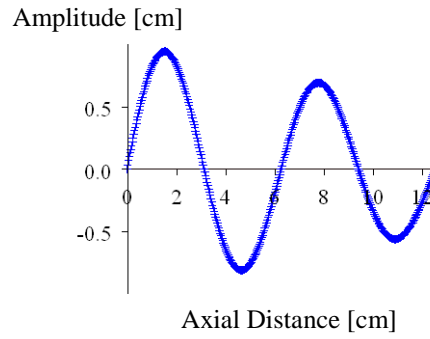


Figure 5.14. 2-d representation of single phase helix.

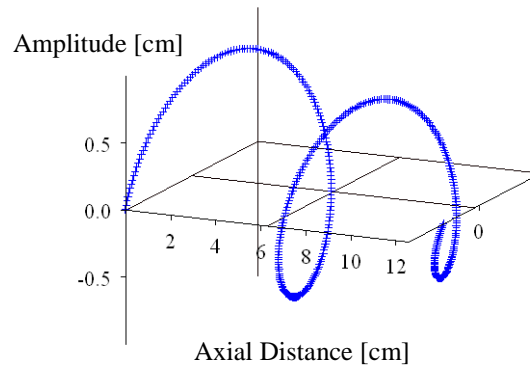


Figure 5.15. 3-d helix represented by the series of 2d phase shifted waves.

Consequently, to image the entire wave, 3-dimensional b_z profiles were made at 22 axially separate cross-sections. Each cross section consisted of scans in the XY plane for approximately 75 data points per cross-section or about 1650 data points per 3-dimensional contour map. The distance between data points in a cross-section varied between 1.2 - 1.4 mm while each axial cross-section was separated by approximately 1.5 cm. The data point / node-numbering scheme and contour plots were constructed in Techplot 10. A typical 2-dimensional cross-section scheme is shown in Figure 5.16.

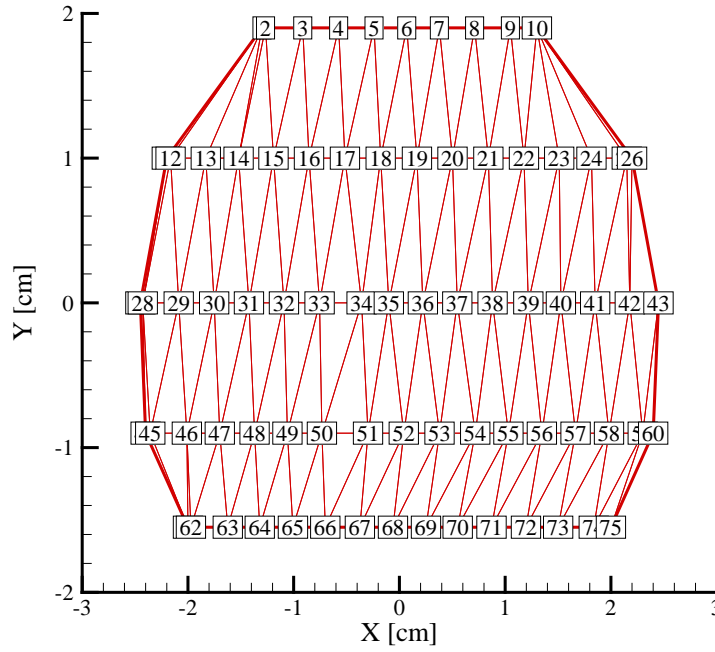


Figure 5.16. Node numbering scheme for typical 2-d b_z cross-section.

The compiled 3-dimensional b_z contour plots are shown in Figure 5.17 for the cases of 22.6 cm, 14.2 cm, and 11.2 cm antenna lengths; as previously defined. Additionally, 2-dimensional (x,z) contour plots in the $y = 0$ plane are shown in Figure 5.18 for b_z . In the case of all 3 antenna lengths, the edge of the antenna is set at $z = 0$. This is to facilitate the determination of the helicon wavelength. The actual location of each antenna edge with respect to the applied magnetic field was given in Figure 5.9. As illustrated in Figure 5.17 and Figure 5.18, the shortest antenna length does not necessarily correspond to the shortest axial wavelength helicon. This is likely due to the 14.2 cm antenna propagating at a resonance with the cylindrical tubes geometric radial dimensions. The antenna couples energy to the plasma more efficiently and exhibits a more defined wave pattern. This interpretation will later be complemented where the 14.2 cm antenna is shown to exhibit the highest plasma density.

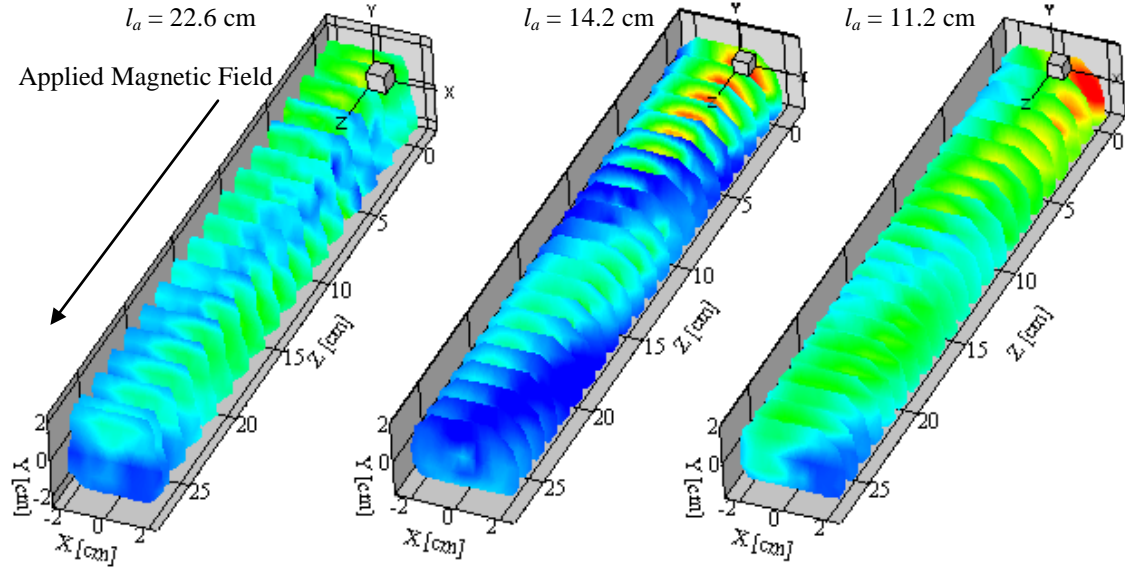


Figure 5.17. Three dimensional helicon b_z fields. Antenna lengths: 22.6, 14.24, and 11.19 cm. Antenna edge located at $z = 0$ cm. Wave propagation and static magnetic field in the $+z$ direction.

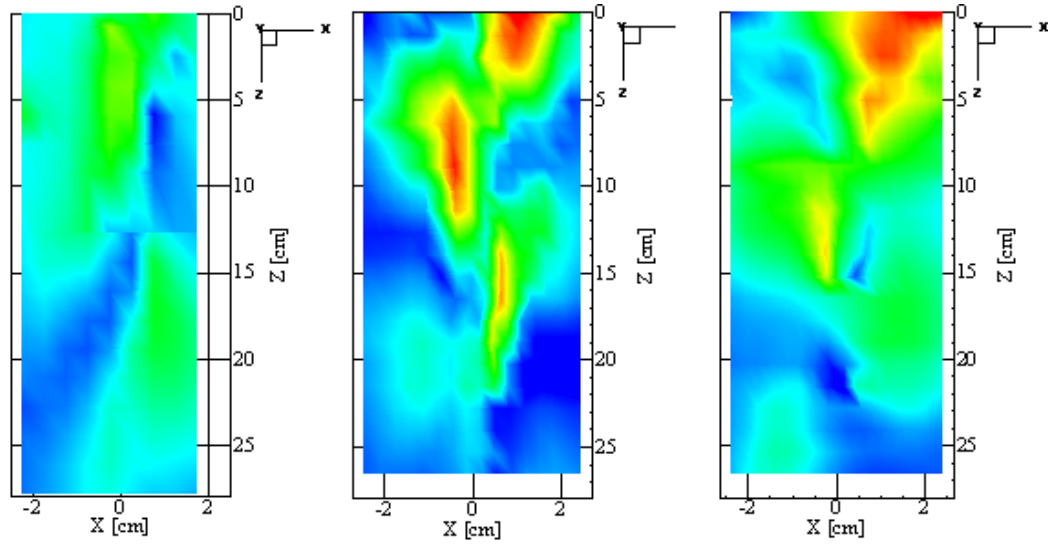


Figure 5.18. Two dimension b_z wave fields taken across center of tube. Antenna lengths of 22.6, 14.2, and 11.2 cm. Antenna location is at $z = 0$ cm and wave propagation and static magnetic field are in the $+z$ direction.

From inspection of Figure 5.17 and Figure 5.18, the helicon wavelengths can be determined. These values in comparison to the antenna length and expected wavelength are given in Table 5.1. Since each antenna is a $\frac{1}{2}$ turn helical ($m = +1$) antenna, the expected helicon wavelengths are defined by $\lambda_{||} = 2l_a$.

Table 5.1. Summary of Expected and Measured Wavelengths.

3-d Antenna Length l'_a [cm]	Expected Wavelength $\lambda_{ } = 2l'_a$ [cm]	Measured Axial Wavelength (z-direction only) λ_z [cm]
22.6	45.2	~25
14.2	28.4	~15
11.2	22.4	~19

In contrast, the expected wavelength may also be calculated from the density profiles at different downstream locations. As an example of this, the radial density profiles from Figure 5.4 are matched with a theoretical Gaussian profile (Figure 5.19) and the wavenumbers and wavelengths for each case are numerically solved.

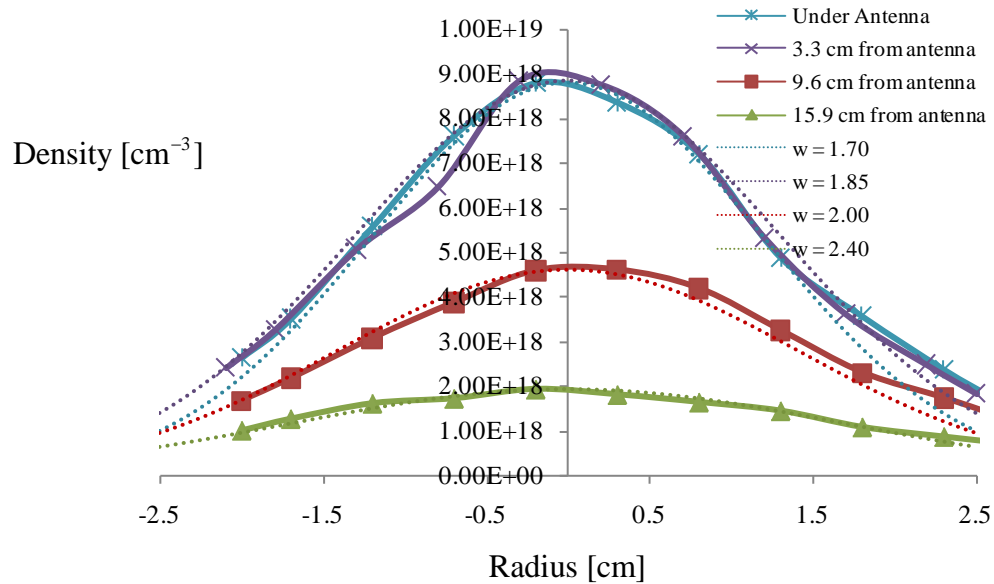


Figure 5.19. Radial density profiles matched with Gaussian to be numerically solved for the wavelength. The full antenna length is 22.6 cm.

The resulting wavelengths for each profile are shown in Figure 5.20. As would be expected, lower densities and broader Gaussian profiles yield longer anticipated wavelengths. However, the expected wavelengths are still longer than the measured ones reported above. Recall, the wavelengths reported in Table 5.1 and from inspection of

Figure 5.17 and Figure 5.18 are based solely on the +z directed values and do not yet account for the helical nature (r - component).

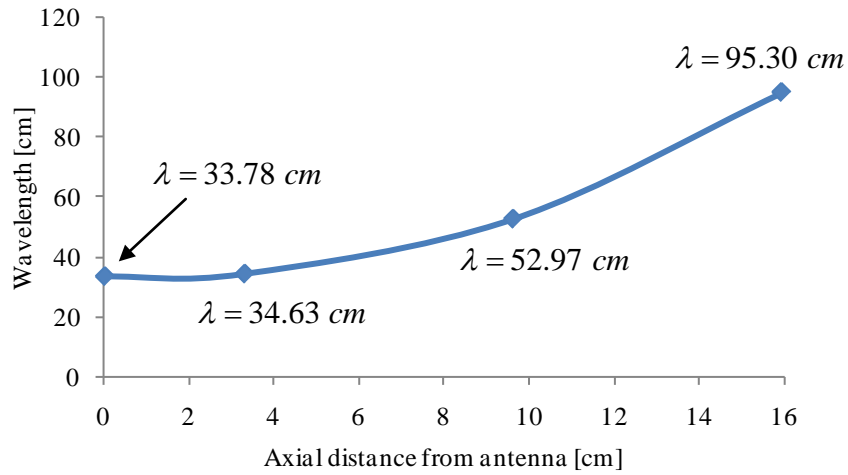


Figure 5.20. Wavelength solution based on axial varying Gaussian density profiles.

5.2.3 Three Dimensional Wavelengths

The 14.2 cm antenna is used as a template for the following analysis. From the contour plots of Figure 5.17, the results indicate the waves have a finite ‘thickness’ or radius to its structure. This is illustrated more accurately in Figure 5.21 for the 14.2 cm antenna as the wave decreases in radial structure from ~ 1 cm at the axial $z = 0 \text{ cm}$ location to ~ 0.75 cm one ‘wavelength’ ‘downstream’ at $z = 15 \text{ cm}$.

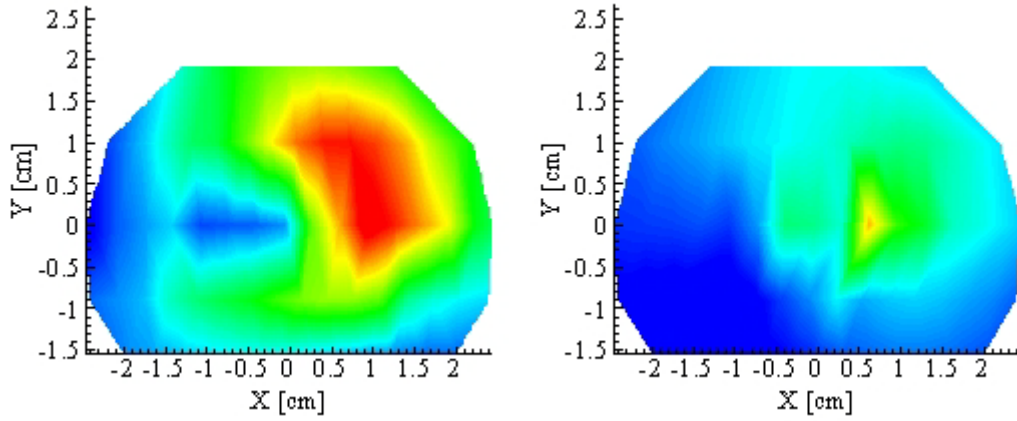


Figure 5.21. 2-d cross sections showing the radial decrease in the wave over an axial length. Radial length decreases from ~ 1 cm to ~ 0.75 cm over ~ 15 cm axially.

The full wavelength can then be calculated by using a linear decrease in the radial structure (which is valid from the slow damping observed from the 2-d profiles of Figure 5.10 – Figure 5.12) and taking the average radius over 1 wavelength to obtain

$$\begin{aligned}\lambda_{Helicon} &\cong \sqrt{\lambda_z^2 + \left[2\pi \times \frac{1}{2}(r_1 + r_2) \right]^2} \\ \lambda_{Helicon} &\cong \sqrt{(15)^2 + \left[2\pi \times \frac{1}{2}(1 + 0.75) \right]^2} \\ \lambda_{Helicon} &\cong 15.98 \text{ cm}\end{aligned}\tag{5.7}$$

This differs from the 2-d wavelengths measured in Figure 5.11 (depending on the spatial location of measurement) by anywhere from 16 % to 37 %. Additionally, it differs from the expected value of 28.48 cm by 78 % based off of the antenna length expectation.

Similar results are obtained for the other two antennae tested where the full three dimensional wavelengths are $\sim 25.1 \pm 0.5$ cm, 16.0 ± 0.5 cm, and 19.08 ± 0.5 cm in reference to the 22.6 cm, 14.2 cm, and 11.2 cm antennae respectively.

Although the full measured wavelengths are shorter than those predicted by either the 3-d antenna length or calculated from radial density profiles, the results demonstrate the helicon wavelength is most accurately represented and measured by 3-d imaging. The remaining challenge is to resolve the difference between the theoretically predicted values and those measured in the lab by examining the causes of this discrepancy.

The method explained in Chapter 2, where a unique value of k_z was calculated which satisfied the boundary condition and density profile, employs two main assumptions. The first is that the plasma density profile extends all the way to the walls and the second is the radial profile is constant in the axial direction. We have already shown the radial density profiles in the axial direction are not constant, and as a result the axial wavelength will not be either. However, considering the 22.6 cm antenna length where the measured density profile at $z = 0$ predicts a 33.78 cm wavelength (Figure 5.20) and the measured wavelength from 3-d imaging is 25.1 cm, the difference is 35 %. This is in contrast to the 2-d measured wavelengths from Figure 5.10 which differ from the predicted result anywhere from 54 % to 118 %, depending on the chosen 2-d scan.

5.2.4 b_r , b_θ Measurements

In addition to the b_z field measurements, b_r and b_θ measurements were taken in the $y = 0$ plane. By taking the scans in the $y = 0$ plane, we can redefine the off-axis plasma wave fields b_r and b_θ as b_x and b_y , respectively. Here, b_r or b_x correspond to field lines which point radially inward whereas b_θ or b_y correspond to field lines perpendicular to 'r' and point in the azimuthal direction. These measurements encompass radial scans from $-a$ to

$+a$ in the $x - y$ plane similar to the b_z scans of Figure 5.16. The results for the 14.2 cm antenna are shown in Figure 5.22. The b_z scan is shown again to reference the signal magnitude against the other two directions. For this antenna, the magnitude of the b_z signal amplitude is significantly higher than either the b_r or b_θ signals (up to an order of magnitude larger in some locations). Some of these contour plots will be revisited later when the data are correlated with axial density profiles. For now, the wave profiles on each cross section match those predicted: b_θ is symmetric about $r = 0$ while b_r is peaked on axis and radially decays. The unanticipated result is the axial variation of the b_r profile. b_r is not at the maximum value under the antenna (where one might expect) but rather peaks within one wavelength downstream from the antenna.

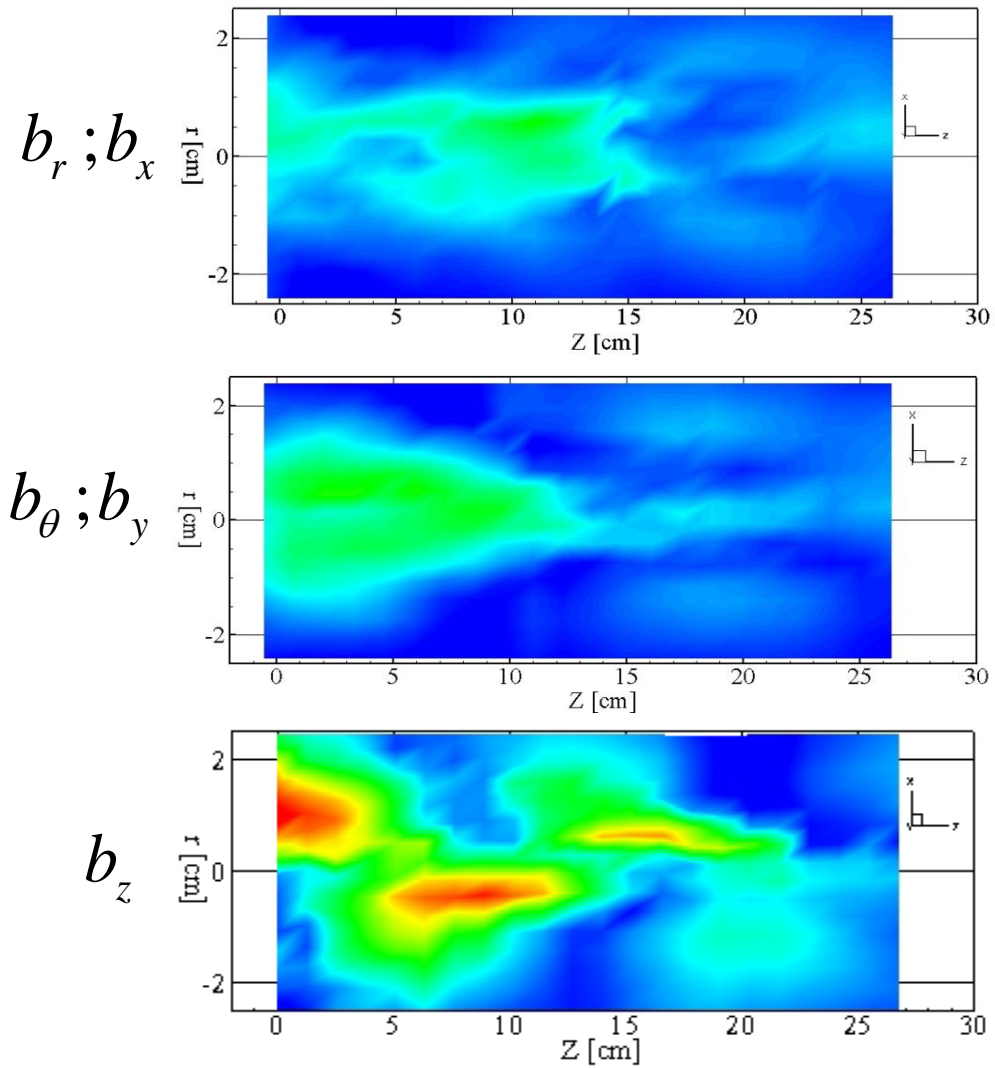


Figure 5.22. b_r , b_θ , b_z wave fields for 14.24 cm antenna. All scans were taken in the $y=0$ plane and therefore b_r and b_θ can also be designated as b_x and b_y , respectively.

This unexpected feature was investigated for the 11.2 cm antenna length and similarly compared. The two b_r comparisons are shown in Figure 5.23 with a noticed similarity: the peak signal amplitude appears downstream of the antenna edge. It is this unanticipated feature that inspired a more thorough analysis of the axial density profiles.

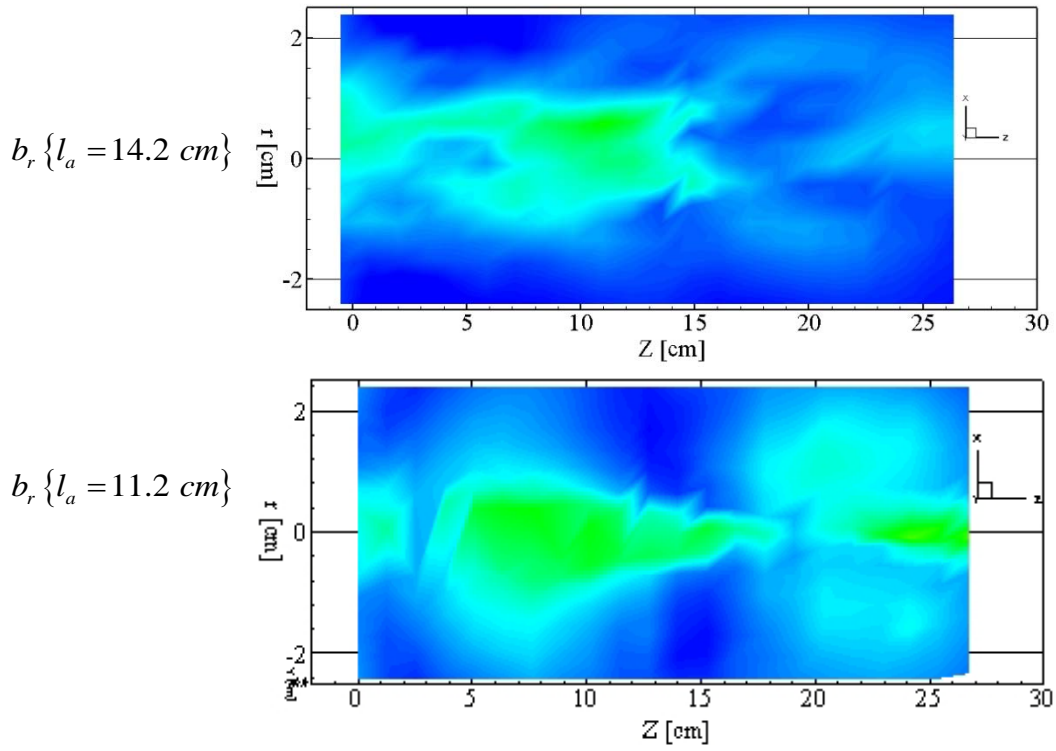


Figure 5.23. Comparison of b_r contour plots for 14.2 cm and 11.2 cm antenna lengths.

5.3 Axial Density Measurements

Axial density scans were conducted for all three of the previously discussed antennae; 22.6 cm, 14.2 cm, and 11.2 cm. The test conditions were 500 Watt input power and 900 Gauss axial magnetic field with the antennae location given in Figure 5.9. Density profiles were constructed along the centerline of a cylindrical plasma column as shown in Figure 5.24 thru Figure 5.26.

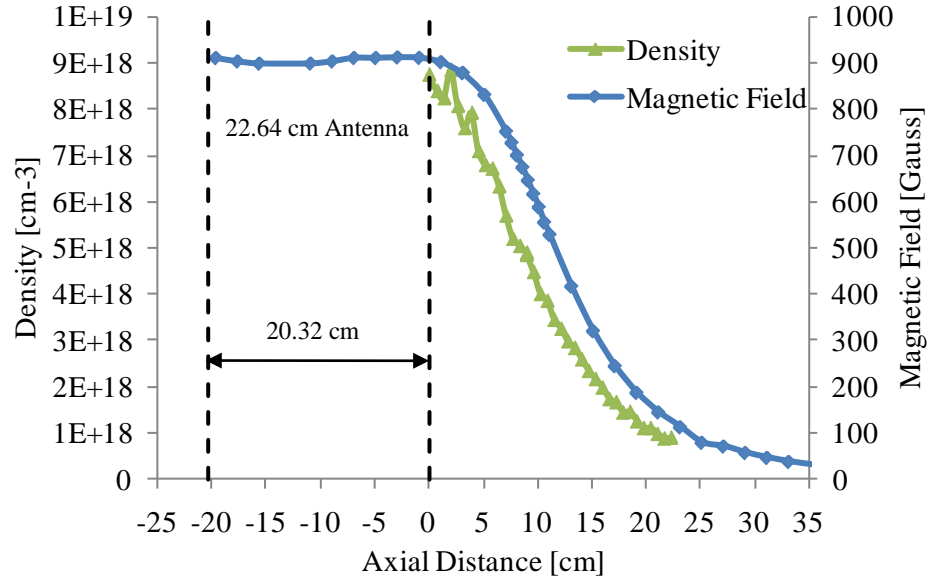


Figure 5.24. Axial density profile down tube centerline for 22.6 cm antenna.
Dashed lines indicate end rings of antenna.

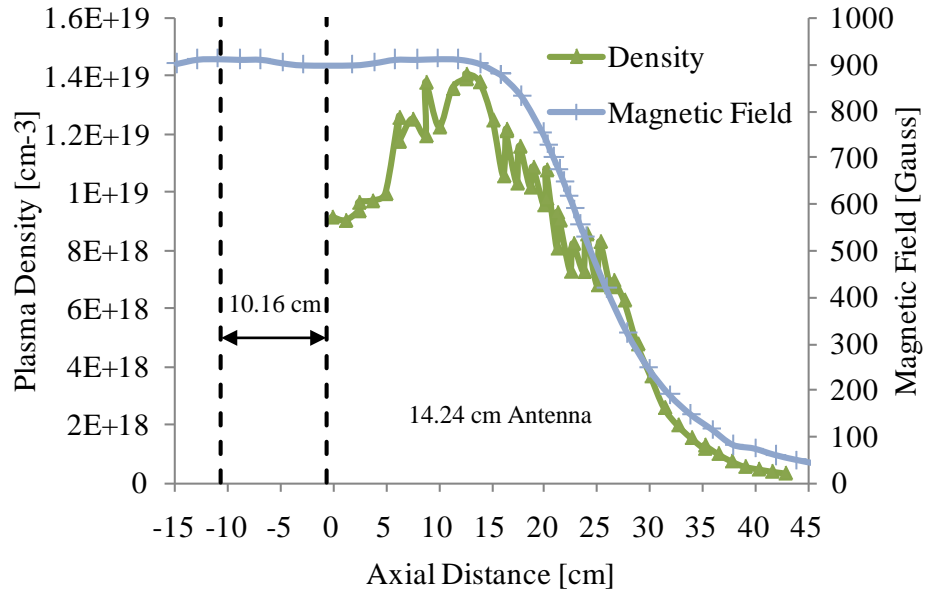


Figure 5.25. Axial density profile down tube centerline for 14.24 cm antenna.
Dashed lines indicate end rings of antenna.

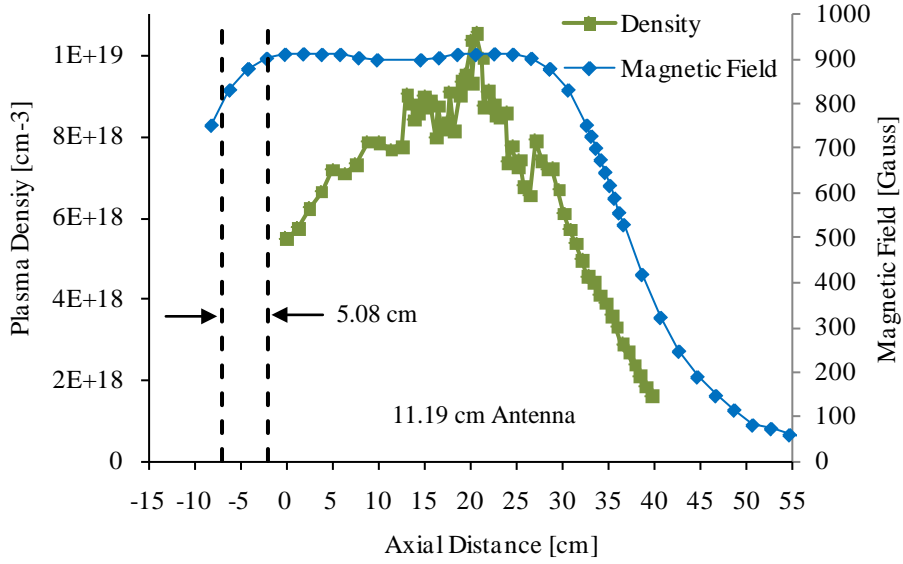


Figure 5.26. Axial density profile down tube centerline for 11.19 cm antenna. Dashed lines indicate end rings of antenna.

The discussion on the structure of each profile begins with returning to the uniform density dispersion relation as given in Chapter 2 as

$$k^2 = \frac{\omega \omega_{pe}^2}{\omega_{ce} c^2 \cos \theta} \quad (5.8)$$

for cylindrical coordinates, and $m = +1$ antenna with $k_{\perp} \gg k_{\parallel}$, this becomes

$$\frac{n}{B_0} = \frac{3.83}{a} \frac{k_z}{e \omega \mu_0} \quad (5.9)$$

Therefore, for a fixed tube radius ‘ a ’, frequency ‘ $\omega = 2\pi f$ ’, the relation n / B_0 should be a constant, or more specifically, proportional to a constant k_z ; if k_z is a fixed value.

Previously, we had discovered the radial density profiles (modeled as Gaussians) were not uniform as the plasma length was traversed away from the antenna. This indicated the axial wavenumber was not constant and as a result, n / B_0 will not be either.

However, for each antenna, n / B_0 is constant in the region where the magnetic field is

decaying; agreeing with the description provided for by a uniform radial density profile. This result is in agreement with the radial profiles taken at distances away from the antenna as previously shown in Figure 5.4.

5.3.1 Downstream Density Peak

The structure of the axial density profiles not yet explained is the region where the density rises downstream of the source antenna; as observed in Figure 5.25 and Figure 5.26 for the 14.2 cm and 11.2 cm antennae, respectively. Downstream density peaks have been previously identified by two different research groups [14, 15]. Additionally, both groups have identified the majority of RF energy absorbed by the plasma is under the antenna. In fact, this has been estimated to be $> 70\text{-}80\%$ of the total energy absorbed within one wavelength of the antenna and heating in the downstream region is nearly negligible [15].

In the next section, we provide an explanation for the rise in the downstream density in terms of a simple energy balance within a plasma volume where a temperature decay $T_e(z)$ occurs in the $+z$ direction. Initially, no assumption of helicon plasma or radial magnetic confinement will be considered. After performing an initial analysis, the model will be applied to the experimental electron temperature profiles for all three antennae with specific emphasis on those which exhibit a downstream density peak.

5.3.1.1 Global Energy Balance Model

The following analysis refers to the plasma volume given in Figure 5.27.

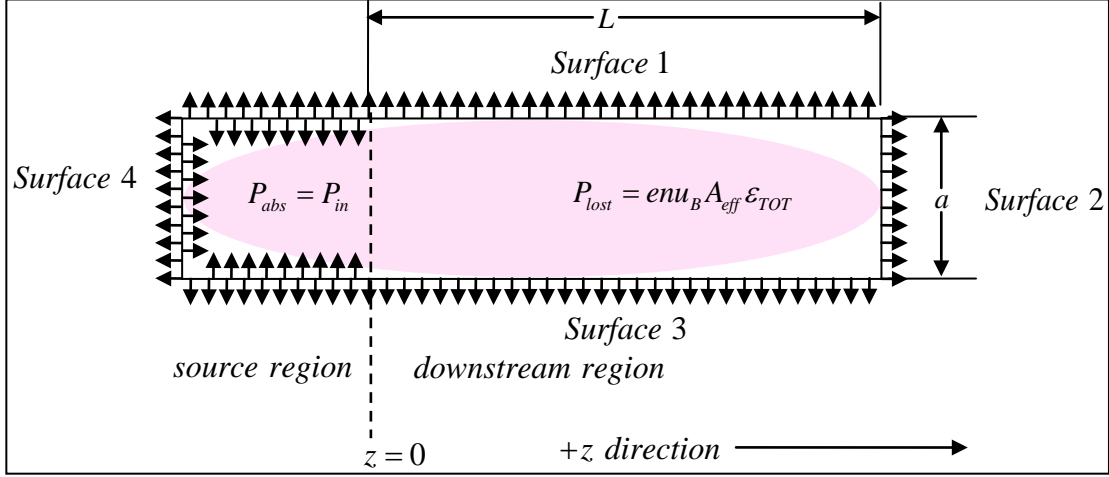


Figure 5.27. Representation of plasma volume for energy balance.

Performing a simple energy balance for determination of the electron density [16]

$$P_{abs} = enu_B A_{eff} \epsilon_T \quad (5.10)$$

Physically, this expression equates the total power absorbed by the plasma P_{abs} to the total power lost. The power lost is equivalent to an electron-ion pair escaping with velocity u_B through an effective area A_{eff} for an energy loss ϵ_{TOT} . In this case, the energy loss can either be due to a collisional process or a sheath loss. The total energy lost is then defined as

$$\epsilon_T = \epsilon_c + \epsilon_e + \epsilon_i \quad (5.11)$$

where ϵ_{TOT} is the total energy lost per electron-ion pair. This is the result of energy lost through ϵ_c (collisional processes; elastic scattering, excitation, ionization), or through electron and ion kinetic energy lost across sheaths near a surface or boundary, ϵ_i and ϵ_e respectively, which are defined by [16]

$$\epsilon_e = 2T_e \quad (5.12)$$

$$\epsilon_i = V_s + \frac{1}{2}T_e \quad (5.13)$$

where V_s is the sheath voltage for an insulating wall defined as

$$V_s = T_e \ln \left(\frac{M}{2\pi m_e} \right)^{1/2} \quad (5.14)$$

substituting (5.14) into (5.13) becomes

$$\varepsilon_i = T_e \ln \left(\frac{M}{2\pi m_e} \right)^{1/2} + \frac{1}{2} T_e \quad (5.15)$$

As the gas in this work is Argon, (5.15) becomes

$$\varepsilon_i = 5.18 T_e \quad (5.16)$$

The remaining energy loss quantity ε_c is the collisional energy loss per electron-ion pair created. This considers electrons that can elastically collide, excite, or ionize the background gas. Therefore, the collisional energy for an electron-ion pair is defined as [16]

$$K_{iz} \varepsilon_c = K_{iz} \varepsilon_{iz} + K_{ex} \varepsilon_{ex} + K_{el} \frac{3m_e}{M} T_e \quad (5.17)$$

For Argon, $\varepsilon_{ex} = 12.14$ Volts and $\varepsilon_{iz} = 15.76$ Volts. The rate constants K_{xx} are given in Lieberman [16] and approximated by

$$K_{el} = 2.336 \times 10^{-14} T_e^{1.609} e^{0.0618(\ln T_e)^2 - 0.1171(\ln T_e)^3} \quad (5.18)$$

$$K_{iz} = 2.34 \times 10^{-14} T_e^{0.59} e^{-17.44/T_e} \quad (5.19)$$

$$K_{ex} = 2.48 \times 10^{-14} T_e^{0.33} e^{-12.78/T_e} \quad (5.20)$$

where the rate constants K_{xx} (m^3/s) are valid for temperatures in the range $\sim 1\text{-}7$ eV [16].

Additionally, the Bohm velocity u_B is defined as

$$u_B = \left(\frac{e T_e}{M} \right)^{1/2} \quad (5.21)$$

Therefore, the final undefined quantity in expression (5.10) is the effective area for particles loss A_{eff} . This can be done for a cylinder with the radius ‘ a ’ and length ‘ L ’ as

$$A_{\text{eff}} = 2S.A._{\text{disk}} h_L + S.A._{\text{cyl}} h_a \quad (5.22)$$

Here, $S.A.$ are the areas for the respective cylindrical surfaces. The “2” in (5.22) references both ends of the cylinder. Therefore, (5.22) may also be written as

$$A_{\text{eff}} = 2\pi a^2 h_L + 2\pi a L h_a \quad (5.23)$$

h_L and h_a are the sheath density ratios, which for an intermediate pressure where the mean free path is less than the device dimensions $\lambda_i \ll (a, L)$ can be approximated by [16]

$$h_L = \frac{n_{sL}}{n_0} \approx 0.86 \left(3 + \frac{L}{2\lambda_i} \right)^{-1/2} \quad (5.24)$$

$$h_a = \frac{n_{sa}}{n_0} \approx 0.80 \left(4 + \frac{a}{\lambda_i} \right)^{-1/2} \quad (5.25)$$

An intermediate pressure is determined based on a mean free path for Argon given by

$$\lambda_i = \frac{1}{n_g \sigma_i} \approx \frac{1}{330 p} \text{ cm} \quad (p \text{ in Torr}) \quad (5.26)$$

for 10 mTorr (5.26) becomes

$$\lambda_i \approx 0.3 \text{ cm} \quad (5.27)$$

and knowing ‘ a ’ and ‘ L ’ are much larger than ~ 0.3 cm, the intermediate pressure sheath density ratios will be valid.

Returning to the energy balance (5.10) and rearranging for the density,

$$n = \frac{P_{\text{abs}}}{e u_B(T_e) A_{\text{eff}}(a, L) \varepsilon_T(T_e)} = n(T_e, a, L) \quad (5.28)$$

and for a fixed ‘ a ’ and ‘ L ’, the density becomes solely a function of the electron temperature profile; albeit a very complex function of electron temperature as illustrated by substitution for quantities with a temperature dependence

$$n = \frac{P_{abs}}{e \left(\frac{eT_e}{M} \right)^{1/2} A_{eff}} \frac{1}{\left(\frac{K_{iz}\epsilon_{iz} + K_{ex}\epsilon_{ex} + K_{el}\frac{3m}{M}T_e}{K_{iz}} + 2T_e + T_e \ln \left(\frac{M}{2\pi m_e} \right)^{1/2} + \frac{1}{2}T_e \right)} \quad (5.29)$$

5.3.1.2 Sample Temperature Profiles

At this point, it is instructive to assume a temperature profile in order to observe the behavior of the density in the axial direction. To conform to the experiment the following quantities are specified: cylindrical tube radius $a = 2.5 \text{ cm}$, length $L = 0.5 \text{ m}$, neutral Argon gas pressure = 10 mTorr, with 500 Watts absorbed power. Additionally, an exponentially decaying temperature profile with initial temperature $T_{e0} = 6 \text{ eV}$ is defined as

$$T_e(z) = T_{e0} e^{-\alpha(z-z_0)} \quad (5.30)$$

We further let $z_0 = 0$ and the decay constant $\alpha = 3$ so that the axial temperature profile is illustrated in Figure 5.28.

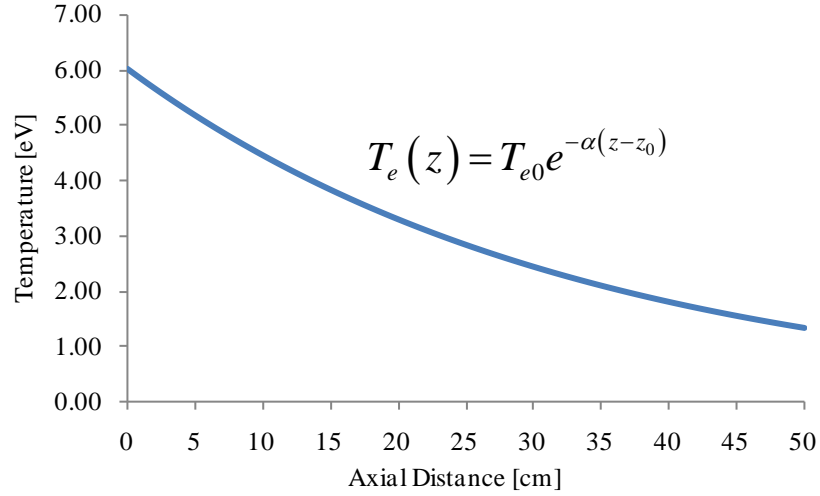


Figure 5.28. Exponentially decaying axial temperature profile.

Using the temperature profile in (5.30) the axial density variation can be solved at each “z” location and is shown in Figure 5.29.

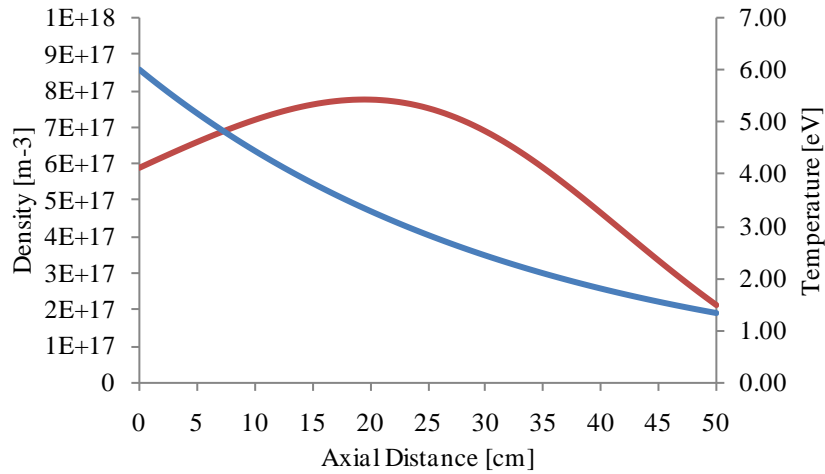


Figure 5.29. Axial density variation based on an exponentially decaying temperature profile illustrating a downstream peak in the plasma density.

The downstream density peak is slightly unexpected based on the fact that no assumption was made regarding an increased ionization rate or other effect that takes place outside the source region; $z = 0$. To better understand why this occurs, the quantities that vary with T_e or ‘z’ in (5.28) are more closely examined.

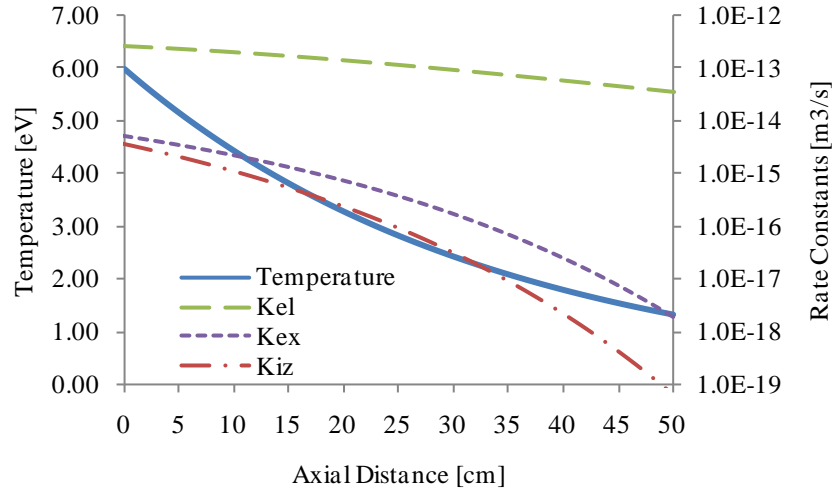


Figure 5.30. Rate constants K_{xx} variation due to temperature profile.

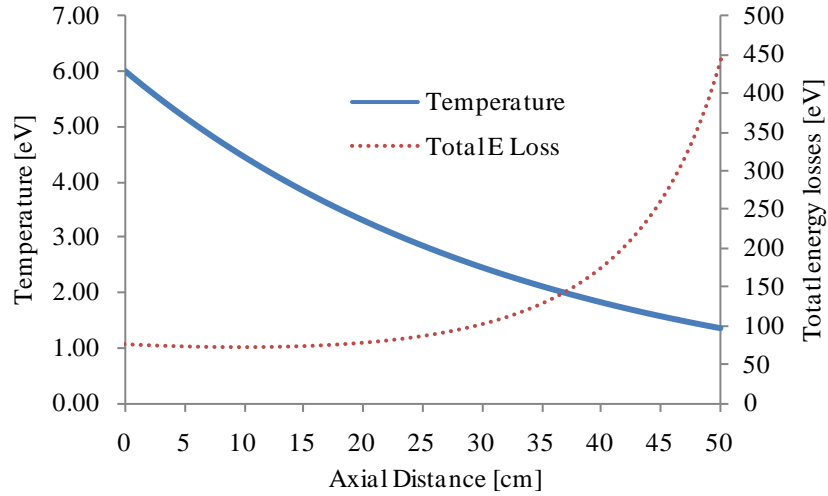


Figure 5.31. Total energy loss ϵ_{TOT} due to temperature profile.

With regards to Figure 5.30 and Figure 5.31, as the temperature decreases, the collisional rates, K_{el} , K_{ex} , and K_{iz} all decrease thereby increasing the total energy loss downstream.

The decaying or cooling electron temperature has the effect of decreasing the ion velocity which causes the density to rise. This effect is countered by an increase in energy loss from collisional and sheath processes forcing the density to decrease. However, the rate of decay of the electron temperature will initially cause the downstream density to rise prior to decaying away from the source.

Therefore, dependent upon how the electron temperature decay is modeled as well as some specified initial conditions, one can obtain a reasonable idea of how the plasma

density is going to behave. Furthermore, the analysis to this point has considered a simple energy balance and has not included any effects such as an external magnetic field or wave heating to explain the downstream phenomenon.

5.3.1.3 Application to the Present Data

Returning to the 11.2 cm antenna, the measured density and temperature profiles are shown in Figure 5.32.

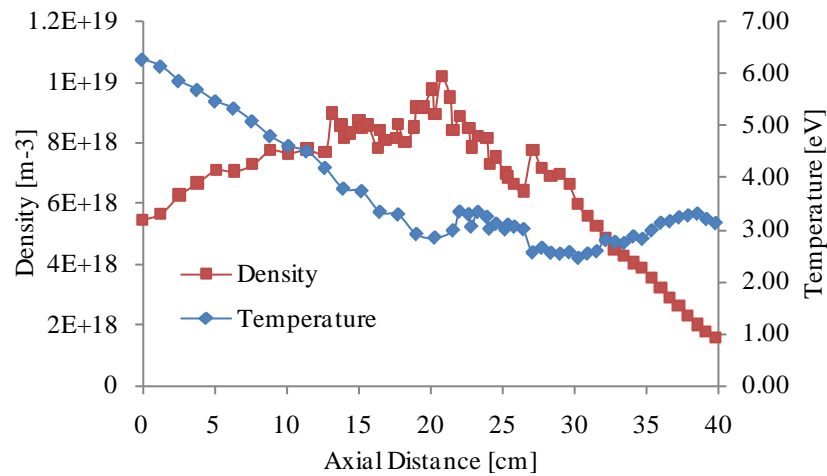


Figure 5.32. Measured density and electron temperature profiles for 11.2 cm antenna.

The rise in temperature beyond about 30 - 35 cm downstream is presumed to be due to insufficient probe compensation at the lower collected electron currents; a smaller collected electron current will cause a rise in the sheath impedance according to equation (4.12) where the probe impedance remains fixed. At these ‘far’ downstream conditions, a larger probe tip would have had the effect of collecting a larger electron current reducing the error due to impedance ratios. A larger compensation probe at these conditions would also have ‘tracked’ the plasma potential to a higher degree yielding more precise electron temperature measurements. The electron temperature profile is

approximated as shown in Figure 5.33 with corresponding error bars on every other measured data point. As previously discussed, the larger error in the electron temperature for the downstream locations is due to a decrease in the collected saturation current which will force the sheath impedance to rise with respect to the fixed probe impedance.

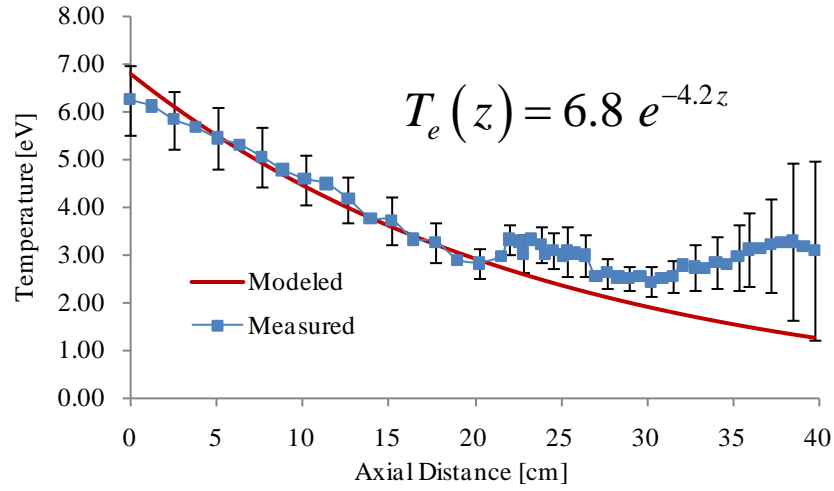


Figure 5.33. Modeled and measured electron temperature profiles.

Using the modeled electron temperature and following the same procedure for calculating the density as outlined above, the measured and expected density can be compared for a plasma length of 40 cm. This is shown in Figure 5.34.

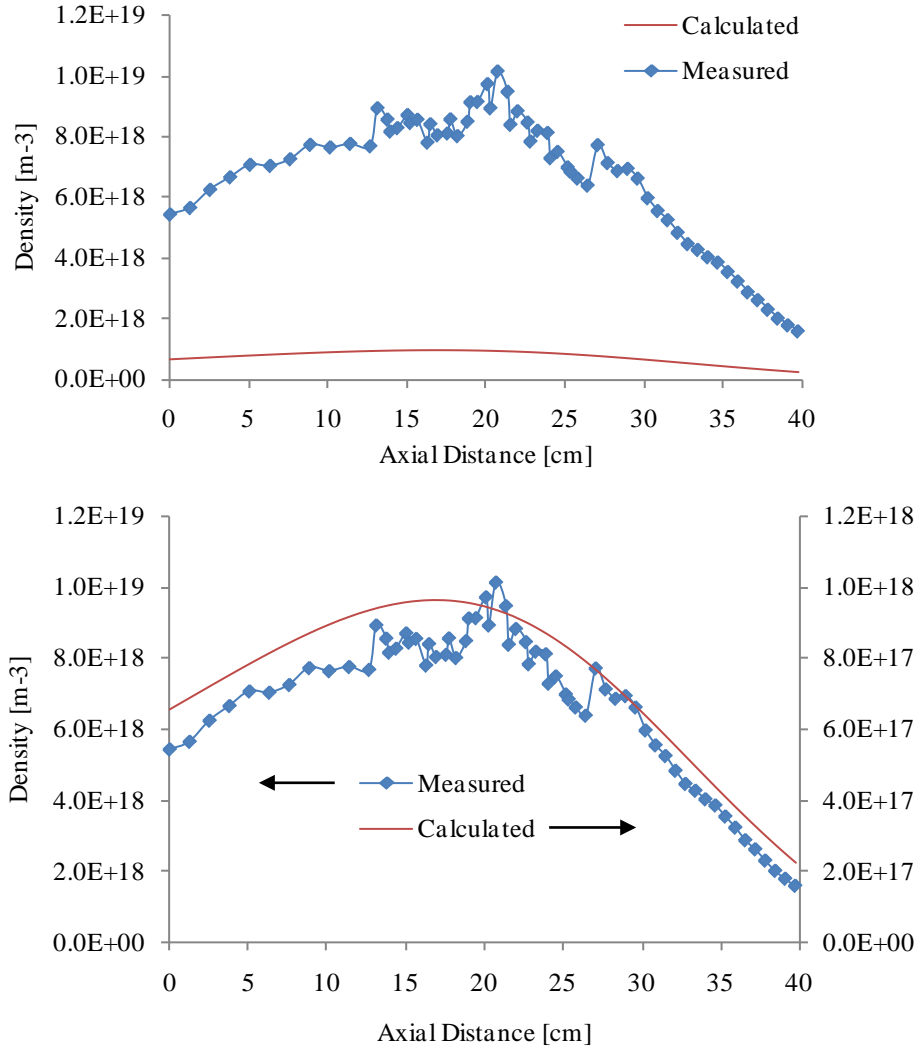


Figure 5.34. Modeled and measured density profiles for 11.2 cm antenna.
The top graph is shown on the same scale while the bottom scales are separated.

A discrepancy between the order of magnitudes of the calculated and measured plasma densities is immediately apparent from Figure 5.34. However, also obvious is the remarkable agreement between the structures of the two profiles. Therefore, what remains is to account for the order of magnitude difference between the two profiles. To do this we will have to make some modifications to the plasma volume described in Figure 5.27. First, consider particle loss only across surfaces 1, 2, and 3 in the downstream region. This has the effect of altering equation (5.22) and (5.23) so the first

term accounts for only the one $S.A_{DISK}$ cross-section; only surface 2 should be included for this area since small losses would be expected in the direction of surface 4 from the magnetic field pointing in the +z direction. Equation (5.22) becomes

$$A_{eff} = S.A_{disk} h_L + S.A_{cyl} h_a \quad (5.31)$$

or

$$A_{eff} = \pi a^2 h_L + 2\pi a L h_a \quad (5.32)$$

This alteration has a negligible effect on the total A_{eff} because $L \gg a$ in (5.32). However, returning to (5.28) for the density, the effective area for particle loss is going to remain the term which has the greatest impact on the order of magnitude for the resultant density. Therefore, we take into consideration the axially applied B_0 field which radially confines the plasma. We can introduce a “loss factor” into (5.31) such that

$$A_{eff} = \chi_{DISK} (S.A_{disk} h_L) + \chi_{CYL} (S.A_{cyl} h_a) \quad (5.33)$$

where χ_{DISK} and χ_{CYL} are identified as percent confinement quantities, i.e., $0 \leq \chi \leq 1$. For the current data we assume no change to the axial losses so that $\chi_{DISK} = 1.00$, but for the relatively strong magnetic field, $B_0 = 900 \text{ Gauss}$, we set $\chi_{CYL} = 0.10$ stating that 90% of the original plasma is now confined by the magnetic field. This is also reiterated as:

The magnetic field alters the effective area for particles loss in the radial direction (across the surface area of a cylindrical boundary) so the effective area is reduced to $1/10^{th}$ of the original magnitude.

Utilizing these definitions alters the predicted density profiles such that close agreement with the measured density is achieved. This is illustrated in Figure 5.35.

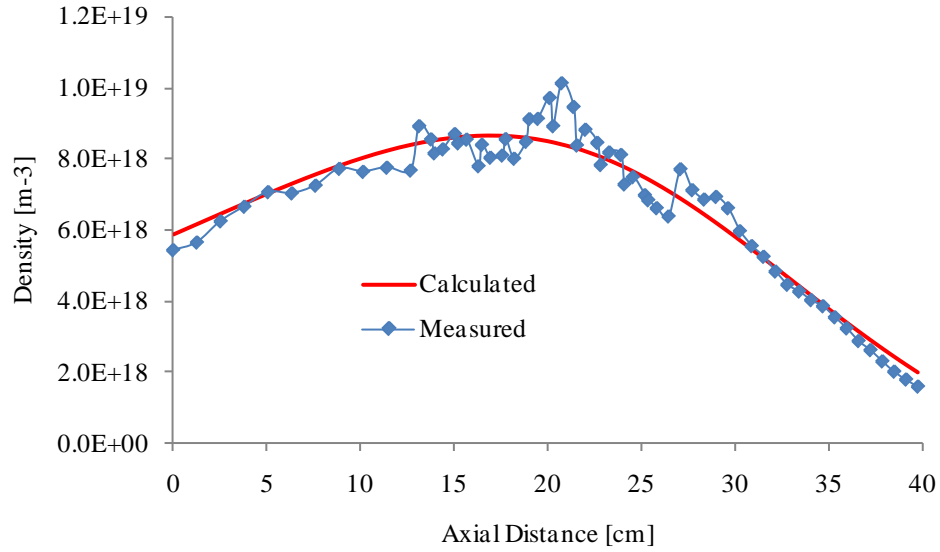


Figure 5.35. Refined calculated profile assuming confinement factors for particle loss areas.

A similar analysis is performed for the 14.2 cm antenna where a downstream density peak was also observed. The measured density and temperature profiles for this condition are shown in Figure 5.36 where the rise in temperature downstream is again presumed to be the result of insufficient probe compensation (due to the saturation current as previously discussed) for the densities and currents measured.

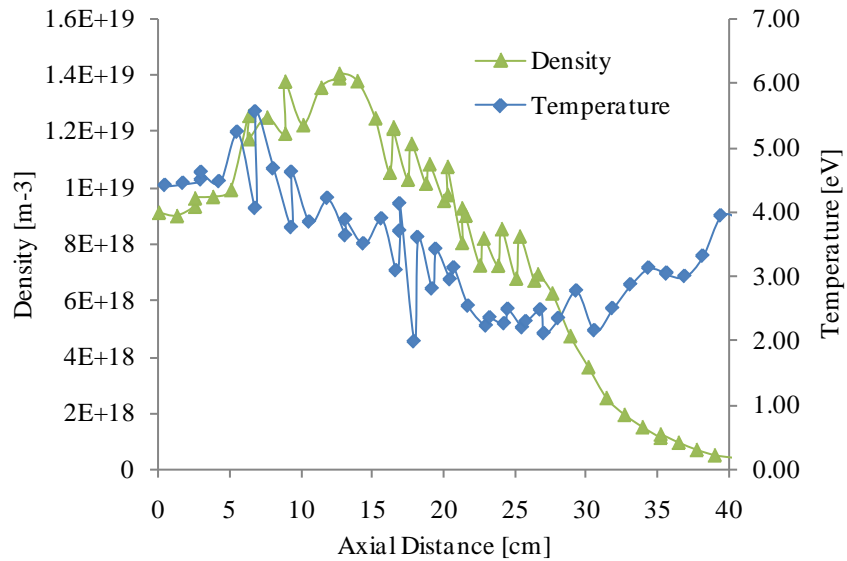


Figure 5.36. Measured density and temperature profiles for 14.2 cm antenna.

The modeled temperature profile is again assumed to be an exponential decay. The initial temperature and decay constants were selected to provide the best fit to the measured density and temperature profiles. The plasma length was 40 cm and the cylindrical plasma radius was 2.5 cm. These results are shown in Figure 5.37 (with error bars for selected temperature data points) and Figure 5.38. In this case, the axial loss factor, $\chi_{DISK} = 1.00$ was not adjusted, however, the radial loss factor was adjusted to $\chi_{CYL} = 0.06$ in order for the density magnitudes to reach agreement.

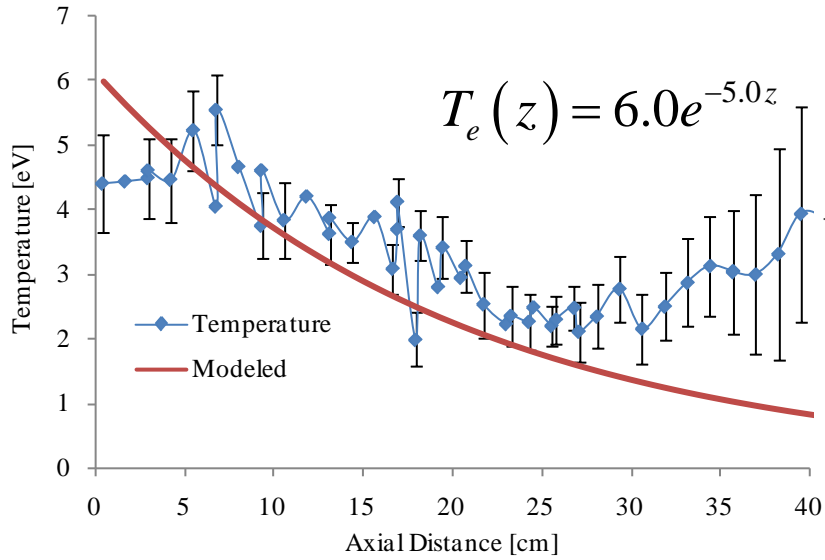


Figure 5.37. Measured and modeled temperature profiles for the 14.2 cm antenna.

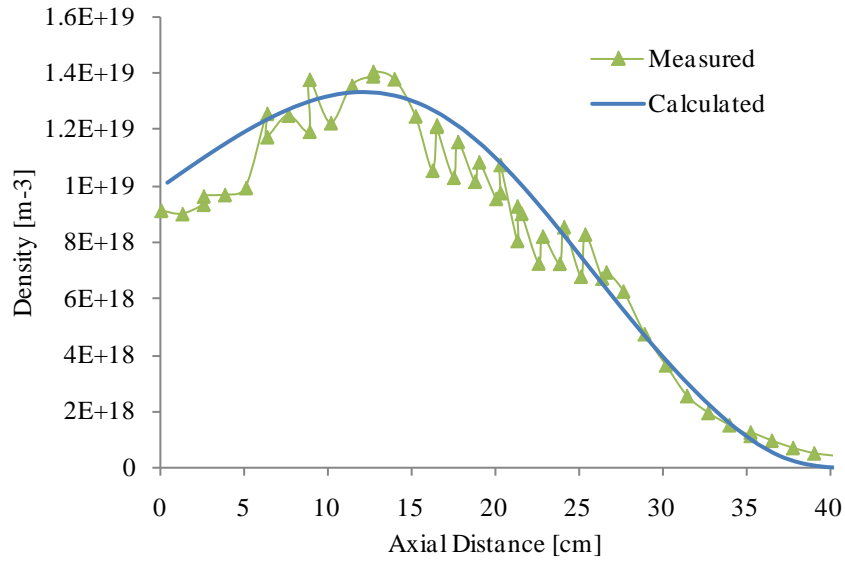


Figure 5.38. Measured and calculated density profiles for the 14.2 cm antenna.

The final axial density profile analysis was performed for the 22.6 cm antenna. Although there was not a downstream density peak observed, the model still accurately predicted the density based off an exponential decaying temperature profile and a radial confinement factor $\chi_{CYL} = 0.10$. The results are shown in Figure 5.39 and Figure 5.40.

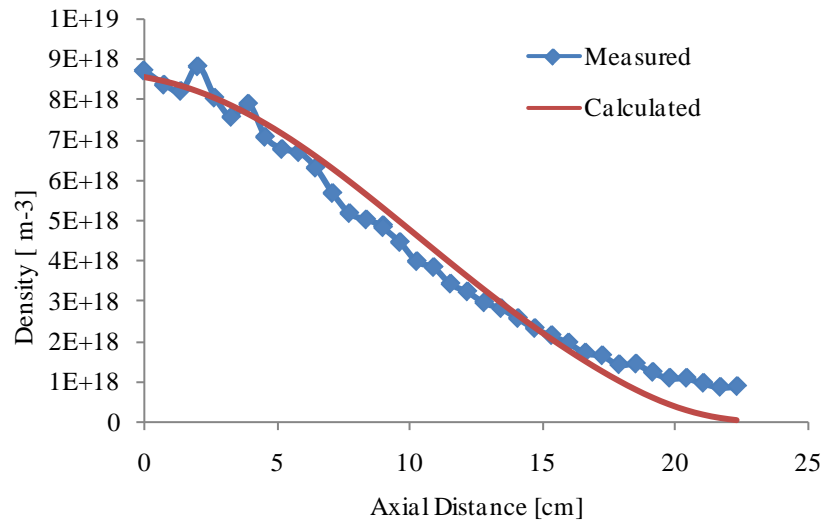


Figure 5.39. Measured and calculated axial density profiles for the 22.6 cm antenna.

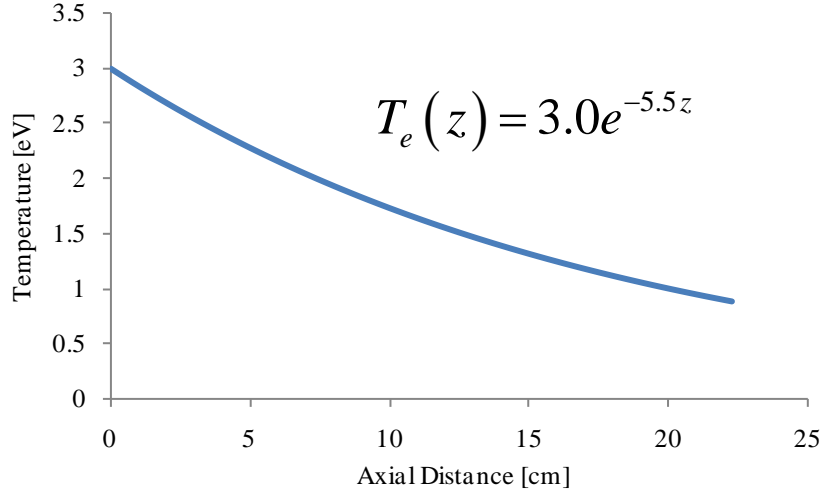


Figure 5.40. Modeled axial electron temperature; axial decay.

The power of this simple model lies in its global nature. It is able to provide an explanation for a downstream density peak without assuming any applied magnetic fields or wave particle interactions. The model has been adapted to account for radial confinement which exists when a magnetic field is applied by supplying a few correction factors. However, it was necessary to change the correction factor for confinement between the different antennae even though the applied magnetic field did not change. This suggests that while the model is valid for providing an axial density structure based on a cooling electron temperature, the correction factors may have to be further refined, particularly the radial loss factor χ_{CYL} . Since this factor represents the fraction of the surface area of the cylindrical tube for radial losses, the variation of this term suggests a dependence on a cross field diffusion coefficient. Should a more detailed model of an axial density profile be required, this component of the model may require further investigation. The objective of this model was to explain the formation of a downstream density peak and consequently further analysis of this point is beyond the scope of the current work.

5.4 Additional Cases of Interest: Conical Antennae

Two additional cases of interest which were tested in this work were for conical tube geometry. Three dimensional antenna lengths of 22.6 cm were used for both cases and their results will briefly be presented.

5.4.1 Converging Conical Antenna

A converging conical tube operating at 500 Watts in a peak 900 Gauss static magnetic field is studied. The result of three dimensional imaging of the propagating wave is shown in Figure 5.41. The edge of the antenna is located at $z = 0$ and the magnetic field is in the $+z$ direction.

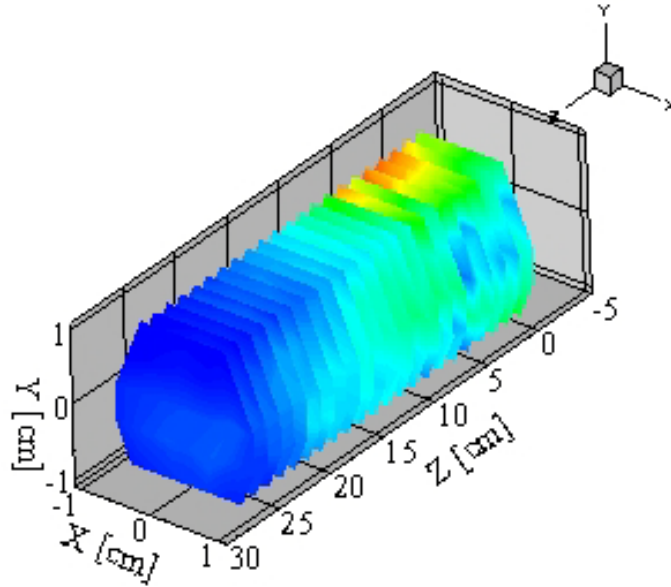


Figure 5.41. Converging conical axial b_z scans.

The radial scans for each cross section span ± 1.0 cm. This differs from the cylindrical tubes where scans were complete from ± 2.4 cm. The radial scans were limited due to probe access at the narrow end of the conical tube; however, a detailed representation of

the wave fields is given by Figure 5.41. The b_z scans indicate the wave terminates approximately 20 cm downstream of the antenna. This is believed to be a consequence of the plasma interaction with the wall as propagation is toward more narrow radii whereby the properties of the plasma dielectric no longer meet conditions necessary for helicon wave propagation. This explanation is complemented by the axial density profile illustrated in Figure 5.42. The peak density values obtained are less than any of the cylindrical antennae tested and the axial density drop occurs in a region closer to the antenna as a result of the narrowing tube radius moving downstream. The scale of the probe size to tube diameter regarding interference with the wave may also play a role.

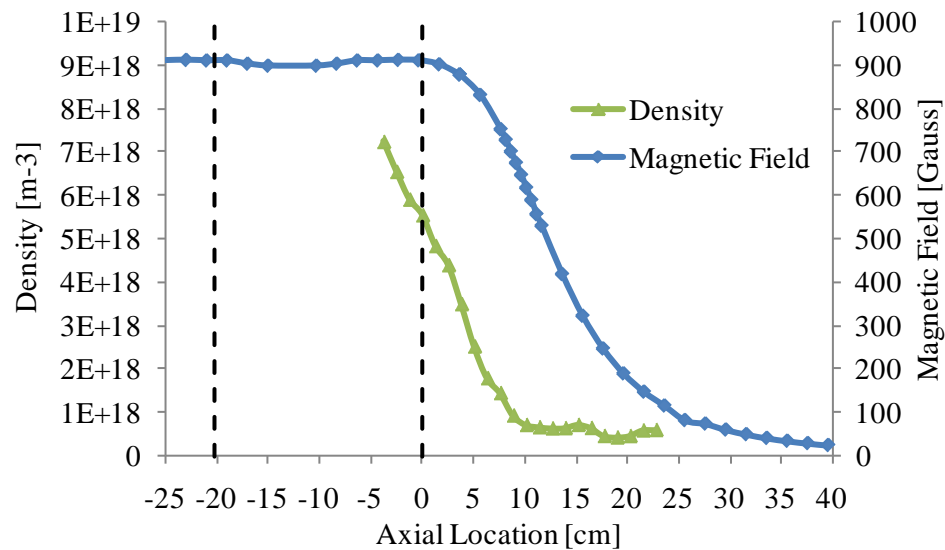


Figure 5.42. Converging conical tube axial density profile.
Dashed lines indicate the end rings of the antenna.

5.4.2 Diverging Conical Antenna

The second case of interest was a diverging conical tube. The test conditions were the same at 500 Watts 900 Gauss and the three dimensional antenna length was 22.6 cm. It is similar to the converging tube and since both ends of the tube were attached to conflat

flanges, testing this condition simply required “flipping” the quartz tube around. Three dimensional imaging of the wave via b_z scans are shown in Figure 5.43.

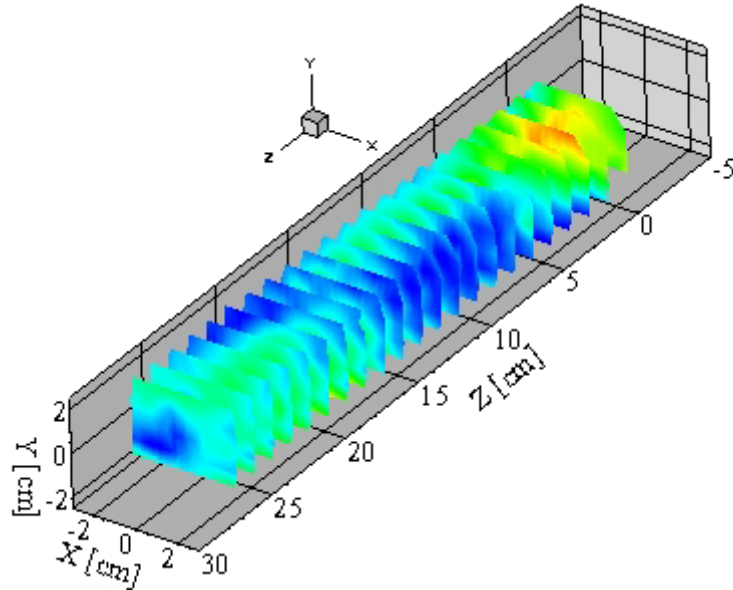


Figure 5.43. Diverging conical axial b_z scans.

The results of the b_z imaging show results familiar to the cylindrical tube of the same antenna length, 22.6 cm (Figure 5.17). The measured wavelength for the diverging tube was 25.8 ± 0.5 cm; slightly longer than the 25.1 cm cylindrical counterpart. The difference lies in the radial width component as describe previously.

Axial density measurements were taken and compared against those of the cylindrical tube of same antenna length; Figure 5.44. While the density measurements for both versions of the conical tube exhibit similar peak densities, both are still much less than the density values obtained with a traditional cylindrical quartz tube. It is for this reason that further investigation of the conical geometry was abandoned. For the same input power, the cylindrical tube exhibited better performance than its conical counterparts. Performance in terms of the peak density suggests the cylindrical antenna has a higher

coupling efficiency than the conical geometry; though this measurement was not quantified.

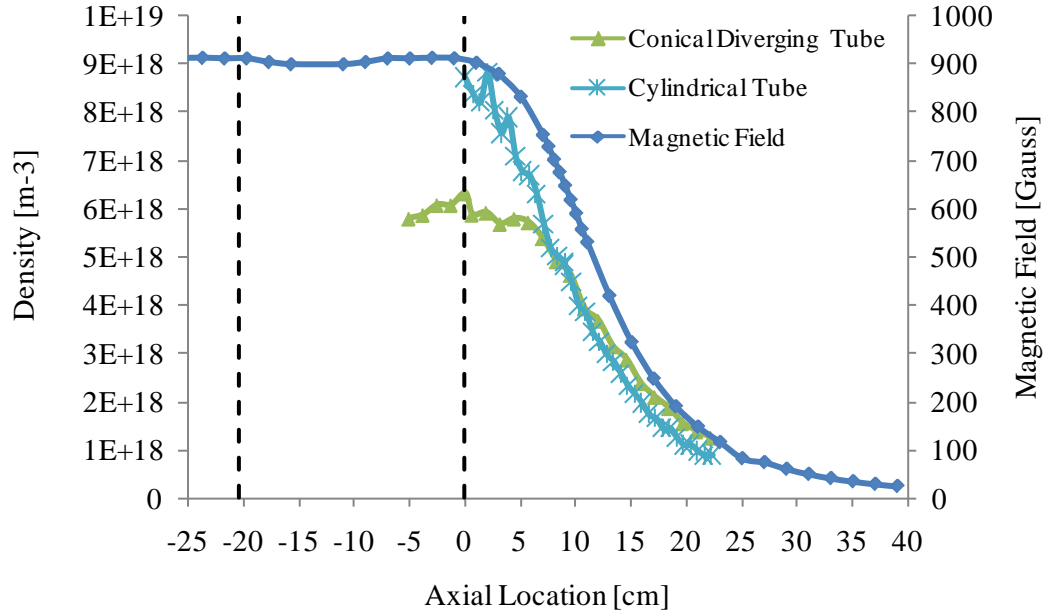


Figure 5.44. Diverging conical tube axial density profile.
Dashed lines indicate the end rings of the antenna.

5.5 Ionization Cost Analysis

A similar analysis with regard to the power balance performed in the previous section can be performed to examine the ionization “cost” in helicon plasma. Ionization cost refers to the total energy (or power) required to produce an electron-ion pair. We can define the ionization cost in terms of equating the power absorbed by the plasma to the power lost similar to (5.10) as

$$P_{abs} = \varepsilon_{TOT} \frac{dN}{dt} \quad (5.34)$$

where the $P_{abs} = 500$ Watts as before and ε_{TOT} is the same total energy required to maintain the plasma discharge due to collisional and sheath losses. dN/dt is the particle loss rate defined as

$$\frac{dN}{dt} = A_{eff} n c_s \quad (5.35)$$

Substituting (5.35) into (5.34) and solving for ε_{TOT} , now referred to as the ionization cost, yields the following expression

$$\varepsilon_{TOT} = \frac{P_{abs}}{A_{eff} n c_s} \quad (5.36)$$

This quantity has already been calculated, from equation (5.11), for each antenna when analyzing the axial density profiles and the result is illustrated in Figure 5.45.

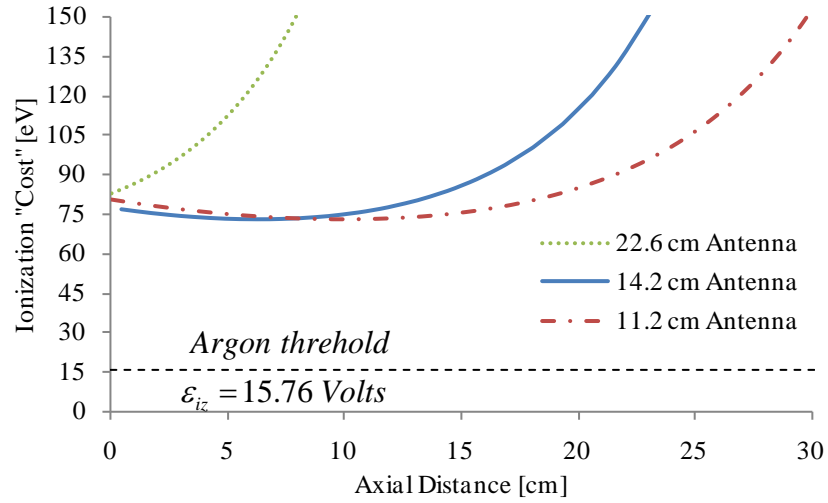


Figure 5.45. Ionization “cost” for the three different antennae tested.

As before, the assumption has been made that the plasma absorbs all 500 Watts of input power and there are no other loss mechanisms such as transmission line losses, matching network impedance losses, or antenna radiation losses. The effective area A_{eff} again has the built-in confinement parameter χ to account for the radial particle confinement due to the static magnetic field.

In each case, the antenna edge is located at $z = 0$, with +z downstream of the antenna.

The useful value of the ionization cost in each case should be taken at $z = 0$ since this is

the antenna edge. Because almost all the RF power is absorbed in the near field region of the antenna (less than one helicon wavelength), assuming 500 Watts of power is being absorbed far downstream is unreasonable. Therefore, the values for the ionization cost at $z = 0$ range from approximately 75 – 85 eV for the helicon discharges investigated in this work.

5.6 Chapter Summary

This chapter has shown the close agreement between measured b_z profiles with magnetic induction probes and those numerically solved b_z profiles when radial density gradients are considered. The onset of helicon waves has been determined through the radial b_z measurements over a wide range of pressures, power, and magnetic field strengths. Utilizing the measured radial density profiles, we were able to solve for the b_z fields as well as the axial wavelength along the magnetic field line. When the single axis z -direction measurement of the axial wavelength was performed, large disagreement with the calculate value was observed. Therefore, this chapter redefined the helicon wavelength in terms of the full wave helix. Three dimensional contour maps were constructed for the first time to visually illustrate a helicon wave. When the 3-d helix is considered, agreement with predicted axial wavelength values is achieved to within 35 %, contrasted with the > 100% differences with 2-d measured wavelengths.

The downstream density peak observed has been modeled in terms of a decaying axial temperature profile away from the antenna / source. The qualitative structure of the model agreed with axial density measurements although it was not until we considered a

radial confinement factor that close quantitative agreement between measured and calculated densities was achieved. The radial confinement factor limited radial losses to 6-10 % and were due to the applied magnetic field.

5.7 References

- [1] J. A. Lehane, and P. C. Thonemann, "An experimental study of helicon wave propagation in a gaseous plasma," *Proceedings of the Physical Society* vol. 85, 1965.
- [2] J. P. Klozenberg, B. McNamara, and P. C. Thonemann, "The dispersion and attenuation of helicon waves in a uniform cylindrical plasma," *Journal Of Fluid Mechanics*, vol. 21, pp. 545-563, 1965.
- [3] R. W. Boswell, "A study of Waves in Gaseous Plasma," Dissertation, School of Physical Sciences, The Flinders University of South Australia, 1970.
- [4] R. W. Boswell, "Very Efficient Plasma Generation by Whistler Waves Near the Lower Hybrid Frequency," *Plasma Physics and Controlled Fusion*, vol. 26, no. 10, pp. 16, 1984.
- [5] F. F. Chen, "Plasma Ionization by Helicon Waves," *Plasma Physics and Controlled Fusion*, vol. 33, no. 4, pp. 26, 1991.
- [6] F. F. Chen, "Physics of helicon discharges," *Physics of Plasmas*, vol. 3, no. 5, pp. 11, 1996.
- [7] F. F. Chen, and H. Torreblanca, "Density jump in helicon discharges," *Plasma Sources Science and Technology*, vol. 16, no. 3, pp. 593-596, 2007.

- [8] M. Light, I. D. Sudit, F. F. Chen *et al.*, "Axial propagation of helicon waves," *Physics of Plasmas*, vol. 2, no. 11, pp. 10, 1995.
- [9] F. F. Chen, I. D. Sudit, and M. Light, "Downstream physics of the helicon discharge," *Plasma Sources Science and Technology*, vol. 5, pp. 8, 1996.
- [10] A. R. Ellingboe, and R. W. Boswell, "Capacitive, inductive and helicon-wave modes of operation of a helicon plasma source," *Physics of Plasmas*, vol. 3, no. 7, pp. 8, 1996.
- [11] C. M. Franck, O. Grulke, A. Stark *et al.*, "Measurements of spatial structures of different discharge modes in a helicon source," *Plasma Sources Science and Technology*, 2005, p. 10.
- [12] M. Light, and F. F. Chen, "Helicon wave excitation with helical antennas," *Physics of Plasmas*, vol. 2, no. 4, pp. 10, 1995.
- [13] S. M. Tysk, C. M. Denning, J. E. Scharer *et al.*, "Optical, wave measurements, and modeling of helicon plasmas for a wide range of magnetic fields," University of Wisconsin, Department of Electrical and Computer Engineering, 2004, p. 40.
- [14] M. Kramer, "Propagation and damping of $m=+1$ and $m=-1$ helicon modes in an inhomogeneous plasma column," *Physics of Plasmas*, vol. 6, no. 4, pp. 7, 1999.
- [15] I. D. Sudit, and F. F. Chen, "Discharge equilibrium of a helicon plasma," *Plasma Sources Science and Technology*, vol. 5, pp. 11, 1995.
- [16] M. A. Lieberman, and A. J. Lichtenberg, *Principles of Plasma Discharges and Materials Processing*, Second ed.: John Wiley & Sons, 2005.

CHAPTER 6: CONCLUSIONS AND FUTURE WORK

This work has consistently completed the cycle: theory – experiment – theory – This chapter will follow the sequential format of the dissertation and highlight the primary results of three dimensional plasma waves and density peaks away from an ionizing source; two subjects within the breadth of helicon work that had yet to be fully explored prior to this research. In addition to the innovative diagnostic achievements (b-dot frequency characterization and data analysis), this work has methodically compared the non-uniform radial density treatment of helicon waves with experimentally measured b_z results. The visual representations of the axial helicon wavelength through three dimensional contour mappings illustrate new insights into helicon physics i.e., the helical nature of the propagating wave and the necessary azimuthal component of the wavelength. Finally, discussion regarding additional areas where further research is warranted will be discussed.

6.1 On Theory

Given that helicon waves are bounded whistler waves, the theoretical treatment of helicons in this research began with the most general assumptions: infinite uniform static medium. The next step was to include a boundary while assuming wave propagation in radially uniform plasma immersed in an infinitely long magnetic field. The resulting dispersion relation essentially coincided with the description of whistler waves in free space. The radially uniform density theory also provides measurable quantities in the laboratory; the b_r , b_θ , and b_z plasma wave fields. The measured results agreed at certain operating conditions with the uniform theory yet still failed to accurately represent all test

conditions. Therefore, non-uniform radial density distributions represented by Gaussian profiles were introduced. The wave fields b_r , b_θ , and b_z were numerically solved for subject to a vanishing b_r , radial magnetic field component, on the boundary. However, the Gaussian density representations did not precisely correspond with the experimentally determined density profiles. While the agreement between the density profiles and wave fields is strong, the differences are not necessarily negligible and cannot simply be attributed to measurement error. Therefore, a suggestion for further analysis would be to include a vacuum ‘gap’ layer between the insulating boundary and bulk plasma. The present work considered the plasma density profile to extend to the tube wall while in a laboratory discharge a vacuum gap layer or sheath will exist. Taking this into account in a future numerical solution may provide even further agreement with laboratory quantities.

Theoretical consideration also showed that inclusion of finite electron mass and collisionality within the plasma volume generated a second branch to the dispersion relation for helicon waves. This second branch is called the Trivelpiece-Gould (TG-) branch; a radially directed electron cyclotron wave. The radially directed nature of this wave was shown to stem from the waves perpendicular wavenumber being much larger than the parallel wavenumber; $k_\perp \gg k_\parallel$. It is this radial TG- wave that is believed to be responsible for the high degree of ionization within helicon plasma from which electrons gain energy. The existence of an electron wave in the near field region of the source antenna is consistent with reports that the majority of RF energy is absorbed near the antenna and not transported axially downstream [1]. It is also consistent with the

relatively high ($\sim 6 - 7$ eV) electron temperatures observed near the antenna region. This branch was additionally shown to be obscured at higher magnetic fields (greater than a few hundred Gauss). This was a result of the short perpendicular wavelength at higher magnetic fields (typically less than 1.0 cm). Therefore, this is an extremely difficult wave to measure because of its short radial nature. To date, there has only been one experimental measurement with a J-dot probe which measured TG- waves in a helicon discharge [2]. Additionally, this wave is more readily observed at lower magnetic fields (< 100 Gauss), which were shown to increase the radial wavelength and may possibly ease the measurement difficulty. However, at lower magnetic fields, the peak densities ($\sim 10^{17} \text{ m}^{-3}$) are significantly lower and the benefits of this operational regime are indeterminate. Though, if a useful application is found, further measurement of TG-waves may be warranted.

6.2 On Diagnostics

Identification of helicon waves was demonstrated through a few different methods. Utilization of the matching network power spectrum demonstrated wave propagation when a sharp drop in the reflected power was observed. However, this effect was also explained by the matching networks dynamic capacitive limitation, i.e., the variable range of the vacuum capacitors within the matching network were not large enough for the plasma impedance range to equate a 50Ω resistive load. A future project may desire to report the capacitance values of the matching network in a very detailed fashion over a wide power and magnetic field operating spectrum. This should readily demonstrate the validity of the matching network's limitations.

Measurements with magnetic field probes in a high frequency plasma environment have been shown to have some difficulty in implementation. Internal measurements where spatial characterization of the plasma parameters was desired faced multiple challenges. First, for both b-dot probes and RF compensated Langmuir probes, the size of the probe with respect to the plasma volume demonstrated probe interference near borderline helicon wave conditions. In the case of b-dot probes, the nominal probe size to non-intrusively measure the plasma wave fields had to be balanced against the desire for high probe sensitivity which increased with the size of the probe. This work demonstrated that the most time efficient and accurate method to characterize the entire probe system (including line-lengths, cable types, and coupling transformers) was to utilize an impedance analyzer where the entire frequency range of interest was assessed; 40 Hz – 110 MHz in this report. Post processing of data required performing a Fourier frequency analysis to compensate for spurious signals to remove unwanted harmonics of the driving frequency. If this had not been given thorough attention, large errors in quantifying the wave amplitudes would have been present.

The impedance analyzer used to characterize the b-dot probes also served to rapidly identify hundreds of impedance curves for the blocking filters used in Langmuir probe compensation. Because the plasma sheath impedance can be on the order of a few $k\Omega$'s, the blocking filters required impedances much larger. This requirement is due to the AC signal being much larger than the DC component of interest. Through utilizing large AC impedance at the fundamental and second harmonic of the driving frequency, the

blocking filters acted as voltage dividers so that the AC current being collected was minimized. However, the capacitance from the cable lengths from the probe tip to the data acquisition (oscilloscope in this work) caused the large filter impedance to drop by nearly an order of magnitude. While still much greater than the plasma sheath impedance, shorter line lengths (or possibly additional filters) in future work would further minimize the AC contribution. This effect was most evident when calculating the electron temperature at lower densities; or lower DC current collection.

As a final note on the Langmuir probe analysis, the voltage sweeps performed were for ± 100 Volts and it may prove worthy to sweep to a slightly higher voltage in the electron saturation region. This could not be reliably performed in this work since the voltage supply was ± 1000 Volts but saturated at 40 mA. This is still quite a large current in the electron saturation region, however, either due to inadequate compensation at these large voltages or probe size being too large (collecting more current) the voltage supply became current limited premature of + 100 Volts.

6.3 On Three Dimensional Results

This work provided the first report on three dimensional imaging of a helicon wave. The contour plots over a full wavelength for three separate antenna lengths provided an insightful visualization to helicon waves. They introduced a radial component (that decreased axially) which had not been considered before. This aided in explaining why previous reports on helicon wavelength may have been underestimated. It also explains why two dimensional measurements may disagree with theoretical predictions more than

anticipated. The contour plots also showed agreement with theoretical profiles when the b_r and b_θ profiles were measured. Scanning of this measurement took place in the $y = 0$ plane (or vertical centerline of the tube). To fully image all components of the wave, b_r , b_θ , and b_z , three dimensional scans of the ' r ' and ' θ ' components should be taken; although little additional information may be revealed (unless one is investigating the radial TG- wave near the antenna). Consequently, this was one reason this was not performed in this work, even though the scanning hardware allowed for $-x$, $-y$, $-z$ scans. Radial and poloidal scans would be more difficult unless modifications were made. However, full $-x$ and $-y$ scans could be complete and the converted to the cylindrical counterparts, $-r$ and $-\theta$, through a coordinate transformation.

It is also an unfortunate outcome that performing the three dimensional sweeps was so time intensive. The only way this process might be expedited is to include additional probes that can acquire data simultaneously. However, this may introduce further intrusion to the magnetic environment and obscure the results.

6.4 On Downstream Density Peak and Model

Axial measurements of the plasma density revealed an unexpected feature; a peak downstream from the ionizing source (antenna). The peak was first observed when the 14.2 cm antenna length was tested. To investigate whether the peak was due to the external magnetic field, it was believed shortening and moving the antenna (11.2 cm length) would cause the peak to shift axial locations. If the peak had not shifted axial locations, then the cause of the downstream peak would have to be related to the

externally applied magnetic field. Fortunately, the peak shifted axial locations forcing the possibility that the rise in density was a consequence of increased wave absorption by the plasma. However, since an increase in electron temperature downstream was not observed and due to the multiple reports estimating wave absorption to be $> 70\%$ in the near field region of the antenna, an alternative explanation was sought. This work demonstrated a simple explanation for the rise in downstream density that is caused by a decaying electron temperature as a result of collisional processes. In both cases however, performing a simple energy balance where particles escape a cylindrical volume through radial and axial end losses underestimated the expected density by an order of magnitude. To this point, the density calculation had not considered any applied magnetic field. This prompted the introduction of particle confinement factors to account for the magnetic field. Because the magnetic field was uniform over the regions where the density peaks were observed, a lumped correction factor could be applied uniformly over the axial region where the area for particle loss was perpendicular to the applied field.

The objective of performing the energy balance was to formulate an explanation for the downstream density peak. While the model provided this result, the basis for the particle confinement factors has yet to be defined. Future work should refine this model to explain the confinement factors, which are needed because of the applied magnetic field. These factors are most likely dependent on a radially diffusion coefficient; such as Bohm diffusion in a magnetic field.

Additionally, due to the difficulty in quantifying the electron temperature in the axial direction (which is a basis for the density model), measurement of the temperature should be verified by a separate diagnostic. The Langmuir probe's compensation at lower densities should also be enhanced to provide more accurate values at these operating conditions.

6.5 On Possible Use as an Electric Propulsion Device

The ionization cost analysis was determined in part to assess the viability of using a helicon source in an electric propulsion capacity. The $\sim 75 \text{ eV} - 85 \text{ eV}$ required to produce each electron – ion pair is not as vast an improvement as would have been desired when compared to state of the art electric propulsion Hall thrusters where the ionization cost ranges $\sim 80 \text{ eV} - 90 \text{ eV}$. However, this particular device was not specifically designed to optimize the ionization cost.

With regards to utilizing helicons as a stand-alone propulsion device, some groups have reported claims of a double layer formation in which ions are axially accelerated out of the device. However, the claim has not been independently confirmed or shown to be inherent to helicon generated plasma. This could in part be due to double layer formation resulting from discontinuous changes in geometry. Since nearly all helicon work to date has consisted of a discharge chamber connected to a larger diameter diffusion chamber, the formation of a double layer in these setups could be the result of sudden changes in geometry, which would cause a discontinuous change in potential structure. Additionally, the formation of a helicon double layer had been observed at relatively low

pressures (< 1 mTorr) where the mean free path for collisions approaches device lengths. Results presented here showed no evidence of quantifiable helicon wave formation at pressures below 2 mTorr; the lower pressures considered at 500 Watts could not produce a high enough density to allow wave propagation.

Utilizing helicon waves as a source for a secondary acceleration stage may prove more attractive in terms of overall efficiency if the ionization cost can be further lowered. This could be achieved by further increasing the density at a given power by utilizing a stronger static magnetic field. Also, using helicon waves solely as an ionization source would remove the complexity of plasma detachment from a magnetic field. Regardless, helicons do offer attractive features for propulsive devices such as: high density formation, electrode-less operation, and the ability to operate on nearly any gaseous propellant.

6.6 Final Summary

This work has provided some valuable insight into the significance of the helicon wavelength. Three dimensional imaging of the waves illustrated the necessary components toward reevaluating the full helix definition of wavelength; as opposed to two dimensional measurements. Propagating waves into a dense ($\sim 10^{19} \text{ m}^{-3}$) plasma medium demonstrated the wavelength decreases by nearly two orders of magnitude with respect to the free space wavelength; $f = 13.56 \text{ MHz} \rightarrow \sim 22 \text{ meters}$. The antenna length did not appear to play a significant role on the length of helicon waves. The wavelength of helicons was shown (both theoretically and experimentally) to be determined by the

radial density profile of the medium as well as by the constancy of this radial profile in the axial direction. As a consideration for future work, determining the optimal antenna length would be valuable. This aspect was demonstrated by neither the longest (24.6 cm) nor the shortest (11.2 cm) length antennae generating the greatest densities. The 14.2 cm antenna created the most dense medium for helicon waves and was also shown to propagate the shortest axial helicon wave. This “optimization” effect is most likely due to a coupling efficiency between antenna and plasma and could also be related to the geometrical radius of the cylindrical discharge tube.

6.7 References

- [1] I. D. Sudit, and F. F. Chen, “Discharge equilibrium of a helicon plasma,” *Plasma Sources Science and Technology*, vol. 5, pp. 11, 1995.
- [2] D. D. Blackwell, T. G. Madziwa, D. Arnush *et al.*, “Evidence for Trivelpiece-Gould Modes in a Helicon Discharge,” *Physical Review Letters*, vol. 88, no. 14, pp. 4, 2002.

APPENDIX A: PLASMA WAVES MODEL

This Appendix will follow the development of the cold plasma dispersion relation (CPDR) to obtain the plasma dielectric tensor. Due to the complex mathematical nature of plasma waves, the best description of the results is given schematically by a Clemmow-Mullaly-Allis (CMA) diagram. The derivation here follows that found in Swanson [1] and Stix [2] and the important features will be reproduced.

A.1 Derivation of the CPDR

The derivation of the CPDR begins with the equation of motion for a single species ‘ j ’ in an electromagnetic field:

$$m_j \frac{dv_j}{dt} = q_j (E + v_j \times B) \quad (\text{A.1})$$

with Maxwell’s equations

$$\nabla \times E = -\frac{\partial B}{\partial t} \quad (\text{A.2})$$

$$\nabla \times B = \mu_0 \left(j + \epsilon_0 \frac{\partial E}{\partial t} \right) \quad (\text{A.3})$$

here, the expression for the total plasma current is given by

$$j = \sum_j n_j q_j v_j \quad (\text{A.4})$$

The plasma is presumed to be uniform and homogeneous in space and time and so solutions will take the form,

$$\begin{aligned} E &= E_1 e^{i(k \cdot r - \omega t)} \\ B &= B_0 + b_1 e^{i(k \cdot r - \omega t)} \\ v &= v_1 e^{i(k \cdot r - \omega t)} \end{aligned} \quad (\text{A.5})$$

Here, B_0 is the applied static field in the z-direction and is assumed $|b_1| \ll |B_0|$. With the Fourier transforms according to

$$\begin{aligned}\nabla &\rightarrow ik \\ \frac{\partial}{\partial t} &\rightarrow -i\omega\end{aligned}$$

the equation of motion now becomes,

$$-i\omega m_j v_{1j} = q_j (E_1 + v_{1j} \times B_0) \quad (\text{A.6})$$

Solving for the velocity

$$\begin{aligned}v_{xj} &= \frac{iq_j}{m_j(\omega^2 - \omega_{cj}^2)} (\omega E_x + i\varepsilon_j \omega_{cj} E_y) \\ v_{yj} &= \frac{iq_j}{m_j(\omega^2 - \omega_{cj}^2)} (-i\varepsilon_j \omega_{cj} E_x + \omega E_y) \\ v_{zj} &= \frac{iq_j}{m_j \omega} E_z\end{aligned} \quad (\text{A.7})$$

Here, $\varepsilon_j = q_j / |q_j|$ is the sign of the charge for the species and ω_{cj} is the cyclotron frequency given by,

$$\omega_{cj} = \frac{|q_j| B_0}{m_j} \quad (\text{A.8})$$

If rotating coordinates are now defined as,

$$\begin{aligned}v_{\pm} &= v_x \pm v_y \\ E_{\pm} &= E_x \pm iE_y\end{aligned} \quad (\text{A.9})$$

along with the definition of the plasma frequency,

$$\omega_{pj}^2 = \frac{n_j q_j^2}{m_j \varepsilon_0} \quad (\text{A.10})$$

Then the current density can be written,

$$\begin{aligned}
j_{\pm} &= i\varepsilon_0 \sum_j \frac{\omega_{pj}^2}{(\omega \mp \varepsilon_j \omega_{cj})} E_{\pm} \\
j_z &= i\varepsilon_0 \sum_j \frac{\omega_{pj}^2}{\omega} E_z
\end{aligned} \tag{A.11}$$

Now define the electrical current density by,

$$j = \sigma \cdot E \tag{A.12}$$

and the electric displacement vector by,

$$D = \varepsilon_0 \mathbf{K} E \tag{A.13}$$

where the dielectric tensor \mathbf{K} is given by,

$$\mathbf{K} = 1 - \frac{\sigma}{i\omega\varepsilon_0} \tag{A.14}$$

Finally, to obtain the equivalent dielectric tensor \mathbf{K} , the plasma current (A.15) and the displacement current (A.16) must be combined such that

$$j - i\omega\varepsilon_0 E \equiv -i\omega\varepsilon_0 \mathbf{K} E \tag{A.17}$$

where \mathbf{K} is now given by,

$$\mathbf{K} = \begin{pmatrix} S & -iD & 0 \\ iD & S & 0 \\ 0 & 0 & P \end{pmatrix} = \begin{pmatrix} K_1 & K_2 & 0 \\ -K_2 & K_1 & 0 \\ 0 & 0 & K_3 \end{pmatrix} \tag{A.18}$$

and each element is defined as,

$$K_1 \equiv S \equiv \frac{1}{2}(R + L) = 1 - \sum_j \frac{\omega_{pj}^2}{\omega^2 - \omega_{cj}^2} \tag{A.19}$$

$$iK_2 \equiv D \equiv \frac{1}{2}(R - L) = \sum_j \frac{\varepsilon_j \omega_{cj} \omega_{pj}}{\omega(\omega^2 - \omega_{cj}^2)} \tag{A.20}$$

$$K_3 \equiv P = 1 - \sum_j \frac{\omega_{pj}^2}{\omega^2} \tag{A.21}$$

$$K_1 + iK_2 \equiv R \equiv S + D = 1 - \sum_j \frac{\omega_{pj}^2}{\omega(\omega + \varepsilon_j \omega_{cj})} \quad (\text{A.22})$$

$$K_1 - iK_2 \equiv L \equiv S - D = 1 - \sum_j \frac{\omega_{pj}^2}{\omega(\omega - \varepsilon_j \omega_{cj})} \quad (\text{A.23})$$

Here, R, L, S, D, and P refer to the notation that describes right, left, sum, difference, and plasma wave terms in reference to the dielectric tensor elements.

A.2 The CMA Diagram

At this point, it is of interest to analyze the different types of waves that can propagate within plasma dielectric. To do this, boundaries can be constructed that represent the cutoffs and resonances of each wave by setting R, L, and S equal to zero and infinity, resulting in i.e.,

$$R \rightarrow \infty \text{ (electron cyclotron resonance)}$$

$$L \rightarrow \infty \text{ (ion cyclotron resonance)}$$

$$S \rightarrow 0 \text{ (upper \& lower hybrid frequencies)}$$

and then graphing the change in $\frac{\omega_{ce}}{\omega}$ with respect to $\frac{\omega_p^2}{\omega^2}$ where ω_{ce} is the electron

cyclotron frequency, ω_p is the electron plasma frequency, and ω is the driving frequency.

When considering the cutoffs and resonances for a two species plasma, namely ions and electrons, we must construct the diagram using equations A.17-A.21 with the substitution for the ion mass as $m_i = 1836 m_e$. This redefines the ion plasma and cyclotron frequencies such that

$$\omega_{pi}^2 = \frac{q^2 n_e}{\epsilon_0 m_i} = \frac{q^2 n_e}{1836 \epsilon_0 m_e} = \frac{\omega_{pe}^2}{m_i / m_e} \quad (\text{A.24})$$

and

$$\omega_{ci} = \frac{qB_0}{m_i} = \frac{qB_0}{1836 m_e} = \frac{\omega_{ce}}{m_i / m_e} \quad (\text{A.25})$$

Solving A.17-A.21 for the cutoffs and resonances, we obtain the CMA diagram. This is shown in Figure A.1 where the mass ratio is taken to be $m_i / m_e = 5$ to illustrate the cutoffs and resonances.

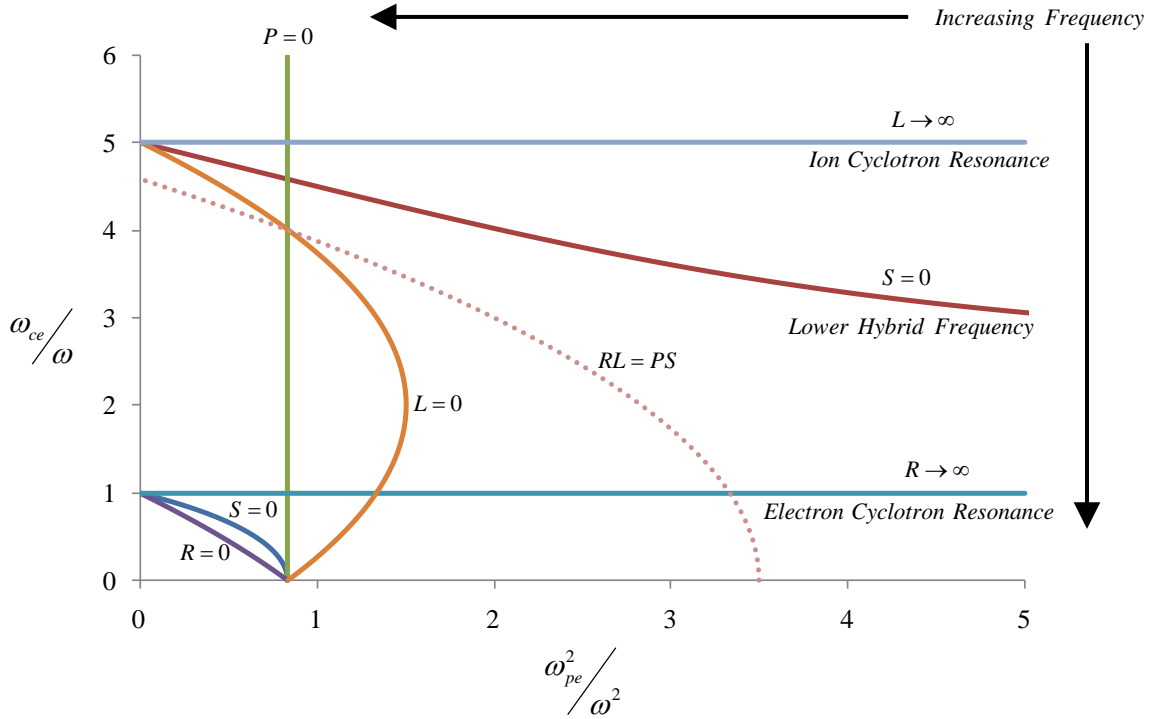


Figure A.1. CMA diagram with $m_i / m_e = 5$.

At this point, to better understand the influence the mass ratio has, we can consider a few different gases such as Helium, Argon, and Xenon driven at $f = 13.56$ MHz. The CMA diagram can then be transformed into a n vs. B_0 graph as shown in Figure A.2

where the location of the various ion and electron resonances are given in terms of magnetic field. It is no surprise that the ion cyclotron resonant B-field increases with increased mass, however, the point of interest for helicon waves (usually defined between the lower hybrid and electron cyclotron frequencies) is that the ' B_0 -space' decreases for lighter gases, i.e., helicon waves for Helium should range $\sim 5 \text{ Gauss} < B_0 < \sim 295 \text{ Gauss}$.

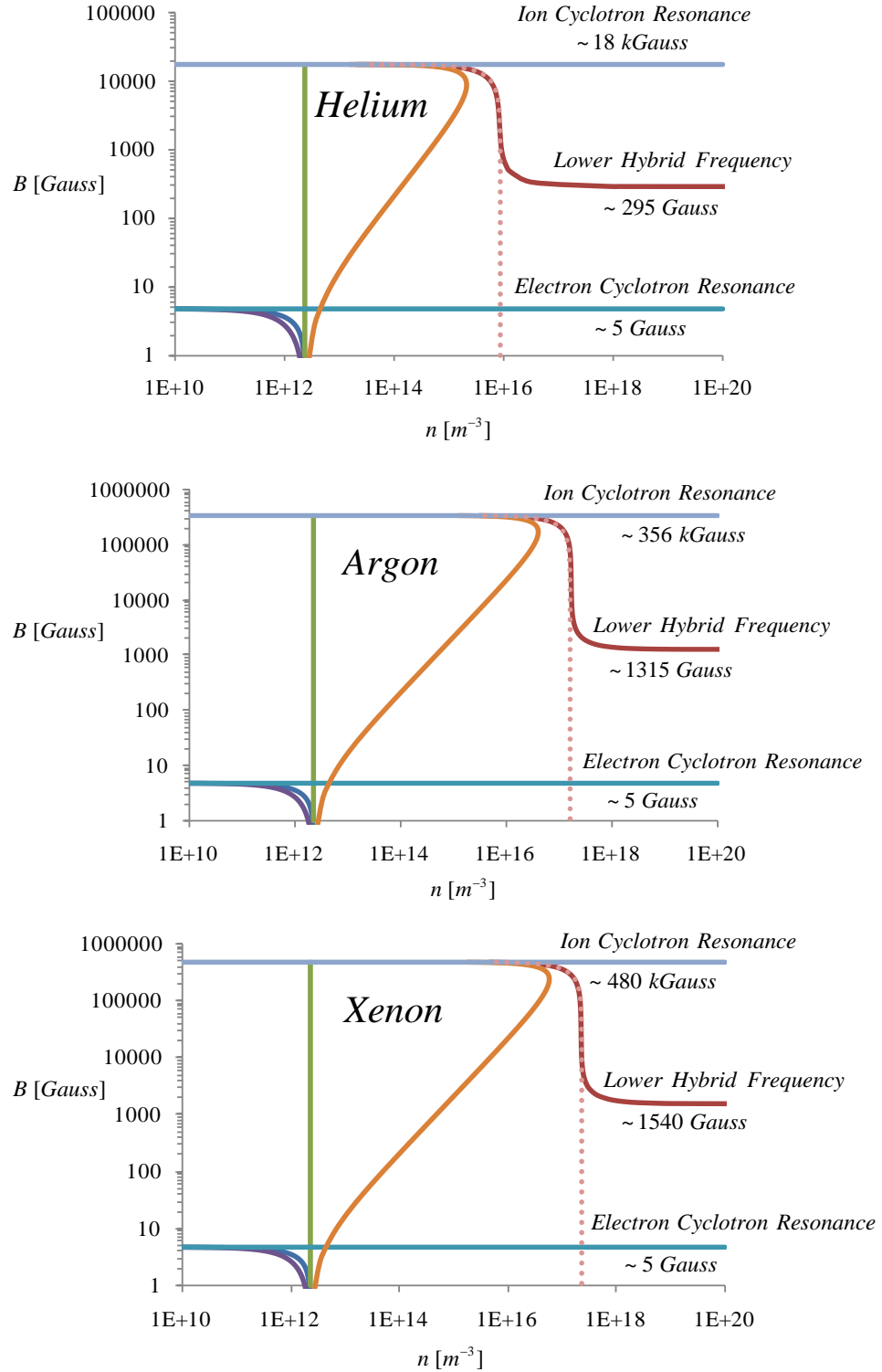


Figure A.2. Density vs. Magnetic field graphs for Helium, Argon, and Xenon driven at 13.56 MHz.

A.3 References

- [1] D. G. Swanson, *Plasma Waves*, Second ed.: IOP Publishing, 2003.
- [2] T. H. Stix, *The Theory of Plasma Waves*: McGraw-Hill, 1962.

APPENDIX B: CODE FOR NON-UNIFORM DENSITY WAVE FIELDS

This Appendix provides the code implemented in MATHEMATICA for solving the non-uniform radial density magnetic field profiles described in Chapter 2. The primary outputs are graphs and data tables for the b_z and b_z' profiles as well as the wavenumbers and wavelengths that satisfy the boundary conditions for each particular profile.

B.1 MATHEMATICA Code

```
Clear[c,ε,freq,ω,μ,λ1,λ2,λ3,λ4,λ5,λ6,k1,k2,k3,k4,k5,k6,k0,a,B0,n0,e,m,γ1,γ2,γ3,γ4,γ5,γ6,w1,w2,w3,w4,w5,w6,r,α1,α2,α3,α4,α5,α6,β1,β2,β3,β4,β5,β6,s1,s2,s3,s4,s5,s6,f1,f2,f3,f4,f5,f6,g1,g2,g3,g4,g5,g6,n1,n2,n3,n4,n5,n6,s11,s22,s33,s44,s55,s66]
```

(* Clears the variables used in the program *)

```
c=299792458;  
ε=8.85418782*10^-12;  
freq=13.56*10^6;  
ω=2 π freq;  
μ=1.25663706*10^-6;
```

(* Defines constants *)

```
k1=23.710;  
k2=23.3013155;  
k3=22.38015;  
k4=21.09145;  
k5=19.60375;  
k6=16.9723;
```

(* Values for wave numbers that satisfy the boundary condition *)

```
λ1=2 π / k1  
λ2=2 π / k2  
λ3=2 π / k3  
λ4=2 π / k4  
λ5=2 π / k5  
λ6=2 π / k6
```

(* Calculates the wavelength for each profile *)

```
k0=ω/c;  
a=0.030;  
B0=0.09;  
e=1.60217646*10^-19;  
m=1;
```

(* Some more constants specific to the experiment *)

$$\begin{aligned}\gamma_1 &= 1 - (k_0/k_1)^2; \\ \gamma_2 &= 1 - (k_0/k_2)^2; \\ \gamma_3 &= 1 - (k_0/k_3)^2; \\ \gamma_4 &= 1 - (k_0/k_4)^2; \\ \gamma_5 &= 1 - (k_0/k_5)^2; \\ \gamma_6 &= 1 - (k_0/k_6)^2;\end{aligned}$$

(* Defines γ ; term that accounts for displacement current *)

$$n_0 = 1.0 \cdot 10^{19};$$

(* Initial peak centerline density value *)

$$\begin{aligned}w_1 &= 0.005; \\ w_2 &= 0.010; \\ w_3 &= 0.015; \\ w_4 &= 0.021; \\ w_5 &= 0.030; \\ w_6 &= 1;\end{aligned}$$

(* Exponents for Gaussian profiles *)

$$\begin{aligned}n_1[r_] &:= n_0 \exp(-(r/w_1)^2) \\ n_2[r_] &:= n_0 \exp(-(r/w_2)^2) \\ n_3[r_] &:= n_0 \exp(-(r/w_3)^2) \\ n_4[r_] &:= n_0 \exp(-(r/w_4)^2) \\ n_5[r_] &:= n_0 \exp(-(r/w_5)^2) \\ n_6[r_] &:= n_0 \exp(-(r/w_6)^2)\end{aligned}$$

(* Radial density profiles *)

$$\begin{aligned}\alpha_1[r_] &:= \omega/k_1 (e^{\mu} n_1[r]) / B_0 \\ \alpha_2[r_] &:= \omega/k_2 (e^{\mu} n_2[r]) / B_0 \\ \alpha_3[r_] &:= \omega/k_3 (e^{\mu} n_3[r]) / B_0 \\ \alpha_4[r_] &:= \omega/k_4 (e^{\mu} n_4[r]) / B_0 \\ \alpha_5[r_] &:= \omega/k_5 (e^{\mu} n_5[r]) / B_0 \\ \alpha_6[r_] &:= \omega/k_6 (e^{\mu} n_6[r]) / B_0\end{aligned}$$

$$\begin{aligned}\beta_1[r_] &:= \alpha_1[r]^2 - k_1^2 \gamma_1^2 \\ \beta_2[r_] &:= \alpha_2[r]^2 - k_2^2 \gamma_2^2 \\ \beta_3[r_] &:= \alpha_3[r]^2 - k_3^2 \gamma_3^2 \\ \beta_4[r_] &:= \alpha_4[r]^2 - k_4^2 \gamma_4^2 \\ \beta_5[r_] &:= \alpha_5[r]^2 - k_5^2 \gamma_5^2 \\ \beta_6[r_] &:= \alpha_6[r]^2 - k_6^2 \gamma_6^2\end{aligned}$$

(* Defining wavenumbers *)

$$\begin{aligned}f_1[r_] &:= 1/r - (2 \alpha_1[r] \alpha_1'[r]) / \beta_1[r] \\ f_2[r_] &:= 1/r - (2 \alpha_2[r] \alpha_2'[r]) / \beta_2[r] \\ f_3[r_] &:= 1/r - (2 \alpha_3[r] \alpha_3'[r]) / \beta_3[r] \\ f_4[r_] &:= 1/r - (2 \alpha_4[r] \alpha_4'[r]) / \beta_4[r] \\ f_5[r_] &:= 1/r - (2 \alpha_5[r] \alpha_5'[r]) / \beta_5[r] \\ f_6[r_] &:= 1/r - (2 \alpha_6[r] \alpha_6'[r]) / \beta_6[r]\end{aligned}$$

```

g1[r_]:=β1[r]/γ1-m^2/r^2-m/k1 α1'[r]/(γ1 r) (1+(2 k1^2 γ1^2)/β1[r])
g2[r_]:=β2[r]/γ2-m^2/r^2-m/k2 α2'[r]/(γ2 r) (1+(2 k2^2 γ2^2)/β2[r])
g3[r_]:=β3[r]/γ3-m^2/r^2-m/k3 α3'[r]/(γ3 r) (1+(2 k3^2 γ3^2)/β3[r])
g4[r_]:=β4[r]/γ4-m^2/r^2-m/k4 α4'[r]/(γ4 r) (1+(2 k4^2 γ4^2)/β4[r])
g5[r_]:=β5[r]/γ5-m^2/r^2-m/k5 α5'[r]/(γ5 r) (1+(2 k5^2 γ5^2)/β5[r])
g6[r_]:=β6[r]/γ6-m^2/r^2-m/k6 α6'[r]/(γ6 r) (1+(2 k6^2 γ6^2)/β6[r])

```

(* Defining f(r) and g(r) from defined in Chapter 2 *)

```

Solve[α1[rs1]==γ1 k1,rs1];
Solve[α2[rs2]==γ2 k2,rs2];
Solve[α3[rs3]==γ3 k3,rs3];
Solve[α4[rs4]==γ4 k4,rs4];
Solve[α5[rs5]==γ5 k5,rs5];
Solve[α6[rs6]==γ6 k6,rs6];

```

(* Solves for location of singularity *)

```

s1=NDSolve[{Bz1''[r]+f1[r]Bz1'[r]+ g1[r]Bz1[r]==0,m α1[a] Bz1[a]+a k1 γ1
Bz1'[a]==0,Bz1'[.0005]==1},Bz1[r],{r,0.0001,a}]
s11=NDSolve[{Bz1''[r]+f1[r]Bz1'[r]+ g1[r]Bz1[r]==0,m α1[a] Bz1[a]+a k1 γ1
Bz1'[a]==0,Bz1'[.0005]==1},Bz1[r],{r,0.0001,a}]

```

```

s2=NDSolve[{Bz2''[r]+f2[r]Bz2'[r]+ g2[r]Bz2[r]==0,m α2[a] Bz2[a]+a k2 γ2
Bz2'[a]==0,Bz2'[.0001]==1},Bz2[r],{r,0.0001,a}]
s22=NDSolve[{Bz2''[r]+f2[r]Bz2'[r]+ g2[r]Bz2[r]==0,m α2[a] Bz2[a]+a k2 γ2
Bz2'[a]==0,Bz2'[.0001]==1},Bz2[r],{r,0.0001,a}]

```

```

s3=NDSolve[{Bz3''[r]+f3[r]Bz3'[r]+ g3[r]Bz3[r]==0,m α3[a] Bz3[a]+a k3 γ3
Bz3'[a]==0,Bz3'[.0001]==1},Bz3[r],{r,0.0001,a}]
s33=NDSolve[{Bz3''[r]+f3[r]Bz3'[r]+ g3[r]Bz3[r]==0,m α3[a] Bz3[a]+a k3 γ3
Bz3'[a]==0,Bz3'[.0001]==1},Bz3[r],{r,0.0001,a}]

```

```

s4=NDSolve[{Bz4''[r]+f4[r]Bz4'[r]+ g4[r]Bz4[r]==0,m α4[a] Bz4[a]+a k4 γ4
Bz4'[a]==0,Bz4'[.0001]==1},Bz4[r],{r,0.0001,a}]
s44=NDSolve[{Bz4''[r]+f4[r]Bz4'[r]+ g4[r]Bz4[r]==0,m α4[a] Bz4[a]+a k4 γ4
Bz4'[a]==0,Bz4'[.0001]==1},Bz4[r],{r,0.0001,a}]

```

```

s5=NDSolve[{Bz5''[r]+f5[r]Bz5'[r]+ g5[r]Bz5[r]==0,m α5[a] Bz5[a]+a k5 γ5
Bz5'[a]==0,Bz5'[.0001]==1},Bz5[r],{r,0.0001,a}]
s55=NDSolve[{Bz5''[r]+f5[r]Bz5'[r]+ g5[r]Bz5[r]==0,m α5[a] Bz5[a]+a k5 γ5
Bz5'[a]==0,Bz5'[.0001]==1},Bz5[r],{r,0.0001,a}]

```

```

s6=NDSolve[{Bz6''[r]+f6[r]Bz6'[r]+ g6[r]Bz6[r]==0,m α6[a] Bz6[a]+a k6 γ6
Bz6'[a]==0,Bz6'[.0001]==1},Bz6[r],{r,0.0001,a}]
s66=NDSolve[{Bz6''[r]+f6[r]Bz6'[r]+ g6[r]Bz6[r]==0,m α6[a] Bz6[a]+a k6 γ6
Bz6'[a]==0,Bz6'[.0001]==1},Bz6[r],{r,0.0001,a}]

```

(* Solves differential equations for each profile and stores the output array in “sx” and “sxx”

```

Plot[{Bz1[r]/.s1,Bz2[r]/.s2,Bz3[r]/.s3,Bz4[r]/.s4,Bz5[r]/.s5,Bz6[r]/.s6},{r,0.0005,a},PlotRange->{{0,a},{-
.0002,.0015}}, AxesLabel->{Radius,Bz}]

```

```
Plot[{Bz1'[r]/.s11,Bz2'[r]/.s22,Bz3'[r]/.s33,Bz4'[r]/.s44,Bz5'[r]/.s55,Bz6'[r]/.s66},{r,0.0005,a},PlotRange→
{{0,a},{-.0002,.0015}}, AxesLabel→ {Radius,Bz'}]
```

```
Plot[{n1[r],n2[r],n3[r],n4[r],n5[r],n6[r]},{r,0,a},AxesLabel→{Radius,Density},PlotRange→{{0,a},{0,n0}}]
Plot[{n'[r]},{r,0,a},AxesLabel→{Radius, Density Prime}];
```

```
Plot[{ $\alpha$ [r]},{r,0,a},AxesLabel→{Radius,Alpha}];
Plot[{ $\alpha'$ [r]},{r,0,a},AxesLabel→{Radius,Alpha Prime}];
```

```
Plot[{ $\beta$ [r]},{r,0,a},AxesLabel→{Radius,Beta}];
```

```
Plot[{f[r]},{r,0,a},AxesLabel→{Radius,f}];
Plot[{g[r]},{r,0,a},AxesLabel→{Radius,g}];
```

(* Plots of radially varying quantities *)

```
Export["Bz1.csv",Table[Bz1[r]/.s1,{r,0.0005,a,.00005}]];
Export["Bz2.csv",Table[Bz2[r]/.s2,{r,0.0005,a,.00005}]];
Export["Bz3.csv",Table[Bz3[r]/.s3,{r,0.0005,a,.00005}]];
Export["Bz4.csv",Table[Bz4[r]/.s4,{r,0.0005,a,.00005}]];
Export["Bz5.csv",Table[Bz5[r]/.s5,{r,0.0005,a,.00005}]];
Export["Bz6.csv",Table[Bz6[r]/.s6,{r,0.0005,a,.00005}]]];
```

```
Export["Bz11.csv",Table[Bz1'[r]/.s11,{r,0.0005,a,.00005}]];
Export["Bz22.csv",Table[Bz2'[r]/.s22,{r,0.0005,a,.00005}]];
Export["Bz33.csv",Table[Bz3'[r]/.s33,{r,0.0005,a,.00005}]];
Export["Bz44.csv",Table[Bz4'[r]/.s44,{r,0.0005,a,.00005}]];
Export["Bz55.csv",Table[Bz5'[r]/.s55,{r,0.0005,a,.00005}]];
Export["Bz66.csv",Table[Bz6'[r]/.s66,{r,0.0005,a,.00005}]]];
```

(* Exports bz and bz' to table arrays of numeric data *)

APPENDIX C: IGOR CODE FOR FFT OF B-DOT SIGNALS

The following code was implemented in IGOR for rapid analysis of b-dot probe signals.

The outputs are 5 graphs: 2 raw data signals, 2 FFT signals corresponding to the raw data, and 1 trace corresponding to the phase delay between both signals. The outputs are shown in Figure C.1 at the start of this Appendix with the code to follow. Additionally, the wave amplitudes for each probe obtained from the FFT analysis and the numerical value of the phase between the two signals is computed. The naming convention of the two different probes is: “Probe” and “Reference”. For this example trace, the output values are

Frequency of Maximum: 13.33 MHz
Probe FFT Value at the Max: 46606.2
Probe FFT Value at 13.56 MHz: 46072.3

Frequency of Maximum: 13.48 MHz
Reference FFT Value at the Max: 4980.33
Reference FFT Value at 13.56 MHz: 4972.04

Time Shift between Signals: -2.9408e-08

Probe Signal: 3.686 V
Reference Signal: 0.398 V
Phase in Degrees: -143.558 degrees

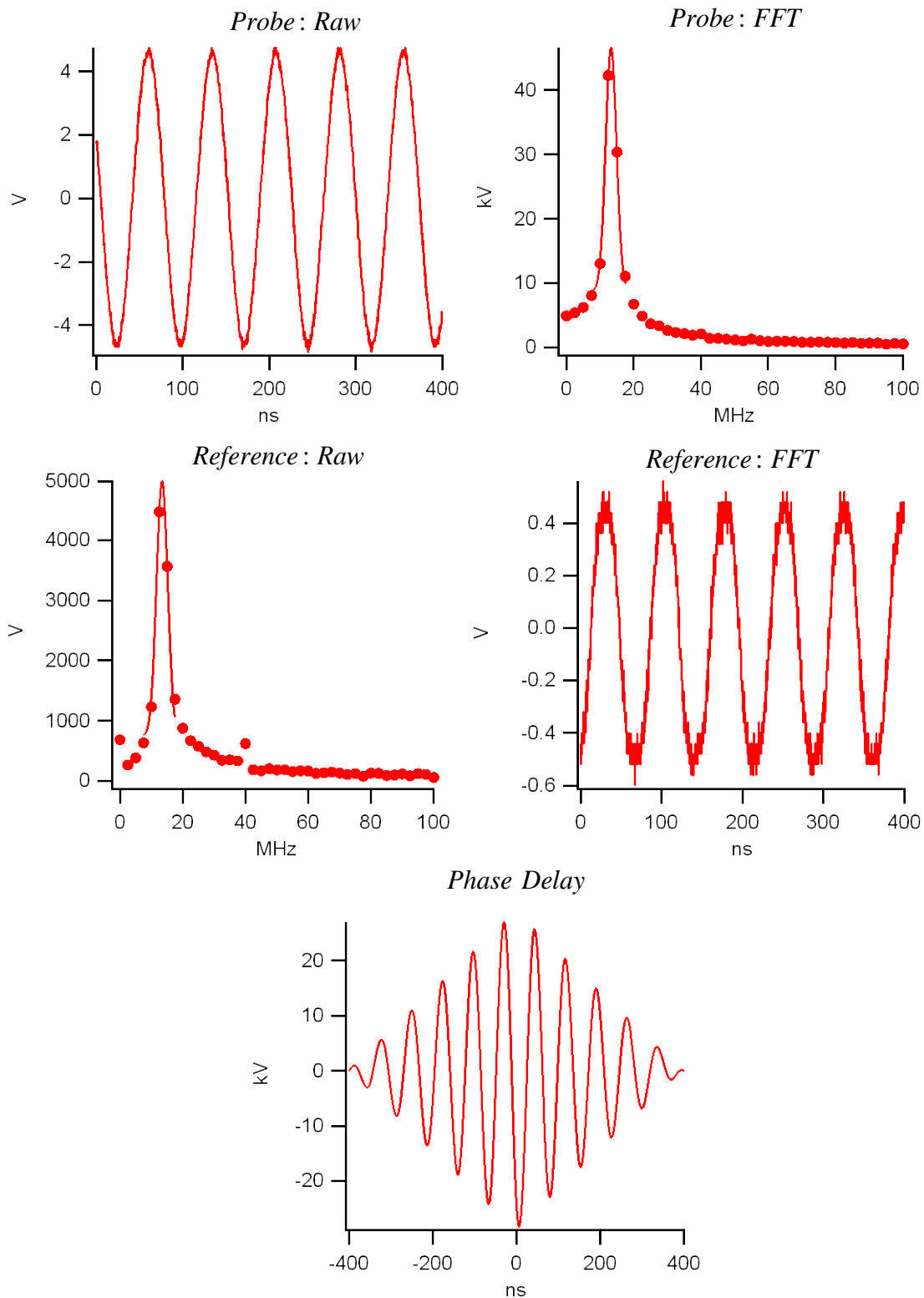


Figure C.1. Output from IGOR code of analysis of b-dot probe signals.

C.1 Code Written and Implemented in IGOR

```
#pragma rtGlobals=1
// Use modern global access method.

Function all()
    variable /G psig
    variable /G Phase
    variable /G rsig

    SetScale/P x 0,1.6e-11,"s", X_0_
    SetScale d 0,0,"V", X_0_
//Set Scale for Probe

    SetScale/P x 0,1.6e-11,"s", X_1_
    SetScale d 0,0,"V", X_1_
//Set Scale For Reference

    FFT/OUT=3/DEST=Probe_FFT X_0_
    FFT/OUT=3/DEST=Reference_FFT X_1_
//FFT of Probe and Reference

    Display /W=(16.5,39.5,411,248) X_0_
    Display /W=(15.75,268.25,410.25,476.75) X_1_
    Display /W=(416.25,41,810.75,249.5) Probe_FFT
    SetAxis bottom 0,1e+08
    ModifyGraph mode=2,lsz=5
    ShowInfo
    Display /W=(415.5,268.25,810,476.75) Reference_FFT
    SetAxis bottom 0, 1e+08
    ModifyGraph mode=2,lsz=5
    ShowInfo
//Graph Size and Locations and Format

//Activate Graph and Place Cursors on the Graph

    DoWindow /F Graph2
    ShowInfo /W=Graph2
    Cursor /P A,Probe_FFT, 3
    Cursor /P B,Probe_FFT, 7
    CurveFit /q gauss Probe_FFT[pcsr(A),pcsr(B)] /D

//Fit Reference FFT with Gaussian

    wave fit_Probe_FFT
```

```

//Statistics for Fit
wavestats /q fit_Probe_FFT

printf "Frequency of Maximum: %.2W1PHz\r", V_maxloc

//Output Max Value and Frequency

printf "Probe FFT Value at the Max: %g\r", V_max
cursor /P A ,fit_Probe_FFT, ( x2pnt(fit_Probe_FFT, 13.56e6))

//Output Value and 13.56 MHz

printf "Probe FFT Value at 13.56 MHz: %g\r", vcsr(A)

psig=vcsr(A)*2/numpts(X_0_)

DoWindow /F Graph3

//Activate Graph and Place Cursors on the Graph

ShowInfo /W=Graph3
Cursor /P A,Reference_FFT, 3
Cursor /P B,Reference_FFT, 7
CurveFit /q gauss Reference_FFT[pcsr(A),pcsr(B)] /D

//Fit Reference FFT with Gaussian

wave fit_Reference_FFT

//Statistics for Fit

wavestats /q fit_Reference_FFT

printf "Frequency of Maximum: %.2W1PHz\r", V_maxloc

//Output Max Value and Frequency

printf "Reference FFT Value at the Max: %g\r", V_max
cursor /P A ,fit_Reference_FFT, ( x2pnt(fit_Reference_FFT, 13.56e6))
printf "Reference FFT Value at 13.56 MHz: %g\r", vcsr(A )

//Output Value and 13.56 MHz

rsig=vcsr(A)*2/numpts(X_1_)

//Converting FFT Output to Volts

```

```

Duplicate/O X_1_,W_Correlation;DelayUpdate

//Using correlation to find phase between probe and reference signal

Correlate X_0_, W_Correlation;DelayUpdate
Display /W=(16.5,497,411,705.5) W_Correlation
wavestats /q W_Correlation
print "Time Shift between Signals:", V_maxloc
Phase=(360*V_maxloc/(1/13.56e6))

printf "\r"
printf "Probe Signal: %8.3f", psig

//Display Outputs to use in Excel

printf " V \r"
printf "Reference Signal: %8.3f", rsig
printf " V \r"
printf "Phase in Degrees: %8.3f", Phase
printf " degrees \r"
printf "\r"

DoWindow /H

KillWindow Graph4
KillWindow Graph3
KillWindow Graph2
KillWindow Graph1
KillWindow Graph0

//Closing Windows

KillWaves /A/Z; KillVariables /A/Z; KillStrings /A/Z

//Clearing Data

end

```

APPENDIX D: SAMPLE IV CHARACTERISTIC AND ANALYSIS

This Appendix will analyze a representative IV characteristic obtained in RF helicon plasma at 10 mTorr, 500 Watts, 900 Gauss, and 13.56 MHz. The analysis will follow the method by Ruzic in “Electric Probes for Low Temperature Plasmas” [1].

D.1 Constructing an IV Characteristic

Langmuir probe analysis of an IV characteristic begins by measuring the current to a probe tip while sweeping the voltage between the ion and electron saturation regions. The ion saturation region of an IV characteristic occurs when the probe tip is biased at such a high negative voltage with respect to the floating potential that electrons are repelled from the probe tip and only ions are collected. The corollary is the electron saturation region where the probe tip is biased at such a high positive voltage with respect to floating potential that only electrons are collected and nearly all ions are repelled. The floating potential referred to here is the voltage at which an equal current due to ions and electrons are collected at the probe tip and therefore the total current to the probe is zero. These regions are shown below in a representative IV characteristic.

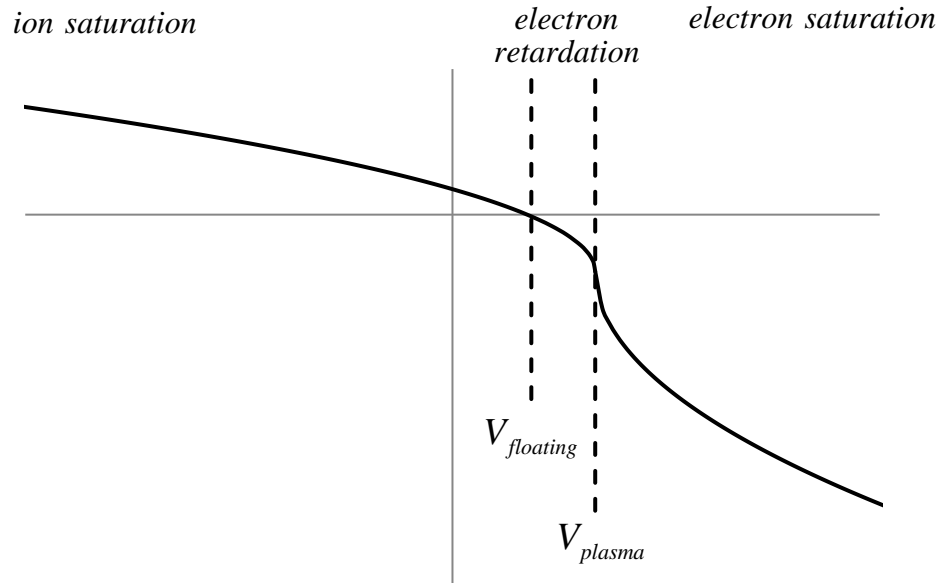


Figure D.1. Representative IV Characteristic with clearly defined regions and transitions.

Typical construction of an IV characteristic is accomplished through independent measurement of 1) the swept voltage to the probe tip and 2) the current drawn by the probe. These two traces are then recorded on an oscilloscope: voltage vs. time; current vs. time. The voltage and current vs. time traces are shown in Figure D.2.

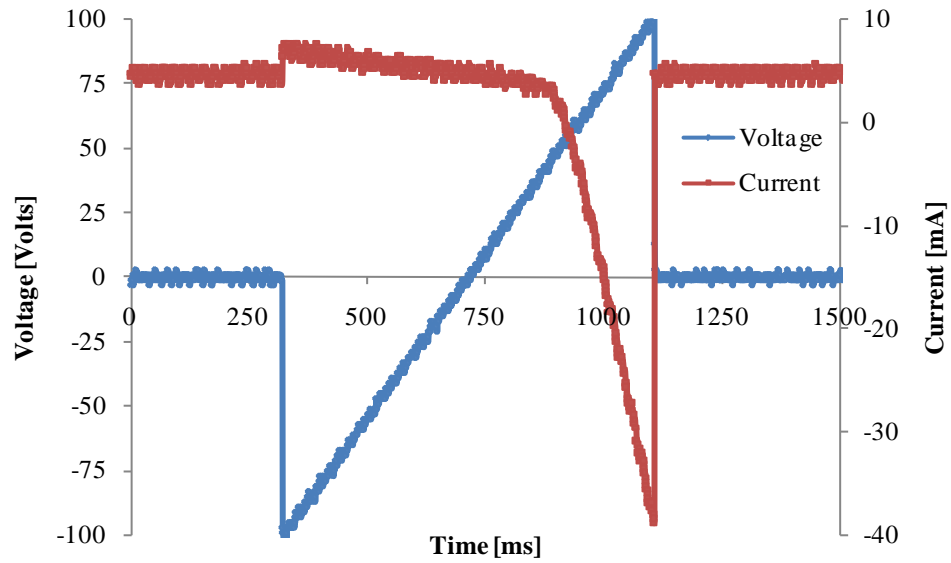


Figure D.2. Voltage vs. time; Current vs. time data used to construct raw IV Characteristic.

The raw voltage vs. time and current vs. time traces can then be used to construct the IV characteristic. However, because of residual RF noise present in the traces as seen as small oscillations in Figure D.2 and to make the 25,000 data point sample set more manageable for processing, a 1000 point cubic spline was fit to the data. Both the raw IV trace and the cubic spline fit are shown in Figure D.3.

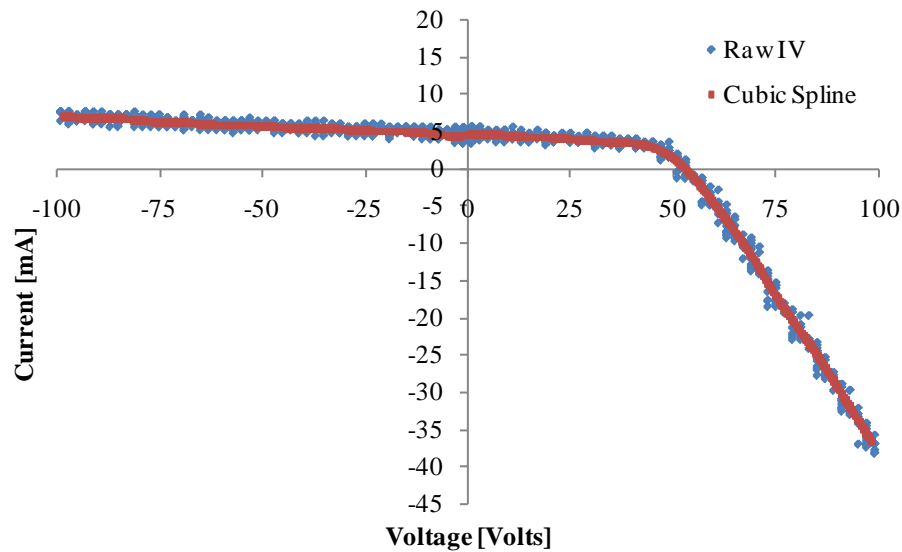


Figure D.3. Raw IV Characteristic with 1000 point cubic spline fit.

As a matter of preference, the current here at large negative potentials is positive because it is due to ion currents while the current is negative at large positive potentials resulting from electrons. The differences between the well defined characteristic of Figure D.1 and the measured IV characteristic Figure D.3 primarily lay in the electron saturation and electron retardation regions of the curve; sometimes referred to as the transition region. The remainder of this appendix will focus on obtaining the relevant quantities from the IV characteristic in order to accurately quantify the plasma.

D.2 Analysis of IV Characteristic

In order to begin the analysis, we first need to determine what regime the plasma is in, i.e., collisionless vs. collisional and thin vs. thick sheath. This determination is based on the radius of the measuring probe, the Debye length, and the mean free path for electron-neutral collisions. For the majority of the analysis performed in this work, the neutral pressure was 10 mTorr. Using the definition of the mean free path for electron-neutral collisions

$$\lambda_0 = \frac{1}{n_0 \sigma} \quad (\text{D.1})$$

where the collisional cross section σ is approximated as $5 \times 10^{-19} \text{ m}^2$, the mean free path reduces to

$$\lambda_0 = \frac{0.61}{p(\text{mTorr})} \text{m} \quad (\text{D.2})$$

and from $p = 10 \text{ mTorr}$, $\lambda_0 = 0.61 \text{ cm}$.

The cylindrical probe radius (tungsten wire) was $r_p = 0.01443$ cm and the last quantity to determine is the Debye length given as

$$\lambda_D = \sqrt{\frac{\epsilon_0 k T_e}{e^2 n_e}} \cong 7430 \sqrt{\frac{T_e [eV]}{n_e [m^{-3}]}} \quad (D.3)$$

However, to get an estimate for the Debye length and determine the plasma regime, we require an estimate for T_e and n_e . As a first approximation for helicon plasma where densities are approximately $10^{18} - 10^{19} \text{ m}^{-3}$ and assuming a temperature of 5 eV, the Debye length will be approximately, 0.0005 - 0.0016 cm and $4\lambda_D \rightarrow 0.0021 - 0.0066$ cm. Therefore, for the plasma in consideration here,

$$\begin{aligned} 4\lambda_D < r_p < \lambda_0 \\ 0.0066 \text{ cm} < 0.01443 \text{ cm} < 0.61 \text{ cm} \end{aligned} \quad (D.4)$$

the regime is collisionless thin sheath [1]. However, as long as we know that the sheath is collisionless, a thin sheath, thick sheath, or transitional between the two can be solved by the Lafromboise method. This is a solution to Poisson's equation based on the ratio of the probe radius to Debye length. In this case the ion current to the probe is given by [1]

$$n_e [m^{-3}] \cong 1.6 \times 10^{15} \sqrt{\frac{\mu [amu]}{T [eV]}} \frac{I [amps]}{A_{probe} [m^2] j_i^*} \quad (D.5)$$

where $\mu = 40$ for Argon, $A_{probe} = 2.72 \times 10^{-6} \text{ m}^2$, and j_i^* is a dimensionless quantity which accounts for ion acceleration in the pre-sheath and is graphically determined in Figure D.4.

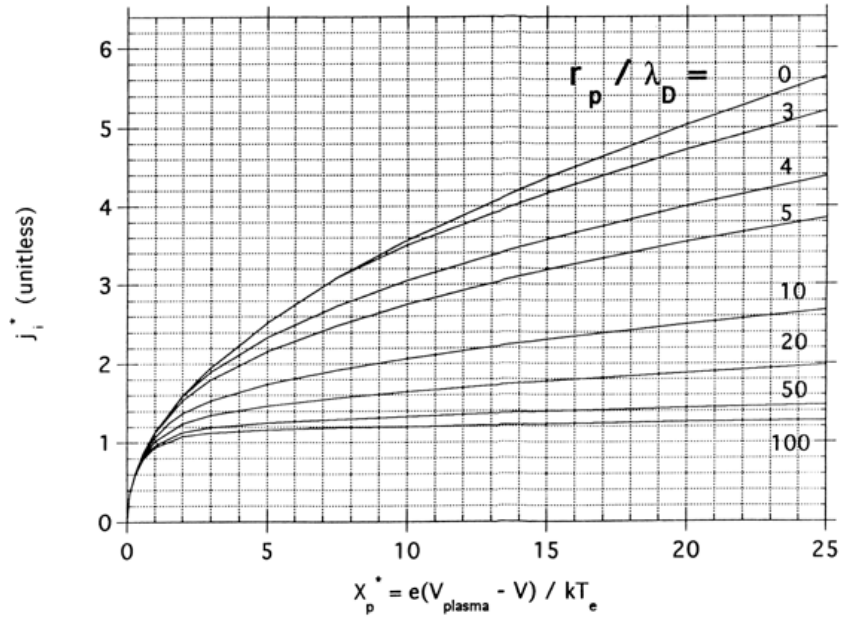


Figure D.4. Lafromboise plot for various values of probe radius to Debye length.
Plot taken from Ruzic (1994).

However, since j_i^* is a function of Debye length, which is a function of density, the equation for the density becomes transcendental and requires an iterative solution. In Figure D.4, the sheath is considered “thick” for $r_p / \lambda_D \rightarrow 0$ and “thin” for $r_p / \lambda_D \rightarrow 100$. Additionally, an approximation to the curves in terms of X_p^* for j_i^* can be utilized. For example, in terms of a thick sheath approximation, the curve fit is given as

$$j_i^* \cong 1.127 \left(X_p^* \right)^{1/2} \quad (\text{D.6})$$

and since

$$X_p^* = \frac{e(V_{\text{plasma}} - V)}{kT_e} \quad (\text{D.7})$$

(D.6) and (D.7) are inserted into (D.5) to give

$$n_e [m^{-3}] \cong 1.42 \times 10^{15} \frac{I [\text{amps}] \sqrt{\mu [\text{amu}]}}{A_{\text{probe}} [m^2] \sqrt{(V_{\text{plasma}} - V) [\text{Volts}]}} \quad (\text{D.8})$$

which is independent of electron temperature. Furthermore, while the thick sheath case was selected as a starting point where $r_p / \lambda_D \rightarrow 0$, the curve could have been approximated for any of the ratios in Figure D.4 and the only change would be the numerical constant in (D.8). Additionally, because an iterative method to solution is being utilized, the only effect that the initial constant has is on the initial convergence, i.e., the initial ratio of r_p / λ_D will converge more quickly if the initial estimate for the density is “close” to the final solution. Approximations to the curves in terms of constants which can be used in (D.6) can be seen in Figure D.5. This representation is only used to illustrate that an approximation to remove the electron temperature in terms of X_p^* was originally given in the “thick” sheath case, though other approximations could be used which would not alter the final solution for the density.

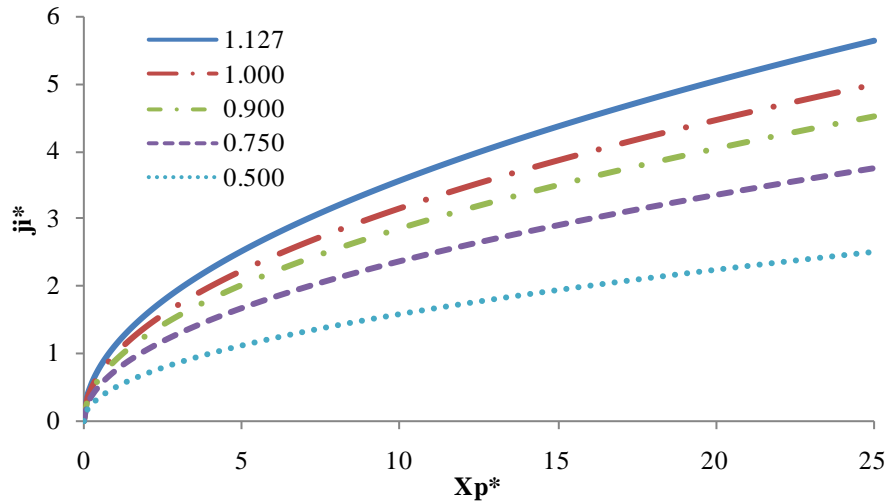


Figure D.5. Approximate constant values for probe radius to Debye length ratios.

Therefore, according to (D.5) or (D.8), the quantities to calculate the plasma density have been identified. As is the situation in most RF plasma IV characteristics, the difficult quantity to identify is the plasma potential. This also makes accurate measurement of the electron temperature difficult.

D.3 Plasma Potential, Electron Temperature, and Density

Typically, the plasma potential can be identified in two ways. Primarily it is done through identifying the “knee” in the IV trace, although, as seen from Figure D.3, this location can be ambiguous. Therefore, the next step is to calculate the derivative of the current with respect to voltage and find the maximum / minimum (depending on whether the current was taken to be positive or negative). However, the derivative method toward obtaining the plasma potential is often obscured in the transition region where there is a large amount of noise as is often the case in RF plasma. Therefore, the method used in this work is to first remove the ion current by approximating the ion current in the ion saturation region (through a parabola apex at the plasma potential V_{plasma}) and subtracting it from the total current. This leaves a trace for the electron current to the probe as a function of voltage. Then the log of the electron current vs. voltage can be plotted as shown in Figure D.6.

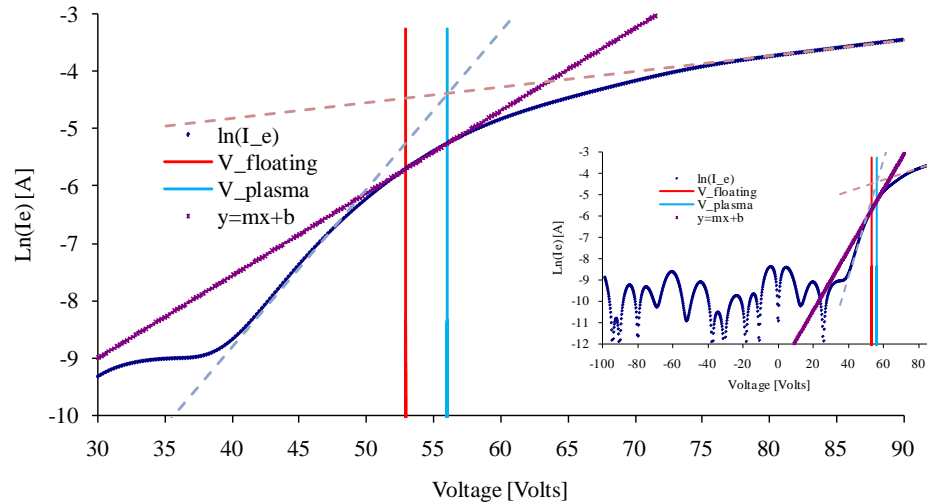


Figure D.6. Plot of $\text{Ln}(I_e)$ vs. Voltage for determine the plasma potential.

Approximating the linear region before the plasma potential and the linear region in the electron saturation region, the plasma potential is given by the intersection of the two

lines as shown in Figure D.6 to be $V_{\text{plasma}} = 56.03$ Volts. The floating potential (location where total current is zero; equal parts electron and ion current) is found from the IV characteristic, Figure D.3, as $V_{\text{floating}} = 52.87$ Volts. The approximation used to calculate the plasma potential is based on the correct subtraction of the ion current from the total current dependent on identifying the correct plasma potential. The values used to calculate the ion current can be adjusted, which will change the calculated electron current and alter the $\ln(I_e)$ graph, Figure D.6. Therefore, altering the approximation to the ion current will affect the value of the plasma potential and in turn the density; however, after a few iterations on subtracting the ion current, the plasma potential usually converges to a single value and has little affect on changing the value of the density. However, there will be a much more significant effect on using the plasma potential to obtain the electron temperature. The electron temperature is found from taking the inverse slope of a line drawn through the region between the floating and plasma potentials; also shown in Figure D.6. In this case, the slope of the line for this plasma potential results in an electron temperature of 6.96 eV; since this was a single data trace, the only error considered was the sheath / probe impedance for the collected saturation current. Utilizing the method described at the end of Chapter 4, the error calculated was 7.8 % resulting in a T_e of 6.96 ± 0.54 eV.

The next step in calculating the density is to insert the corresponding values with this temperature into (D.5). Using the plasma potential and electron temperature, along with an appropriate value for the ion saturation current at approximately

$$eV_{\text{sat}} = eV_{\text{plasma}} - X_p^* kT_e \quad (\text{D.9})$$

where letting $X_p^* = 15$, so that $V_{\text{sat}} \cong -50$ Volts and $r_p / \lambda_D \cong 7$ so that $j_i^* = 3$, the initial value for the plasma density according to (D.5) is $2.69 \times 10^{18} \text{ m}^{-3}$. The iterative method then proceeds based on the new value for the Debye length calculated from this density so that the new $r_p / \lambda_D \cong 12$ and $j_i^* = 2.8$. After 4 iterations, j_i^* changes by only a small amount and the final density is given by $n \cong 4.04 \times 10^{18} \text{ m}^{-3}$.

An alternative method of obtaining a first calculation for the density is to use the slope in the line of the I^2 vs. ΔV graph in accordance with (D.8).

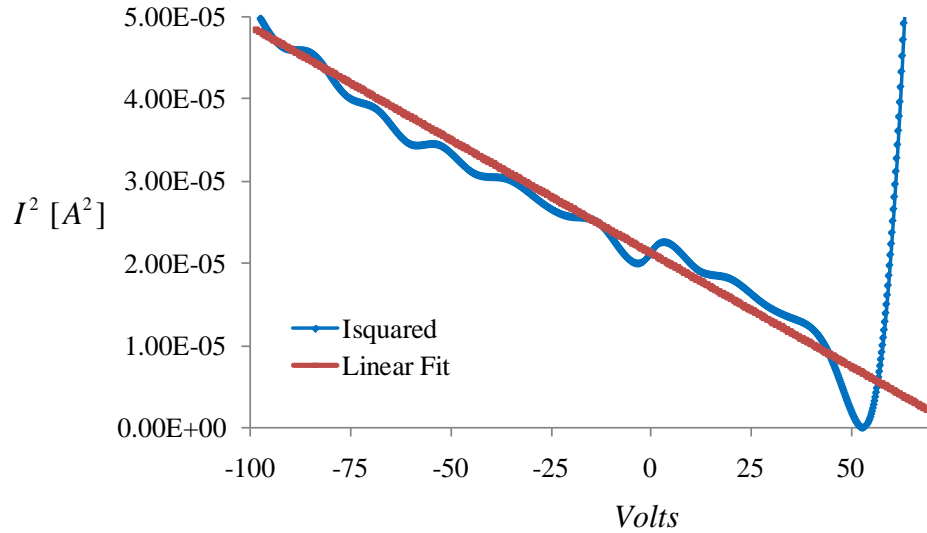


Figure D.7. Plot of I^2 vs. Voltage.

The slope can then be used in (D.8) as

$$n_e [\text{m}^{-3}] \cong 1.42 \times 10^{15} \frac{\sqrt{\mu [\text{amu}]} }{A_{\text{probe}} [\text{m}^2]} m_{\text{slope}} \quad (\text{D.10})$$

where $m_{\text{slope}} = \sqrt{\left| \frac{\Delta I^2}{\Delta V} \right|}$. Using this method, $m_{\text{slope}} = 5.26 \times 10^{-4}$ and $n \cong 1.74 \times 10^{18} \text{ m}^{-3}$.

This method gives a density (for this particular case) which is 35% lower than that calculated with the iterative Lafromboise method. The difference is explained by the fact the expression (D.8) uses the limit for $r_p / \lambda_D \rightarrow 0$ which is for a very “thick” sheath, whereas using the Lafromboise iterative method, the result for the density is based off a converged value of $r_p / \lambda_D \rightarrow 14.43$ and more accurately accounts for the effective ion collection area as opposed to the geometric area of the probe.

This method was implemented as obtained in an EXCEL workbook from Dr. Martin Neumann. Small variations were made to more efficiently analyze IV characteristics such as using the VLOOKUP function in EXCEL. However, all subjective user input data and graphical interpretation lies with the current author as it was the author’s responsibility to ensure accurate data interpretation in the analysis program.

D.4 References

- [1] D. N. Ruzic, *Electric Probes for Low Temperature Plasmas*, New York: The American Vacuum Society Education Committee, 1994.

APPENDIX E: μ WAVE INTERFEROMETER: CALIBRATION – ANALYSIS

This Appendix will address the analysis and derivation for obtaining the plasma density as a function of phase change measured by the interferometer signal which traverses the plasma column of chord length ' l '. The analysis as it is presented here is only unique in the sense of how the interferometer is setup. It should be widely applicable due to the general analysis as far as the separation of both interferometer branches referenced here as: I- and Q-.

E.1 AFRL's Microwave Interferometer

The general layout of AFRL's microwave interferometer is shown in Figure E.1

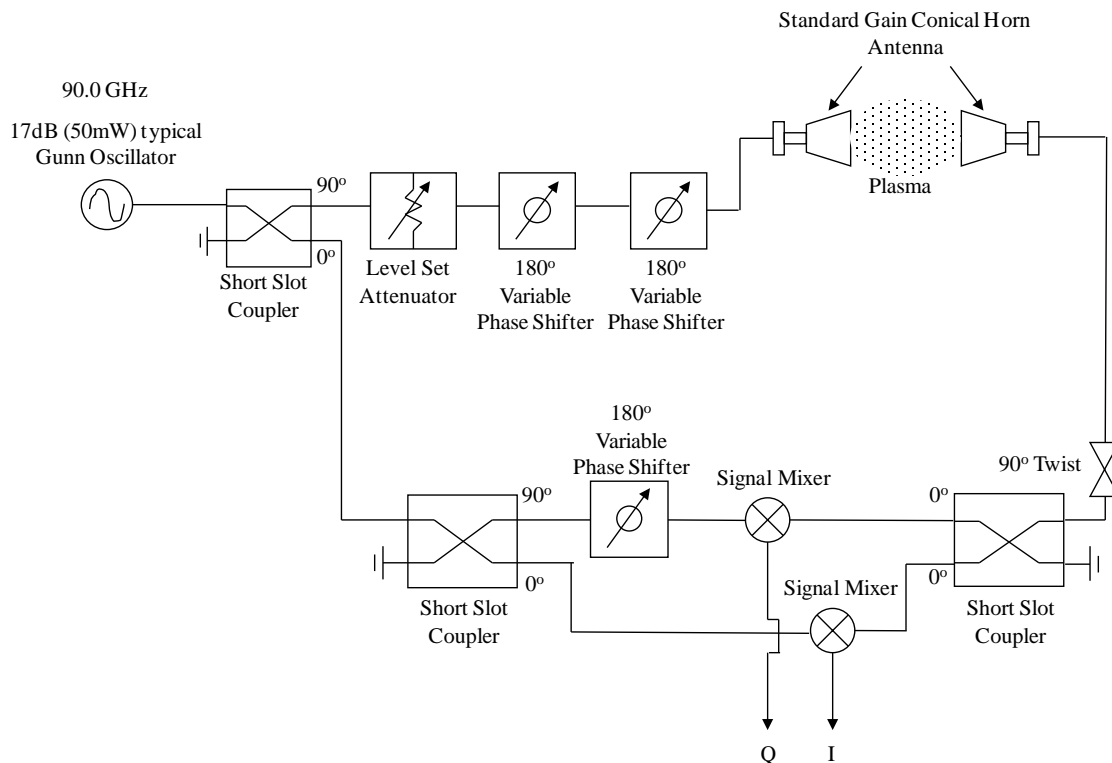


Figure E.1. Schematic of the millimeter I/Q Phase Bridge Interferometer.

The Gunn Oscillator launches a 90.0 GHz, 17dB (50mW) *sin* wave with a tuning bandwidth of 8 GHz and a frequency stability of 5 MHz. As the wave passes through the short slot coupler, it is split into two separate waves that are separated in phase by 90°. The first wave or the upper wave in Figure E.1 is transmitted at approximately 13 dB through the short slot coupler and phase shifted by 90°. This is the leg of the interferometer that will pass through the plasma. After being transmitted across the plasma length '*l*', the signal is again shifted 90° through a waveguide twist and separated through another short slot coupler. This is to ensure that the signal arriving at the right hand side of both the “I” and “Q” mixers in Figure E.1 are at the same phase angle. This is due to the 90° shift from the first short slot coupler and the additional 90° shift from the waveguide twist, i.e., ideally the phase change in the wave on the right hand side of the diagram is due to traversing the plasma and is only out of phase with respect to which it was originally, θ_{int} .

The bottom leg of the interferometer is only attenuated in power through the first short slot coupler. No phase shift is initially introduced until the signal is again separated through the second short slot coupler. The wave arriving at the “Q” mixer is shifted 90° by the second short slot coupler and the wave arriving at the “I” mixer is again unaffected in phase but attenuated in power.

The resulting waves arriving at the “I” mixer both have a zero degree phase shift. As a result the output voltage of this wave is given by:

$$V_{OUT_I} = A_I \sin(\theta) + V_{OFF_I} \quad (E.1)$$

where $V_{OFF,I}$ is some offset voltage introduced by supplying power to the mixer and A_I is the arriving amplitude of the combined waves due to their power attenuation from traveling through the short slot couplers and across the plasma.

Similarly, for the “Q” mixer, where the arriving waves are 90° out of phase, the output voltage is given by:

$$V_{OUT_Q} = A_Q \sin(\theta + 90^\circ) + V_{OFF_Q} \quad (E.2)$$

or

$$V_{OUT_Q} = A_Q \cos(\theta) + V_{OFF_Q} \quad (E.3)$$

where A_Q is again the arriving amplitude of the combined waves and $V_{OFF,Q}$ is the voltage offset due to the supply power.

It should be explained at this point that “ θ ” is the phase change due to all external factors including those changes due to traversing the plasma. Other factors or sources that could introduce phase errors result from non-uniformity in the path lengths between the two arms, vibrations in the room, temperature gradients throughout the waveguide, and any medium other than plasma between the conical gain horns such as a quartz tube or other obstruction. The motivation is now to isolate the phase change that is only due to the plasma. Once this is obtained, then following a suitable analysis, the radially integrated electron density can be obtained. However, because “ θ ” is due to all the sources of phase change,

$$\theta = \theta_{plasma} + \theta_{\Delta PathLength} + \theta_{Vibrations} + \theta_{etc.....} \quad (E.4)$$

we can rewrite this as,

$$\theta = \theta_{plasma} + \theta_0 \quad (E.5)$$

where θ_0 is the phase error due to all external sources which can be obtained through proper calibration.

At this point we can now solve (E.1) and (E.3) for the total phase change “ θ ”. (E.1)

becomes,

$$\sin(\theta) = \frac{V_{OUT_I} - V_{OFF_I}}{A_I} \quad (E.6)$$

and (E.3) becomes,

$$\cos(\theta) = \frac{V_{OUT_Q} - V_{OFF_Q}}{A_Q} \quad (E.7)$$

Dividing (E.6) by (E.7) we obtain,

$$\tan(\theta) = \frac{A_Q}{A_I} \frac{V_{OUT_I} - V_{OFF_I}}{V_{OUT_Q} - V_{OFF_Q}} = \beta \quad (E.8)$$

We can now rewrite the total phase shift in terms of its component parts as given by (E.5)

and separate out $\tan(\theta)$,

$$\frac{\sin(\theta_{plasma} + \theta_I)}{\cos(\theta_{plasma} + \theta_Q)} = \beta \quad (E.9)$$

Here, θ_I and θ_Q are the phase errors introduced to each mixer “I” and “Q” respectively,

not inclusive of the phase change due to the plasma.

Expanding the *sin* and *cos* in terms of their summation identities,

$$\sin(\theta_{plasma} + \theta_I) = \sin(\theta_{plasma})\cos(\theta_I) + \cos(\theta_{plasma})\sin(\theta_I) \quad (E.10)$$

$$\cos(\theta_{plasma} + \theta_Q) = \cos(\theta_{plasma})\cos(\theta_Q) - \sin(\theta_{plasma})\sin(\theta_Q) \quad (E.11)$$

Inserting (E.10) and (E.11) into equation (E.9) we obtain,

$$\frac{\sin(\theta_{plasma})\cos(\theta_I) + \cos(\theta_{plasma})\sin(\theta_I)}{\cos(\theta_{plasma})\cos(\theta_Q) - \sin(\theta_{plasma})\sin(\theta_Q)} = \beta \quad (E.12)$$

Multiplying the left hand side of (E.12) by $\frac{1/\cos(\theta_{plasma})}{1/\cos(\theta_{plasma})}$ we obtain,

$$\frac{\tan(\theta_{plasma})\cos(\theta_I) + \sin(\theta_I)}{\cos(\theta_Q) - \tan(\theta_{plasma})\sin(\theta_Q)} = \beta \quad (E.13)$$

Rearranging (E.13) we have,

$$\tan(\theta_{plasma})\cos(\theta_I) + \sin(\theta_I) = \beta\cos(\theta_Q) - \beta\tan(\theta_{plasma})\sin(\theta_Q) \quad (E.14)$$

Finally, solving in terms of $\tan(\theta_{plasma})$, we obtain,

$$\tan(\theta_{plasma}) = \frac{\beta\cos(\theta_Q) - \sin(\theta_I)}{\cos(\theta_I) + \beta\sin(\theta_Q)} \quad (E.15)$$

and the phase change due to the plasma is given by,

$$\theta_{plasma} = \tan^{-1} \left\{ \frac{\beta\cos(\theta_Q) - \sin(\theta_I)}{\cos(\theta_I) + \beta\sin(\theta_Q)} \right\} \quad (E.16)$$

Therefore, having an expression for the phase change due to the plasma, the remainder is left to calibration and measurement. Measurement will come in the form of a voltage deflection due to the presence of plasma or any other material between the conical gain horns, so at this point it is a matter of calibrating the phase errors and amplitude differences between both I- and Q- branches.

E.2 Calibration and Analysis

Calibration begins with voltage measurement of the I- and Q- signals when there is no plasma present. In the current calibration, the quartz tube is within the conical gain horns in order to get a baseline calibration so that later the only change between the horns will be the presence of Argon plasma. Calibration encompasses inserting a Mica sheet within the 'top' branch of the waveguide. By slowly moving a well-known material incrementally further into the waveguide, this causes the traversing wave to be phase shifted, i.e., simulating a plasma deflection although in this case, we are performing a calibration over a full 360 degree rotation accomplished by moving the Mica sheet. The raw data signal of performing this is shown in Figure E.2 where the vertical line represents the location where data will be taken, i.e, after the Mica sheet has induced a full 360 degree wave phase shift, the Mica was then reinserted to a known 'phase location'. This location was selected as a point where both branches were nearly 90 degrees out of phase with respect to each other so as to minimize large phase errors that could otherwise be introduced.

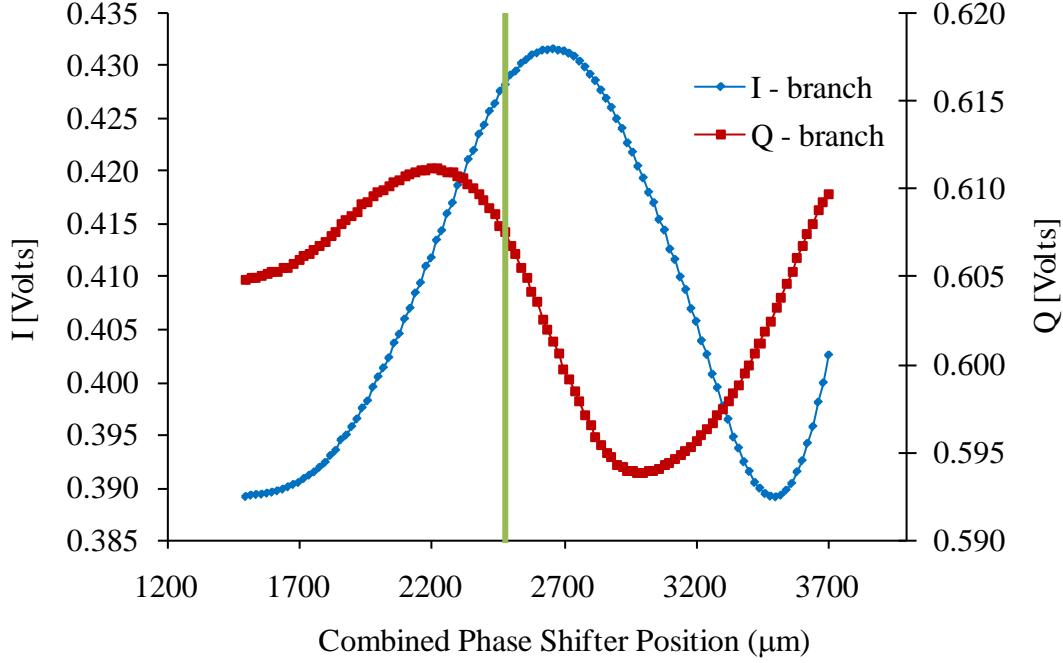


Figure E.2. Raw signals from both I- and Q- branch as the Mica sheet is incrementally inserted further into the waveguide causing a phase shift.

The next step is to calculate the signal amplitude. This is most easily accomplished by removing the average voltage offset V_{OFF_I} and V_{OFF_Q} then taking $\frac{1}{2}$ the difference between the maximum and minimum values. In this case, the wave amplitudes and offsets for use in (E.8) for calculation of β are $A_I = 21.3$ mV, $A_Q = 8.7$ mV, $V_{OFF_I} = 410.34$ mV, and $V_{OFF_Q} = 602.50$ mV. The amplitudes are not equal because both signals are attenuated differently as they traverse their respective path lengths and short slot couplers while the voltage offsets are also not equal due to small differences in the mixer electronics, most likely circuit impedances.

The final step is to calibrate the phase shifts in each branch which are the result of path length differences, presence of quartz tube, thermal effects, mechanical vibrations, and any other such external influences. In the ideal case where there would be no Mica sheet

for calibration, data would be taken at the zero location as shown with the normalized data in Figure E.3.

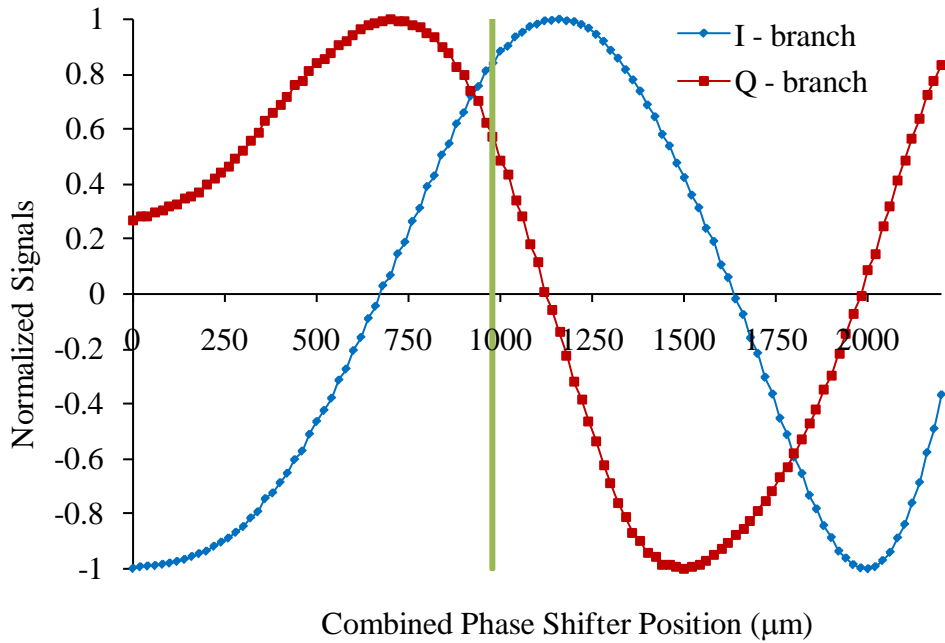


Figure E.3. Normalized and horizontally shifted I- and Q- branches as the Mica sheet is traversed across the waveguide.

Clearly, these waves at the zero location are not pure *sin* or *cos* waves as would be expected. In fact, at the zero location they are significantly shifted from their ideal behavior. The I-branch (*sin*) does not start to behave like a (*sin*) wave until the Mica sheet is inserted approximately 680 μm into the waveguide while the Q-branch (*cos*) does not behave ideally until approximately the same location. Therefore, it was decided to move the Mica sheet to a location (fairly arbitrary yet easily quantifiable) in the region where the wave behavior more nearly resembles the ideal behavior. To do this, both normalized waves were 2π scaled and the location corresponding to the Mica sheet insertion was obtained. The result is shown in Figure E.4.

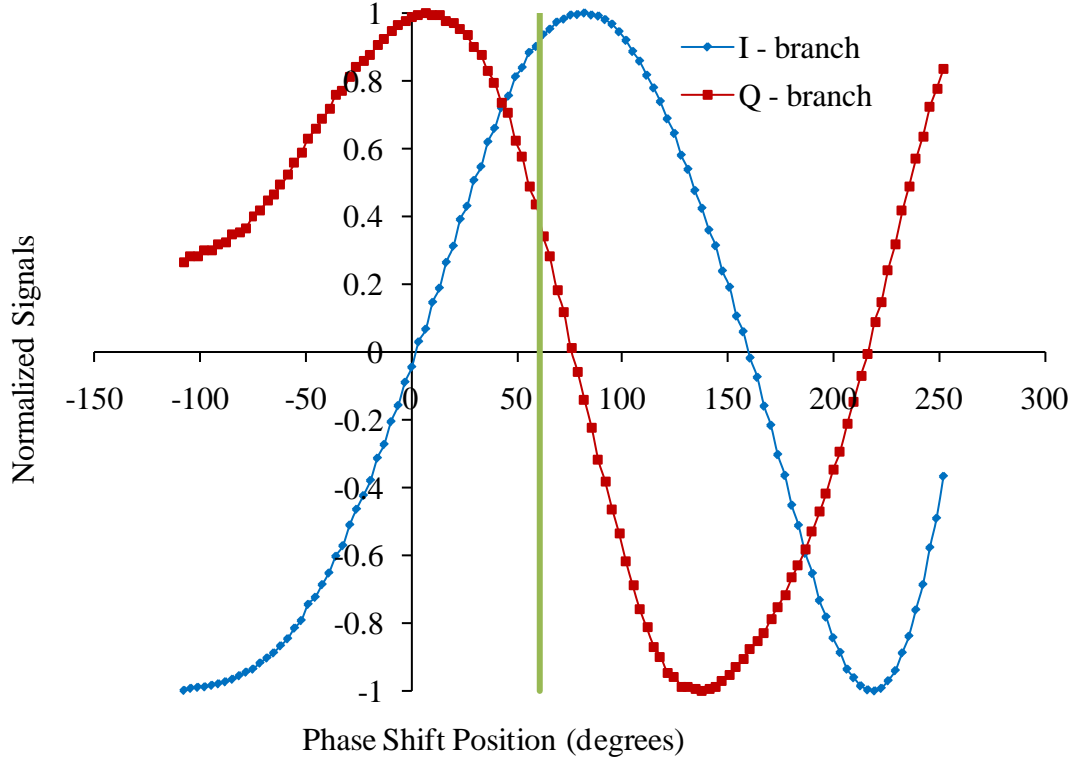


Figure E.4. Normalized and 2π scaled location of the Mica sheet insertion for the point where interferometry data was taken.

The resulting shift in the I-branch (\sin) was $\theta_I = 62.08$ degrees while the Q-branch (\cos) $\theta_Q = 60.79$ degrees.

With the calibration values now obtained (A_I , A_Q , θ_I , and θ_Q) for use in (E.16), a plasma deflection will induce a voltage difference so that θ_{plasma} can be calculated. As an example, consider the voltage deflection due to 500 Watt inductive plasma as shown in Figure E.5. The average voltage deflections are measured as $\Delta V_{I_{\text{AVG}}} = 2.31 \text{ mV}$ and $\Delta V_{Q_{\text{AVG}}} = 0.42 \text{ mV}$. With the above calibration values, (E.16) can then be used to obtain $\theta_{\text{plasma}} = 7.88 \text{ degrees} = 0.1375 \text{ radians}$. This can then be used to calculate the chord-averaged plasma density in the usual manner i.e.,

$$\frac{-}{n_e} = \frac{4\pi m_e \epsilon_0 c^2}{e^2} \frac{\Delta \theta_{plasma}}{\lambda_0 l} \quad (\text{E.17})$$

where λ_0 is the wavelength corresponding the 90 GHz frequency ~ 3.33 mm and ' l ' is the path length of the plasma, in this case ~ 5 cm. Substituting the values yields a plasma density of $\sim 2.93 \times 10^{17} \text{ m}^{-3}$.

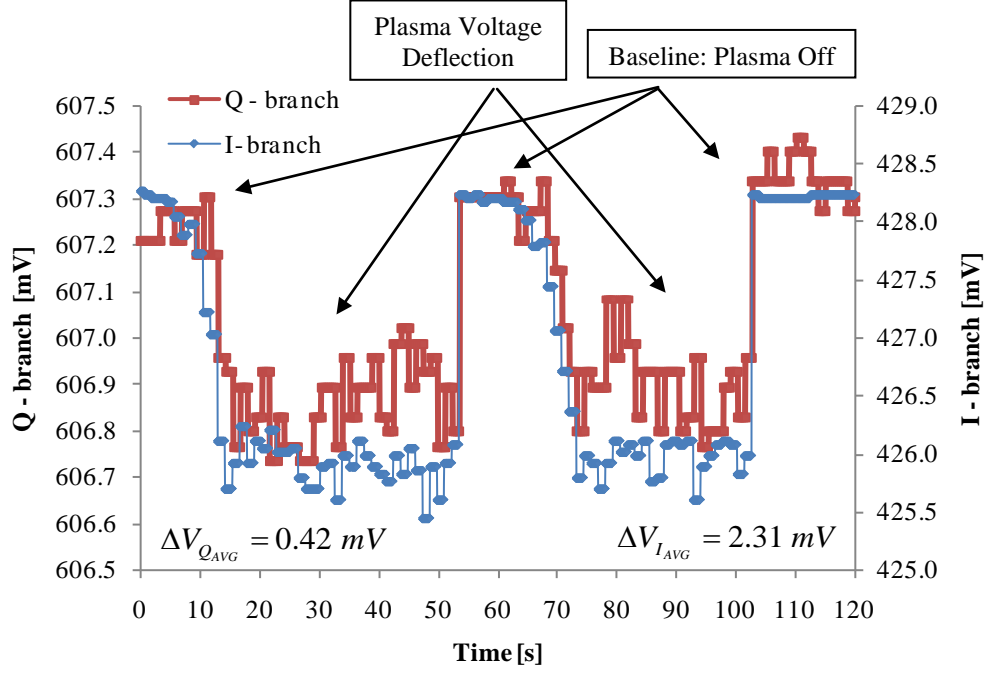


Figure E.5. Voltage deflections in the I- and Q- branches of the microwave interferometer used to obtain β .

APPENDIX F: RADIAL b_z FIELDS – PRESSURE, POWER, MAGNETIC FIELD

This Appendix compares the differences between the measured radial b_z profiles and those predicted by considering the numerical solutions to a non-uniform radial density profile. In each case shown in Figure F.1 – Figure F.6, the GREEN border cases demonstrate strong agreement with the predicted fields. The “w” value for each predicted profile refers to width of the input Gaussian density profile. YELLOW border cases indicate what would be interpreted as a helicon wave profile had the probe not interfered with the wave as the probe was radially scanned. All scans took place underneath the end ring of the “downstream” antenna. RED border cases illustrate a flat profile where power (density) and / or magnetic field conditions were insufficient for the medium to support helicon wave propagation. Additional conditions were considered for the case of 0.5 mTorr primarily as an investigation into reported helicon double layers. All conditions investigated at 0.5 mTorr demonstrated no wave propagation indicative of the increased difficulty in propagation of helicon waves at lower pressures; difficulty in terms of power and / or magnetic field requirements as compared to higher pressure cases. Not all conditions within each power – magnetic field matrix were investigated after the determination of “no-wave propagation” below a minimum power or magnetic field was made.

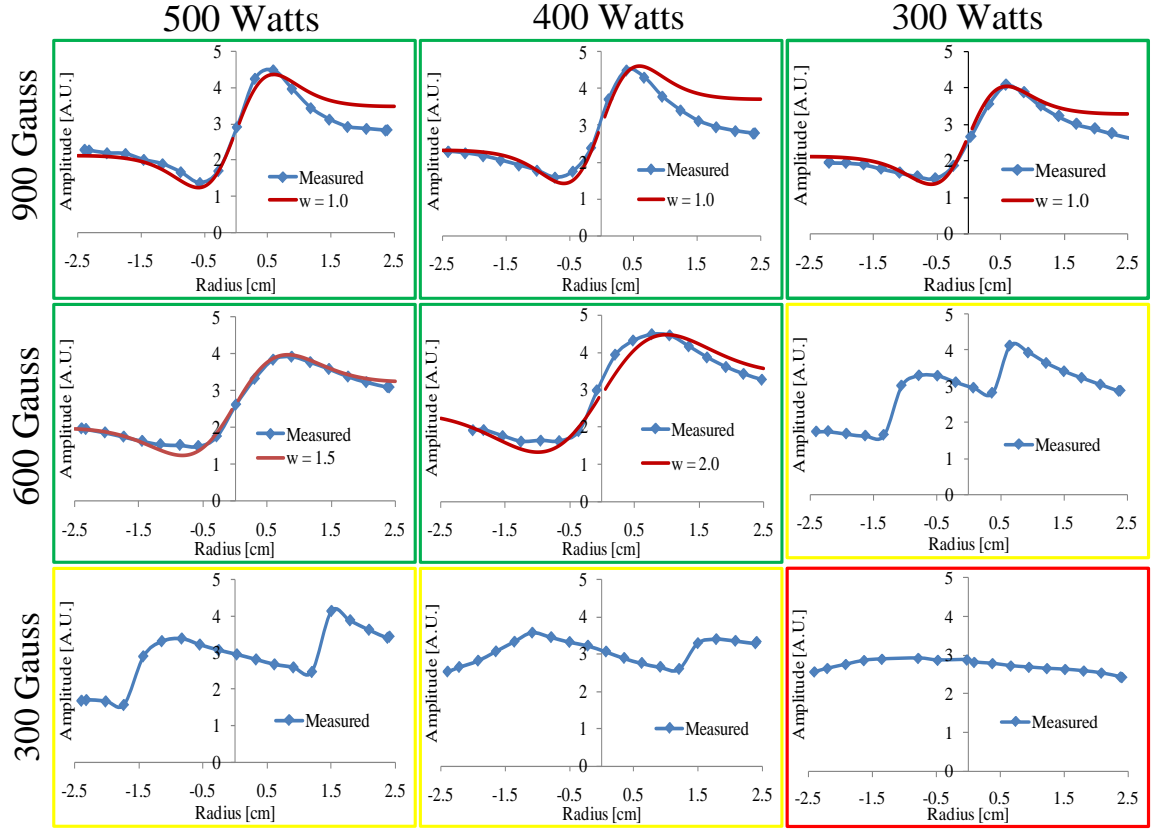
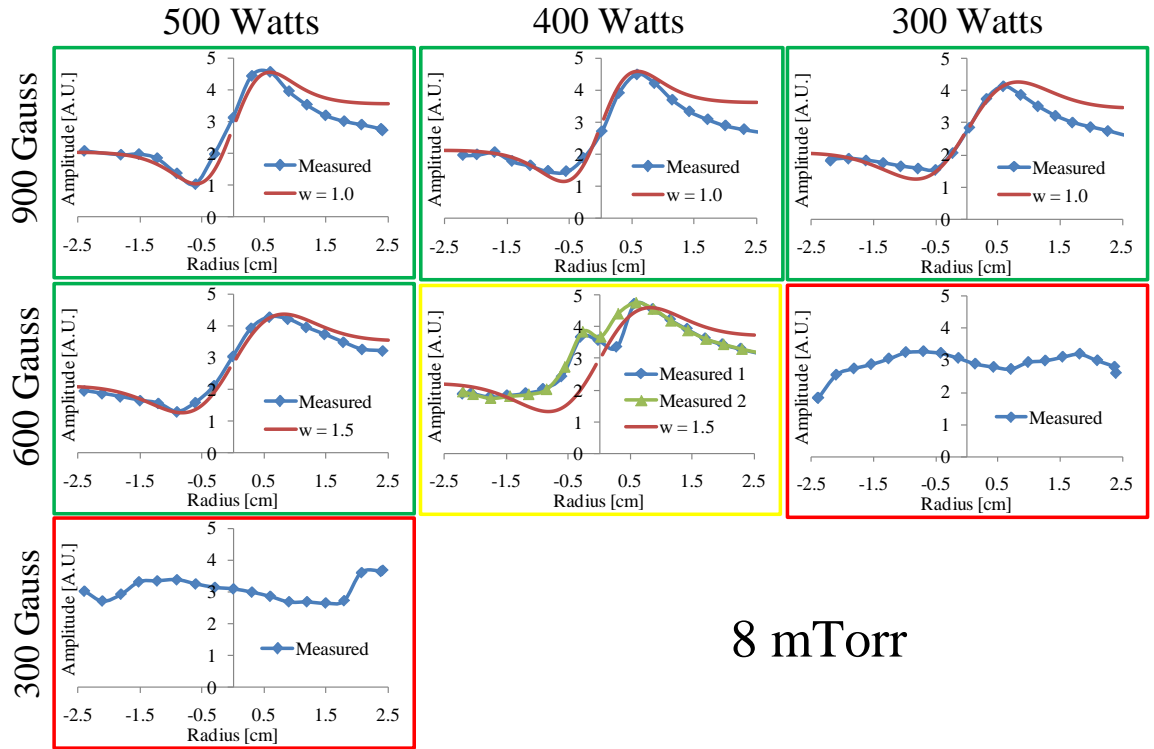


Figure F.1. b_z profiles at 10 mTorr and various input power and magnetic field strengths.



8 mTorr

Figure F.2. b_z profiles at 8 mTorr and various input power and magnetic field strengths.

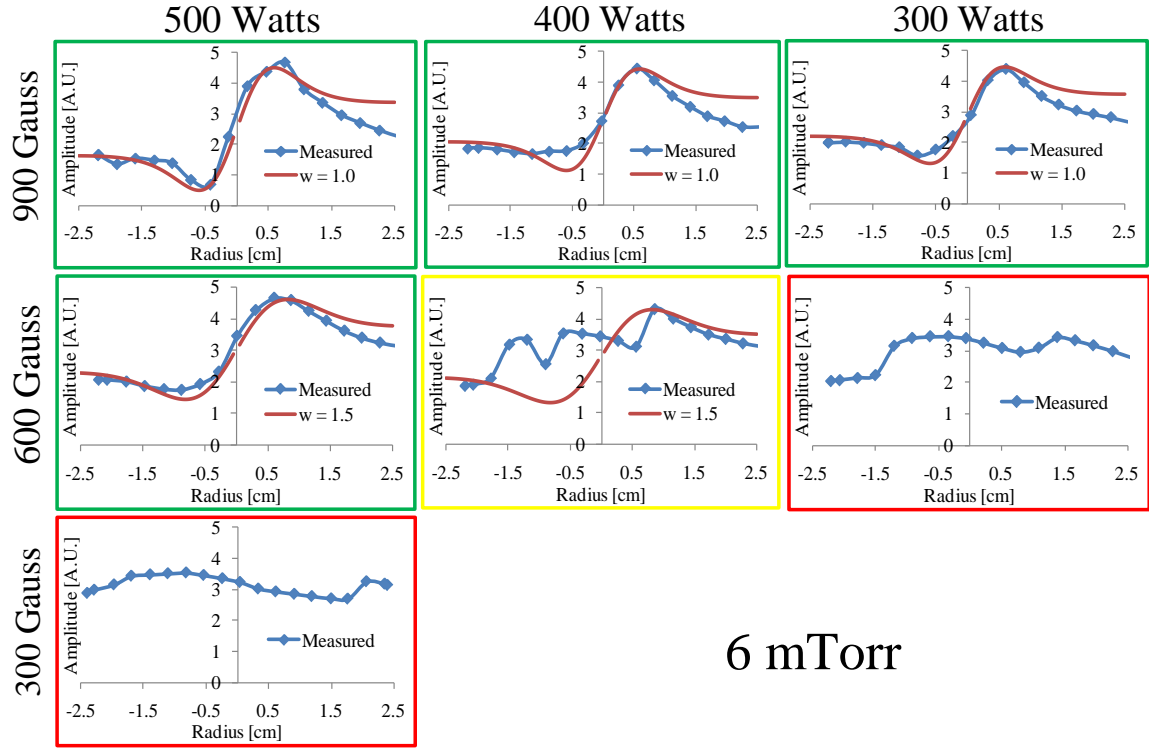


Figure F.3. b_z profiles at 6 mTorr and various input power and magnetic field strengths.

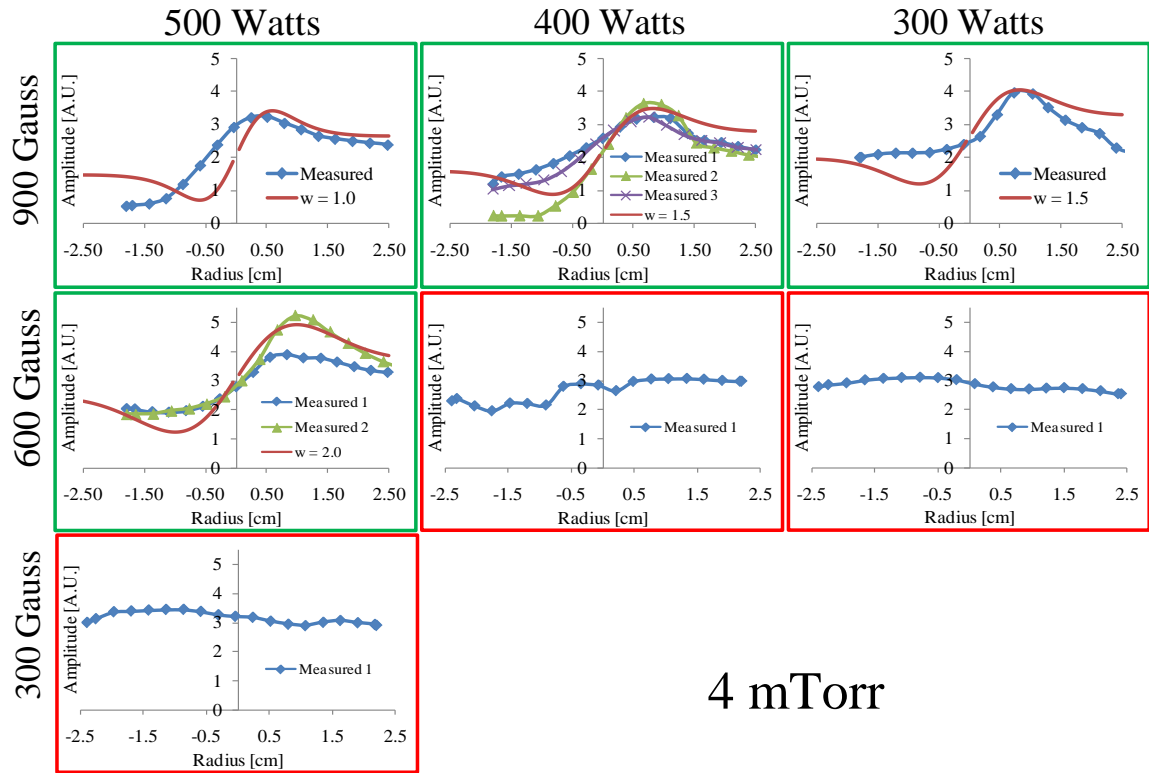


Figure F.4. b_z profiles at 4 mTorr and various input power and magnetic field strengths.

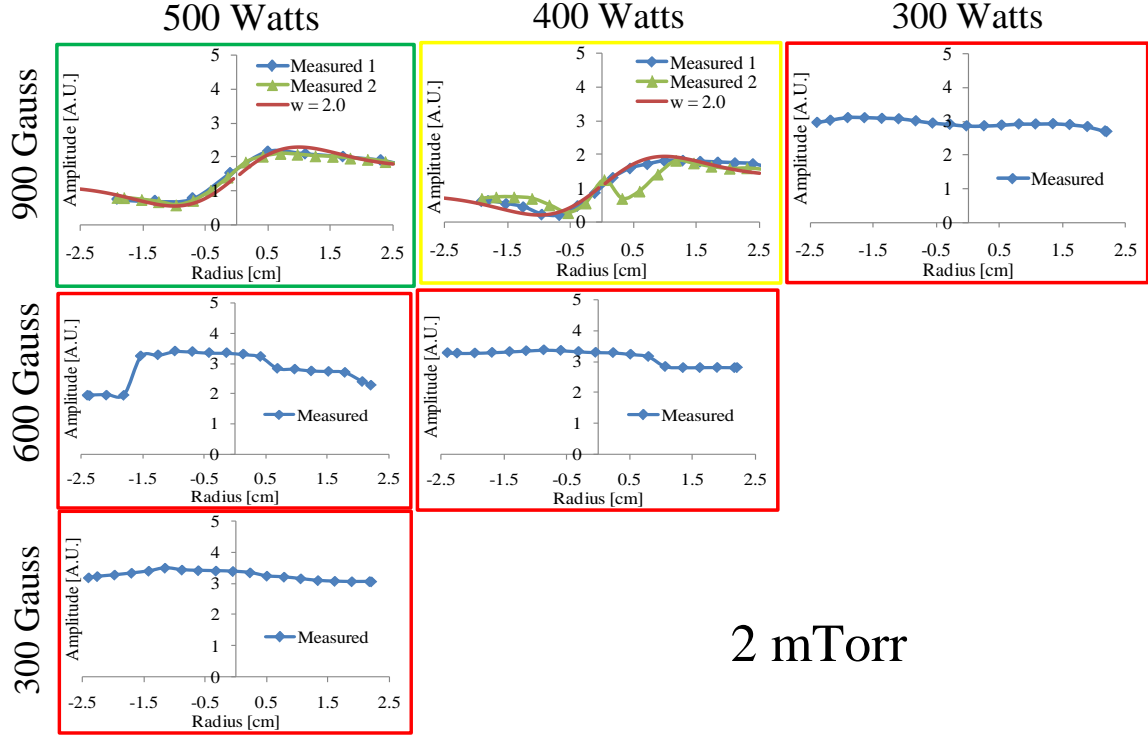


Figure F.5. b_z profiles at 2 mTorr and various input power and magnetic field strengths.

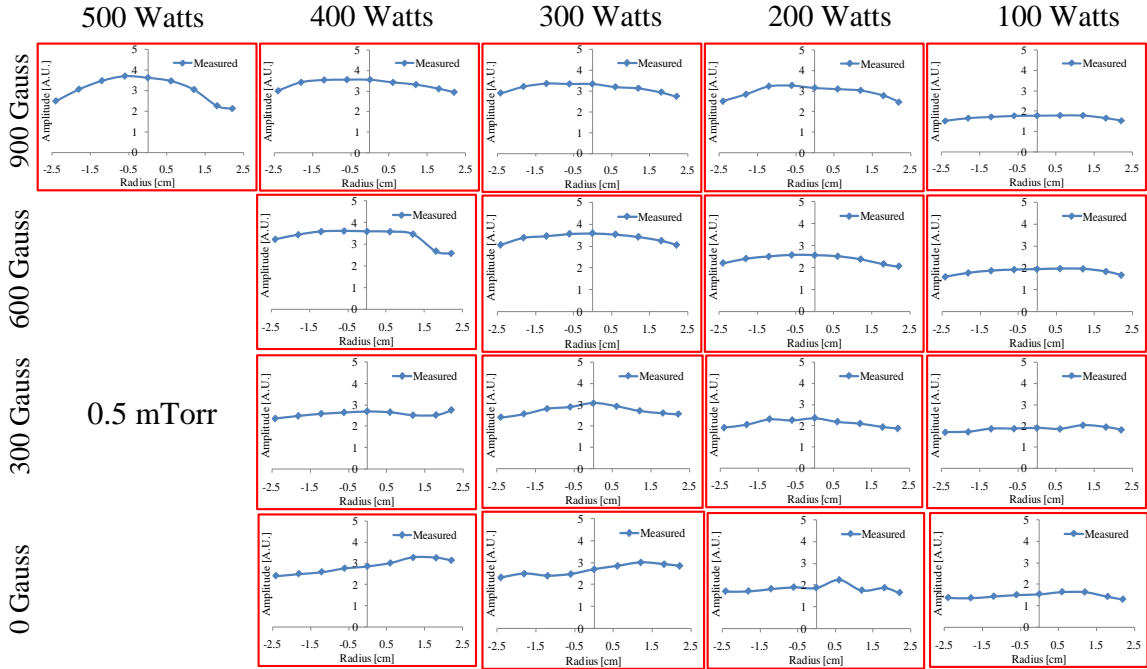


Figure F.6. b_z profiles at 0.5 mTorr and various input power and magnetic field strengths.

Michael Patrick Reilly
University of Illinois @ Urbana-Champaign
Department of Nuclear, Plasma, & Radiological Engineering
5105 West 105th Place
Oak Lawn, IL 60453
Cell: (708) 951-1100
mreilly@illinois.edu

EDUCATION

Ph.D. University of Illinois @ Urbana-Champaign
Nuclear, Plasma, & Radiological Engineering, August 2009
Dissertation: “*Three Dimensional Imaging of Helicon Plasma Waves via Magnetic Induction Probes*”
Research Advisor: Professor George H. Miley

M.S. University of Illinois @ Urbana-Champaign
Nuclear, Plasma, & Radiological Engineering, October 2005
Thesis: “*Investigation of Plume Expansion and Surface Characterization of a Micro Laser Plasma Thruster for Satellite Application*”
Research Advisor: Professor George H. Miley

B.S. University of Illinois @ Urbana-Champaign
Aeronautical & Astronautical Engineering, August 2003

EXPERIENCE / RECENT POSITIONS

Research Scientist: Air Force Research Laboratory,
Electric Propulsion Laboratory, Edwards AFB, CA. May 2004 – Current

DoD Secret Clearance

Helicon Waves and Radio Frequency Plasma Discharges.

- Extensive 3-D imaging of helicon plasma waves for quantifying and visualizing the helicon wavelength
- Work on the design of RF source geometries with specific attention to diagnostics for probes in mid-high frequencies: *b-dot / RF Langmuir / microwave interferometry* (b_r , b_θ , b_z / plasma density / electron temperature)
- Provide routine in-house written and oral presentations of ongoing research
- Responsible for designing and building the Electric Propulsions RF plasma facility (~50k initial budget)
- Responsible for tasking and overseeing the work and progress of summer hires and Air Force cadets
- Electrostatic discharge site monitor for Electric Propulsion Laboratory ensuring all equipment & personnel work up to date and compliant

Micro Laser Plasma Thruster.

- Work on millisecond ablation of polymer targets
- Assess viability for future small satellite use

Research Engineer: Starfire Industries LLC.

Champaign, IL. January 2005-May 2006

Pseudo Spark Plasma Switch; fast optical triggering of plasma for EUV applications

- Responsible for daily laboratory activities including data collection and assisting with reports as part of Small Business Innovation Research (SBIR) contracts

Teaching Assistant: Nuclear, Plasma, & Radiological Engineering

UIUC. Aug 2003-Dec 2003

Materials in Nuclear Engineering.

Research Assistant: Air Force Research Laboratory, Electric Propulsion Lab, Edwards

AFB, CA. May 2003-Aug 2003.

Internship working on Micro Pulsed Plasma Thrusters for Air Force Satellites.

- Work on the construction and testing of coaxial designed thrusters through laser interferometry (single color), surface thermography, and pulsed currents

JOURNAL PUBLICATIONS

M. P. Reilly, W. Lewis, and G. H. Miley, "Magnetic field probes for use in radio frequency plasma," *Review of Scientific Instruments*, vol. 80, no. 5, pp. 053508-5, 2009.

M. P. Reilly, G. H. Miley, and W. A. Hargus, "Plume Expansion and Ionization in a Micro Laser Plasma Thruster," *Journal of Propulsion and Power*, vol. 24, no. 1, pp. 7, 2008.

PRESENTATIONS / CONFERENCE PAPERS

G. H. Miley, H. Momota, L. Wu, Reilly, M., *et al.*, "IEC Thrusters for Space Probe Applications and Propulsion." Space, Propulsion & Energy Sciences International Forum: SPESIF, 2009, pp. 164-174.

M. P. Reilly, G. H. Miley, D. E. Kirtley *et al.*, "Effects of Helicon Wave Propagation Based on a Conical Antenna Design: Part I," in The 30th International Electric Propulsion Conference, Florence, Italy, 2007, pp. 17.

D. E. Kirtley, A. D. Gallimore, J. Haas, Reilly, M., "High Density Magnetized Toroid Formation and Translation within XOCOT: An Annular Field Reversed Configuration Plasma Concept," in The 30th International Conference on Electric Propulsion, Florence, Italy, 2007, pp. 19.

M. P. Reilly, G. H. Miley, and W. A. Hargus, "Plume Expansion and Ionization in a Micro Laser Plasma Thruster," in 41st AIAA/ASME/SAE/ASEE Joint Propulsion Conference & Exhibit, Tucson, Arizona, 2005, pp. 13.

RESEARCH INTERESTS

RF / high frequency plasma and diagnostic development, high energy density plasma, fusion concepts (magnetic and inertial), plasma wave-particle interactions, pulsed electronics

PROFESSIONAL SOCIETIES

American Physical Society, American Institute of Aeronautics and Astronautics, American Nuclear Society

CURRENT SUPPORT

Research support is provided by the Air Force Research Laboratory at Edwards AFB, CA

REFERENCES

Excellent references available upon request